2013

Ternary III-Nitride Semiconductors for Thermoelectricity and Light Emitters

Jing Zhang
Lehigh University

Ternary III-Nitride Semiconductors for Thermoelectricity and Light Emitters

by

Jing Zhang

Presented to the Graduate and Research Committee of
Lehigh University
in Candidacy for the Degree of
Doctor of Philosophy

in

Electrical Engineering

Lehigh University

September 2013

Dissertation Signature Sheet

Approved and recommended for acceptance as a dissertation in partial fulfillment of the requirements for the degree of Doctor of Philosophy.

_____
Date

_____
Prof. Nelson Tansu
(Ph.D. Advisor)

_____
Accepted Date

Committee Members:

_____
Prof. Nelson Tansu
(Committee Chair)

_____
Prof. Filbert J. Bartoli

_____
Prof. Yujie Ding

_____
Prof. Michael J. Stavola

Acknowledgements

During my Ph.D. studies in Lehigh University since August 2009, I have received a lot of help from people surrounding me. First of all, I would like to express special thanks to my Ph.D. advisor, Prof. Nelson Tansu. Prof. Tansu is the person who introduced me to the field of III-Nitride semiconductors, which have important applications for photonics, optoelectronics and thermoelectricity. As my Ph.D. advisor, Prof. Tansu has been spending countless hours to teach me knowledge and skills in order for me to grow quickly into a mature and outstanding researcher in the field of III-Nitride semiconductors. In addition to that, I was given a lot of precious opportunities ever since the first beginning of my Ph.D. studies in Lehigh. Ever since my second semester at Lehigh, I went to a conference to give a presentation already. Thus, I was able to travel to multiple conferences every year to present my research works, discuss with researchers in the field, and know excellent professional colleagues from different institutions, which is very helpful and beneficial for me in order to grow into a mature researcher. In addition to that, I was very fortunate to have access to the state-of-the-art facilities in Lehigh such as the metalorganic chemical vapor deposition (MOCVD) reactor, the clean room facility, as well as the characterization equipments. The MOCVD lab was set up by Prof. Tansu and the early students in our group, and I appreciate the chance to work on research projects by using the MOCVD reactor in house in Lehigh. Other than technical aspect, Prof. Tansu always pays a lot of attention to maximize the potential of each student, and he always tries his best to improve every aspects of the student. Prof. Tansu also serves as an important role that always inspires us and teaches us to become strong, confident and independent individuals, so that we can be very ready for future positions either in industry or academia.

I am also thankful that Prof. Bartoli, Prof. Ding, and Prof. Stavola would serve as my Ph.D. committee, who have spent valuable time with me and offered me helpful suggestions.

I would like to express sincere thanks to my seniors in Prof. Tansu's group: Dr. Ronald A. Arif, Dr. Yik-khoon Ee, Dr. Hua Tong, and Prof. Hongping Zhao. Specifically, Dr. Arif and Dr. Ee have spent a lot of efforts in order to set up the MOCVD system. Dr. Hua Tong is the senior student worked very closely with me for the projects toward III-Nitride thermoelectricity, who taught me a

lot of basic knowledge and skills on this topic. Prof. Hongping Zhao serves as a very good example for me, as I also want to pursue an academic career after Ph.D. graduation. Hongping worked closely with me on the topic of ultraviolet lasers, and she also taught me knowledge on theory of III-Nitride semiconductor physics. Besides, she also offered a lot of help for me during my first two years in Lehigh. Special thanks will go to Guangyu Liu, who has the most overlap with me during my Ph.D. studies in Lehigh. Guangyu is one year senior than me, and she is always very patient and willing to offer help to others. We have also spent a lot of time together working on the reactor, including a lot of MOCVD growths and maintenance works. We have had countless discussions on our research projects when we encounter difficulties, and we also encourage each other during difficult times. I am also thankful to our current group members, Peifen Zhu and Chee-Keong Tan, as well as undergraduate students working in our lab: Peter O. Weigel and Nicholas Lay. I would also like to thank our past postdoctoral research fellows, Dr. Mohammad Jamil, Dr. Gensheng Huang, and Dr. Rengbo Song, from whom I have learnt a lot toward MOCVD reactor maintenance. I am grateful to our cleanroom manager Anthony Jeffers, who provided me training on various cleanroom equipments, who also helped me to resolve problems during fabrication processes. In addition, I want to thank our past group members who have shared time with me in the lab and offered me help: Dr. Marco Mastrapasqua, Takahiro Toma, Xiao-Hang Li, Tidapan Sursattayawong, Vincent Handara, Shaofei Zhang, Joseph Mulhern, and NanLung Wu. I would also like to thank Ms. Anne L. Nierer, who used to be our secretary of the center, had offered assistances in many ways for us.

Most importantly, I would like to thank my parents for their unconditional love, support, and strong faith in me during my four years in Lehigh. My father, Mr. Ming Zhang (张明) has always being served as a role model for me, who is very brave, hard-working, and accomplished. My mother, Ms. Yunping Liu (刘郧萍), who is a very graceful lady, has always offered me great love, patience, care, and support. Without my dear parents, I can hardly become who I am today. I am also very grateful for my dear friends surrounding me, especially during the beginning of my graduate study. I am very fortunate to have lots of people supporting and helping me in pursuing my academic and research goals.

Table of Contents

List of Tables

Page

List of Figures

Abstract

III-Nitride semiconductors have significant applications for lasers and energy-efficient technologies including solid state lighting. Specifically, the use of InGaN alloy is of great interest as visible light emitting diodes (LEDs) active region. Conventional LEDs employ InGaN quantum wells (QWs) grown on GaN templates, which lead to large QW strain from the lattice mismatch between InGaN QW and GaN substrate / barriers. Our works have pursued the design of InGaN QWs with large optical matrix element to address the charge separation issue, resulting in 3X enhanced efficiency for green-emitting LEDs. In addition to employing large overlap QWs design, my research work has extended the approach by using ternary InGaN substrate for realizing QWs with reduced strain and polarization fields in the QWs. For green- and red-emitting InGaN QWs on ternary substrate, the spontaneous emission rates were found as ~3 times of the conventional approach.

In contrast to the progress in visible nitride emitters, advances have only been realized for ultraviolet (UV) LEDs recently. The pursuit of efficient UV lasers has been limited to 1) growth challenges of high quality AlGaN gain media; 2) lack of understanding in gain characteristics of the QW employed for UV laser. My work has pointed out the first time about the physical challenge of the AlGaN QWs, which is related to the valence subbands crossover in high Al-content AlGaN QWs gain media. The valence subbands crossover is of key importance to realize large transverse-magnetic polarized gain for deep-UV lasers. We have also proposed the novel AlGaN-delta-GaN QW structure, which led to large transverse-electric polarized gain for mid-UV lasers.

Furthermore, the high power density requirements in III-Nitride devices lead to the demand of solid state cooling technology, particularly for nitride-based thermoelectric materials that can be integrated with GaN devices. Our works presented the high thermoelectric figure of merit Z^*T value from lattice-matched AlInN alloy grown by metalorganic chemical vapor deposition (MOCVD), which represent the record Z^*T value reported for any III-nitride semiconductors. In addition, we have proposed the novel nanostructure engineering of three-layer superlattice for ~2-times enhanced thermoelectric properties for solid state cooling applications.

Chapter 1: Introduction to III-Nitride Semiconductors

1.1 Nitride-based Semiconductors for Energy Applications

III-Nitride semiconductors (AlN, GaN and InN) have great importance in laser diodes and energy-related application. Significant advances in the III-Nitride materials have led to applications for lasers and light-emitting diodes (LEDs) for solid state lighting [1-20], thermoelectricity [22, 23], high power transistors [21] and solar cells [24-26]. The progress and development in those fields will be reviewed in details in the following sections.

1.1.1 Solid-State Lighting (SSL)

Solid State Lighting (SSL) technology has the potential to reduce U.S. lighting energy usage by nearly one half and contribute significantly to the nation's climate change solutions, as stated by the U.S. Department of Energy (DOE) [27], which encourages research and development breakthroughs in efficiency and performance related to SSL.

Different from conventional incandescent bulbs (which use thermal radiation) or fluorescent tubes, SSL refers to light emitted by solid-state electroluminescence from Light Emitting Diodes (LEDs) or Organic Light Emitting Diodes (OLEDs) [27], while the use of LEDs has attracted more attention due to the faster research and development progress.

Light Source	Range of Typical Rated Life (hours)* (varies by specific lamp type)	Estimated Useful Life (L_{70})
Incandescent	750-2,000	
Halogen incandescent	3,000-4,000	
Compact fluorescent (CFL)	8,000-10,000	
Metal halide	7,500-20,000	
Linear fluorescent	20,000-30,000	
High-Power White LED		35,000-50,000**

Figure 1-1: *Summary of life time of conventional light sources and LEDs. [28]*

There are several superior advantages by the use of LEDs, such as directional light emission, compact profile, superior optical control, energy efficiency, breakage resistance, reduced

maintenance, and long lifetime [28]. Figure 1-1 shows the comparison of life time of conventional light sources and white LED. For the compact fluorescent (CFL) lamp, the longest life time is estimated as 10,000 hours; while for the fluorescent lamp, the longest life time is estimated as 30,000 hours, which are only ~20%-60% for the life time of high-power white LED.

Therefore, by switching lighting to LEDs, it is estimated that the energy costs in the nation will be reduced by $250 billion over the next two decades, and the electricity consumption for lighting will be reduced by nearly one half, as shown in figure 1-1. In addition, the market of LED lighting will be increased significantly, which is expected to represent 36% of lumen-hour sales on the general illumination market by 2020, and grow to 74% by 2030. [29]

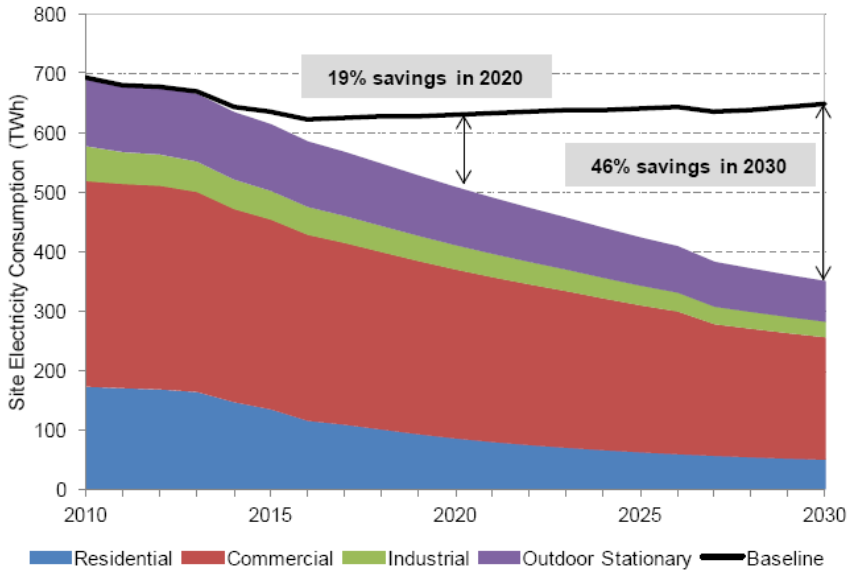

Figure 1-2: *Forecasted U.S. Lighting Energy Consumption and Savings, 2010 to 2030 [29].*

In order to be used as general light source, high-performance white LEDs are required [30]. Since LEDs emit nearly monochromatic light, in contrast with incandescent and fluorescent lamps, which will lead to applications such as traffic lights and exit signs.

There are generally three ways to generate white light from the use of LEDs, as illustrated in figure 1-3 [1, 30]. The first method is by using phosphor-converted LEDs (pc-LEDs). There are two straightforward ways to realize white pc-LEDs: 1) UV LED (emission wavelength λ~ 400 nm) with blue ($Ca_{10}(PO_4)_6Cl_2:Eu^{2+}$) and yellow (YAG: Ce^{3+}) phosphors [31], and 2) blue LED (λ~ 440-460 nm) with yellow (YAG: Ce^{3+}) phosphor [1]. The pc-LEDs will lead to the color rendering index

(CRI) [32] of ~70-80, which are suitable for less demanding applications such as outdoor lighting [1]. The second method is to use the “multichip” approach by combining red, green, and blue (RGB) LEDs, which will result in white light emission. The three color system (RGB) will lead to CRI values of 85 or less [33]; while the use of four-color (RYGB) system can achieve CRI > 95 [34]. Those multichip white LEDs will be suitable for applications such as indoor illumination that requires CRI > 80 [1]. The third method is the use of hybrid LED approach, which combines green phosphor with red and blue LEDs, since currently the LED performance is most limited in the green–yellow region [1].

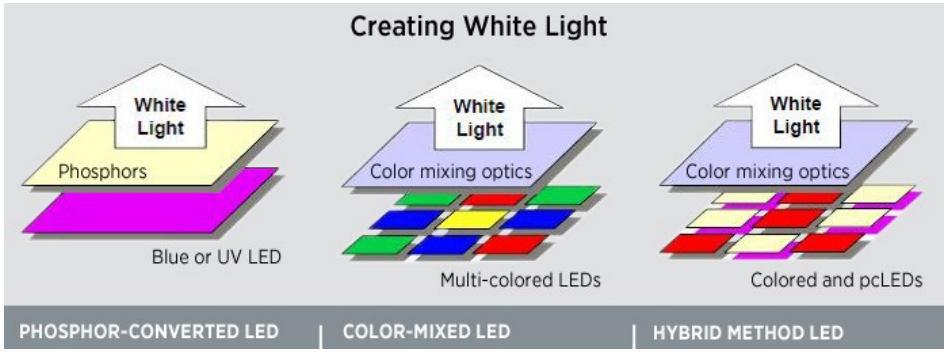

Figure 1-3: *Illustration of three ways to create white light by LEDs [30].*

The III-Nitride semiconductors are widely used for blue and green LEDs. The typical Nitride-based LED structure employing InGaN as active region is shown in figure 1-4. The major breakthrough for InGaN-based blue LEDs was in the early 1990s, which is the first demonstration of the efficient and reliable blue and green LEDs using InGaN-based active regions [35].

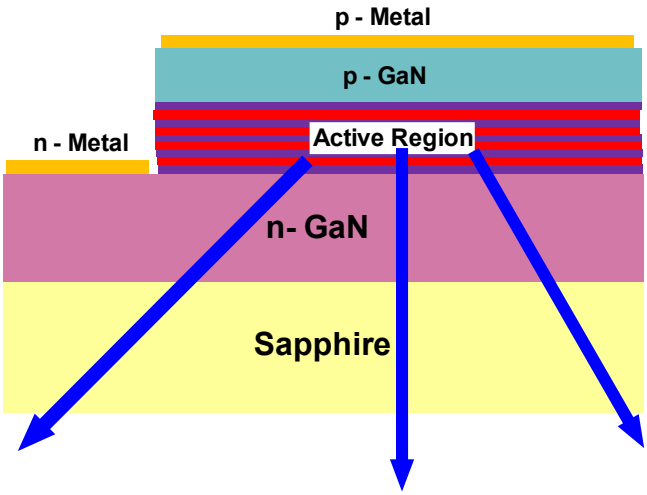

Figure 1-4: *Typical InGaN-based LED device structure.*

The fields of III-Nitride based LEDs have made significant progress in the past decade [1-20]. However, there are still two main challenges limiting the performance of Nitride base LEDs: 1) efficiency droop with increased operating current density, and 2) challenge in realizing high-efficiency green Nitride based LED. Extensive works have been pursued in order to address these two issues in order to achieve high efficiency blue and green LEDs.

1.1.2 Thermoelectricity Applications

The thermoelectric devices have drawn significant attention during recent years because of their applications in solid-state energy conversion such as thermoelectric refrigeration and power generation. The applications such as solid state cooling and power generation are based on two important thermoelectric effects: 1) Seebeck effect (for power generation), and 2) Peltier effect (for thermoelectric cooling and heat pumping) [36, 37]. The Seebeck effect is defined as the generation of a voltage across a conductor when there is a temperature difference. The generated voltage is reflected from the internal electric field, which is caused by the diffusion of the charged carriers (electrons or holes) from the hot side to the cold side, as shown in figure 1-5 (a). The illustration of Peltier effect is shown in figure 1-5 (b). When a current is applied to the interface of two joined-together conductors, there will be an excess or deficiency in the energy at the junction due to the different Peltier coefficients from the two conductors. Thus, heating effect will be caused by the release of the excess energy to the lattice of the junction; while cooling effect will be caused by the supply of deficient energy by the lattice of the other junction.

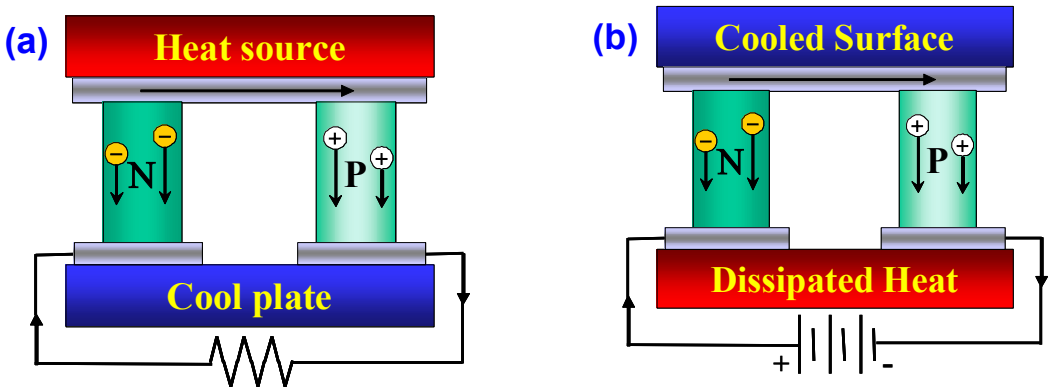

Figure 1-5: *Illustrations of (a) Seebeck effect, and (b) Peltier effect.*

Figure 1-6 shows a typical thermoelectric cooler device structure employing the Peltier effect. Many pairs of p-type and n-type semiconductor elements are interconnected on the cold and the hot sides. Thus, when a current is applied through the elements in series, the heat will be released from the hot side, and leaving the other side cold.

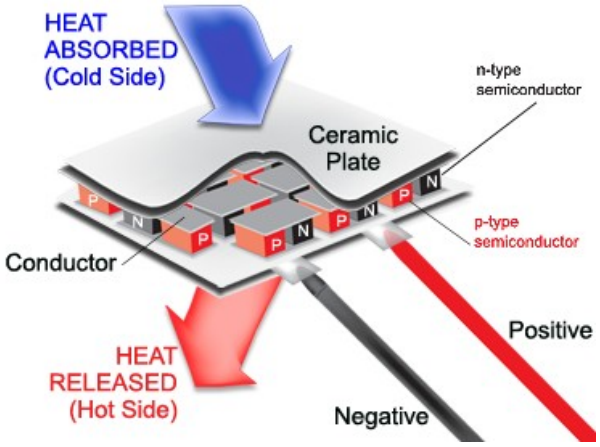

Figure 1-6: *Typical thermoelectric cooler device structure. [38]*

Figure 1-7 shows commercially available thermoelectric power generator devices employing the Seebeck effect. Due to the temperature difference between the hot side and cold side of the conductors, a current will be generated and flow through external load. The thermoelectric power generator devices can have potential important applications for energy efficiency in transportation such as light-duty passenger vehicles, light-duty vans/ trucks, and medium, heavy-duty vehicles, in order to convert the wasted heat into electricity [49].

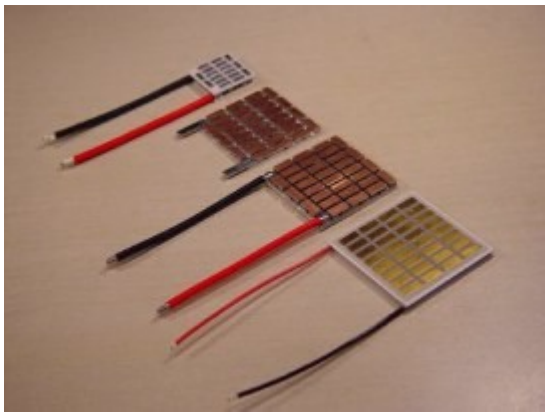

Figure 1-7: *Commercially available thermoelectric power generator. [39]*

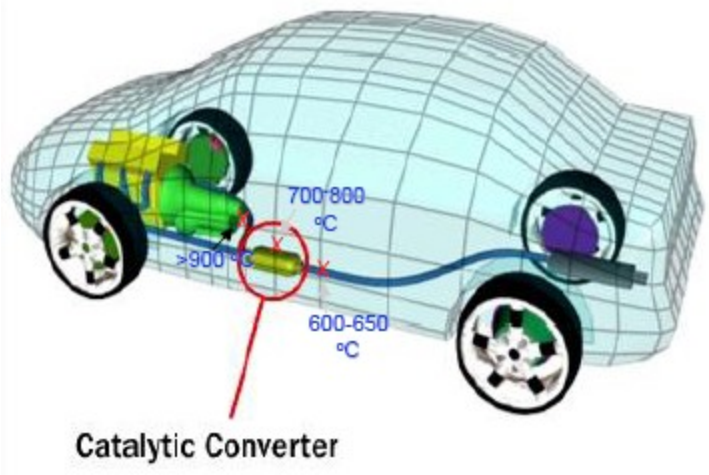

Figure 1-8: *Thermoelectric application of energy efficiency in transportation. [49]*

The efficiency of thermoelectric devices is determined by the thermoelectric figure of merit:

$$Z = \frac{S^2 \cdot \sigma}{\kappa} \tag{1-1}$$

where *S* is the Seebeck coefficient, σ is the electrical conductivity and K is the thermal conductivity. In order to achieve high efficiency, materials with high Seebeck coefficient, high electrical conductivity and low thermal conductivity are in demand. The thermoelectric figure of merit has the units of [K^{-1}], which usually appears in a product with average device temperature T. Therefore, the dimensionless figure of merit *Z*T* is always cited to represent the efficiency of thermoelectric devices that fabricated from different materials.

The thermoelectric figure of merit *Z*T* is the most important parameter for high-efficiency thermoelectric materials and devices. The heavily-doped semiconductors are found to be the most promising materials with best *Z*T* values [36, 37]. For insulators, the electrical conductivity σ is very low. For the case of metals, the Seebec coefficients are low. In addition, the thermal conductivity of metal is dominated by electrons, which is proportional to the electrical conductivity in most cases from the Wiedmann–Franz law. Thus, it is difficult to realize high *Z*T* by the use of metals.

For the case of semiconductors, the total thermal conductivity is contributed from both the electron thermal conductivity (K_e) and phonon thermal conductivity (K_p). The phonon thermal

conductivity (K_p), which is the major component of the total thermal conductivity, can be reduced significantly by several engineering approaches such as alloying and nanostructures.

Figure 1-9 summarizes the dimensionless figure of merit *Z*T* as a function of temperature for different materials [36, 37]. The highest *Z*T* value from semiconductor alloys is around 1, which is obtained by Bi_2Te_3. Currently, the commercial state of the art thermoelectric cooling materials are based on alloys of Bi_2Te_3 with Sb_2Te_3 (such as $Bi_{0.5}Sb_{1.5}Te_3$, p-type) and Bi_2Te_3 with Bi_2Se_3 (such as $Bi_2Te_{2.7}Se_{0.3}$, n-type) [36]. Besides, the *Z*T* value can be further enhanced by using superlattice design, which is realized as high as 2.5 at around room temperature by Bi_2Te_3/ Se_2Te_3 superlattice.

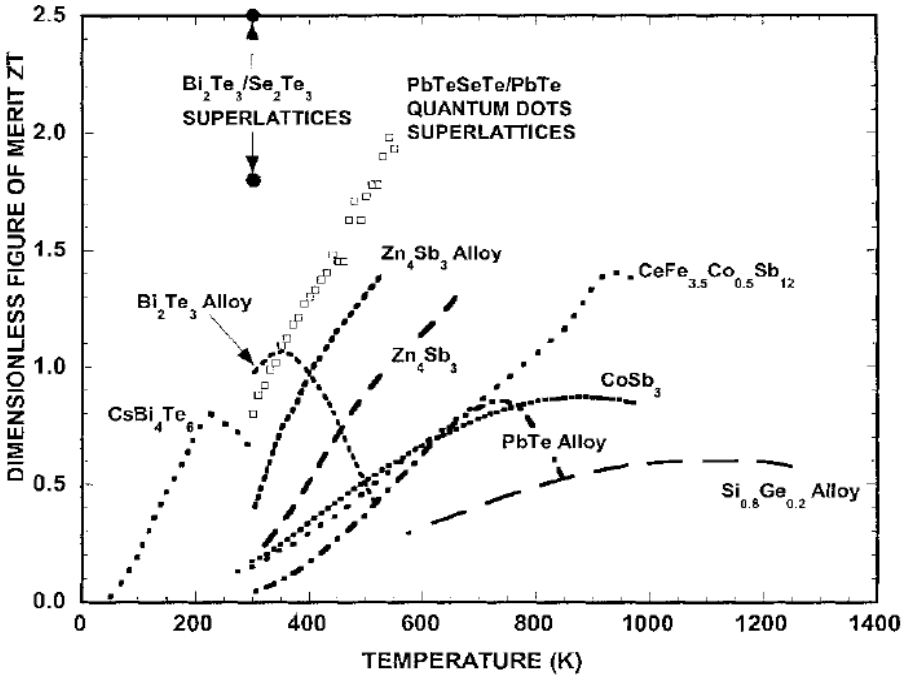

Figure 1-9: *The dimensionless figure of merit as a function of temperature for different materials. [36]*

Both the thermoelectric cooler and thermoelectric power generator have important applications on various aspects. The thermoelectric cooler has been employed for the temperature stabilization of high power semiconductor lasers and picnic coolers, and the market is expected to be increase significantly [36]. For the case of thermoelectric power generator, the thermoelectric materials such as PbTe and $Si_{0.8}Ge_{0.2}$ have been used in deep space radioisotope thermoelectric power generators that operate at ~900°C with a maximum efficiency of about 7%

[36]. The market for thermoelectric power generator will expect growth more than $40 million (figure 1-10) in the following applications [40]: 1) wireless sensors powered by thermoelectric generators in environments where temperature differentials exist, 2) waste heat recovery systems in vehicles, 3) consumer applications such as powering mobile phones, watches or other consumer electronics, and 4) military and aerospace applications such as radioisotope thermoelectric generators in space probes, satellites, etc.

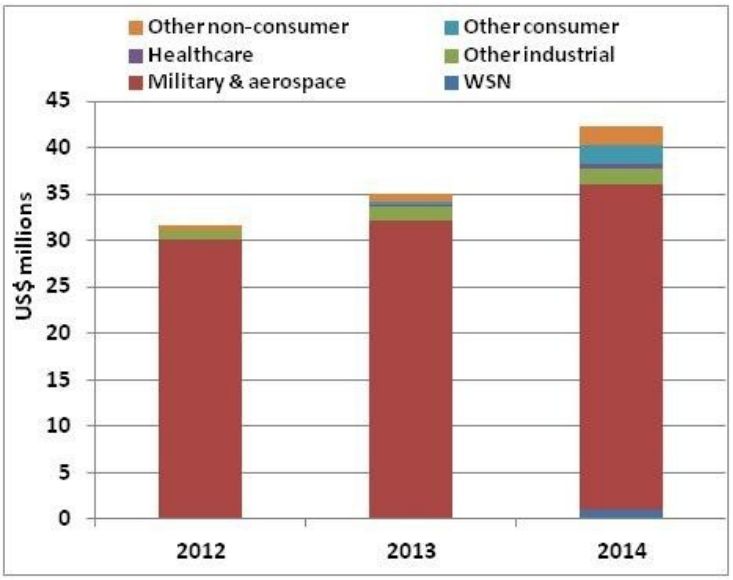

Figure 1-10: *IDTechEx report Thermoelectric Energy Harvesting: Devices, Applications & Opportunities 2012-2022. [40]*

1.1.3 High-Power Transistors and Solar Cells

The GaN power transistors operating at millimeter wave and beyond have important applications on cell phones, satellites, and TV broadcasting [41].

The use of AlGaN/ GaN heterostrcuture is of great interest for high-power microwave devices and circuits applications due to the large critical breakdown electric field, high electron mobility, higher thermal conductivity, large conduction band discontinuity between GaN and AlGaN and the presence of polarization fields that allow the confinement of large two-dimensional electron gas (2DEG).

Therefore, GaN HEMTs are extremely promising for power electronics applications from power conditioning to microwave amplifiers and transmitters for satellite communications, high-performance radars, and commercial ground base stations [42].

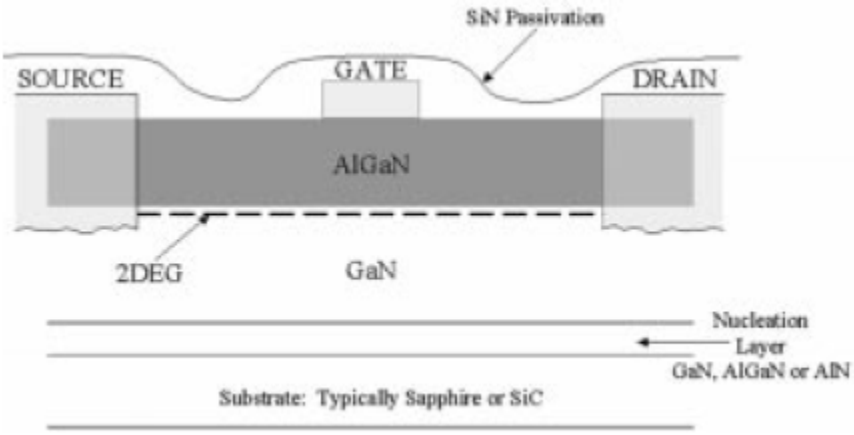

Figure 1-11: *Typical AlGaN/ GaN HEMT device structure. [21]*

The typical AlGaN/ GaN HEMT device structure is shown in Figure 1-11 [21]. The epitaxial layers can be grown by metalorganic chemical vapor deposition (MOCVD). One challenge of the epitaxy is related to the nucleation layer on lattice-mismatched substrates. For sapphire substrate, the nucleation layer consists of GaN or AlN deposited at a low temperature around 600 °C, which is then heated up to the growth temperature of the main layer [21]. Therefore, material growth optimization is an important aspect in order to improve the efficiency of the GaN HEMT.

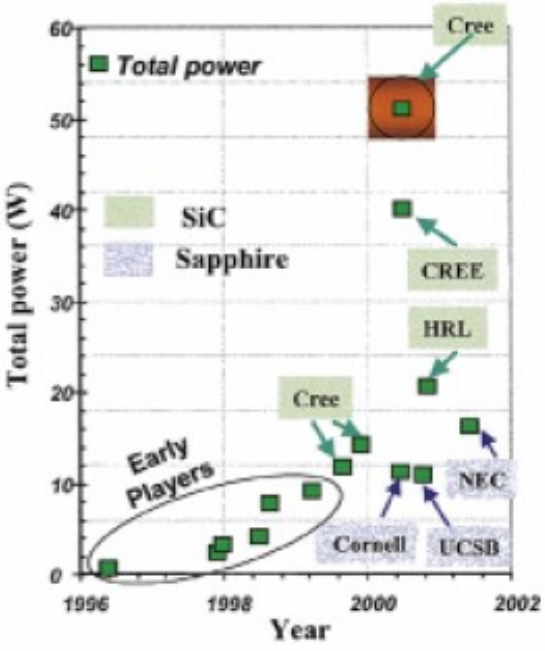

Figure 1-12: *progress in the total power available from AlGaN/GaN HEMTs [21].*

Figure 1-12 reviews the progress in the total power available from AlGaN/GaN HEMTs [21]. One-order higher power density and higher efficiency are obtained by GaN HEMTs, in comparison with the Si- and GaAs-based RF and microwave transistors. Therefore, ten times reduction in device size can be realized by GaN HEMTs for similar output power [21].

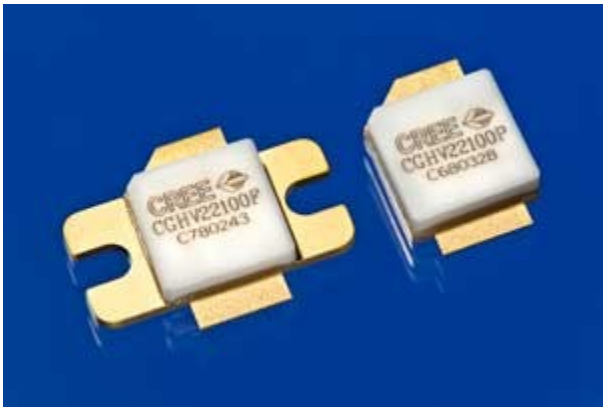

Figure 1-13: *Cree's GaN HEMT designed for high efficiency, high gain and wide bandwidth capabilities. [43]*

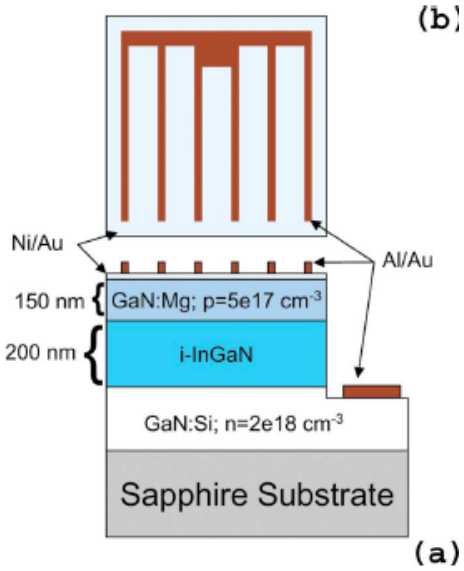

Figure 1-14: *(a) Typical InGaN/GaN double heterojunction p-i-n solar cell devices structure, (b) contact grid layout. [25]*

The commercially available GaN HEMTs are important in the power transistor market [42]. For example, Cree recently introduces a range of new GaN HEMT devices (as shown in figure 1-13), which enables a significant reduction in the energy needed to power cellular networks, which is estimated to consume more than 100 TWh of electricity per year (approximate value of $12

billion), while 50–80% of the networks' power is consumed by the systems' power amplifiers and feed infrastructure. Thus, the use of new GaN HEMT radio base-station power amplifiers can improve the efficiency by 20% [43].

Nitride based semiconductors are potential candidates for solar cells due to the direct bandgap ranging from 0.7 eV for InN up to 3.4 eV for GaN, which covers most of the solar spectrum. Besides, the III-Nitride alloys exhibit very strong absorption of approximately 10^5 cm^{-1} at the band edge, which will absorb a large fraction of the incident light in a few hundred nanometers of material [25]. Thus, the InGaN/ GaN multiple QWs with high In-content will have the potential for realizing enhanced efficiency for solar cells [24-26].

Figure 1-14 shows a typical $In_{0.12}Ga_{0.88}N$/GaN double heterojunction p-i-n solar cell devices structure [25], which resulted in devices with fill factors greater than 75%. The peak external quantum efficiency can be achieved greater than 60%, and the quantum efficiency spectrum showed a flat spectral response from 370 to 410 nm [25]. Therefore, further optimization of the material growths, as well as device design should be pursued for III-Nitride solar cells.

1.2 III-Nitrides for Applications of Ultraviolet (UV) Laser Diodes

Mid-UV (λ ~250-320 nm) and Deep-UV (λ ~220-250 nm) lasers and LEDs have important applications covering biochemical agent identification, flame detection, germicidal air and water purification, surface disinfection, currency validation, medical, military (space-to-space communications), industrial (photo-chemical) curing, printing, instrumentation, effect lighting and forensic analysis. Thus, the market for UV equipment of all types is conservatively estimated at over $5 billion [44]. The conventional and common method to produce UV light is based on the mercury lamp [45]. Visible light can be obtained by using low-pressure mercury tubes emitting at 254 nm converted by appropriate phosphors. Higher pressure in the mercury tubes will lead to emission wavelength at 365 nm.

However, there are many disadvantages and drawbacks of conventional mercury lamps [44, 45]: 1) the mercury lamps are mechanically fragile and susceptible to breakage, which are limited to a lifetime of about 1000 hours, 2) the high operating temperatures (600-900 °C) from low /high

pressure mercury lamps limit certain applications such as photo-chemical curing, 3) lack of tunability of wavelength and output power, and 4) mercury lamps lead to environmental pollution ultimately.

Oppositely, solid state light-emitting devices based on III–Nitride semiconductors (typically employ wide band-gap material AlGaN) have many advantages [44, 45]: 1) miniaturization in device size, 2) strong chemical resistance, high temperature and high power capability, 3) lower power consumption, 4) tunability of wavelength and output power, and 5) environmental friendly. Therefore, the use of III-Nitride semiconductors as active region for UV LEDs and lasers has attracted a lot of attentions.

The ultraviolet spectrum is shown in figure 1-15 [46, 47], which covers emission wavelengths from 100 nm up to 400 nm. The UV spectrum is divided into four categories, namely, Vacuum UV (100-200 nm), UV-C (200-280 nm), UV-B (280-315 nm), and UV-A (315-400 nm).

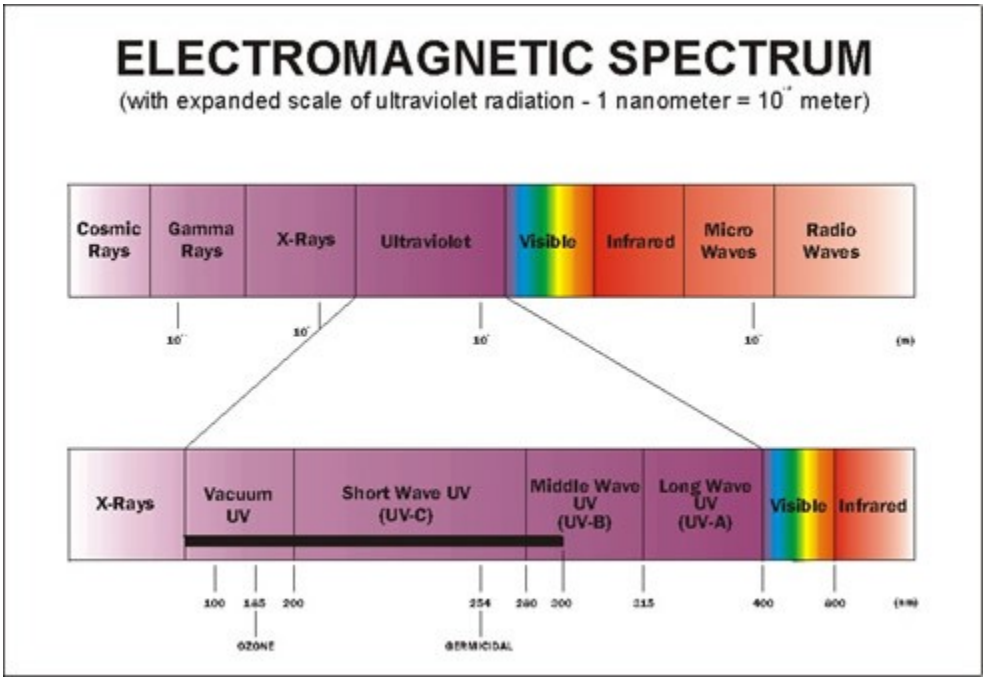

Figure 1-15: *Ultraviolet spectrum. [46, 47]*

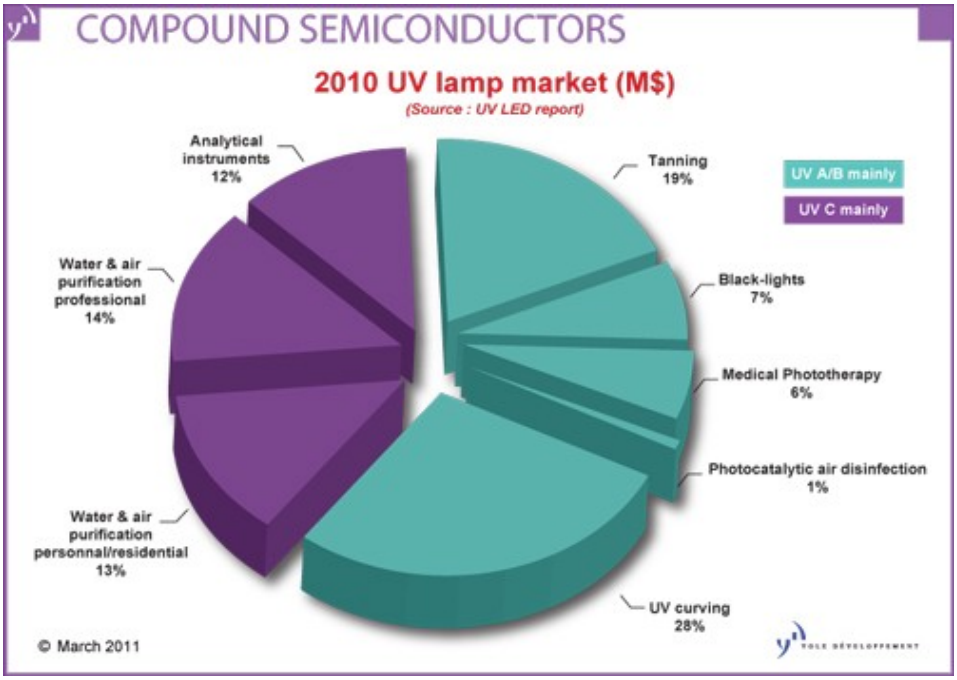

Figure 1-16: *Analysis of UV lamp market in 2010. [48]*

Since the UV LEDs and lasers have important applications for specific wavelengths, such as sterilization of surface areas and water with λ ~ 240-280nm, forensic and bodily fluid detection and analysis with λ ~ 250-405 nm, as well as protein analysis and drug discovery with λ ~ 270-300 nm.

Therefore, the UV lamp market is expected to increase at an annual growth rate of almost 30% from $25 million to more than $100 million in 2016, according to market research firm Yole Développemement [48], which provides an analysis of the UV LED industry compared to major market metrics of the current traditional UV lamp market as shown in figure 1-16.

1.3 Research Works Accomplished

1.3.1 Theoretical Modeling of Thermal Conductivity from Three-Layer Superlattice Design

The numerical method was developed from the lattice dynamical theory in order to calculate the cross-plane thermal conductivity of proposed three-layer superlattices structure. The phonon

mean free path is included into the calculation, thus the minimum thermal conductivity occurs at the crossover of the particle-like model and wave-like model of the phonons. The studies focus on the effect of mass ratio, layer thickness, and mean free path on the minimum thermal conductivity of the three-layer superlattice design. The minimum thermal conductivity of the three-layer superlattice structure is approximately half of that of the conventional two-layer superlattice structure. This finding indicates that the thermoelectric figure of merit for superlattice structure can further be enhanced by ~2-times from the use of the three-layer superlattice design.

1.3.2 High-Temperature Thermoelectric Characterizations of AlInN Alloys

The Seebeck coeeficients of AlInN alloys, grown by metalorganic chemical vapor deposition (MOCVD), with In-contents (*x*) from 0.38% up to 21.34% were characterized and analyzed from room temperature (*T* = 300 K) up to high temperature (*T* = 382 K). The Seebeck coefficients of the n-type AlInN alloys show significant enhancement at higher temperature up to 382 K, in comparison to those measured at room temperature. Large Seebeck coefficients (602.0 μV/K - 1233.2 μV/K) were obtained for the lattice-matched $Al_{0.83}In_{0.17}N$ alloy (n= 5.1×10^{18} cm^{-3}) from T = 300 K up to T = 382 K. The improvement of Seebeck coefficients for the n-type AlInN alloys will lead to ~1.5 - 4 times improvement of the thermopower at higher temperatures.

1.3.3 Physics and Novel Nanostructure Engineering of AlGaN-Based UV LEDs and Lasers

The effect of crystal-field split-off hole (CH) and heavy-hole (HH) bands crossover on the gain characteristics of AlGaN QW with AlN barriers was discovered and analyzed for the optical gain characteristics of high Al-content AlGaN quantum wells (QWs) for deep UV lasers. Attributing to the strong transition between conduction – CH bands, the transverse-magnetic (TM) spontaneous emission recombination rate is enhanced significantly for high Al-content AlGaN QWs. Large TM-polarized material gain is shown as achievable for high Al-content AlGaN QWs, which indicates the feasibility of TM-lasing for lasers emitting at ~220-230 nm.

The AlGaN-delta-GaN QWs structure was proposed by inserting an ultra-thin GaN layer into high Al-content AlGaN-delta-GaN QW active region. The optical gain characteristics of high Al-content AlGaN-delta-GaN QWs are investigated for mid- and deep-UV lasers. The insertion of an ultra-thin GaN layer in high Al-content AlGaN QWs leads to strong valence subbands rearrangement. Attributing to the strong transition between the conduction and heavy-hole subbands, large optical gain is achievable for high Al-content AlGaN-delta-GaN QWs as gain media for mid- and deep-UV lasers emitting at ~250-300 nm.

The comprehensive optimization studies on the gain characteristics of AlGaN-delta-GaN QWs with various delta-GaN positions and Al-content AlGaN QW compositions were analyzed for the mid- and deep-UV spectral regimes. Attributing to the valence subband rearrangement and enhanced electron and hole wavefunction overlap, the use of optimized asymmetric AlGaN-delta-GaN QWs structures result in ~7 times increase in material gain, in comparison to that of conventional AlGaN QW. Large material gains can be maintained at λ ~ 240-250 nm for the asymmetric AlGaN-delta-GaN QWs structures. Despite the improved material gain for the asymmetric QW structures, the finding shows that large material gain can be obtained for both symmetric and asymmetric AlGaN-delta-GaN QWs, which indicates the flexibility and robustness in the experimental implementations of this concept in device structures. The reduced threshold carrier densities obtained from the optimized delta QWs structures are important for the suppression of the non-radiative recombination current densities, which reduces the threshold current densities. Therefore, by employing asymmetric QW design, with optimized GaN delta layer position and asymmetric AlGaN-composition layers, the optimized optical gain and lower threshold carrier densities are achievable for the AlGaN-delta-GaN QW structures with realistic design applicable for UV lasers.

The staggered AlGaN QWs structure was proposed for UV lasers. There are two main effects by employing the staggered QW structures: (1) further enhanced TM-polarized gain with engineered optical matrix element by broadening the concept from the InGaN QW system with large electron-hole wave function overlap (Γ_{e_hh}) design, and (2) polarization engineering of

AlGaN QW system to achieve high transverse-electric (TE)-polarized optical gain from dominant C-HH transition.

1.3.4 Substrate Engineering for High-Efficiency Light-Emitting Diodes (LEDs) and Lasers

The spontaneous emission characteristics of green- and red-emitting InGaN QWs on ternary InGaN substrate are analyzed, and the radiative recombination rates for the QWs grown on ternary substrate were compared with those of InGaN QWs on GaN templates. For green- and red-emitting InGaN QWs on $In_{0.15}Ga_{0.85}N$ substrate, the spontaneous emission rates were found as ~2.5-3.2 times of the conventional approach. The enhancement in spontaneous emission rate can be achieved by employing higher In-content InGaN ternary substrate, which is also accompanied by a reduction in emission wavelength blue-shift from carrier screening effect. The use of InGaN substrate is expected to result in the ability for growing InGaN QWs with enhanced spontaneous emission rates, as well as reduced compressive strain, applicable for green- and red-emitting light-emitting diodes.

The optical gain and threshold characteristics of InGaN QWs on ternary InGaN substrate emitting in green and yellow spectral regimes were analyzed. By employing the ternary substrates, the material gains were found as ~3-5 times higher than that of conventional method with reduced wavelength shift. The threshold carrier density is reduced by ~15%-50% from the use of ternary substrate method for green- and yellow-emitting lasers.

1.4 Report Organization

There are twelve chapters in this report, which are organized as follow:

Chapter 1 presents an introduction of III-Nitride semiconductors, which mainly focuses on the laser and energy-efficient applications, including SSL, thermoelectricity, and high-power transistors and solar cells. In addition, the research works that have been accomplished are summarized and briefly reviewed.

Chapter 2 reviews the current status of III-Nitride semiconductors for device applications mainly focusing on three topics: 1) thermoelectricity, 2) AlGaN QWs UV lasers, and 3) substrate engineering for visible LEDs and lasers.

Chapter 3 introduces the details of MOCVD growths for III-Nitride semiconductors, as well as the device fabrication process.

Chapter 4 focuses on both the theoretical and experimental aspects of III-Nitride semiconductors for thermoelectric applications. The thermoelectric characterizations of AlInN alloys have been presented with measurement details. Theoretical modeling has also been reviewed for III-Nitride semiconductors.

Chapter 5 presents a brief summary on the thermal conductivity measurement methods for both bulk materials and thin film materials.

Chapter 6 presents the high temperature thermoelectric characterizations for III-Nitride materials grown by MOCVD. The Seebeck coefficients of AlInN alloys with various In-contents are characterized at high temperatures, which are also compared with the Seebeck coefficients of binary InN and AlN alloys.

Chapter 7 presents the proposed novel three-layer superlattice design for thermoelectric applications. The numerical model is developed for the calculation of the thermal conductivity for the three-layer superlattice structures.

Chapter 8 introduces the numerical simulation and material parameters for optical properties of III-Nitride semiconductors, which includes the band structure and wave function calculations based on the 6-band ***k·p*** method, the spontaneous radiative recombination rate and optical gain calculation, and the carrier lifetime and radiative efficiency calculation formulations.

Chapter 9 presents a comprehensive study on the physics for gain characteristics of AlGaN QWs UV lasers, especially for the effect of the valence band crossover in AlGaN QWs.

Chapter 10 presents the study on enhanced optical gain by novel nanostructure engineering of AlGaN-based UV lasers. The design of AlGaN-delta-GaN QW, engineering of AlGaN-delta-GaN QW, and the design of staggered AlGaN QW are proposed and studied comprehensively for mid- and deep-UV lasers applications.

Chapter 11 focuses on the approach of substrate engineering for high-efficiency visible LEDs and lasers. Comprehensive studies are carried out for spontaneous emission characteristics of InGaN QWs on ternary substrates for LEDs, as well as optical gain characteristics of InGaN QWs on ternary substrates for lasers.

Chapter 12 summarizes research works on various topics toward the application of III-Nitride semiconductors, and the future outlook is presented.

References for Chapter 1

[1] M. H. Crawford, “LEDs for solid-state lighting: performance challenges and recent advances,” IEEE J. Sel. Top.Quantum Electron. 15(4), 1028–1040 (2009).

[2] D. D. Koleske, A. J. Fischer, A. A. Allerman, C. C. Mitchell, K. C. Cross, S. R. Kurtz, J. J. Figiel, K. W. Fullmer, and W. G. Breiland, “Improved brightness of 380 nm GaN light emitting diodes through intentional delay of the nucleation island coalescence,” Appl. Phys. Lett. 81(11), 1940–1942 (2002).

[3] J. Han and A. V. Nurmikko, “Advances in AlGaInN blue and ultraviolet light emitters,” IEEE J. Sel. Top. Quantum Electron. 8(2), 289–297 (2002).

[4] M. Kneissl, D. W. Treat, M. Teepe, N. Miyashita, and N. M. Johnson, “Continuous-wave operation of ultraviolet InGaN/InAlGaN multiple-quantum-well laser diodes,” Appl. Phys. Lett. 82(15), 2386–2388 (2003).

[5] D. Queren, A. Avramescu, G. Brüderl, A. Breidenassel, M. Schillgalies, S. Lutgen, and U. Strauß, “500 nm electrically driven InGaN based laser diodes,” Appl. Phys. Lett. 94(8), 081119 (2009).

[6] K. Okamoto and Y. Kawakami, “High-efficiency InGaN/GaN light emitters based on nanophotonics and plasmonics,” IEEE J. Sel. Top. Quantum Electron. 15(4), 1199–1209 (2009).

[7] H. Zhao, J. Zhang, G. Liu, and N. Tansu, “Surface plasmon dispersion engineering via double-metallic Au/Ag layers for III-nitride based light-emitting diodes,” Appl. Phys. Lett. 98(15), 151115 (2011).

[8] J. Henson, A. Bhattacharyya, T. D. Moustakas, and R. Paiella, “Controlling the recombination rate of semiconductor active layers via coupling to dispersion-engineered surface plasmons,” J. Opt. Soc. Am. B 25(8), 1328–1335 (2008).

[9] X. Li, S. Kim, E. E. Reuter, S. G. Bishop, and J. J. Coleman, “The incorporation of arsenic in GaN by
metalorganic chemical vapor deposition,” Appl. Phys. Lett. 72(16), 1990–1992 (1998).

[10] T. Jung, L. K. Lee, and P.-C. Ku, “Novel epitaxial nanostructures for the improvement of InGaN LEDs efficiency,” IEEE J. Sel. Top. Quantum Electron. 15(4), 1073–1079 (2009).

[11] X. Li, S. G. Bishop, and J. J. Coleman, “GaN epitaxial lateral overgrowth and optical characterization,” Appl. Phys. Lett. 73(9), 1179–1181 (1998).

[12] J. Liu, J. Limb, Z. Lochner, D. Yoo, J.-H. Ryou, and R. D. Dupuis, “Green light-emitting diodes with p-
InGaN:Mg grown on C-plane sapphire and GaN substrates,” Phys. Status Solidi., A Appl. Mater. Sci. 206(4), 750–753 (2009).

[13] W. Lee, J. Limb, J.-H. Ryou, D. Yoo, M. A. Ewing, Y. Korenblit, and R. D. Dupuis, “Nitride-based green lightemitting diodes with various p-type layers,” J. Disp. Technol. 3(2), 126–132 (2007).

[14] G. R. Mutta, P. Ruterana, J. L. Doualan, M. P. Chauvat, F. Ivaldi, S. Kret, N. A. K. Kaufmann, A. Dussaigne, D. Martin, and N. Grandjean, “Investigation of the In composition in InGaN/GaN quantum wells deposited by MOVPE and/or MBE with emission from violet to green,” Phys. Status Solidi, B Basic Res. 248(5), 1187–1190 (2011).

[15] C. H. Chao, S. L. Chuang, and T. L. Wu, “Theoretical demonstration of enhancement of light extraction of flipchip GaN light-emitting diodes with photonic crystals,” Appl. Phys. Lett. 89(9), 091116 (2006).

[16] K. McGroddy, A. David, E. Matioli, M. Iza, S. Nakamura, S. DenBaars, J. S. Speck, C. Weisbuch, and E. L. Hu, “Directional emission control and increased light extraction in GaN photonic crystal light emitting diodes,” Appl. Phys. Lett. 93(10), 103502 (2008).

[17] J. J. Wierer, A. David, and M. M. Megens, “III-nitride photonic-crystal light-emitting diodes with high extraction efficiency,” Nat. Photonics 3(3), 163–169 (2009).

[18] X. H. Li, R. Song, Y. K. Ee, P. Kumnorkaew, J. F. Gilchrist, and N. Tansu, “Light extraction efficiency and radiation patterns of III-nitride light-emitting diodes with colloidal microlens arrays with various aspect ratios,” IEEE Photon. J. 3(3), 489–499 (2011).

[19] Q. Xi, M. F. Schubert, J. K. Kim, E. F. Schubert, M. Chen, S. Y. Lin, W. Liu, and J. A. Smart, “Optical thin-film materials with low refractive index for broadband elimination of fresnel reflection,” Nat. Photonics 1, 176–179 (2007).

[20] S. Chhajed, W. Lee, J. Cho, E. F. Schubert, and J. K. Kim, “Strong light extraction enhancement in GaInN lightemitting diodes by using self-organized nanoscale patterning of p-type GaN,” Appl. Phys. Lett. 98(7), 071102 (2011).

[21] U. K. Mishra, P. Parikh, and Y. F. Wu, “AlGaN/GaN HEMTs-an overview of device operation and applications,” Proc. IEEE 90(6), 1022–1031 (2002).

[22] B. N. Pantha, R. Dahal, J. Li, J. Y. Lin, H. X. Jiang, and G. Pomrenke, “Thermoelectric properties of InxGa1-xN alloys,” Appl. Phys. Lett. 92(4), 042112 (2008).

[23] J. Zhang, H. Tong, G. Y. Liu, J. A. Herbsommer, G. S. Huang, and N. Tansu, “Characterizations of seebeck coefficients and thermoelectric figures of merit for AlInN alloys with various in-contents,” J. Appl. Phys. 109(5), 053706 (2011).

[24] R. Dahal, B. Pantha, J. Li, J. Y. Lin, and H. X. Jiang, “InGaN/GaN multiple quantum well solar cells with long operating wavelengths,” Appl. Phys. Lett. 94(6), 063505 (2009).

[25] C. J. Neufeld, N. G. Toledo, S. C. Cruz, M. Iza, S. P. DenBaars, and U. K. Mishra, “High quantum efficiency InGaN/GaN solar cells with 2.95 eV band gap,” Appl. Phys. Lett. 93(14), 143502 (2008).

[26] O. Jani, I. Ferguson, C. Honsberg, and S. Kurtz, “Design and characterization of GaN/InGaN solar cells,” Appl. Phys. Lett. 91(13), 132117 (2007).

[27] http://www1.eere.energy.gov/buildings/ssl/sslbasics_whyssl.html

[28] http://apps1.eere.energy.gov/buildings/publications/pdfs/ssl/lifetime_white_leds.pdf, DOE report “Lifetime of White LEDs”.

[29] http://apps1.eere.energy.gov/buildings/publications/pdfs/ssl/ssl_energy-savings-report_jan-2012.pdf, DOE report “Energy Savings Potential of Solid-State Lighting in General Illumination Applications”.

[30] http://www1.eere.energy.gov/buildings/ssl/sslbasics_ledbasics.html

[31] Y. Narukawa, I. Niki, K. Izuno, M. Yamada, Y. Murazaki, and T. Mukai, “Phosphor-Conversion White Light Emitting Diode Using InGaN Near-Ultraviolet Chip”, Jpn. J. Appl. Phys. Vol. 41 (4A), L371–L373 (2002).

[32] F. So, J. Kido, and P. E. Burrows, “Organic light-emitting diodes for solid-state lighting,” MRS Bull., vol. 33, pp. 663–669, 2008.

[33] A. Zukauskas, R. Vaicekauskas, F. Ivanauskas, R. Gaaska, and M. S. Shur, “Optimization ofwhite polychromatic semiconductor lamps,” Appl. Phys. Lett., vol. 80, pp. 234–236, 2002.

[34] J. M. Phillips, M. E. Coltrin,M. H. Crawford, A. J. Fischer, M. R. Krames, R. Mueller-Mach,G.O.Mueller,Y.Ohno, L. E. S. Rohwer, J.A. Simmons, and J. Y. Tsao, “Research challenges to ultra-efficient inorganic solid-state lighting,” Laser Photon. Rev., vol. 1, pp. 307–333, 2007.

[35] S. Nakamura, T. Mukai, and M. Senoh, “Candela-class high-brightness InGaN/AlGaN double-heterostructure blue-light-emitting diodes,” Appl. Phys. Lett., vol. 64, pp. 1687–1689, 1994.

[36] G. Chen, M.S. Dresselhaus, G. Dresselhaus, J.-P. Fleurial, T. Caillat, “Recent developments in thermoelectric materials”, International Materials Reviews, vol. 48, pp. 45-66(22), 2003.

[37] G. Chen, Nanoscale Energy Transport and Conversion, Oxford University Press, 2005.

[38] http://www.teamwavelength.com/info/temperaturecontrollers.php

[39] http://www.thermoelectric-generator.com/thermoelectric_power_modules_for_sale_.htm

[40] http://www.energyharvestingjournal.com/articles/thermoelectric-generators-a-750-million-market-by-2022-00004631.asp?sessionid=1

[41] U. K. Mishra, L. Shen, T. E. Kazior, and Y.-F. Wu, “GaN-Based RF Power Devices and Amplifiers”, vol. 96, pp. 287-305, Proceedings of the IEEE, 2008.

[42] G. Meneghesso, G. Verzellesi, F. Danesin, F. Rampazzo, F. Zanon, A. Tazzoli, M. Meneghini, and E. Zanoni, “Reliability of GaN High-Electron-Mobility Transistors: State of the Art and Perspectives”, vol. 8, pp. 332-343, IEEE transactions on device and materials reliability, 2008.

[43] http://www.cree.com/news-and-events/cree-news/press-releases/2012/october/50v-gan-hemt

[44] D. Birtalan, and W. Nunley, Optoelectronics: Infrared-visible-ultraviolet Devices and Applications, CRC Press, 2009.

[45] M. Asif Khan, M. Shatalov, H. P. Maruska, H. M. Wang and E. Kuokstis, “Physics of UV Materials and Devices and Their Applications”, Jpn. J. Appl. Phys., vol. 44, pp. 7191-7206, 2005.

[46] http://www.drb-mattech.co.uk/uv%20spectrum.html

[47] http://www.spacewx.com/Docs/ISO_PRF_21348_e.pdf

[48] http://www.semiconductor-today.com/news_items/2011/MAR/YOLE_180311.html

[49] T.J. Hendricks, and J. A. Lustbader, “Advanced thermoelectric power system investigations for light-duty and heavy duty applications,” Proceedings ICT 2002, Thermoelectrics, 2002.

Chapter 2: Current Status of III-Nitride Semiconductors for Device Applications

Significant progress has been developed in the III-Nitride semiconductors for the applications in laser diodes and energy-related applications. In this chapter, the current status and challenges for III-Nitride semiconductors are reviewed in details on three main aspects: thermoelectricity, AlGaN-based mid- and deep- Ultraviolet (UV) lasers, as well as the substrate engineering approach for InGaN-based visible LEDs and lasers.

2.1 Current Status and Challenges of Thermoelectricity

2.1.1 Introduction of Thermoelectric Materials and Important Applications

The potential of thermoelectrics has been recognized as transformative energy conversion technology, attributed to the ability to convert heat directly into electricity, and the thermoelectric materials have been employed extensively in fields such as space power generation and a variety of cooling applications [1]. Specifically, the radioisotope heat-powered thermoelectric generator has been used for space probes, which converts heat generated by radioactive decay to electric power. For the aspect of solid-state cooling applications, the thermoelectric materials have been employed for temperature control for high-power semiconductor lasers, seat coolers in high-end cars, as well as solid-state coolers in compact refrigerators [6].

Despite the important applications leading to a large potential market for thermoelectrics, as well as the great potential for energy conversion technology from the thermoelectric materials, the thermoelectric devices are not in common use today, which are mainly used in niche markets where energy availability, reliability and simplicity are more crucial than the performance [1]. There are two main challenges for high-efficiency thermoelectric devices: 1) low efficiency relative to mechanical cycles from thermoelectric devices, and 2) engineering challenges from thermoelectric materials.

The efficiency of thermoelectric materials and devices is determined by the dimensionless thermoelectric figure of merit (Z^*T):

$$Z*T = \frac{S^2 \cdot \sigma}{\kappa} * T \,, \tag{2-1}$$

where S is the Seebeck coefficient, σ is the electrical conductivity and K is the thermal conductivity.

The most common commercially available thermoelectric material is Bi_2Te_3 alloy, which has achieved a Z*T value ~1 at room temperature, as shown in figure 1-8.

The progress of enhancing the $Z*T$ values by the use of bulk thermoelectric materials has been developing slowly due to the physical challenges, which provides the motivation for engineering approaches for increased $Z*T$ values. Recently, the most important method for the engineering approach is related to the field of low-dimensional thermoelectricity, which is enabled by materials nanoscience and nanotechnology [2].

There are two main engineering approaches for the field of low-dimensional thermoelectricity:

1) bulk thermoelectric materials containing nanoscale inclusions, or bulk materials with nanostructures and many interfaces such as nanocomposites containing a coupled assembly of nanoclusters showing short-range low dimensionality embedded in a host material [4, 5];

2) nanostructured thermoelectric materials such as superlattices [7], quantum dots [8], or nanowires [9, 10].

The principles of low-dimensional thermoelectric materials are related to: 1) the use of quantum-confinement effect to enhance Seebeck coefficient and to control Seebeck coefficient and electrical conductivity independently; 2) the use of numerous interfaces to scatter phonons more effectively than electrons to reduce the thermal conductivity [2].

Figure 2-1 shows a summary of thermoelectric figure of merit $Z*T$ as a function of temperature of current state of the art thermoelectric materials [1]. Some nanostructured thermoelectric materials show $Z*T$ values higher than 1 at room temperature, such as PbTe/PbS [12], $Na_{0.95}Pb_{20}SbTe_{22}$ [11], $Pb_{0.98}Tl_{0.02}Te$ [13], and $Pb_{1+x}Sb_yTe$ [14].

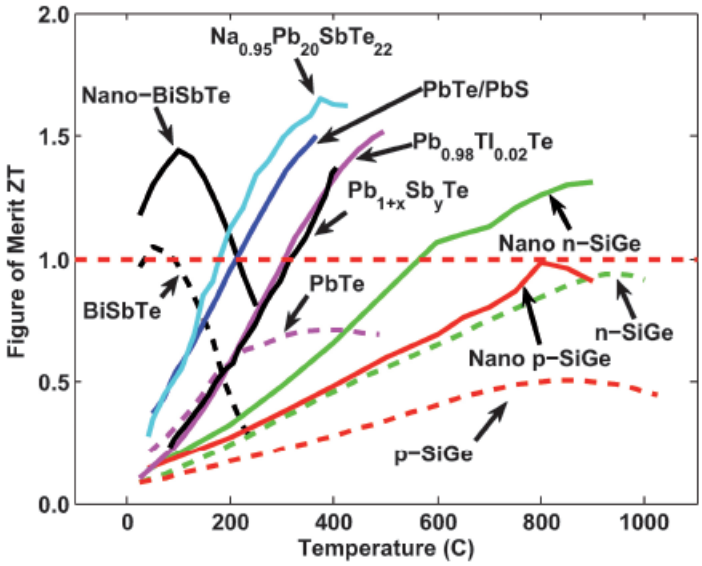

Figure 2-1: *Summary of thermoelectric figure of merit Z*T as a function of temperature of current state of the art thermoelectric materials. [1]*

In addition, the studies on the nanostructured III-V semiconductors have also been pursued [15-17]. Figure 2-2 shows the study of the thermal conductivity of the superlattice structure with the period of 10 nm $In_{0.53}Ga_{0.28}Al_{0.19}As$/ 20 nm $In_{0.53}Ga_{0.47}As$ containing epitaxially embedded ErAs (0.3%) nanoparticles with different doping levels [15]. From the study, it shows that the measured total thermal conductivity of the ErAs:InGaAs/InGaAlAs superlattices is almost independent of doping and has an average value of 2.8 W/(mK) with an uncertainty of 0.5 W/(mK), which is lower than that of the InGaAs thin film.

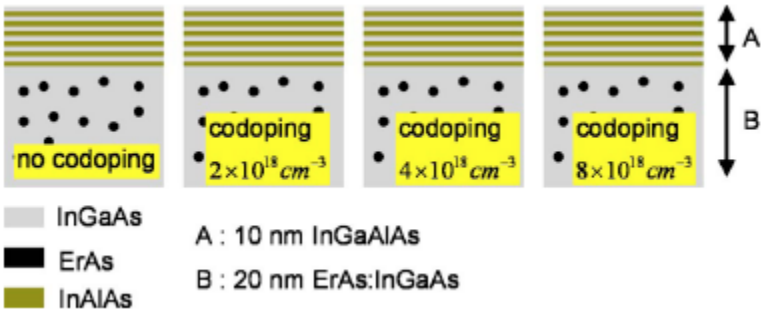

Figure 2-2: *The schematics of one period of ErAs:InGaAs/InGaAlAs with different doping levels [15].*

Further study reported the fabrication and characterization of thermoelectric power generator modules by the use of 16×16 segmented elements consisting of 0.8 mm thick Bi_2Te_3 and 50nm thick ErAs: $(InGaAs)_{1-x(}InAlAs)_x$ with 0.6% ErAs by volume, as shown in figure 2-3. The obtained output power was up to 6.3 W at 610 K. The thermoelectric figure of merit *Z*T* was measured for ErAs:InGaAlAs, which was obtained as ~0.1-1.1 from 300 K up to 830 K.

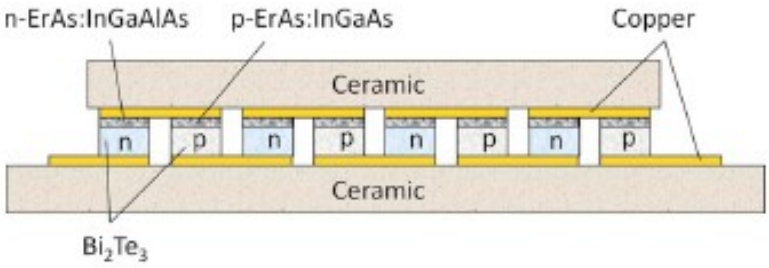

Figure 2-3: *The schematic structure of the segmented element generator module of ErAs:InGaAlAs and Bi_2Te_3 [16].*

2.1.2 III-Nitride Semiconductors for Thermoelectric Applications

High power density and high-temperature requirements in III-Nitride based device technologies are of great importance for lasers [18-23], light-emitting diodes [24-39], transistors [40], and solar cells [41, 42].

The use of active solid state cooling technology [43] is of great importance for efficient thermal management in high power devices. The availability of III-nitride thermoelectric materials, which can be directly integrated with GaN device technology, has an important role for active thermal cooling and efficiency improvement in nitride-based high-power devices operating at high current density and high temperature.

Promising thermoelectric figures of merit (*Z*T*) have been reported for III-nitride materials [44-59], in particular for materials based on AlGaN [52, 53], InGaN [54, 55], and AlInN [56, 57, 59] alloys. The thermoelectric properties for RF-sputtered AlInN had also been reported [44-47].

Figure 2-4 shows GaN-based thermoelectric power generator [50], which were measured to have a maximum open circuit voltage of 0.3V with a maximum output power of 2.1 μW with a relatively small temperature difference (ΔT) of 30 K with an average temperature of 508 K. This

proof of concept GaN-based thermoelectric power generator device also shows good suitability for high temperature (825 K) thermoelectric applications.

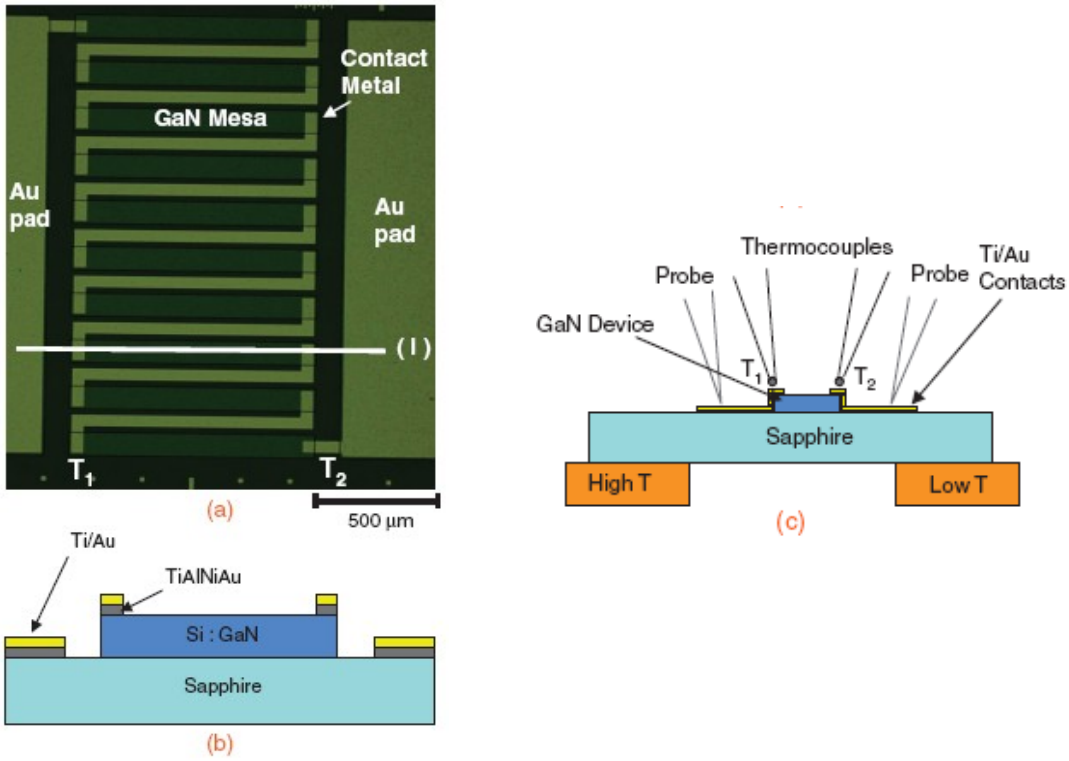

Figure 2-4: *The (a) Optical Image of 10× device. Scale bar = 500 µm. (b) Cross section of device along (i) in (a). (c) Schematic diagram of measurement setup. [50].*

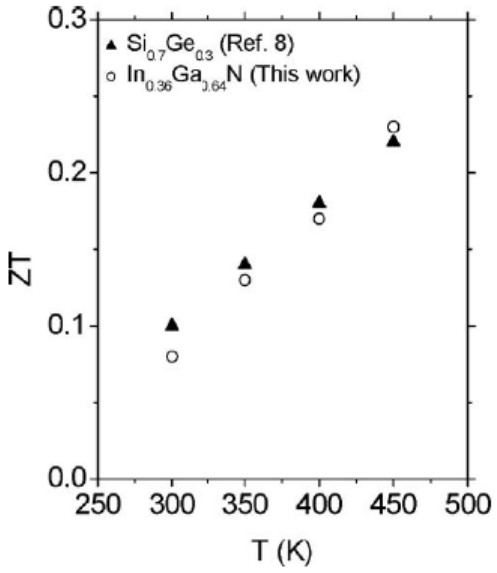

Figure 2-5: *The measured Z*T values for $In_{0.36}Ga_{0.64}N$ alloy as a function of temperature [54].*

Recent works on InGaN alloys have been shown to have very promising *Z*T* at room temperature [54, 55]. Pantha and co-workers have also reported the power factor and thermal conductivity of InGaN alloys at elevated temperature (T~450 K), which demonstrated its promise as the new thermoelectric material. The *Z*T* value was measured as ~0.08 at 300 K and ~0.23 at 450 K for $In_{0.36}Ga_{0.64}N$ alloy, as shown in figure 2-5. For higher temperature measurement, the maximum value of the power factor was obtained at 750 K, with Seebeck coefficient and electrical conductivity for the $In_{0.3}Ga_{0.7}N$ alloy as 280 μV/K and 93 $(\Omega cm)^{-1}$, respectively, as shown in figure 2-6.

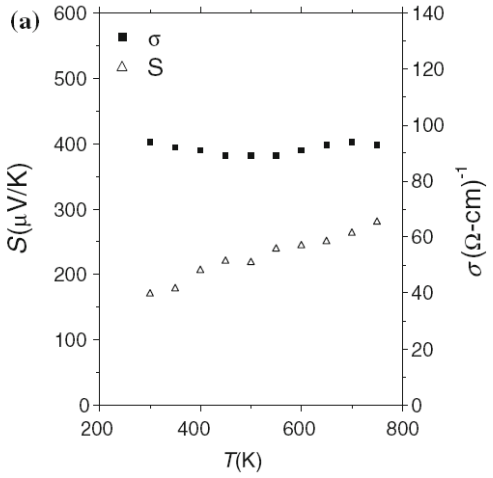

Figure 2-6: *The measured electrical conductivity (σ) and Seebeck coefficient (S) as a function of temperature of $In_{0.3}Ga_{0.7}N$ alloy with electron concentration 7×10^{18} cm^{-3} [55].*

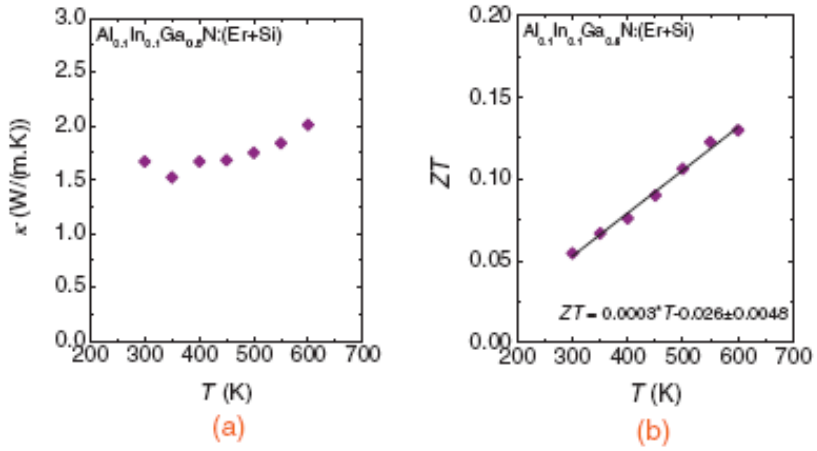

Figure 2-7: *The measured (a) temperature-dependent thermal conductivity of $Al_{0.1}In_{0.1}Ga_{0.8}N$: (Er+Si) alloy, and (b) temperature-dependent Z*T of $Al_{0.1}In_{0.1}Ga_{0.8}N$: (Er+Si) alloy [58].*

Recently, Pantha and co-workers have also extended their works into the use of (Er+Si)-doped AlInGaN with low In-content ~10% and Al-content ~ 14%, resulting in promising *Z*T* values up to high temperature [42]. The incorporation of (Er+Si)-dopants in the quaternary AlInGaN alloys lead to reduction in thermal conductivity by ~ 2.5-times, which leads to the very promising improvement in *Z*T* values of this material [58].

The thermoelectric properties for RF-sputtered AlInN had also been reported [44-47], which has a low thermoelectric figure of merit ~0.1 at high temperature ~900 K.

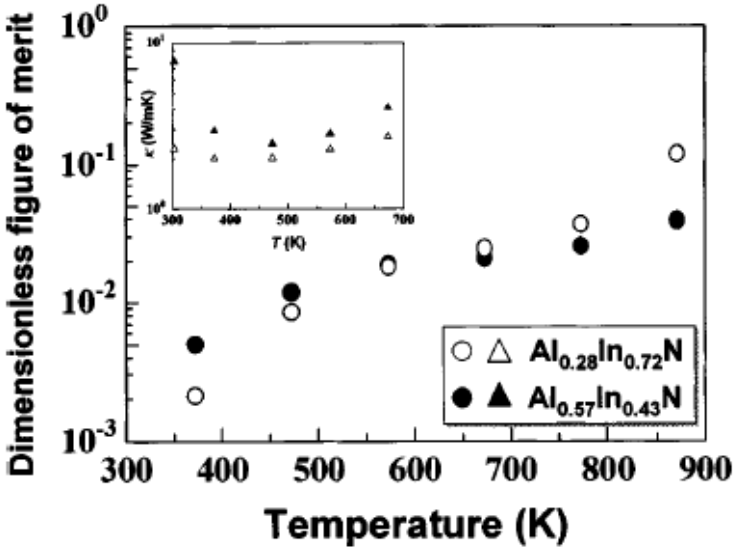

Figure 2-8: *The measured Z*T values as a function of temperature for* RF-sputtered AlInN alloy *[45].*

Our recent works [56, 57, 59] reported high *Z*T* value for AlInN alloys with various In-contents grown on GaN template by metalorganic vapor phase epitaxy (MOVPE) at room temperature (T = 300 K). The thermoelectric figure of merit (*Z*T*) values of the n-$Al_{1-x}In_xN$ alloys were measured as high as 0.391 up to 0.532 at T = 300 K, as shown in figure 2-9. The use of high In-content (*x* = 21.34%) AlInN alloys leads to significant reduction in thermal conductivity [K = 1.62 W/(mK)] due to the increased alloy scattering, however, the optimized thermoelectric material was obtained for AlInN alloy with In-content of 17% attributed to its large power factor.

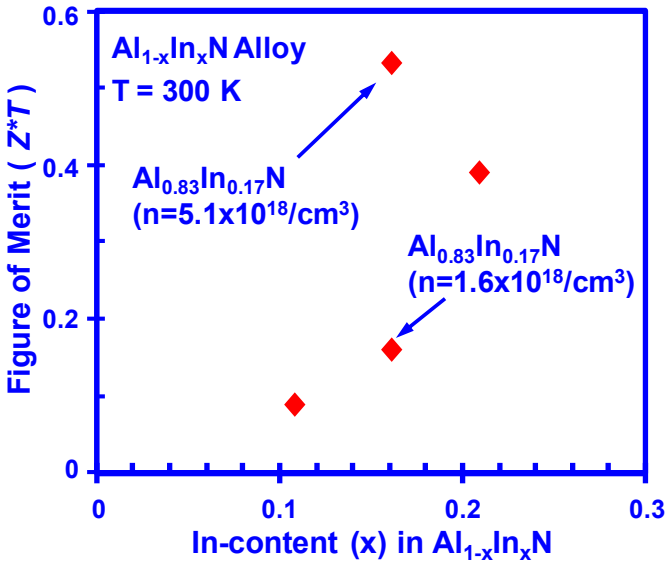

Figure 2-9: *The Z*T values for $Al_{1-x}In_xN$ alloys with various In-contents (x) from x=0.11 up to x=0.2134 at T=300K [57].*

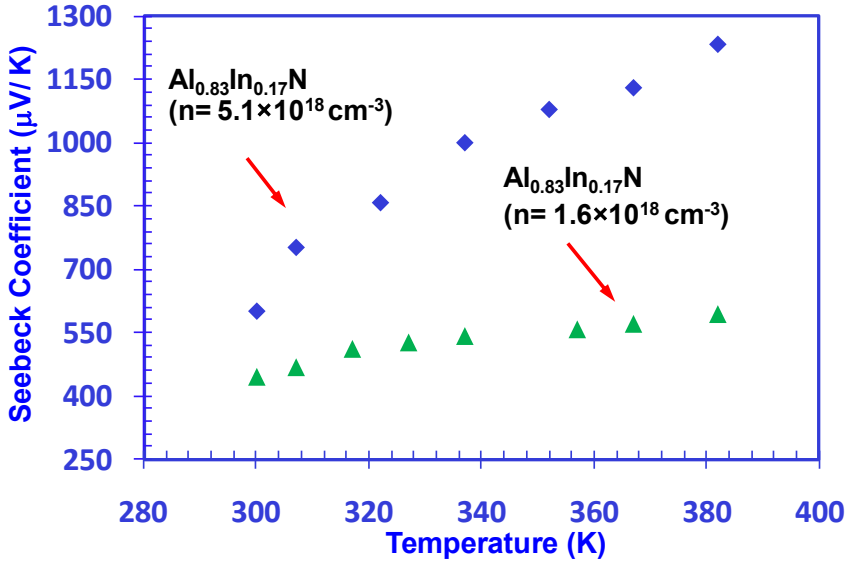

Figure 2-10: *The measured Seebeck coefficients for n-type $Al_{0.83}In_{0.17}N$ ($n=5.1\times10^{18}cm^{-3}$ and $n=1.6\times10^{18}cm^{-3}$) alloys from T=300K up to T=382K [59].*

Furthermore, the Seebeck coeeficients of AlInN alloys grown by MOVPE, with In-contents (*x*) from 0.38% up to 21.34% were characterized and analyzed from room temperature (*T* = 300 K) up to high temperature (*T* = 382 K), as shown in figure 2-10 [59]. The Seebeck coefficients of the n-type AlInN alloys show significant enhancement at higher temperature up to 382 K, in

comparison to those measured at room temperature. Large Seebeck coefficients (602.0 μV/K – 1233.2 μV/K) were obtained for the lattice-matched $Al_{0.83}In_{0.17}N$ alloy (n= 5.1×10^{18} cm^{-3}) from T = 300 K up to T = 382 K. The improvement of Seebeck coefficients for the n-type AlInN alloys will lead to ~1.5- 4 times improvement of the thermopower at higher temperatures.

2.2 Current Status of AlGaN QWs UV Lasers

2.2.1 Challenges and Limitations for Deep UV Lasers

In contrast to the progress in high performance visible LEDs and lasers, the realization of electrically-injected mid- (wavelength (λ) ~250-320 nm) and deep-ultraviolet (UV) (λ ~220-250 nm) AlGaN quantum wells (QWs) lasers have been limited to emission wavelength ~320-360 nm [60-77]. As shown in figure 2-11, the shortest emission wavelength obtained for electrically-injected AlGaN QWs lasers has been limited to λ ~ 336 nm [73].

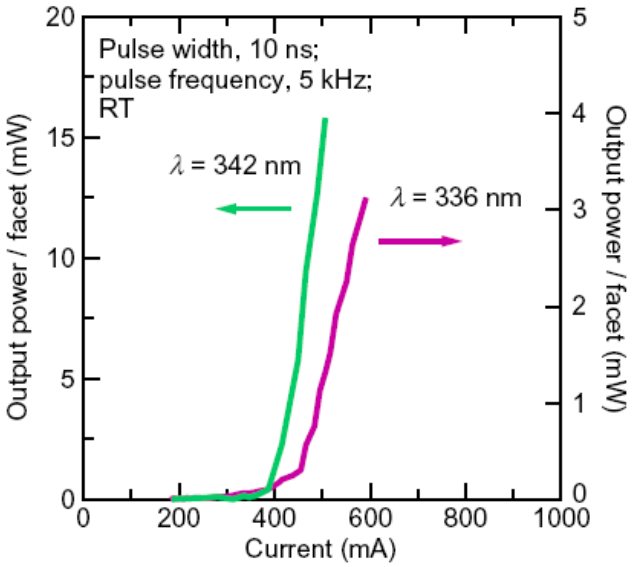

Figure 2-11: *The L–I characteristics for the AlGaN MQW laser diodes lasing at the wavelengths of 342 and 336 nm at T=300 K [73].*

For shorter emission wavelength at deep UV spectral regimes, only optically-pumped deep-UV lasers had been realized [69]. As shown in figure 2-12, the emission wavelength obtained for optically-pumped AlGaN QWs lasers was λ ~ 241.5 nm [69].

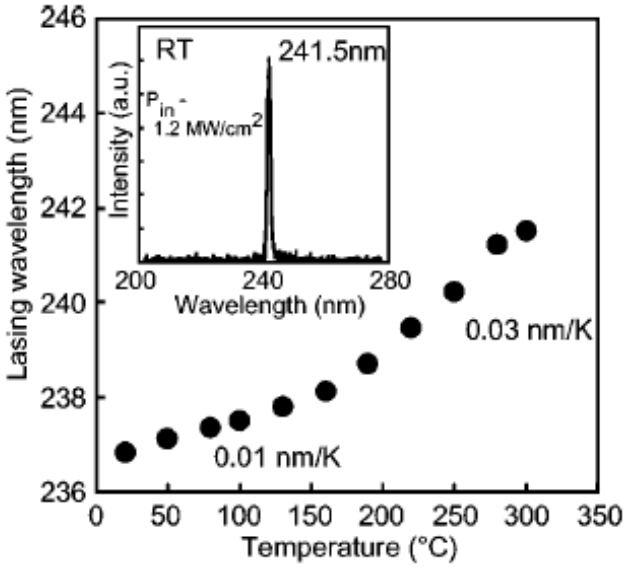

Figure 2-12: *The temperature dependence of lasing wavelength of a deep-UV laser, with λ~ 241.5 nm at room temperature [69].*

The challenges in realizing the electrically-injected mid- and deep-UV AlGaN QWs lasers can be summarized as follow: 1) the growth challenges to achieve high quality p-type AlN and high Al-content AlGaN gain media (figure 2-13), and 2) the lack of understanding on physics of the gain characteristics of mid- and deep-UV AlGaN QWs.

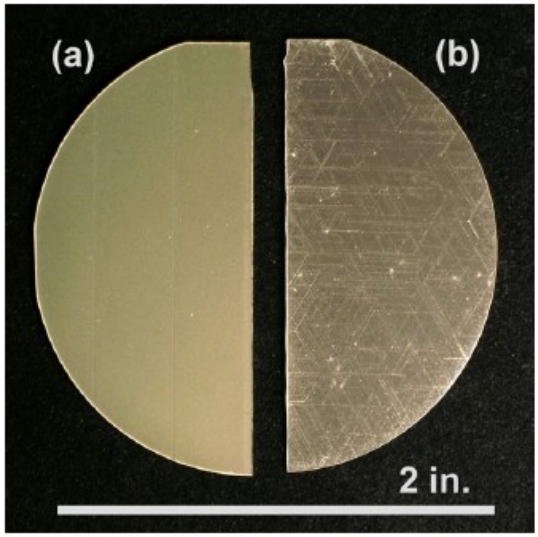

Figure 2-13: *The (a) optimized crack-free wafer, and (b) cracking wafer for AlGaN QWs laser diodes [73].*

2.2.2 State-of-the-Art AlGaN QW Lasers – Mid UV and Deep UV

The optical properties for both low [78-80] and high Al-content [81, 82] AlGaN QWs lasers have been reported recently, while the studies are relatively lacking on gain properties of high Al-content AlGaN QWs.

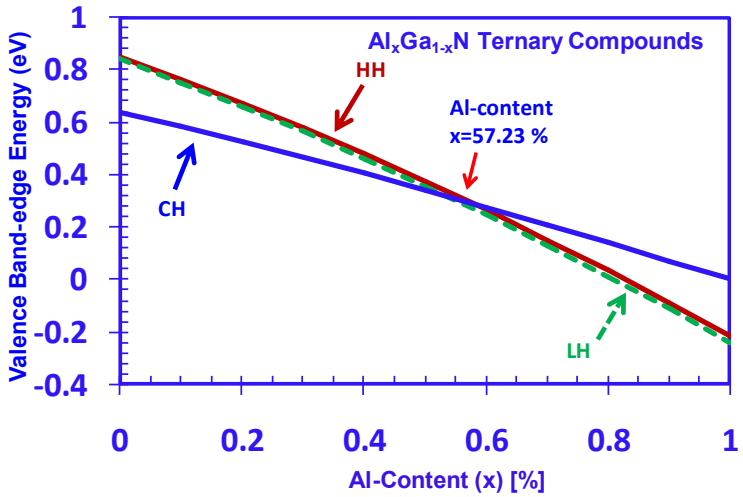

Figure 2-14: *The energy band edges of the HH, LH and CH bands as a function of Al-content (x) for Al$_x$Ga$_{1-x}$N ternary compounds [81].*

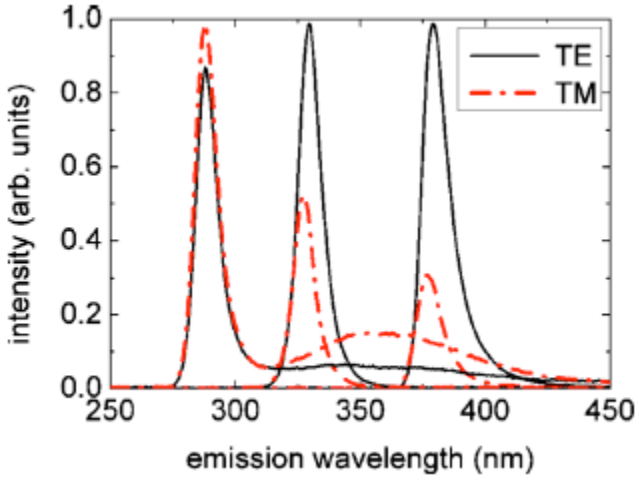

Figure 2-15: *The TE and TM polarized in-plane emission spectra of 379, 329, and 288 nm AlGaN QWs LEDs [83].*

Our previous work [81] has revealed the valence subbands crossover (figure 2-14) in high Al-content AlGaN QWs. In high Al-content AlGaN QWs, the valence subbands crossover leads to strong conduction (C) -crystal-field split-off hole (CH) transition, which results in large transverse-

magnetic (TM)-polarized optical gain for λ ~220-230 nm. Recent experimental works have also confirmed the dominant TM-polarized emission dominant for shorter wavelength with higher Al-content of AlGaN QWs LEDs [83, 84], as shown in figure 2-15, which is in agreement with our theoretical prediction [81].

The subsequent paper has also studied about the temperature and barrier effect on the polarization properties of AlGaN QWs [85]. Recently, theoretical work by Sharma and co-authors [86] has also confirmed the valence subbands crossover for AlGaN alloys on $Al_{0.85}Ga_{0.15}N$ substrate, in agreement with previous finding [81]. Furthermore, subsequent theoretical work [87] has discussed the strain effect by using various AlGaN substrates or templates on the crossover of AlGaN alloys. Very recent study by G. A. Garrett and co-authors has experimentally confirmed our theoretical prediction of the CH and heavy hole (HH) bands crossover for AlGaN QWs by showing that the dominant photoluminescence polarization switched from transverse-electric (TE) polarized (λ ~ 253 nm) to TM-polarized (λ ~ 237 nm) emissions, as shown in figure 2-16 [88].

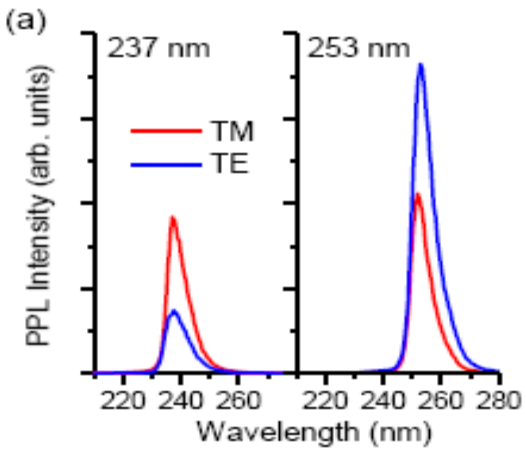

Figure 2-16: *The qualitative comparison of PL emission of AlGaN laser diode heterostructures grown on bulk AlN [88].*

In order to address the issue of low optical gain at λ ~ 250-300 nm, we recently proposed the AlGaN-delta-GaN QW structure (figure 2-17) [89] by inserting an ultra-thin GaN layer into high Al-content (x) $Al_xGa_{1-x}N$-delta-GaN QW active region. The use of AlGaN-delta-GaN QWs resulted in strong valence subbands mixing, which led to large TE-polarized gain at λ ~ 240-300 nm, attributing to the dominant C-HH transition.

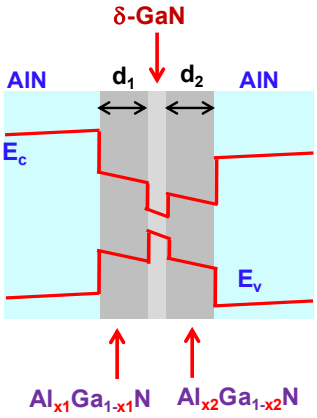

Figure 2-17: *The schematics energy band lineups of the $Al_{x1}Ga_{1-x1}N$/ delta-GaN/ $Al_{x2}Ga_{1-x2}N$ QW structure with AlN barriers [89].*

Recent experimental work by Taniyasu and co-authors [90] has reported the polarization properties of the deep-UV emission from AlN/GaN short-period superlattices. The study revealed that stronger TE-polarized deep-UV emission can be obtained by inserting a very thin GaN layer into AlN active region, similar with our prediction based on high Al-content $Al_xGa_{1-x}N$-delta-GaN QW structure [89].

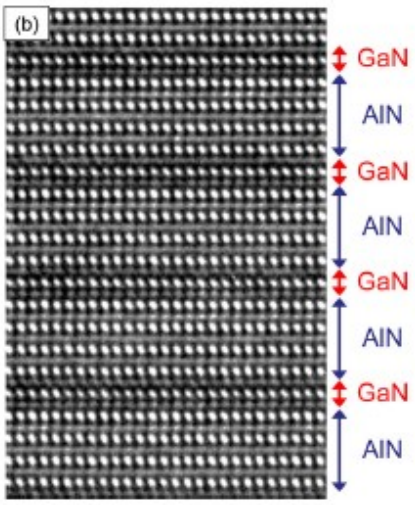

Figure 2-18: *The cross-sectional TEM image of AlN/ GaN superlattices [90].*

Furthermore, we have reported a comprehensive optimization study on the optical gain and threshold characteristics of AlGaN-delta-GaN QWs with varying delta-GaN positions and AlGaN QWs compositions for the mid- and deep-UV spectral regimes.

2.3 Current Status and Motivation of Substrate Engineering

2.3.1 Challenges of Conventional InGaN QWs LEDs and Lasers

III-Nitride semiconductors have applications for lasers and energy-efficient technologies, including solid state lighting. Specifically, the use of InGaN alloy is of great interest as light-emitting diodes (LEDs) active region. In conventional approach, the growths of visible LEDs employ InGaN quantum wells (QWs) grown on GaN templates, which lead to the existence of large QW strain arisen from the large lattice mismatch ($\Delta a/a$) between InGaN QW and GaN substrate / barrier materials. The compressive strain in InGaN QW, with respect to GaN substrate or template, leads to large piezoelectric polarization in the QW. The large piezoelectric polarization, in addition to spontaneous polarization, leads to charge separation effect in QW, which reduces the optical matrix element in InGaN QW [35, 91]. The large QW strain and charge separation issues lead to additional challenges in achieving high-efficiency green- and red-emitting InGaN QWs, as illustrated in figure 2-19.

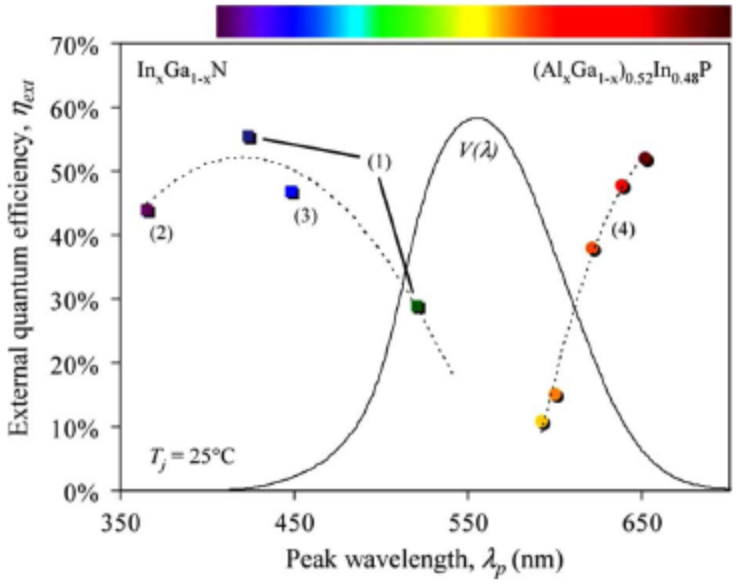

Figure 2-19: *State-of-the-art external quantum efficiency (EQE) for LEDs emitting at various wavelengths [24].*

Several approaches by using InGaN QWs with large overlap designs have also been pursued to address the charge separation issue, such as two-layer and three-layer staggered InGaN QWs (figure 2-20) [95-97], InGaN-delta-InN QW [32], and linearly-shaped staggered InGaN QWs [27].

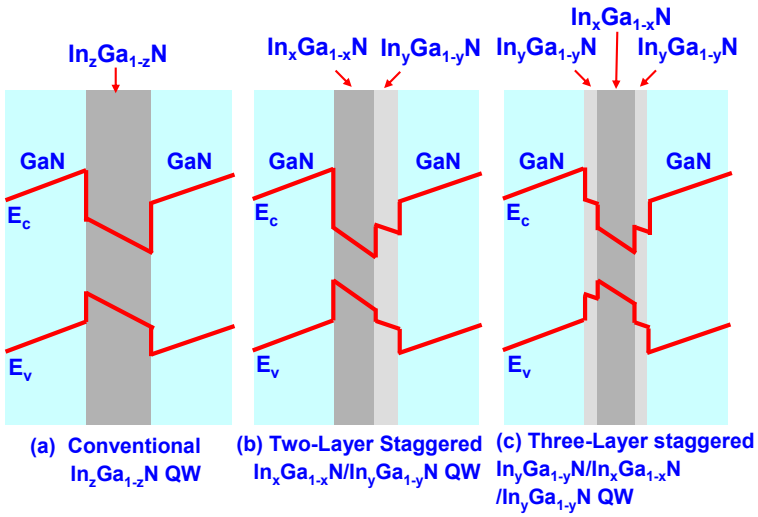

Figure 2-20: *Schematics of the (a) conventional $In_zGa_{1-z}N$-GaN QW; (b) two-layer staggered $In_xGa_{1-x}N$ / $In_yGa_{1-y}N$ QW; and (c) three-layer staggered $In_yGa_{1-y}N$ / $In_xGa_{1-x}N$ / $In_yGa_{1-y}N$ QW structures [27].*

2.3.2 Motivations of Substrate Engineering

Previously, Shimizu and co-workers had reported the growths of InGaN ternary templates on sapphire substrates by metalorganic vapor phase epitaxy, which demonstrated that smooth InGaN alloys can be obtained by employ AlN buffer layer (figure 2-21) [100]. Recent works by hydride vapor phase epitaxy have also led to successful growths of high quality InGaN ternary substrates (figure 2-22), which are applicable for LED epitaxy [102].

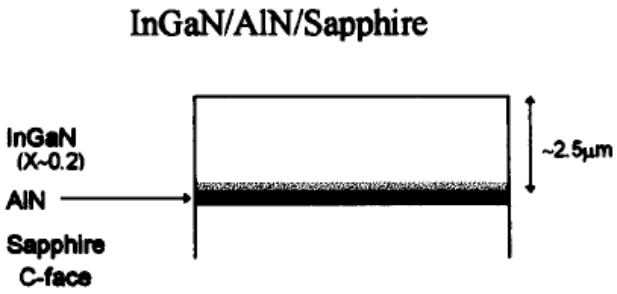

Figure 2-21: *Schematic of InGaN growth on and AlN buffer layer [100].*

The use of InGaN substrate has the potential for enabling the growth of InGaN QW with reduced QW strain. Recent work by Sharma and Towe [103] has pointed out the possibility of achieving emission wavelength in the green up to red spectral regimes by using InGaN QW on

$In_{0.15}Ga_{0.85}N$ substrate. In addition, the use of strain-compensated InGaN / InGaN QW [104], similar to staggered QW, has also been proposed for green-emitting QWs on ternary substrate. However, up to today, no comprehensive studies on the spontaneous emission characteristics of InGaN QW grown on InGaN substrate have been reported, and these studies are important in order to clarify on the optical properties and optimized QWs grown on ternary substrates for nitride-based LEDs.

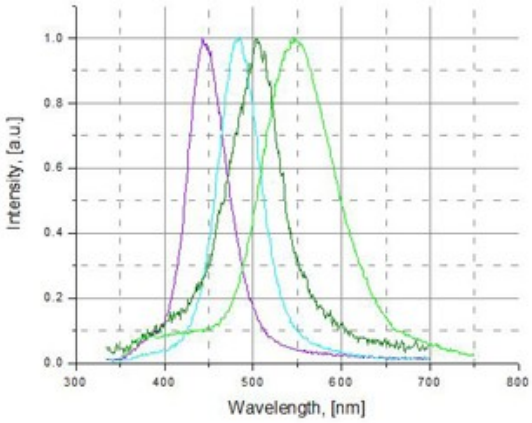

Figure 2-22: *PL spectra for HVPE-grown InGaN layers for violet, blue, and green spectrum regions [102].*

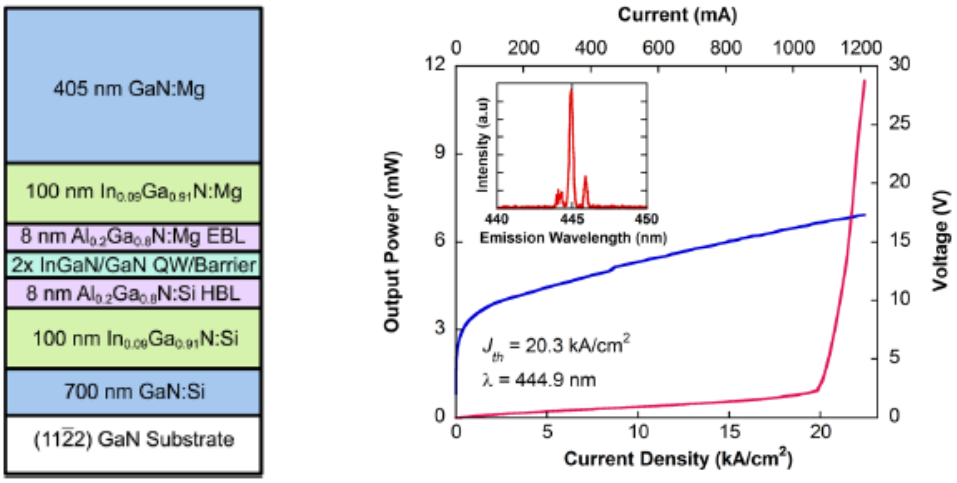

Figure 2-23: *Schematic and pulsed L-I-V characteristics of semipolar laser grown on an intentionally stress-relaxed n-$In_{0.09}Ga_{0.91}N$ template [106].*

Recently, experimental work [106] had also reported an electrically-injected semipolar laser grown on an intentionally stress-relaxed n-$In_{0.09}Ga_{0.91}N$ template, which shows the feasibility of

the ternary template for lasers. These initial works have shown the potential of this method for achieving high performance visible LEDs and lasers. However, comprehensive studies on the optical gain and threshold characteristics of InGaN QWs on ternary InGaN substrate or template are still lacking.

2.4 Summary

In summary, the current status and challenges for III-Nitride semiconductors are reviewed in details on three main aspects: thermoelectricity, AlGaN-based mid- and dee-UV lasers, as well as the substrate engineering approach for InGaN-based visible LEDs and lasers, which provides motivations for research and engineering approaches in order to address the challenges and limitations for III-Nitride based semiconductors materials and devices for applications in laser diodes and energy-related applications.

References for Chapter 2

[1] A.J. Minnich, M.S. Dresselhaus, Z.F. Ren, and G. Chen, “Bulk nanostructured thermoelectric materials: current research and future prospects,” Energy and Environmental Science, vol. 2, pp. 466-479, Feb. 2009.

[2] M. S. Dresselhaus, G. Chen, M. Y. Tang, R. G. Yang, H. Lee, D. Z. Wang, Z. F. Ren, J.-P. Fleurial, P. Gogna, “New Directions for Low-Dimensional Thermoelectric Materials,” Advanced Materials, vol. 19, pp. 1043–1053, April, 2007.

[3] G. Chen, M.S. Dresselhaus, G. Dresselhaus, J.P. Fleurial, T. Caillat, “Recent developments in thermoelectric materials,” International materials reviews, vol. 48, pp. 45-66, Feb. 2003.

[4] M. S. Dresselhaus, G. Chen, M. Y. Tang, R. G. Yang, H. Lee, D. Z. Wang, Z. F. Ren, J. P. Fleurial, P. Gogna, in Materials and Technologies for Direct Thermal-to-Electric Energy Conversion, MRS Symp. Proc. (Eds: J. Yang, T. P. Hogan, R. Funahashi, G. S. Nolas), Materials Research Society Press, Pittsburgh, PA 2005, pp. 3–12.

[5] M. S. Dresselhaus, J. P. Heremans, in Thermoelectrics Handbook: Macro to Nano (Ed: D. M. Rowe), Taylor and Francis, CRC, Boca Raton, FL 2006, Ch. 39, p. 39-1–39-24.

[6] L. E. Bell, Science, 321, 1457, 2008.

[7] R. Venkatasubramanian, E. Siivola, T. Colpitts and B. O'Quinn, Nature, 413, 597, 2001.

[8] T. C. Harman, P. J. Taylor, M. P. Walsh and B. E. LaForge, Science, 297, 2229, 2002.

[9] A. I. Hochbaum, R. Chen, R. D. Delgado, W. Liang, E. C. Garnett, M. Najarian, A. Majumdar and P. Yang, Nature, 451, 163, 2008.

[10] A. I. Boukai, Y. Bunimovich, J. Tahir-Kheli, J.-K. Yu, W. A. Goddard Iii and J. R. Heath, Nature, 451, 168, 2008.

[11] P. F. P. Poudeu, J. D'Angelo, A. D. Downey, J. L. Short, T. P. Hogan, and M. G. Kanatzidis, Angew. Chem., Int. Ed., 45, 3835, 2006.

[12] J. Androulakis, C. H. Lin, H. J. Kong, C. Uher, C. I. Wu, T. Hogan, B. A. Cook, T. Caillat, K. M. Paraskevopoulos and M. G. Kanatzidis, J. Am. Chem. Soc., 129, 9780, 2007.

[13] J. P. Heremans, V. Jovovic, E. S. Toberer, A. Saramat, K. Kurosaki, A. Charoenphakdee, S. Yamanaka and G. J. Snyder, Science,321, 554, 2008.

[14] J. Sootsman, H. Kong, C. Uher, J. D'Angelo, C. I. Wu, T. Hogan, T. Caillat, and M. Kanatzidis, Angew. Chem., Int. Ed. , 47, 8618, 2008.

[15] W. Kim, S. L. Singer, A. Majumdar, D. Vashaee, Z. Bian, A. Shakouri, G. Zeng, J. E. Bowers, J. M. O. Zide, and A. C. Gossard, Appl. Phys. Lett. 88, 242107 (2006).

[16] G. Zeng, J.-H. Bahk, J. E. Bowers, H. Lu, A. C. Gossard, S. L. Singer, A. Majumdar, Z. Bian, M. Zebarjadi, and A. Shakouri, Appl. Phys. Lett. 95, 083503 (2009).

[17] X. Liu, A.T.Ramu, J.E.Bowers, C.J.Palmstrøm, P.G.Burke, H.Lu, A.C.Gossard, Journal of Crystal Growth, 316, 56–59, 2011.

[18] R. M. Farrell, D. F. Feezell, M. C. Schmidt, D. A. Haeger, K.M. Kelchner, K. Iso, H. Yamada, M. Saito, K. Fujito, D. A. Cohen, J. S. Speck, S P. DenBaars, and S. Nakamura, Jpn. J. Appl. Phys., 46, L761 (2007).

[19] D. Queren, A. Avramescu, G. Bruderl, A. Breidenassel, M. Schillgalies, S. Lutgen, and U. Strau, Appl. Phys. Lett., 94, 081119 (2009).

[20] M. Abid, T. Moudakir, Z. Djebbour, G. Orsal, S. Gautier, A. En Naciri, A. Migan-Dubois, and A. Ougazzaden, J. Crys. Growth, 315, 283 (2011).

[21] A. Venkatachalam, B. Klein, J.-H Ryou, S. C. Shen, R. D. Dupuis, P. D. Yoder, IEEE J. Quantum Electron., 46, 238 (2010).

[22] D. S. Sizov, R. Bhat, J. Napierala, C. Gallinat, K. Song, and C. Zah, Applied Physics Express, 2, 071001 (2009).

[23] T. Miyoshi, S. Masui, T. Okada, T. Yanamoto, T. Kozaki, S. Nagahama, and T. Mukai, Appl. Phys. Expr., 2, 062201 (2009).

[24] M. H. Crawford, IEEE J. Sel. Top. Quantum Electron., 15, 1028 (2009).

[25] N. F. Gardner, G. O. Muller, Y. C. Shen, G. Chen, S. Watanabe, W. Gotz, and M. R. Krames, Appl. Phys. Lett., 91, 243506 (2007).

[26] M. H. Kim, M. F. Schubert, Q. Dai, J. K. Kim, E. F. Schubert, J. Piprek, and Y. Park, Appl. Phys. Lett., 91, 183507 (2007).

[27] H. Zhao, G. Liu, J. Zhang, J. D. Poplawsky, V. Dierolf, and N. Tansu, Optics Express, 19, A991 (2011).

[28] J. J. Wierer, A. David, and M. M. Megens, Nat. Photon., 3, 163 (2009).

[29] X. H. Li, R. Song, Y. K. Ee, P. Kumnorkaew, J. F. Gilchrist, and N. Tansu, IEEE Photonics Journal, 3, 489 (2011).

[30] T. Jung, L. K. Lee, and P. C. Ku, IEEE J. Sel. Top. Quantum Electron., 15, 1073 (2009).

[31] X. Li, S. G. Bishop, J. J. Coleman, Appl. Phys. Lett., 73, 1179 (1998).

[32] H. P. Zhao, G. Y. Liu, and N. Tansu, Appl. Phys. Lett., 97, 131114, (2010).

[33] K. McGroddy, A. David, E. Matioli, M. Iza, S. Nakamura, S. DenBaars, J. S. Speck, C. Weisbuch, and E. L. Hu, Appl. Phys. Lett., 93, 103502 (2008).

[34] S. Chhajed, W. Lee, J. Cho, E. F. Schubert, and J. K. Kim, Appl. Phys. Lett., 98, 071102 (2011).

[35] J.-H. Ryou, P. D. Yoder, J. Liu, Z. Lochner, H. Kim, S. Choi, H. J. Kim, R. D. Dupuis, IEEE J. Sel. Top. Quantum Electron., 15, 1080 (2009).

[36] X. Li, S. Kim, E. E. Reuter, S. G. Bishop, and J. J. Coleman, Appl. Phys. Lett., 72, 1990 (1998).

[37] D. D. Koleske, A. J. Fischer, A. A. Allerman, C. C. Mitchell, K. C. Cross, S. R. Kurtz, J. J. Figiel, K. W. Fullmer, and W. G. Breiland, Appl. Phys. Lett., 81, 1940 (2002).

[38] T. Shioda, Y. Tomita, M. Sugiyama, Y. Shimogaki, and Y. Nakano, IEEE J. Sel. Top. Quantum Electron. 15, 1053 (2009).

[39] T. Paskova, and K. R. Evans, IEEE J. Sel. Top. Quantum Electron. 15, 1041 (2009).

[40] U. K. Mishra, P. Parikh, and Y. F. Wu, Proc. of the IEEE, 90, 1022 (2002).

[41] R. Dahal, B. Pantha, J. Li, J. Y. Lin, and H. X. Jiang, Appl. Phys. Lett., 94, 063505 (2009).

[42] C. J. Neufeld, N. G. Toledo, S. C. Cruz, M. Iza, S. P. DenBaars, and U. K. Mishra, Appl. Phys. Lett., 93, 143502 (2008).

[43] G. Chen and A. Shakouri, J. Heat Transfer, 124, 242 (2002).

[44] S. Yamaguchi, Y. Iwamura, and A. Yamamoto, Appl. Phys. Lett., 82, 2065 (2003).

[45] S. Yamaguchi, R. Izaki, K. Yamagiwa, K. Taki, Y. Iwamura, and A. Yamamoto, Appl. Phys. Lett., 83, 5398 (2003).

[46] S. Yamaguchi, R. Izaki, N. Kaiwa, S. Sugimura and A. Yamamoto, Appl. Phys. Lett., 84, 5344 (2004).

[47] S. Yamaguchi, R. Izaki, Y. Iwamura, and A. Yamamoto, Physica Stat. Solidi (a), 201, 225 (2004).

[48] R. Izaki, N. Kaiwa, M. Hoshino, T. Yaginuma, S. Yamaguchi, and A. Yamamoto, Appl. Phys. Lett., 87, 243508 (2005).

[49] S. Yamaguchi, R. Izaki, N. Kaiwa, and A. Yamamoto, Appl. Phys. Lett., 86, 252102 (2005).

[50] A. Sztein, H. Ohta, J. Sonoda, A. Ramu, J. E. Bowers, S. P. DenBaars, and S. Nakamura, Appl. Phys. Exp., 2, 111003 (2009).

[51] E. N. Hurwitz, M. Asghar, A. Melton, B. Kucukgok, L. Su, M. Orocz, M. Jamil, N. Lu, I. T. Ferguson, J. Elec. Materials, 40, 513 (2011).

[52] W. Liu, A. A. Balandin, J. Appl. Phys., 97, 073710 (2005).

[53] W. Liu, and A. A. Balandin, J. Appl. Phys., 97, 123705 (2005).

[54] B. N. Pantha, R. Dahal, J. Li, J. Y. Lin, H. X. Jiang, and G. Pomrenke, Appl. Phys. Lett., 92, 042112 (2008).

[55] B. N. Pantha, R. Dahal, J. Li, J. Y. Lin, H. X. Jiang, and G. Pomrenke, J. Electro. Mater., 38, 1132 (2009).

[56] H. Tong, J. Zhang, G. Liu, J. A. Herbsommer, G. S. Huang, and N. Tansu, Appl. Phys. Lett., 97, 112105 (2010).

[57] J. Zhang, H. Tong, G. Liu, J. A. Herbsommer, G. S. Huang, and N. Tansu, J. Appl. Phys., 109, 053706 (2011).

[58] B. N. Pantha, I. Feng, K. Aryal, J. Li, J. Y. Lin, and H. X. Jiang, Applied Physics Express, 4, 051001 (2011).

[59] J. Zhang, S. Kutlu, G.Y.Liu, and N. Tansu, J. Appl. Phys., 110, 043710, (2011).

[60] A. Yasan, R. McClintock, K. Mayes, D. Shiell, L. Gautero, S. R. Darvish, P. Kung, and M. Razeghi, "4.5 mW operation of AlGaN-based 267 nm deep-ultraviolet light-emitting diodes," Appl. Phys. Lett., vol. **83**, no. 23, pp. 4701-4703, Oct. 2003.

[61] A. J. Fischer, A. A. Allerman, M. H. Crawford, K. H. A. Bogart, S. R. Lee, R. J. Kaplar, W. W. Chow, S. R. Kurtz, K. W. Fullmer, and J. J. Figiel, "Room-temperature direct current operation of 290 nm light-emitting diodes with milliwatt power levels," Appl. Phys. Lett., vol. **84**, no. 17, pp. 3394-3396, Apr. 2004.

[62] V. Adivarahan, S. Wu, J. P. Zhang, A. Chitnis, M. Shatalov, V. Mandavilli, R. Gaska, and M. A. Khan, "High-efficiency 269 nm emission deep ultraviolet light-emitting diodes," Appl. Phys. Lett., vol. **84**, no. 23, pp. 4762-4764, Jun. 2004.

[63] Z. Ren, Q. Sun, S. Y. Kwon, J. Han, K. Davitt, Y. K. Song, A. V. Nurmikko, H. K. Cho, W. Liu, J. A. Smart, and L. J. Schowalter, "Heteroepitaxy of AlGaN on bulk AlN substrates for deep ultraviolet light emitting diodes," Appl. Phys. Lett., vol. **91**, no. 5, pp. 051116-1–051116-3 (2007).

[64] A. V. Sampath, M. L. Reed, C. Chua, G. A. Garrett, G. Dang, E. D. Readinger, H. Shen, A. Usikov, O. Kovalenkov, L. Shapovalova, V. A. Dmitriev, N.M. Johnson, and M. Wraback, "Double heterostructure ultraviolet light emitting diodes with nanometer scale compositionally inhomogeneous active regions," Physica Status Solidi C, vol. 5, no. 6, pp. 2303-2305, Apr. 2008.

[65] C. G. Moe, M. L. Reed, G. A. Garrett, A. V. Sampath, T. Alexander, H. Shen, M. Wraback, Y. Bilenko, M. Shatalov, J. Yang, W. Sun, J. Deng, and R. Gaska, “Current-induced degradation of high performance deep ultraviolet light emitting diodes,” Appl. Phys. Lett., vol. **96**, no. 21, pp. 213512-1–213512-3, May 2010.

[66] Y. Sakai, Y. Zhu, S. Sumiya, M. Miyoshi, M. Tanaka, and T. Egawa, “Demonstration of AlGaN-Based Deep-Ultraviolet Light-Emitting Diodes on High-Quality AlN Templates,” Jpn. J. Appl. Phys., vol. **49**, pp. 022102-1–022102-4, Feb. 2010.

[67] Y. Taniyasu and M. Kasu, “Surface 210 nm light emission from an AlN p–n junction light-emitting diode enhanced by A-plane growth orientation,” Appl. Phys. Lett., vol. **96**, no. 22, pp. 221110-1–221110-3, Jun. 2010.

[68] H. Hirayama, N. Noguchi, N. Kamata, “222 nm Deep-Ultraviolet AlGaN Quantum Well Light-Emitting Diode with Vertical Emission Properties,” Applied Physics Express, vol. **3**, pp. 032102-1–032102-3, Mar. 2010.

[69] T. Takano, Y. Narita, A. Horiuchi, and H. Kawanishi, “Room-temperature deep-ultraviolet lasing at 241.5 nm of AlGaN multiple-quantum-well laser,” Appl. Phys. Lett., vol. **84**, no. 18, pp. 3567-3569, May. 2004.

[70] M. Kneissl, Z. Yang, M. Teepe, C. Knollenberg, O. Schmidt, P. Kiesel, and N. M. Johnson, S. Schujman, and L. J. Schowalter, “Ultraviolet semiconductor laser diodes on bulk AlN,” J. Appl. Phys., vol. **101**, no. 12, pp. 123103-1–123103-5, Jun. 2007.

[71] V. N. Jmerik, A. M. Mizerov, A. A. Sitnikova, P. S. Kop’ev, S. V. Ivanov, E. V. Lutsenko, N. P. Tarasuk, N. V. Rzheutskii, and G. P. Yablonskii, “Low-threshold 303 nm lasing in AlGaN-based multiple-quantum well structures with an asymmetric waveguide grown by plasma-assisted molecular beam epitaxy on c-sapphire,” Appl. Phys. Lett., vol. **96**, no. 14, pp. 141112-1–141112-3, Apr. 2010.

[72] H. Yoshida, M. Kuwabara, Y. Yamashita, K. Uchiyama, and H. Kan, “Radiative and nonradiative recombination in an ultraviolet GaN/AlGaN multiple-quantum-well laser diode,” Appl. Phys. Lett., vol. **96**, no. 21, pp. 211122-1–211122-3, May 2010.

[73] H. Yoshida, M. Kuwabara, Y. Yamashita, Y. Takagi, K. Uchiyama, and H. Kan, “AlGaN-based laser diodes for the short-wavelength ultraviolet region,” New Journal of Physics, vol. **11**, no. 12, pp. 125013-125027 , Dec. 2009.

[74] M. Kneissl, D. W. Treat, M. Teepe, N. Miyashita, and N. M. Johnson, “Continuous-wave operation of ultraviolet InGaN/InAlGaN multiple-quantum-well laser diodes,” Appl. Phys. Lett., vol. **82**, no. 15, pp. 2386-2388, Apr. 2003.

[75] C. Chen, M. Shatalov, E. Kuokstis, V. Adivarahan, M. Gaevski, S. Rai, and M. Asif Khan, “Optically Pumped Lasing at 353 nm Using Non-polar a-plane AlGaN Multiple Quantum Wells over r-plane Sapphire,” Jpn. J. Appl. Phys., vol. **43**, pp. L1099-L1102, Jul. 2004.

[76] D. A. Haeger, E. C. Young, R. B. Chung, F. Wu, N. A. Pfaff, M. Tsai, K. Fujito, S. P. DenBaars, J. S. Speck, S. Nakamura, and D. A. Cohen, “384 nm laser diode grown on a (2021) semipolar relaxed AlGaN buffer layer,” Appl. Phys. Lett., vol. 100, no. 16, Art. 161107, Apr. 2012.

[77] C. P. Wang, and Y. R. Wu, “Study of optical anisotropy in nonpolar and semipolar AlGaN quantum well deep ultraviolet light emission diode,” J. Appl. Phys., vol. 112, no. 3, Art. 033104, Aug. 2012.

[78] W. W. Chow, M. Kneissl, J. E. Northrup and N. M. Johnson, “Influence of quantum-well-barrier composition on gain and threshold current in AlGaN lasers,” Appl. Phys. Lett., vol. **90**, no. 10, pp. 101116-1–101116-3, Mar. 2007.

[79] W. W. Chow, M. Kneissl, “Laser gain properties of AlGaN quantum wells,” J. Appl. Phys., vol. **98**, no. 11, pp. 114502-1–114502-6, Dec. 2005.

[80] S. H. Park, S. L. Chuang, “Linewidth enhancement factor of wurtzite GaN/AlGaN quantum-well lasers with spontaneous polarization and piezoelectric effects,” Appl. Phys. A, vol. **78**, no. 1, pp. 107–111, Dec. 2004.

[81] J. Zhang, H. Zhao, and N. Tansu, “Effect of crystal-field split-off hole and heavy-hole bands crossover on gain characteristics of high Al-content AlGaN quantum well lasers,” Appl. Phys. Lett., vol. **97**, no. 11, pp. 111105-1–111105-3, Sep. 2010.

[82] S. H. Park, “Theoretical study of optical properties in deep ultraviolet Al-rich AlGaN/AlN quantum wells,” Semicond. Sci. Technol., vol. **24**, no. 3, pp. 035002-1–035002-4 , Feb. 2009.

[83] T. Kolbe, A. Knauer, C. Chua, Z. Yang, S. Einfeldt, P. Vogt, N. M. Johnson, M. Weyers, and M. Kneissl, “Optical polarization characteristics of ultraviolet (In)(Al)GaN multiple quantum well light emitting diodes,” Appl. Phys. Lett., vol. **97**, no. 17, pp. 171105-1–171105-3, Oct. 2010.

[84] T. M. Al tahtamouni, J. Y. Lin, and H. X. Jiang, “Optical polarization in c-plane Al-rich AlN/$Al_xGa_{1-x}N$ single quantum wells,” Appl. Phys. Lett., vol. 101, no. 4, pp. 042103-1–042103-3, Jul. 2012.

[85] T. Kolbe, A. Knauer, C. Chua, Z. Yang, V. Kueller, S. Einfeldt, P. Vogt, N. M. Johnson, M. Weyers, and M. Kneissl, “Effect of temperature and strain on the optical polarization of (In)(Al)GaN ultraviolet light emitting diodes,” Appl. Phys. Lett., **vol. 99**, no. 26, pp. 261105-1–261105-4, Dec. 2011.

[86] T. K. Sharma, and E. Towe, “Impact of strain on deep ultraviolet nitride laser and light-emitting diodes,” J. Appl. Phys., vol. **109**, no. 8, pp. 086104-1–086104-3, Apr. 2011.

[87] T. K. Sharma, D. Naveh, and E. Towe, “Strain-driven light-polarization switching in deep ultraviolet nitride emitters”, Physical Review B, vol. **84**, no. 3, pp. 035305-1–035305-8, Jul. 2011.

[88] G. A. Garrett, P. Rotella, H. Shen, M. Wraback, T. Wunderer, C. L. Chua, Z. Yang, J. E. Northrup, and N. M. Johnson, "Sub-Threshold Time-Resolved Spectroscopy of Mid-UV AlGaN Laser Diode Structures Pseudomorphically Grown on Bulk AlN," in CLEO: Applications and Technology, OSA Technical Digest (online) (Optical Society of America, 2012), paper JTh1L.5.

[89] J. Zhang, H. Zhao, and N. Tansu, “Large optical gain AlGaN-delta-GaN quantum wells laser active regions in mid- and deep-ultraviolet spectral regimes,” Appl. Phys. Lett., vol. **98**, no. 17, pp. 171111-1–171111-3, Apr. 2011.

[90] Y. Taniyasu, and M. Kasu, “Polarization property of deep-ultraviolet light emission from C-plane AlN/GaN short-period superlattices,” Appl. Phys. Lett., vol. **99**, no. 25, pp. 251112-1–251112-4, Dec. 2011.

[91] I. H. Brown, P. Blood, P. M. Smowton, J. D. Thomson, S. M. Olaizola, A. M. Fox, P. J. Parbrook, and W. W. Chow, “Time evolution of the screening of piezoelectric fields in InGaN quantum wells,” IEEE J. Quantum Electron., vol. 42, no. 12, pp. 1202–1208, Nov-Dec. 2006.

[92] A. Venkatachalam, B. Klein, J.-H Ryou, S. C. Shen, R. D. Dupuis, P. D. Yoder, “Design Strategies for InGaN-Based Green Lasers,” IEEE J. Quantum Electron., vol. **46**, no. 2, pp. 238-245, Feb. 2010.

[93] R.M. Farrell, E. C. Young, F. Wu, S.P. DenBaars, and J.S. Speck, “Materials and growth issues for high-performance nonpolar and semipolar light-emitting devices,” Semiconductor Science and Technology, vol. 27, no. 2, pp. 024001-024015, Jan. 2012.

[94] M. C. Schmidt, K.-C. Kim, R. M. Farrell, D. F. Feezell, D. A. Cohen, M. Saito, K. Fujito, J. S. Speck, S. P. Denbaars, and S. Nakamura, “Demonstration of Nonpolar m-Plane InGaN/GaN Laser Diodes,” Jpn. J. Appl. Phys., vol. **46**, pp. L190-L191, Feb. 2007.

[95] R. A. Arif, Y. K. Ee, and N. Tansu, “Polarization Engineering via Staggered InGaN Quantum Wells for Radiative Efficiency Enhancement of Light Emitting Diodes,” Appl. Phys. Lett., vol. 91 (9), Art. 091110, August 2007.

[96] H. P. Zhao, G. Y. Liu, X. H. Li, R. A. Arif, G. S. Huang, J. D. Poplawsky, S. Tafon Penn, V. Dierolf, and N. Tansu, “Design and Characteristics of Staggered InGaN Quantum Well Light-Emitting Diodes in the Green Spectral Regimes,” IET Optoelectron., vol. 3, no. 6, pp. 283-295, Dec. 2009.

[97] H. P. Zhao, and N. Tansu, “Optical Gain Characteristics of Staggered InGaN Quantum Well Lasers,” J. Appl. Phys., vol. 107, Art. 113110, June 2010.

[98] S. H. Park, D. Ahn, B. H. Koo, and J. W. Kim, “Electronic and optical properties of staggered InGaN/InGaN quantum-well light-emitting diodes,” Phys. Stat. Sol. A, vol. 206, no. 11, pp. 2637-2640, Jun. 2009.

[99] S. H. Park, D. Ahn, B. H. Koo, and J. W. Kim, “Dip-shaped InGaN/GaN quantum-well light-emitting diodes with high efficiency,” Appl. Phys. Lett., vol. 95, no. 6, pp. 063507-1-063507-3, Aug. 2009.

[100] M. Shimizu, T. Kawaguchi, K. Hiramatsu, N. Sawaki, Solid-State Electron., vol. 41, no. 2, pp. 145-147, Feb. 1997.

[101] K. Pantzasa, Y. El Gmili, J. Dickerson,S. Gautier, L. Largeau, O. Mauguin, G. Patriarche, S. Suresh, T. Moudakir, C. Bishop, A. Ahaitouf, T. Rivera, C. Tanguy, P.L. Voss, and A. Ougazzaden, “Semibulk InGaN: A novel approach for thick, single phase, epitaxial InGaN layers grown by MOVPE,” J. Crys. Growth (2012), DOI: 10.1016/j.jcrysgro.2012.08.041.

[102] www.eetimes.com/electronics-news/4189123/TDI-claims-first-InGaN-substrate

[103] T. K. Sharma, and E. Towe, “On ternary nitride substrates for visible semiconductor light-emitters,” Appl. Phys. Lett., vol. 96, no. 19, pp. 191105-1-191105-3, May 2010.

[104] S.H. Park, Y.T. Moon, J.S. Lee, H.K. Kwon, J.S. Park, and D. Ahn, “Spontaneous emission rate of green strain-compensated InGaN/InGaN LEDs using InGaN substrate,” Phys. Stat. Sol. (A), vol. **208**, no. 1, pp. 195-198, Jan. 2011.

[105] J. Zhang, and N. Tansu, “Improvement in spontaneous emission rates for InGaN quantum wells on ternary InGaN substrate for light-emitting diodes,”J. Appl. Phys., vol. 110, no. 11, pp. 113110-1-113110-5, Dec. 2011.

[106] P. S. Hsu, M. T. Hardy, F. Wu, I. Koslow, E. C. Young, A. E. Romanov, K. Fujito, D. F. Feezell, S. P. DenBaars, J. S. Speck, and S. Nakamura, “444.9 nm semipolar (1122) laser diode grown on an intentionally stress relaxed InGaN waveguiding layer,” Appl. Phys. Lett. vol. 100, no. 2, pp. 021104-1-021104-4, Jan. 2012.

Chapter 3: MOCVD Epitaxy and Device Fabrication of III-Nitride Semiconductors

In this chapter, the metalorganic chemical vapor deposition (MOCVD) and device fabrication will be discussed in details for III-Nitride semiconductors. The III-Nitride semiconductor materials are grown in house by the use of the MOCVD system, and the devices are fabricated by the use of the clean room facility.

3.1 Introduction to VEECO P-75 GaN MOCVD System

Metalorganic chemical vapor deposition (MOCVD) is an arranged chemical vapor deposition method for growing crystalline layers to create complex semiconductor multilayer structures, which is also known as metalorganic vapor phase epitaxy (MOVPE). MOCVD is the key enabling technology for manufacturing light-emitting diodes (LEDs), laser diodes, transistors, solar cells and other electronic and opto-electronic devices, which is expected to have a potentially growing market.

There are several commonly-used epitaxial growth techniques: 1) hydride vapour phase epitaxy (HVPE), 2) molecular beam epitaxy (MBE), and 3) MOVPE. HVPE, which is a well-developed technique for large scale production, can provide deposition rates of several microns per minute, making it possible to grow hundred microns thick layers. However, the background carrier concentration and material quality remain challenging in HVPE growth. MBE requires growths in high vacuum or ultra-high vacuum (10^{-8} Pa), which is a physical deposition process with a slow growth rate.

Compared with HVPE and MBE, there are several advantages of MOCVD growths [1]: 1) very high quality of grown semiconductor layers, with fast growth rate (a few microns per hour) and controllable doping uniformity; 2) no requirement of ultra high vacuum (compared to MBE), and the chemical reaction takes place at moderate pressures (50 to 500 torr), which is economically advantageous with long system up-time; 3) flexibility of growing different compound

semiconductor materials in the same system; and 4) ability of growing abrupt interfaces, which is very suitable for hetero-structures such as multiple quantum wells.

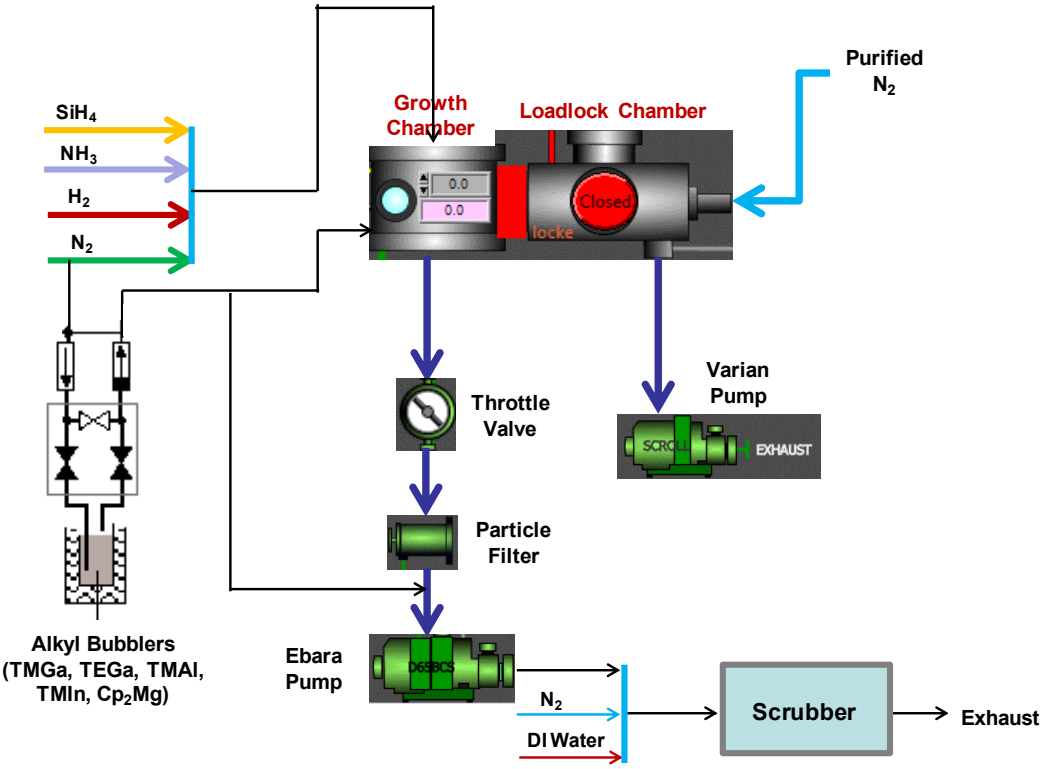

Figure 3-1: *The schematics of Veeco TurboDisc P-75 MOCVD system.*

MOCVD growth is a highly complex process, which has been developed with a lot of progress during last several decades. There are several important parameters for MOCVD process including mixed convective flow, heat transfer for the gas flow as well as for the solids, radiative transfer involving semitransparent materials, gas phase transport and reaction kinetics of reactant species and solid layer deposition from the gas phase on the surface of substrates, reactor components and walls, which will be introduced in details in section 3.2.2. MOCVD reactors design can have different orientations and geometries, while the most common designs are horizontal reactor [2-4] and vertical reactor [5-6]. For the horizontal reactors, the gases are inserted laterally with respect to sample standing horizontally on a slowly-rotating (~60RPM) susceptor plate. For the vertical reactors, the gases are entered from the top of the growth chamber, and the sample is mounted horizontally on a fast-rotating (~500-1000RPM) susceptor

plate. The susceptor is the wafer carrier that holds the substrate during the growth, which is usually rotated to average the growth symmetry and result in increased uniformity.

Figure 3-1 shows the schematics of the vertical-type Veeco TurboDisc P-75 MOCVD reactor system. The P-75 MOCVD system includes the loadlock chamber (for transferring the wafer carriers and substrates for the MOCVD growth), the growth chamber, and the two chambers are connected by the gate valve. The throttle valve underneath the growth chamber is used to control the pressure inside the growth chamber. The loadlock chamber is connected by the Varian pump underneath, and the purified N_2 supply, in order to perform pump and purge processes inside the loadlock chamber. The growth chamber is where the MOCVD growths are taken place, with the gases and Group-III and Group-V precursors flowing inside the vertical-configuration chamber and perform chemical deposition on the substrate.

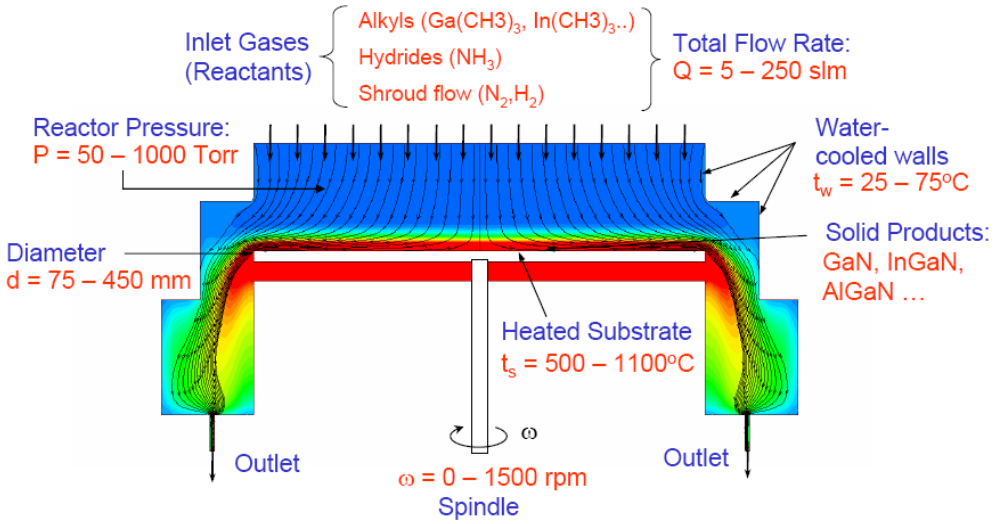

Figure 3-2: *The illustration of geometry and Process Parameters in the Veeco MOCVD TurboDisc Reactor [7].*

The typical epitaxial process steps are as follows: 1) place the substrate on the graphite susceptor (coated by SiC) in the loadlock chamber; 2) the loadlock chamber is closed, followed by pumping and purging N_2; 3) gate valve between the loadlock chamber and growth chamber is opened, then the susceptor is transferred into the growth chamber by using a remote controlled mechanical fork, so that the susceptor will be placed on the tip of a spindle inside the growth

chamber. The spindle is connected to a step motor outside the chamber, which controls the rotation speed of the susceptor (as shown in figure 3-2). 4) The mechanical fork is retrieved back from the growth chamber, and the gate valve will be closed, then the MOCVD growth will be performed in the growth chamber.

The stationary resistive heater is located beneath the susceptor, which is made of rhenium for Veeco P-75 GaN reactor. The thermocouple is pointed close to the bottom of the susceptor. The cooling water from the water chiller is cycled through the channels within the reactor walls to prevent over-heating.

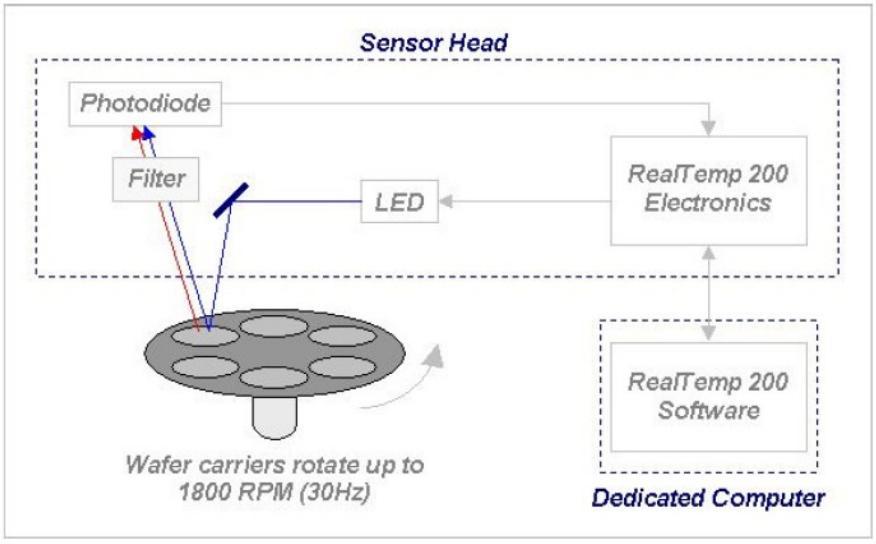

Figure 3-3: *The illustration of Veeco's RealTemp 200 system [8].*

The Veeco's RealTemp 200 (RT 200) system (figure 3-3) is an emissivity compensated pyrometer that works in the P-75 single wafer rotating disk reactor, in order to provide real-time accurate measurement of the wafer surface absolute reflectivity and provides temperature measurements during the deposition of III-Nitride thin films. The RT 200 system combines a reflectometer (for accurate, real time emissivity calculations) and a pyrometer (utilizes measured emissivity for accurate temperature measurements), which consists of an optical head (including an LED, the main and reference photodiodes) with electronics and a dedicated computer with data acquisition board. The LED is thermo-stabilized, with emission wavelength 930 nm, which is modulated at a rate of 5.2 kHz. The main photodiode is used to measure the thermal emission

from the wafers and the LED light reflected by wafers, and then the reflectivity and emission data can be extracted from the raw signal with low noise and high time resolution [8].

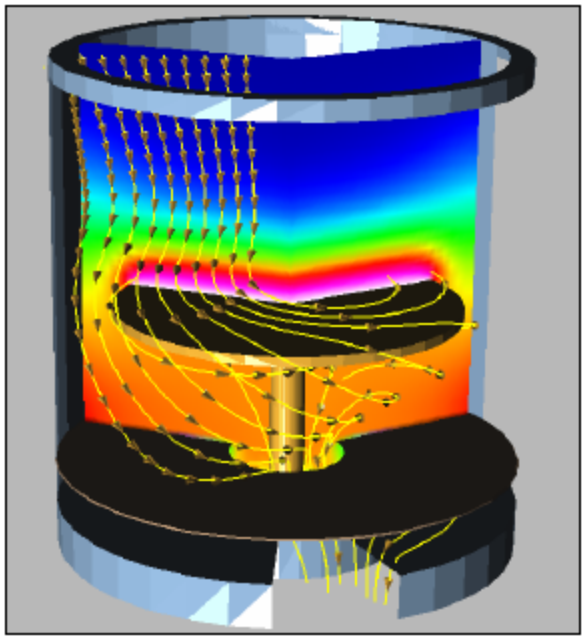

Figure 3-4: *The illustration of simulated flow patterns in rotating disc MOCVD system [7].*

For the P-75 GaN MOCVD system, the metalorganic precursors and p-type dopant are stored in stainless steel bubblers. The metalorganic precursors are: trimethylGallium (TMGa), triethylGallium (TEGa), trimethylAluminum (TMAl), trimethylIndium (TMIn). The p-type dopant is Bis(cyclopentadienyl) Magnesium (Cp_2Mg). The Group-V source is ammonia (NH_3), and the n-type dopant is silane (SiH_4), which are stored in high-pressure gas cylinders. Purified H_2 and/or N_2 gases are employed as ambient gases, and N_2 is employed as carrier gases for alkyls. The gases and precursors of Group-III and Group-V would flow into the growth chamber from the top flow flange, where the even-distributed gas flows would be delivered from the top shower head to the rotating wafer carrier, as shown in figure 3-4.

The mass flow controller (MFC) is employed to accurately control the gas flows. The accuracy of the MFC is 1% of the full scale capacity.

Figure 3-5: *The Vector Ultra 3001 gas scrubber [10].*

The gasses from the outlet of the growth chamber will be pumped out by the Ebara pump, and the exhaust of the pump is connected to the Vector Ultra 3001 gas scrubber (figure 3-5), which uses DI water and nitrogen to absorb pollutants, and the exhaust gases will be released to the main exhaust line for further scrubbing.

3.2 MOCVD Epitaxy of III-Nitride Compound Semiconductors

3.2.1 Introduction of Group-III and Group-V Precursors

The material properties of Group-III and p-type dopant metalorganic precursors are listed in table 3-1.

The TMGa ($(CH_3)_3Ga$) is the used as metalorganic source of Gallium for MOCVD growths of GaN or GaN-based ternary and quaternary alloys. The TEGa ($(C_2H_5)_3Ga$) metalorganic source is the Gallium precursor for MOCVD growth at lower temperature, attributed from the weaker bonding of the larger ethyl radical C_2H_5.

The TMIn ($(CH_3)_3In$) is the metalorganic source for Indium precursor for MOCVD growth of InN, InGaN, or related alloys. The room temperature appearance of TMIn metalorganic source is white crystalline solid.

The TMAl ($(C_2H_5)_2Mg$) is the metalorganic source for Aluminum precursor for MOCVD growth of AlN, AlGaN, AlInN, or related alloys. The room temperature appearance of TMAl metalorganic source is colorless liquid.

The Cp_2Mg ($(C_2H_5)_2Mg$) is used as p-type dopant for GaN or GaN-based alloys. The room temperature appearance of Cp_2Mg metalorganic source is yellow crystalline solid.

Material Properties	**TMGa**	**TEGa**	**TMIn**	**TMAl**	**Cp_2Mg**
Formula	$(CH_3)_3Ga$	$(C_2H_5)_3Ga$	$(CH_3)_3In$	$(CH_3)_3Al$	$(C_2H_5)_2Mg$
Formula Weight (g/ mole)	114.83	156.9	159.93	72.1	154.4
Density (g/ cc)	1.1	1.059	1.568	0.75	1.1
Melting Point (°C)	-15.8	-82	88	15.4	176
Boiling Point (°C)	55.7	143	134	126	300
Appearance	Colorless liquid	Colorless liquid	White crystals	Colorless liquid	Yellow crystalline solid

Table 3-1: *The material properties of Group-III and p-type dopant metalorganic precursors [10-11].*

The Group-V precursor for GaN-based materials is (NH_3). Silane (SiH_4) is used as n-type dopant in GaN or GaN-based alloys.

3.2.2 MOCVD Growth Parameters

The important parameters for MOCVD growth are: growth temperature, rotation speed of the susceptor, chamber pressure, and V/ III ratio during the MOCVD growth.

Those parameters can be controlled by the Epiview software for the Veeco P-75 MOCVD reactor by the use of specific growth recipe for certain GaN-based matieral.

The V/III ratio is defined as the molar ratio of the Group-V gas flow versus the Group-III gas flow inside the growth chamber.

The partial pressure is defined as the pressure that the gas would have if it alone occupies the volume. The sum of the partial pressure of each individual gas in the mixture of gases is defined as the total pressure. The partial pressure of Group-V (N precursor) can be written as:

$$P_{V\_partial} = P_{reactor} \cdot \frac{F_{NH_3}}{F_{NH_3} + F_{carrier\_gas}}, \tag{3-1}$$

where P_{reactor} is the total pressure of the reactor (torr), F_{NH3} (cubic centimeters per minute, sccm) is the flow of NH_3, and $F_{carrier\_\text{gas}}$ (sccm) is the flow of the carrier gas (N_2 or H_2) into the growth chamber.

The calculation of the Group-III partial pressure involves the vapor pressure, since the Group-III metalorganics precursors are either liquid or solid when flowing into the reactor chamber by carrier gases. The vapor pressure ($P_{\text{III\_vapor}}$, torr) has a non-linear relationship with temperature (K), which can be obtained as:

$$\log P_{III\_vapor} = B - \frac{A}{T}, \tag{3-2}$$

where A and B are fitting parameters, and T is the bubbler temperature.

The typical values of A and B parameters for the metalorganic precursors are listed in table 3-2.

Parameter	**TMGa**	**TEGa**	**TMIn**	**TMAl**
A	1703	2162	3204	2143.83
B	8.07	8.083	10.98	8.224

Table 3-2: *The typical A and B values for Group-III metalorganic precursors.*

For the metalorganic precursors with high vapor pressure such as TMGa and TMAl, the double dilution is required to further reduce the flow for precise control of growth rate, which is very important for the growth such as quantum well structure. The double dilution configuration is realized by adding the push flow to the output of the metalorganic precursor bubbler. The effective flow ($F_{III\_effective}$) of Group-III for such double dilution can be written as:

$$F_{III\_effective} = F_{III\_main} \cdot \frac{F_{DD}}{F_{III\_main} + F_{push}} \cdot \frac{P_{III\_vapor}}{P_{III\_bubbler} - P_{III\_vapor}}, \tag{3-3}$$

where F_{III_main} (sccm) is the gas flow controlled by MFC, P_{III_vapor} (torr) is the vapor pressure of Group-III metalorganic precursors, and $P_{III\_bubbler}$ (torr) is the metalorganic bubbler pressure, which is set at 900 torr for the MOCVD system.

For the metalorganic precursors such as TEGa and TMIn, for which the double dilution is not required, the effective flow ($F_{III\_effective}$, sccm) of Group-III can be written as:

$$F_{III\_effective} = F_{III\_main} \cdot \frac{P_{III\_vapor}}{P_{III\_bubbler} - P_{III\_vapor}}, \tag{3-4}$$

The partial pressure of Group-III $P_{III\_partial}$ can be obtained as:

$$P_{III\_partial} = P_{reactor} \cdot \frac{F_{III\_effective}}{F_{tota;}} = P_{reactor} \cdot \frac{F_{III\_effective}}{F_{NH_3} + F_{carrier\_gas}}. \tag{3-5}$$

Thus, the V/ III molar ratio can be obtained as:

$$\frac{V}{III} = \frac{P_{V\_partial}}{P_{III\_partial}}. \tag{3-6}$$

3.2.3 MOCVD Growth of GaN Template on Sapphire Substrate

Attributed to the lack of native substrates, the GaN-based semiconductor materials are usually grown on c-plane sapphire. The lattice mismatch is approximately 16% between GaN and sapphire, which leads to compressively strained GaN layer. High quality GaN material can be obtained by the use of a low temperature GaN buffer layer, and the typical threading dislocation density for the c-plane GaN grown on sapphire substrate is in the range of 10^7 up to 10^9 cm^{-2}.

Figure 3-6 shows the reflectivity and temperature profiles of MOCVD-grown undoped GaN with different stages (1)-(6). The TMGa and NH_3 are used as the precursors for the undoped GaN grown on c-plane sapphire. The growth procedure of the high quality undoped GaN template on sapphire substrate is as follow: (1) cleaning process of the epi-ready c-plane sapphire substrate with H_2 flow of 6000 sccm at 1080 °C for ~3 minutes; (2) low temperature GaN buffer layer (~ 35 nm) growth with growth temperature ~ 515 °C with V/ III ratio of 10416; (3) etch-back process to decompose the two-dimensional low temperature GaN to form the 3D GaN nucleation islands by ramping up the temperature to ~ 1080 °C with decreased reflectivity; (4) and (5) the recovery process when the 3D GaN nucleation islands coalescence with the temperature ~ 1020°C with a V/III=5406 to encourage the lateral growth of GaN on the micron-sized islands with increased in-situ reflectivity; (6) the growth of high temperature (~ 1070°C) undoped GaN layer (~ 3μm) is carried out after the coalescence of 3D GaN nucleation islands, the V/ III ratio is reduced to 2934 to encourage vertical with the growth rate of ~1.77 μm / hour. The MOCVD growth resulted in the undoped GaN template with background concentration of ~ 5.1×10^{16} cm^{-3} and electron mobility of ~ 446 cm^2/ (v·s).

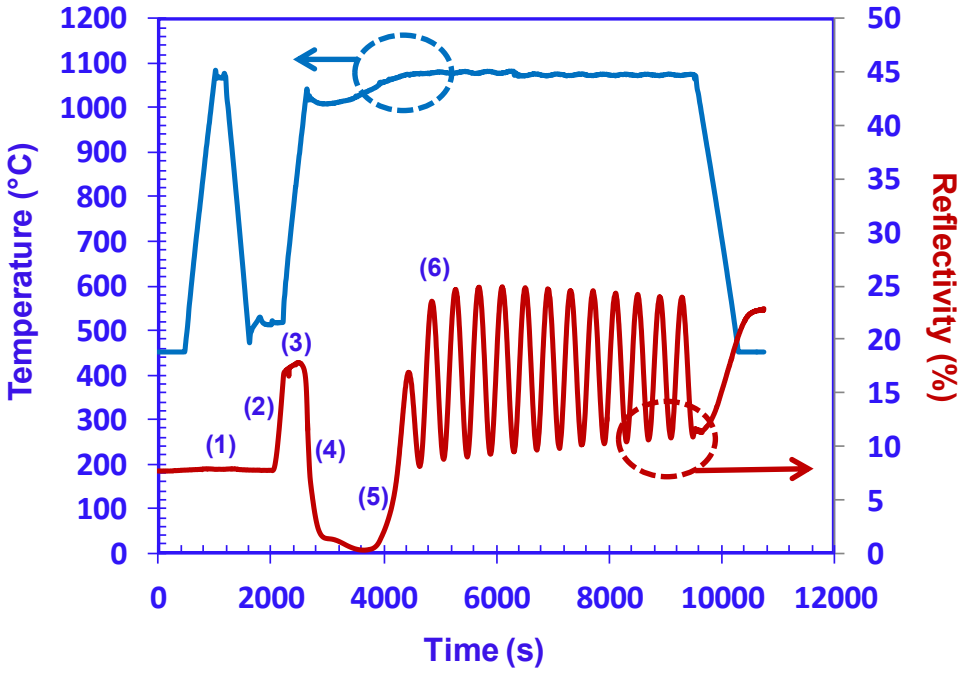

Figure 3-6: *The reflectivity and temperature profiles of MOCVD-grown undoped GaN with different stages (1)-(6).*

3.3 Device Fabrication Process

The devices based on the MOCVD-grown III-Nitride semiconductor alloys are fabricated in the clean room facility for characterizations.

In this section, the two devices fabrication processes will be introduced: 1) the III-Nitride semiconductor devices fabrication for thermal conductivity characterization by the use of 3ω method; 2) the InGaN quantum wells (QWs) based bottom-emitting light emitting diodes (LEDs).

3.3.1 Device Fabrication for Thermal Conductivity Measurement

Figure 3-7 illustrates the schematics of the four point configuration of the metal heater on top of the III-Nitride alloys for thermal conductivity measurements. The 3ω method is employed for the thermal conductivity measurements for III-Nitride semiconductors, which is a well-established technique for thermal conductivity characterizations for both bulk materials [12-14] and thin films [15-17].

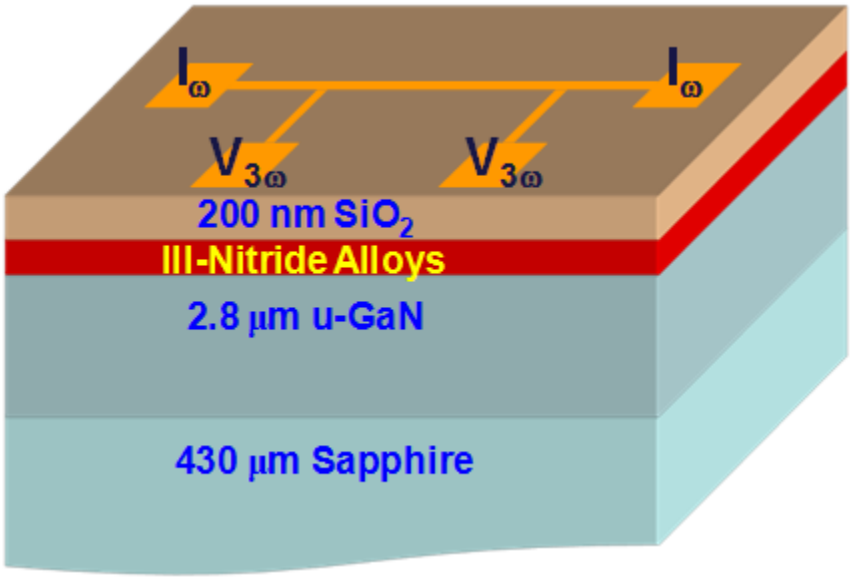

Figure 3-7: *The schematics of the four point configuration of the metal heater on top of the III-Nitride alloys for thermal conductivity measurements.*

The strip metal is deposited on top of the sample under test, as shown in figure 3-7, which serves as the heater and temperature sensor at the same time in order to obtain the thermal conductivity information for the 3ω measurement.

The details of the fabrication processes will be discussed as shown in figure 3-8. The electrical insulating layer in order to insulate the electrical current would be deposited on the sample first, which is the 200 nm SiO_2 deposited by plasma-enhanced chemical vapor deposition (PECVD).

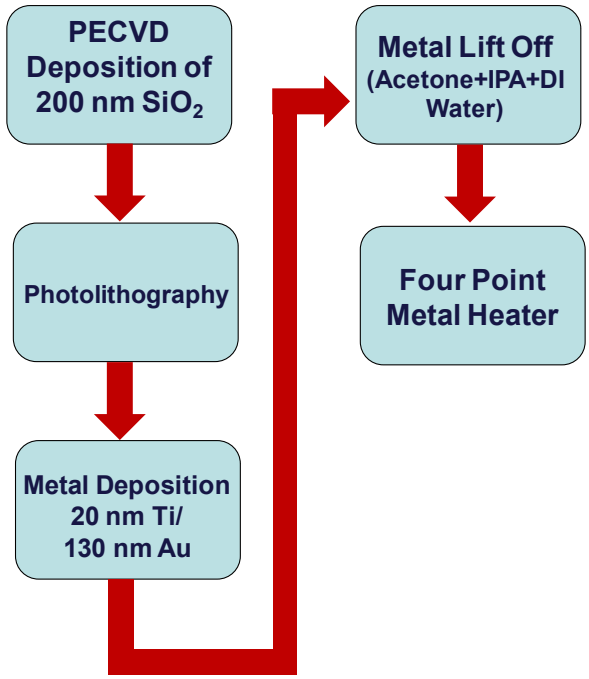

Figure 3-8: *The fabrication process flowchart the four point configuration of the metal heater for thermal conductivity measurements.*

Then the four point configuration of the metal heater will be patterned on top of the sample by photo lithography. The mask design is shown in figure 3-9. There two types of commonly used photolithography processes: 1) by the use of negative photoresist, and 2) by the use of positive photoresist, as illustrated in figure 3-10. For the use of negative photoresist (AZ5209), as shown in figure 3-10(a), the process is as follow: the sample is first spin coated with photoresist, followed by 1 minute of soft bake at 110°C. Then the sample would be exposed with hard contact with the mask for 6 seconds, followed by the 2-minute hard bake at 125°C, after which the sample will be

flood exposed for 45 seconds. Then, the sample will be developed with the AZ300 developer for the 30 seconds.

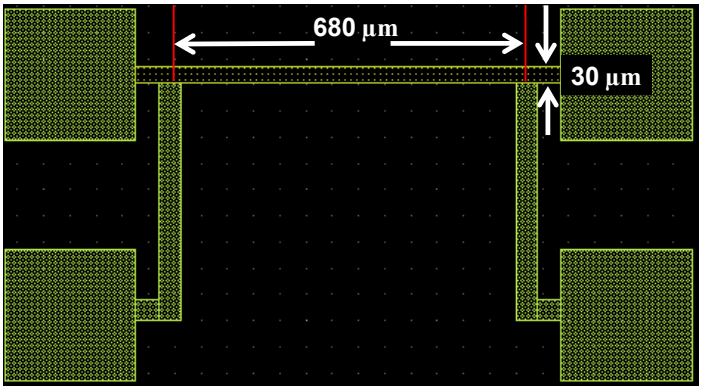

Figure 3-9: *The mask design for the four point metal heater configuration.*

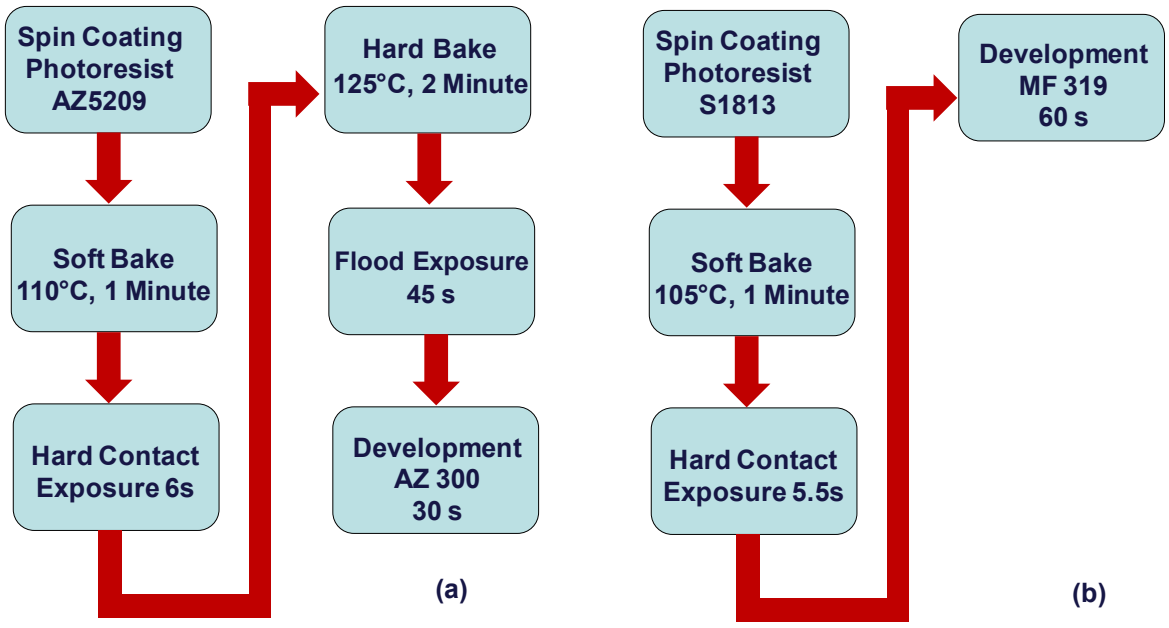

Figure 3-10: *The photolithography process flowcharts for (a) negative photoresist, and (b) positive photoresist.*

For the use of positive photoresist (S1813), as shown in figure 3-10(b), the process is as follow: the sample is first spin coated with photoresist, followed by 1 minute of soft bake at 105°C.

Then the sample would be exposed with hard contact with the mask for 5.5 seconds. Then, the sample will be developed with the MF319 developer for the 60 seconds. Note that only one exposure is required for the use of positive photoresist, which is simpler process compared to that of the negative photoresist.

After the photolithography, the electron beam evaporator is used to deposit 20 nm Ti / 130 nm Au for the metal heater. After the metal lift off by the use of acetone, IPA, and DI water, the pattern for thermal conductivity measurement would be completed, as shown in figure 3-11.

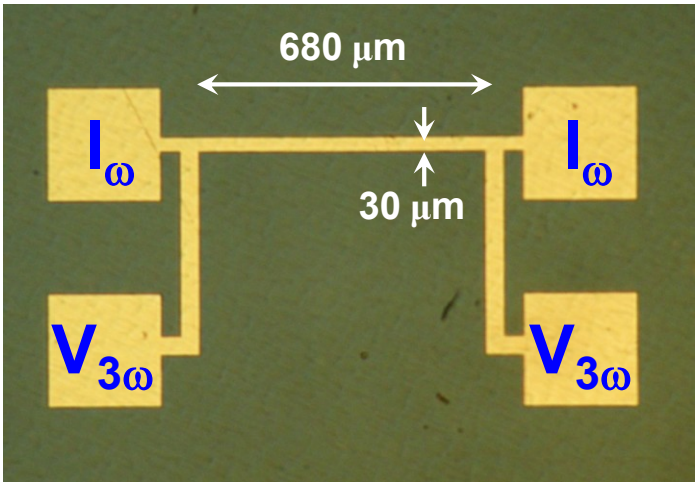

Figure 3-11: *The microscope image of the four point metal heater configuration for thermal conductivity measurements.*

3.3.2 Device Fabrication for Bottom-Emitting LED

The device fabrication process of InGaN QWs based bottom-emitting LEDs will be introduced in this section. The selective area epitaxy (SAE) approach is used for the fabrication of the bottom-emitting LEDs. Typically, the InGaN QWs active region is grown on the n-type GaN substrate on the double-side polished sapphire substrate. The p-type GaN grown on top of the active region is ~200 nm thick.

The growth of the InGaN QWs active region and the p-type GaN layer is performed by the use of the SAE approach, which employs the SiO_2 hard mask on top of the n-type GaN template. The details of the fabrication process flowchart are shown in figure 3-12: a 350 nm thick SiO_2 hard mask is first deposited by PECVD on n-type GaN template, then the sample is patterned with

mesa patterns by photolithography and etched by buffered hydrofluoric ($HF:H_2O$ = 1:30) for 1 minute. After a cleaning process with acetone, IPA, and DI water, the sample would be transferred to the MOCVD growth chamber for the selective area epitaxy of the InGaN QWs active region and the p-type GaN.

Then, the sample will be etched by HF with high concentration ($HF:H_2O$ = 1:1) for 12 hours in order to remove the SiO_2 after high temperature treatment. The next step is the photolithography for the metal patterns, including the n-type metal (20 nm Ti/ 300 nm Au) and p-type metal (20 nm Ni/ 300 nm Au). After the metal deposition and metal lift off, the sample should be annealed by rapid thermal annealing (RTA) in N_2 atmosphere for 40 seconds at 450 °C. Then the LEDs samples will be ready for characterizations.

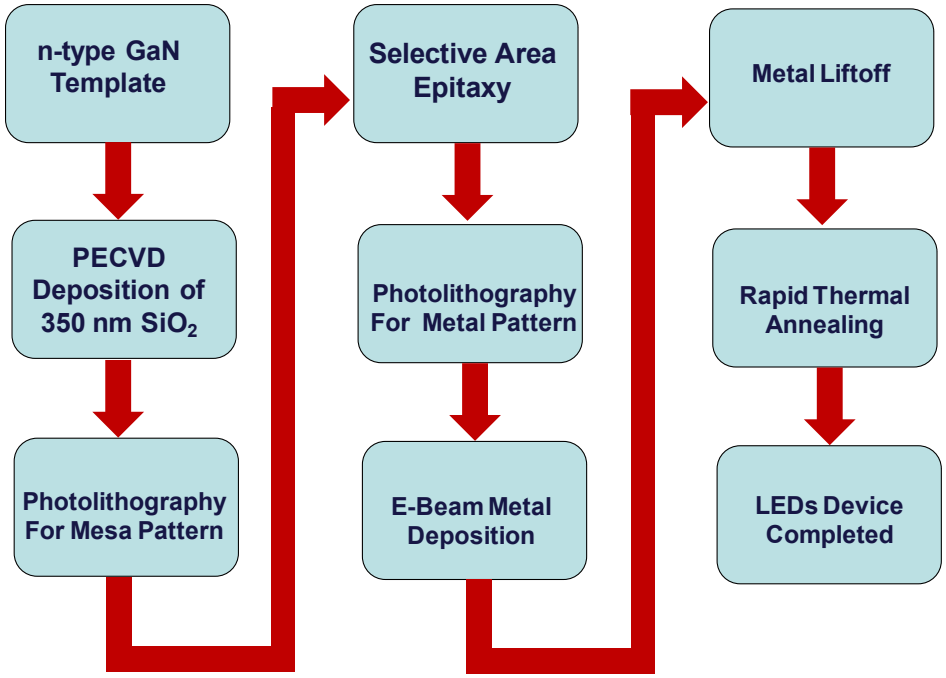

Figure 3-12: *The process flowcharts for InGaN QWs bottom-emitting LEDs.*

3.4 Summary

In summary, the metalorganic vapor phase deposition (MOCVD) and the device fabrication processes are introduced in details in this chapter. The Veeco P75 GaN MOCVD system is introduced. The Group-III metalorganic and Group-V hydride precursors are discussed in details. The important growth parameters such as growth pressures, gases flows, and V/ III ratio are also

introduced. Then the MOCVD growth of undoped GaN template on sapphire substrate by the use of low temperature GaN buffer layer is presented with specific growth stages.

The device fabrication processes are introduced for 1) thermal conductivity measurement, and 2) InGaN-based bottom-emitting LEDs. The device fabrication flow charts with details are presented for both devices, which are fabricated by the used of the clean room fabrication facility.

References for Chapter 3

[1] http://home.icpr.or.kr/~kpscondmat/link/mocvd.pdf

[2] A. G. Thompson, W. Kroll, M. A. McKee, R. A. Stall, and P. Zawadzki, "A Cost of Ownership Model for CVD Processes", III-Vs Review, vol. 8, issue 3, 1995, pp.14-20.

[3] A. G. Thompson, R. A. Stall, P. Zawadzki and G. H. Evans, "The Scaling of CVD Rotating Disk Reactors to Large Sizes and Comparison With Theory", Journal of Electronic Materials, vol. 25, 1996, pp.1487-1494.

[4] A. G. Thompson, R. A. Stall, W. Kroll, E. Armour, C. Beckham, P. Zawadzki, L. Aina and K. Siepel, "Large Scale manufacturing of compound semiconductors by MOVPE", Journal of Crystal Growth, vol. 170, 1997, pp.92-96.

[5] P. M. Frijlink, J. L. Nicolas and P. Suchet, "Layer uniformity in a multiwafer MOVPE reactor for III-V compounds", Journal of Crystal Growth, vol. 107, 1991, pp.166-174.

[6] T. Bergunde, M. Dauelsberg, L. Kadinski, Yu. N. Makarov, V. S. Yuferev, D. Schmitz, G. Strauch and H. Jürgensen, "Process optimization of MOVPE growth by numerical modeling of transport phenomena including thermal radiation", Journal of Crystal Growth, vol. 180, 1997, pp.660-669.

[7] http://www.wpi.edu/academics/che/HMTL/CFD_in_CRE_IV/Mitrovic.pdf

[8] Veeco RealTemp 200 manual.

[9] Vector Ultra 3001 Gas Scrubber manual.

[10] http://www.dow.com/product-line/cvd-precursors/product/optograde-tmga/

[11] http://www.akzonobel.com

[12] D. Cahill and R. Pohl, "Thermal conductivity of amorphous solids above the plateau," Physical Review B, vol. 35, 1987, p. 4067–4073.

[13] D. Cahill, "Thermal conductivity measurement from 30 to 750 K: the 3ω method," Sci. Instrum, vol. 61, 1990, p. 802–808.

[14] D. Cahill, "Erratum: "Thermal conductivity measurement from 30 to 750 K: the 3ω method"," [Rev. Sci. Instrum. 61, 802 (1990)]," Review of Scientific Instruments, vol. 73, 2002, p. 3701.

[15] D. Cahill, H. Fischer, T. Klitsner, and E. Swartz, "Thermal conductivity of thin films: Measurements and understanding," Science & Technology A: Vacuum, Surfaces, and Films, 1989.

[16] D. Cahill, M. Katiyar, and J. Abelson, "Thermal conductivity of a-Si: H thin films," Physical Review B, vol. 50, 1994, p. 6077–6081.

[17] S. Lee and D.G. Cahill, "Heat transport in thin dielectric films," Journal of Applied Physics, vol. 81, 1997, p. 2590.

Chapter 4: III-Nitride Semiconductors for Thermoelectric Applications

In chapter 2, the current status and challenges of thermoelectricity have been introduced with details. Specifically, the thermoelectric materials and important applications have been reviewed, and the progress of III-Nitride semiconductors for thermoelectric applications has been discussed.

In this chapter, the current status and future potential of III-Nitride semiconductors are reviewed for thermoelectric applications. Promising thermoelectric properties have been shown by the III-Nitride semiconductors both in theoretical and experimental aspects.

For the experimental measurement aspect, the thermoelectric properties of AlInN alloys, grown by metalorganic vapor phase epitaxy (MOVPE), with In-contents (x) from 11 % up to 21.34% were characterized and analyzed at room temperature. The thermal conductivities (K) of $Al_{1-x}In_xN$ alloys were measured by 3ω differential method. The electrical conductivities (σ) and Seebeck coefficients (S) of the materials were measured by Hall and thermal gradient methods, respectively.

The thermoelectric figure of merit ($Z*T$) values of the n-$Al_{1-x}In_xN$ alloys were measured as high as 0.391 up to 0.532 at T = 300 K. The use of high In-content (x = 21.34%) AlInN alloys leads to significant reduction in thermal conductivity [K = 1.62 W/(mK)] due to the increased alloy scattering, however, the optimized thermoelectric material was obtained for AlInN alloy with In-content of 17% attributed to its large power factor.

For the theoretical simulation aspect, the thermoelectric properties of n-type wurtzite III-nitride semiconductors were analyzed. The electron scatterings in the alloys were analyzed using Boltzmann transport equation. The total relaxation rate of the dominant electron scatterings includes contributions from the charged dislocation scattering, ionized impurity scattering, deformation potential acoustic phonon scattering, piezoelectric acoustic phonon scattering, polar optical phonon scattering, and non-polar optical phonon scattering. The thermoelectric properties of AlGaN and InGaN alloys requires accurate model for electronic and lattice thermal conductivity, electrical conductivity, and Seebeck coefficients computed for III-Nitride alloys.

Comprehensive model on lattice thermal conductivity is required for accurate simulation. Virtual crystal model is implemented here to simulate the lattice thermal conductivity. The figure of merits (*Z*T*) is obtained from these thermoelectric properties. The experimental and theoretical works are in collaboration with H. Tong [39].

4.1 Introduction to Nitride-Based Thermoelectricity

The high power density requirements in III-Nitride lasers and light-emitting diodes, power transistors, and solar cells lead to the demand for solid state cooling technology [1, 2], in particular for nitride-based alloy that can be integrated with GaN devices.

III-Nitride alloys have shown promising thermoelectric figure of merits (*Z*T*) [3-13], in particular for materials based on AlGaN [10, 11] and InGaN [12, 13] alloys. The thermoelectric properties for RF-sputtered AlInN had also been reported [3-6].

Our works [14, 36] have reported the epitaxy and thermoelectric characteristics of AlInN alloys with various In-contents at room temperature (T = 300 K). All the n-type AlInN films were grown by MOCVD on undoped-GaN (thickness = 2.8 μm; $n_{background}$ ~ 5 x 10^{16} cm^{-3}) template on c-plane sapphire substrates. The investigations of the thermoelectric characteristics for MOVPE-grown AlInN alloys with various In-contents are of great interest for improved understanding of the important parameters necessary to further optimize the *Z*T* value in this material system.

On the aspect of theoretical simulation, accurate numerical simulation will provide useful guideline in III-Nitride based material optimization for thermoelectric applications. Thus, the details of the theoretical modeling for the thermoelectric properties of III-Nitride semiconductors will be discussed in this chapter.

The efficiency of thermoelectric materials and devices are characterized by the thermoelectric figure of merit *Z*T*, which is defined as:

$$Z \cdot T = \frac{S^2 \sigma}{\kappa_e + \kappa_{ph}} T, \tag{4-1}$$

where *S* is the Seebeck coefficient, σ is the electrical conductivity, *T* is the absolute temperature (in Kelvin), K_e is the electronic thermal conductivity, and K_{ph} is the lattice thermal

conductivity. Thus, high-efficiency thermoelectric materials and devices should have large Seebeck coefficient and electrical conductivity, while low thermal conductivity, which have also discussed in chapter 2.

4.2 Thermoelectric Characterizations of AlInN Alloys

All the growths of AlInN films were performed on undoped-GaN (2.8 μm) / sapphire substrates. TMIn and TMAl were used as group III precursors, and NH_3 was used as group V precursor. The growths of GaN template on sapphire substrate were performed by using 30-nm low temperature (T_g=535 °C) GaN buffer, and then followed by high temperature (T_g = 1080 °C) GaN growth. The background n-type carrier concentrations of the GaN templates employed in the studies are 5 x 10^{16} cm^{-3}. The growth temperatures of the n-$Al_{1-x}In_xN$ alloys (~200 nm thick) ranged between 750-790 °C with growth pressure of 20 Torr.

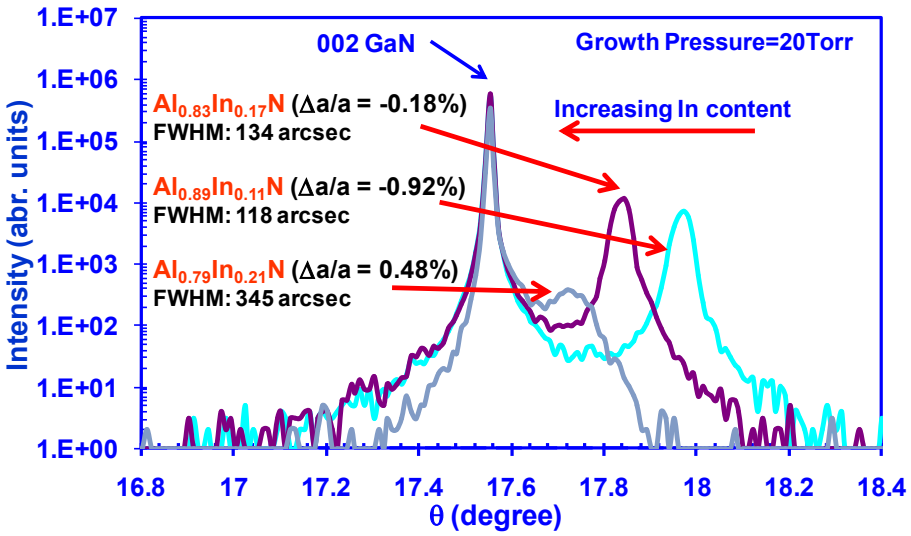

Figure 4-1: *The XRD rocking curves in c-axis for n-Al1-xInxN thin films grown on GaN / sapphire template.*

The In-contents (x) of $Al_{1-x}In_xN$ epilayers were measured by X-ray diffractometer (XRD) for c-axis orientation, resulting in x = 0.11, 0.17, and 0.2134 (figure 4-1). The lattice-mismatch strain in the a-axis (Δa/a) between $Al_{1-x}In_xN$ alloys and GaN as a function of In-content (x) are shown in figure 4-1. As the In-content in $Al_{1-x}In_xN$ alloys reached ~17% ($Al_{0.83}In_{0.17}N$), the Δa/a was measured as -0.18% which corresponded to nearly lattice-matched layer. For $Al_{0.83}In_{0.17}N$ alloys,

the growth temperature and V/III ratio were 780 ^{0}C and 9300, respectively. For $Al_{0.89}In_{0.11}N$ and $Al_{0.79}In_{0.21}N$ alloys, the growth temperatures were 790 ^{0}C and 750 ^{0}C, respectively.

Note that the increasing FWHM of the XRD rocking curves for AlInN with higher In-content can be attributed to the increasing phase separation in the film. Crack-free films were obtained for lattice-matched (*x*=17%) and compressively-strained (*x*=21.34%) samples, while cracks were observed tensile-strained samples (*x*=11%). The MOVPE growth details of the AlInN alloys can be found in reference 36.

4.2.1 The Van der Pauw Hall Method for Electrical Conductivity Measurement

The carrier mobilities of n-$Al_{1-x}In_xN$ alloys were measured by the Hall method, as shown in figure 4-2. The background n-type carrier concentrations for two $Al_{0.83}In_{0.17}N$ samples were measured as $5.1\times10^{18}cm^{-3}$ and $1.6\times10^{18}cm^{-3}$, respectively. For $Al_{0.89}In_{0.11}N$ and $Al_{0.79}In_{0.21}N$ alloys, the background n-type carrier concentrations were measured as $1.1x10^{18}cm^{-3}$ and $2.2\times10^{18}cm^{-3}$, respectively. Note that the two lattice-matched $Al_{0.83}In_{0.17}N$ samples were grown separately by MOVPE, and the difference in the background carrier concentration in the two samples can be attributed to the different impurity conditions from the epitaxy. Our finding is similar to the background carrier concentration range reported by others [41], which reported background doping in the range of $1\text{-}5\times10^{18}cm^{-3}$. The difference in the background doping range for MOVPE-grown AlInN material is attributed to the nitrogen vacancies or residual oxygen impurities [41].

The carrier mobilities were measured as 290 $cm^2/(Vs)$ and 462 $cm^2/(Vs)$ for $Al_{0.83}In_{0.17}N$ ($n=5.1\times10^{18}cm^{-3}$) and $Al_{0.83}In_{0.17}N$ ($n=1.6\times10^{18}cm^{-3}$), respectively. The results show that higher carrier density leads to higher electrical conductivity and lower electron mobility. Despite its relatively low carrier concentration, the $Al_{0.89}In_{0.11}N$ sample exhibits lower carrier mobility, which can be attributed to the cracks in the film. The cracks in the $Al_{0.89}In_{0.11}N$ thin film is related to the dislocation density from the growths of tensile film on GaN template. With higher cracking density, the dominant crystal dislocation scattering reduces the electron mobility in AlInN alloy, which is in agreement with the simulation based on relaxation time approximation.

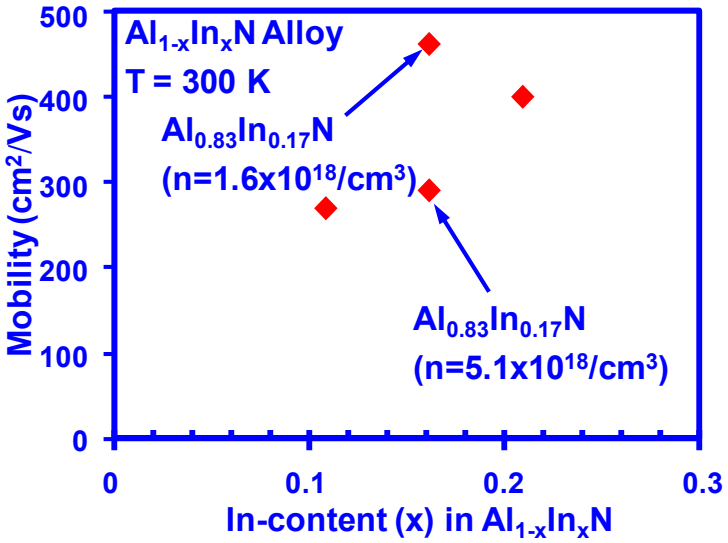

Figure 4-2: *The measured electron mobility for $Al_{1-x}In_xN$ alloys with various In-content (x) from x=0.11 up to x=0.2134 at T=300K.*

4.2.2 Thermal Gradient Method for Seebeck Coefficient Measurement

The Seebeck coefficients were determined by thermal gradient method, as illustrated in figure 4-3(a), which was similar to the method employed in references 36-38. When a temperature gradient was created in the sample [figure 4-3(a)], both the voltage difference and temperature difference were measured. A hotplate was used to create the high temperature. Two type K thermocouples were attached to the top surface of AlInN sample via indium (In) metal to measure temperature difference. The Seebeck voltage was collected from the positive chromel electrodes of the thermocouples at the same time.

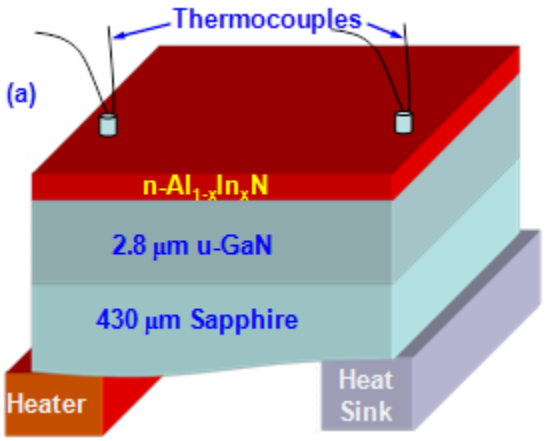

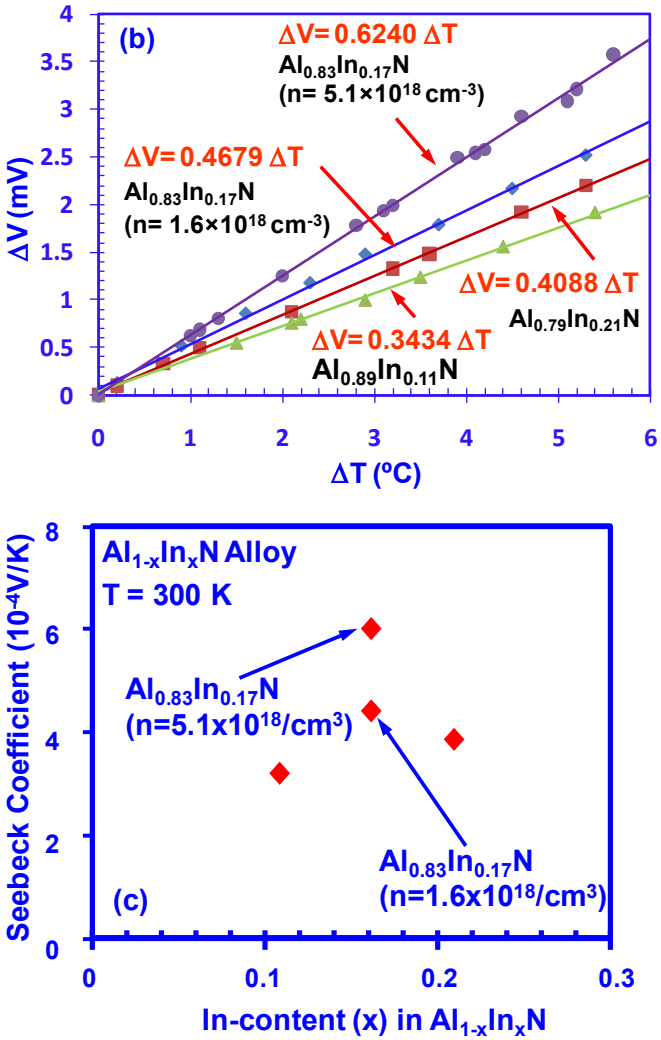

Figure 4-3: *(a) The set up for the thermal gradient method for Seebeck voltage measurements of AlInN samples, (b) Seebeck voltage as a function of the temperature difference, and (c) measured Seebeck coefficients for $Al_{1-x}In_xN$ alloys with various In-content (x) from x=0.11 up to x=0.2134 at T=300K.*

Figure 4-3(b) shows the measured Seebeck voltages as a function of the temperature difference for $Al_{1-x}In_xN$ alloys with various In-content (*x*) from x=0.11 up to x=0.2134 at *T*=300K. The Seebeck voltages for all the $Al_{1-x}In_xN$ samples show good linearity with the measured temperature difference. Note that the measured Seebeck voltages in figure 4-3(b) refer to the total Seebeck coefficients of AlInN and chromel electrodes combined. The corresponding Seebeck coefficients for AlInN films need to be compensated by the Seebeck coefficient of chromel at room temperature (21.5 μV/K) [18]. The Seebeck coefficients of $Al_{1-x}In_xN$ alloys are

shown in figure 4-3(c). The absolute Seebeck coefficients for the AlInN alloys are relatively large, which are in the range of -3.2×10^{-4} V/K up to -6.012×10^{-4} V/K, with the highest value measured for n-$Al_{0.83}In_{0.17}N$ alloy ($n=5.1\times10^{18}cm^{-3}$).

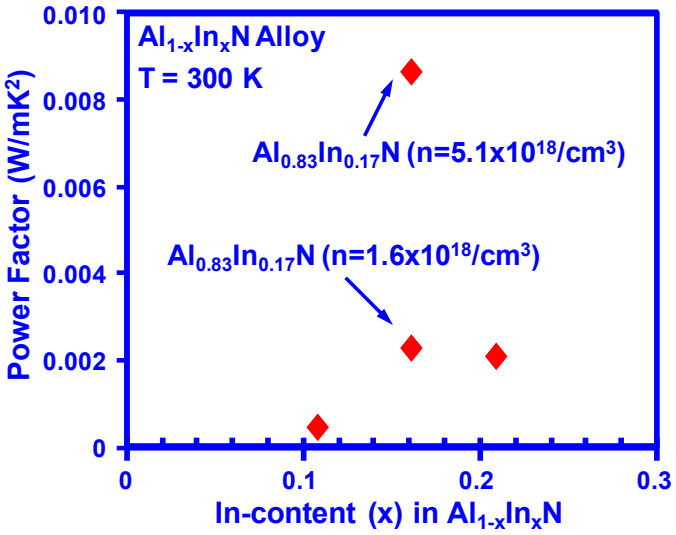

Figure 4-4: *The measured power factors for $Al_{1-x}In_xN$ alloys with various In-content (x) from x=0.11 up to x=0.2134 at T=300K.*

Figure 4-4 shows the measured power factors ($P=S^2\sigma$) for $Al_{1-x}In_xN$ alloys with x = 0.11-0.2134 at T=300 K. The power factors for $Al_{0.89}In_{0.11}N$ ($n=1.1\times10^{18}cm^{-3}$) and $Al_{0.79}In_{0.21}N$ ($n=2.2\times10^{18}cm^{-3}$) were measured as 4.77×10^{-4} W/(mK^2) and 2.11×10^{-3} W/(mK^2), respectively. The higher power factors were obtained for the n-$Al_{0.83}In_{0.17}N$ alloys, which were 8.64×10^{-3} W/(mK^2) and 2.30×10^{-3} W/(mK^2) for $n=5.1\times10^{18}cm^{-3}$ and $n = 1.6\times10^{18}\,cm^{-3}$, respectively. The large power factors for the $Al_{0.83}In_{0.17}N$ alloys are attributed to the large electrical conductivities and Seebeck coefficients. Note that both Seebeck coefficient and electrical conductivity have dependencies on carrier concentration, which in turn lead to the power factor variation with carrier concentration.

4.2.3 The Three Omega (3ω) Method for Thermal Conductivity Measurement

The thermal conductivities of AlInN films were measured by employing the 3ω differential method [12-16], and the details of this method used here were discussed in reference 38. Cross sectional schematic of four-probe 3ω measurement set up for n-$Al_{1-x}In_xN$ films grown on GaN/sapphire template prepared with SiO_2 insulation layer is shown in figure 5(a). The insulating

layers of 200nm SiO_2 were deposited by plasma-enhanced chemical vapor deposition on the AlInN / GaN / sapphire samples, and the metal heater contacts of 20 nm Ti / 130 nm Au were deposited by using electron beam evaporator. The top microscope image of the four-probe 3ω measurement set up for n-$Al_{1-x}In_xN$ films was shown in figure 5(b).

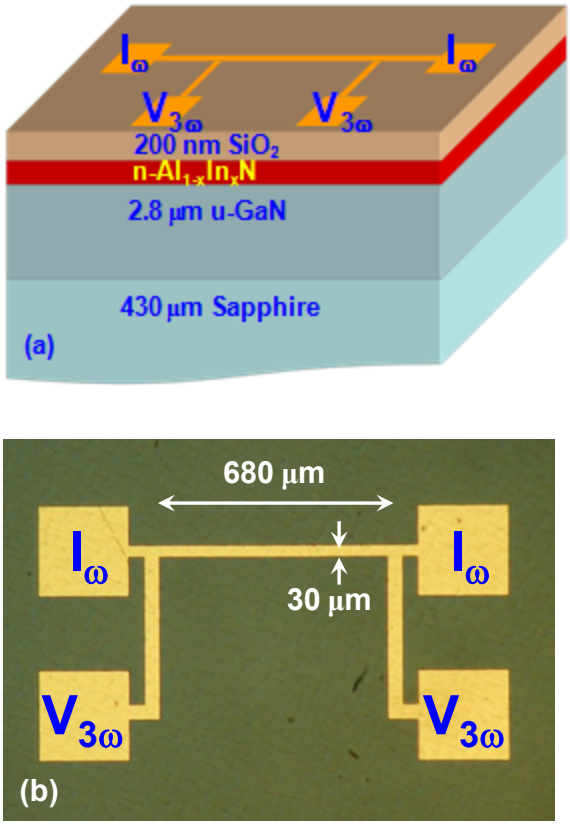

Figure 4-5: *(a) Cross sectional schematic of four-probe 3ω measurement set up for n-$Al_{1-x}In_xN$ films grown on GaN/sapphire template prepared with SiO_2 insulation layer, and (b) the top microscope image of the four-probe 3ω measurement set up for n-$Al_{1-x}In_xN$ films.*

In our 3ω measurement set up [14], a digital lock-in amplifier SR830 was employed to supply the driving AC current (I_ω) with sweeping frequency ω and collect the voltage (V_ω) as well as the third harmonic voltage ($V_{3\omega}$) of the metal stripe. A digital multimeter HP 34401A was used to measure the current in order to obtain the metal heater resistance. The set up of the thermal conductivity measurement for n-$Al_{1-x}In_xN$ thin films is shown in schematics in figure 4-6.

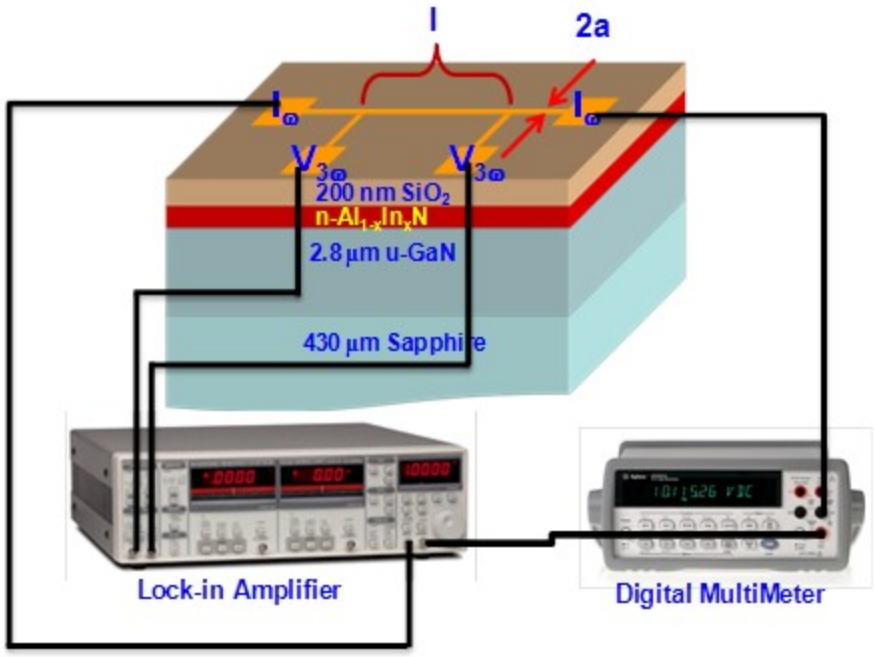

Figure 4-6: *The schematics of the four-probe 3ω thermal conductivity measurement set up for n-$Al_{1-x}In_xN$ films.*

Figure 4-7 shows the principle and measurement process of the 3ω method. When the driving AC current (I_ω) with sweeping frequency ω is supplied to the metal heater with resistance R, the AC Joule heating power would be generated with frequency of 2ω:

$$P_{2\omega} = I_\omega^2 \cdot R, \tag{4-2}$$

which would lead to the creation of temperature oscillation $\Delta T_{2\omega}$. Then the resistance variation would have the component with frequency 2ω:

$$R = R_0 \cdot (1 + \alpha \Delta T_{2\omega}), \tag{4-3}$$

where α is the temperature coefficient. Thus, the voltage across the metal heater would have a component with frequency 3ω. From the measurement set up in figure 4-6, both the voltage (V_ω) as well as the third harmonic voltage ($V_{3\omega}$) of the metal stripe will be collected by the lock-in amplifier. Therefore, the thermal conductivity for the sample under test can be retrieved from the temperature oscillation $\Delta T_{2\omega}$, which is proportional to the third harmonic voltage ($V_{3\omega}$).

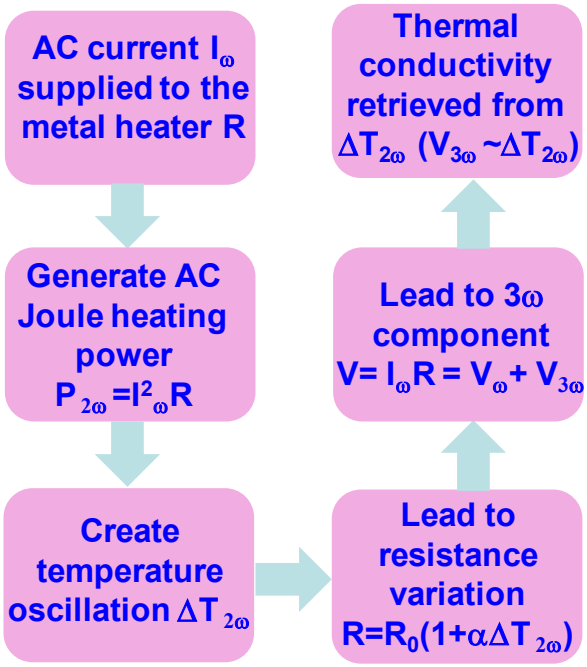

Figure 4-7: *The flowchart of the 3ω method for the thermal conductivity measurement.*

In our studies, all the 3ω measurements were performed at room temperature. The 3ω measurement set up was calibrated by measuring the thermal conductivities of sapphire and SiO_2 using differential [15, 16] and slope [19-22] methods. For calibration purpose, the thermal conductivities of sapphire and SiO_2 (T=300K) were obtained as 41 W/(mK) and 1.1 W/(mK), respectively, in good agreement with reported values [15, 23].

Both the measured voltage V_ω and in-phase $V_{3\omega}$ of the undoped GaN reference sample and the n-$Al_{1-x}In_xN$ samples at *T*=300K are shown in figure 4-8(a) (n-$Al_{0.83}In_{0.17}N$ sample with $n=5.1\times10^{18}cm^{-3}$), figure 4-9(a) (n-$Al_{0.83}In_{0.17}N$ sample with $n=1.6\times10^{18}cm^{-3}$), figure 4-10(a) (n-$Al_{0.79}In_{0.21}N$ sample with $n=2.2\times10^{18}cm^{-3}$), and figure 4-11(a) (n-$Al_{0.89}In_{0.11}N$ sample with $n=1.1\times10^{18}cm^{-3}$). The sweeping frequency of the driving current (ω/2π) ranged from 100Hz to 1000Hz, which insured the thermal penetration depth to be larger than the thickness of thin film while smaller than the thickness of the substrate.

Note that the V_ω and in-phase $V_{3\omega}$ of the undoped GaN template on sapphire were measured as reference samples. To ensure consistency in the measurements, all the GaN template reference samples correspond to identical templates used for the growths of n-$Al_{1-x}In_xN$ samples.

The temperature oscillation amplitude T_{AC} for the samples can be extracted from both the V_ω and $V_{3\omega}$ by using the following relation [14, 15, 19-22]:

$$T_{AC} = 2\frac{V_{3\omega}}{V_\omega}\frac{dT}{dR}R. \tag{4-4}$$

The temperature oscillation amplitudes T_{AC} as a function of frequency in logarithm scale from 100 Hz to 1000 Hz for both the undoped GaN reference sample and the n-$Al_{1-x}In_xN$ samples at T=300K are shown in figure 4-8(b) (n-$Al_{0.83}In_{0.17}N$ sample with n=5.1×$10^{18}$$cm^{-3}$), figure 4-9(b) (n-$Al_{0.83}In_{0.17}N$ sample with n=1.6×$10^{18}$$cm^{-3}$), figure 4-10(b) (n-$Al_{0.79}In_{0.21}N$ sample with n=2.2×$10^{18}$$cm^{-3}$), and figure 4-11(b) (n-$Al_{0.89}In_{0.11}N$ sample with n=1.1×$10^{18}$$cm^{-3}$). Therefore, the temperature raise ΔT_{AC} was obtained by subtracting the T_{AC} of the undoped GaN reference sample from the n-$Al_{1-x}In_xN$ samples. The average value of ΔT_{AC} for the entire frequency range (from 100Hz-1000Hz) was used to calculate the thermal conductivity (K) of the n-$Al_{1-x}In_xN$ samples.

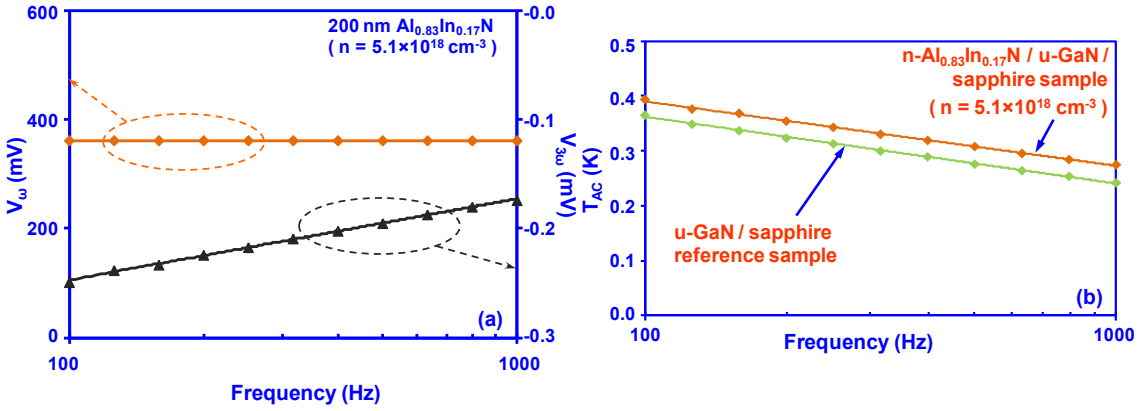

Figure 4-8: *Measured (a) voltage V_ω and in-phase $V_{3\omega}$, and (b) temperature oscillation amplitude (T_{ac}) as a function of frequency in logarithm scale for n-$Al_{0.83}In_{0.17}N$ sample with n=5.1×10^{18} cm^{-3} and undoped GaN/sapphire reference sample at 300 K.*

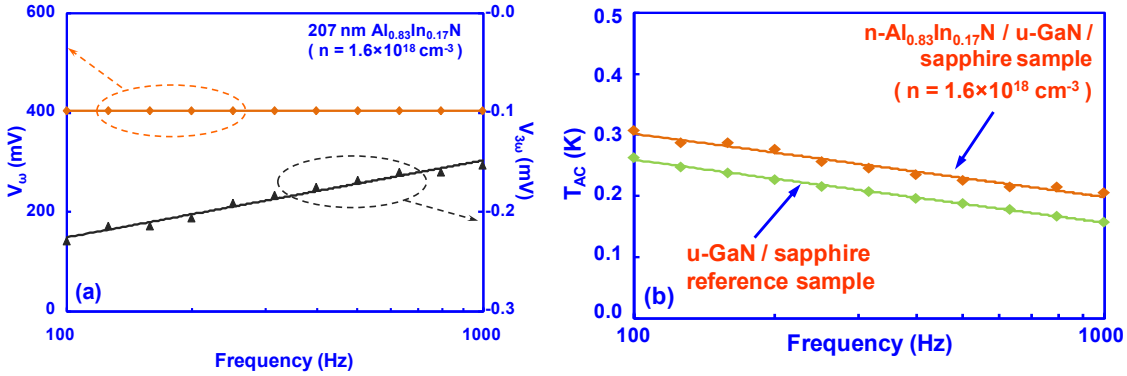

Figure 4-9: *Measured (a) voltage V_ω and in-phase $V_{3\omega}$, and (b) Temperature oscillation amplitude (T_{ac}) as a function of frequency in logarithm scale for n-$Al_{0.83}In_{0.17}N$ sample with $n=1.6\times10^{18}cm^{-3}$ and undoped GaN/sapphire reference sample at 300 K.*

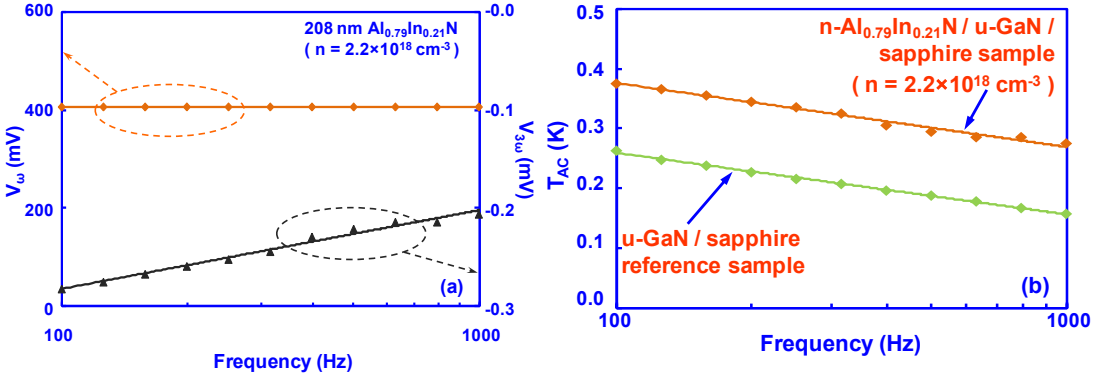

Figure 4-10: *Measured (a) voltage V_ω and in-phase $V_{3\omega}$, and (b) Temperature oscillation amplitude (T_{ac}) as a function of frequency in logarithm scale for n-$Al_{0.79}In_{0.21}N$ sample with $n=2.2\times10^{18}cm^{-3}$ and undoped GaN/sapphire reference sample at 300 K.*

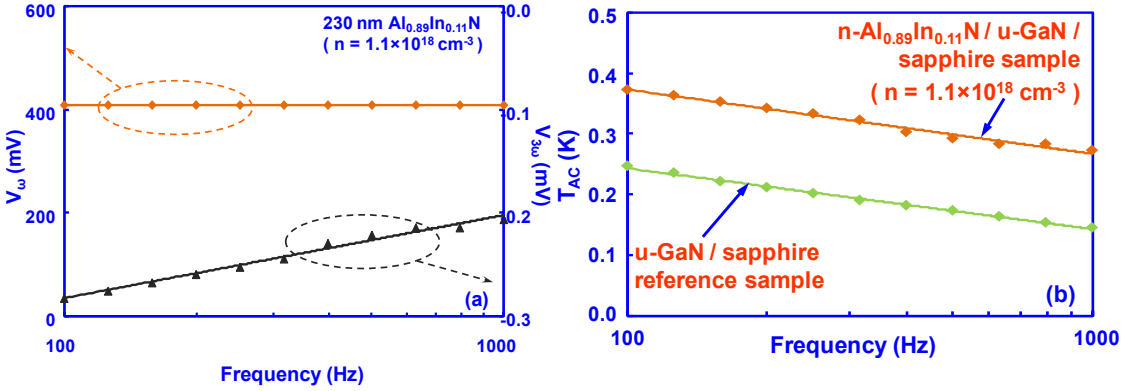

Figure 4-11: *Measured (a) voltage V_ω and in-phase $V_{3\omega}$, and (b) Temperature oscillation amplitude (T_{ac}) as a function of frequency in logarithm scale for n-$Al_{0.89}In_{0.11}N$ sample with $n=1.1\times10^{18}cm^{-3}$ and undoped GaN/sapphire reference sample at 300 K.*

The measured thermal conductivities of $Al_{1-x}In_xN$ alloys with x=0.11-0.2134 at T=300 K were shown in figure 4-12. The thermal conductivities of $Al_{1-x}In_xN$ alloys were measured as 1.62 W/(mK), 4.87 W/(mK), 4.31 W/(mK) and 1.62 W/(mK) for x=0.11, 0.17 ($n=5.1\times10^{18}cm^{-3}$), 0.17 ($n=1.6\times10^{18}cm^{-3}$) and 0.2134, respectively. The reduction in the thermal conductivity of $Al_{1-x}In_xN$ with x=0.2134 can be attributed to the increase in the alloy scattering. However, the low thermal conductivity for the $Al_{0.89}In_{0.11}N$ can be attributed to the cracking from the tensile strain in the alloy.

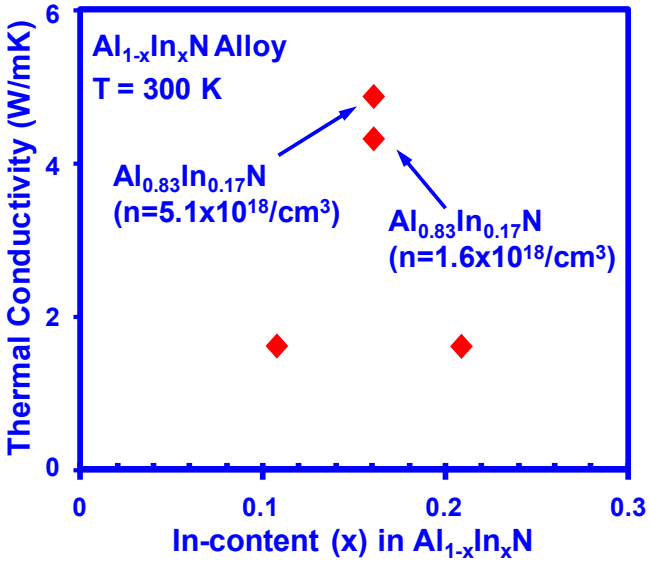

Figure 4-12: *The measured thermal conductivities for $Al_{1-x}In_xN$ alloys with various In-contents (x) from x=0.11 up to x=0.2134 at T=300K.*

4.3 Thermoelectric Figure of Merit of AlInN Alloys

The $Z^*T=P\times T/K$ values for n-$Al_{1-x}In_xN$ alloys at T=300 K are shown in figure 4-13. The Z^*T values (T=300K) for n-$Al_{1-x}In_xN$ alloys were measured as high as 0.391 up to 0.532. The highest Z^*T value (T=300K) was achieved as 0.532 for $Al_{0.83}In_{0.17}N$ ($n=5.1\times10^{18}$ cm^{-3}). The Z^*T values for $Al_{0.79}In_{0.21}N$ ($n = 2.2\times10^{18}cm^{-3}$), $Al_{0.83}In_{0.17}N$ ($n = 1.6\times10^{18}$ cm^{-3}) and $Al_{0.89}In_{0.11}N$ ($n=1.1\times10^{18}$ cm^{-3}) were 0.391, 0.160 and 0.089 respectively.

The thermal conductivities of $Al_{0.83}In_{0.17}N$ with different carrier concentrations are measured as relatively similar, thus the variation of the Z^*T values with carrier concentration is attributed to the carrier-concentration-dependent Seebeck and electrical conductivity parameters. The power factor P for $Al_{0.79}In_{0.21}N$ alloy was similar to that of $Al_{0.83}In_{0.17}N$ ($n=1.6\times10^{18}$ cm^{-3}), however its low

thermal conductivity from the increased alloy scattering led to higher *Z*T* value of 0.391. For $Al_{0.89}In_{0.11}N$ alloy, the high cracking density of the material led to a reduction of the power factor, which resulted in a lower *Z*T* value.

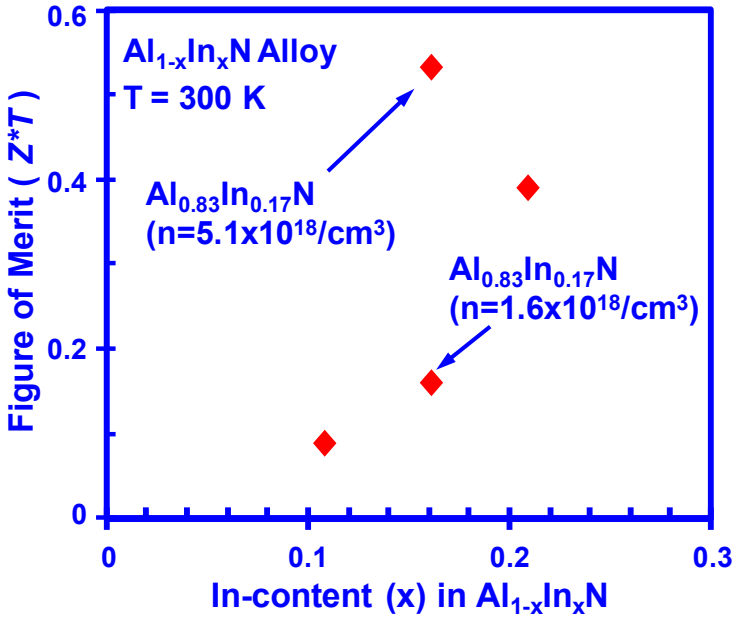

Figure 4-13: *The Z*T values for $Al_{1-x}In_xN$ alloys with various In-contents (x) from x=0.11 up to x=0.2134 at T=300K.*

4.4 Theoretical Characteristics of Thermoelectric Properties of III-Nitride Materials

4.4.1 Boltzmann Transport Equation and Relaxation Time Approximation

The Boltzmann transport equation, which describes the statistical distribution of one particle in a fluid, is used to describe the electron distribution function in the crystal [3], as follow:

$$\frac{\partial f}{\partial t}+\frac{\partial f}{\partial \vec{x}}\cdot\frac{\vec{p}}{m}+\frac{\partial f}{\partial \vec{p}}\cdot\vec{F}=\left.\frac{\partial f}{\partial t}\right|_{collision}, \tag{4-5}$$

where *x* and *p* are position and momentum, *m* is the mass of the particles, *F* is the external force field.

The relaxation time approximation is employed to solve the Boltzmann equation by introducing the total relaxation time τ_{total}. The τ_{total} is used to express the right side collision term in equation

(4-5) including all the electron scattering mechanisms in the semiconductor material, which can be expressed as follow:

$$\left.\frac{\partial f}{\partial t}\right|_{collision} = -\frac{f - f_0}{\tau_{total}}, \tag{4-6}$$

where f_0 represents the equilibrium Fermi distribution function. By employing the Matthiessen's rule, the total relaxation scattering rate can be written as:

$$\tau_{total}^{-1}(k) = \sum_i \tau_i^{-1}(k), \tag{4-7}$$

where τ_i represents the relaxation time of each scattering phenomena of electrons.

4.4.2 Electron Scattering Mechanism

Various electron scattering mechanisms in semiconductors are taken into consideration in the numerical calculation model, which are introduced in figure 4-14 [25]. In this numerical calculation model, six major electron scattering mechanisms are taken into account: 1) the charged dislocation scattering, 2) ionized impurity scattering, 3) deformation potential acoustic phonon scattering, 4) piezoelectric acoustic phonon scattering, 5) polar optical phonon scattering, and 6) non-polar optical phonon scattering. The neutral impurity scattering and alloy scattering are not taken into account. The carrier-carrier scattering rate is relatively negligible in the analysis for III-Nitride alloys, as this term will only be important at very high carrier density.

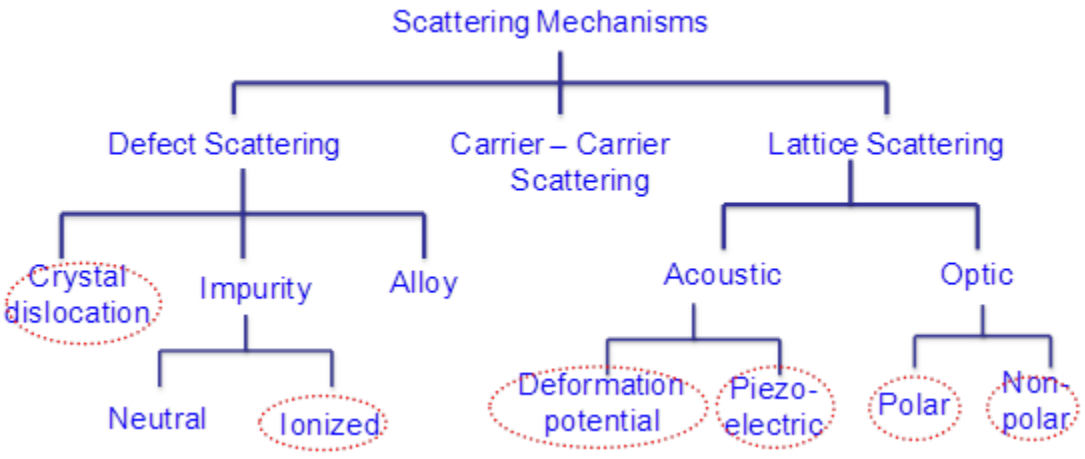

Figure 4-14: *The electron scattering mechanisms in semiconductors.*

The relaxation time for charged dislocation scattering can be expressed as [27]:

$$\tau_{dis}(k) = \frac{\hbar^3 \varepsilon_s^2 c_{lattice}^2}{N_{dis} m_{eff} e^4} \frac{\left(1 + 4\lambda_D^2 k_\perp^2\right)^{3/2}}{\lambda_D^4}, \tag{4-8}$$

where ε_s is the static dielectric constant, $c_{lattice}$ is the lattice constant along the (0001) direction, λ_D is Debye length, $k_\perp$ is the electron wave vector component perpendicular to the dislocation direction, N_{dis} is the dislocation density, m_{eff} is the effective mass.

The relaxation time for the ionized impurity scattering can be obtained as [28]:

$$\tau_{ii}(k) = \frac{2^{9/2} \pi \varepsilon_s^2 m_{eff}^{1/2} E^{3/2}}{Z^2 e^4 N_{ii} \left[\ln(1+b) - b/(1+b)\right]}, \tag{4-9}$$

where Z is the charge number of ionized atom, which equals to 1 for dopant in III-nitride semiconductors, N_{ii} is the ionized impurity density, b is the Brooks-Herring parameter, which is given by

$$b = \frac{8 m_{eff} \varepsilon_s k_B T}{n e^2 \hbar^2} E. \tag{4-10}$$

The relaxation time of the deformation-potential acoustic phonon scattering is expressed as [29]:

$$\tau_{dp}(k) = \frac{4\pi\hbar^4 c_{LA}}{\Xi_D^2 k_B T (2 m_{eff})^{3/2} E^{1/2}}, \tag{4-11}$$

where c_{LA} is the angular average of the elastic constant for longitudinal acoustic (LA) phonon, and Ξ_D is the deformation potential.

The relaxation time of the piezoelectric acoustic phonon scattering is obtained by [29]:

$$\tau_{pe}(k) = \frac{2\pi\varepsilon_s \hbar^2 v}{e^2 K_{av}^2 k_B T} \left[1 + \frac{1}{1 + 8 m_{eff} E / \hbar^2 q_s^2} - \frac{\hbar^2 q_s^2}{4 m_{eff} E} \cdot \ln\left(1 + \frac{8 m_{eff} E}{\hbar^2 q_s^2}\right)\right]^{-1}, \tag{4-12}$$

where v is the electron group velocity, K_{av} is the electromechanical coupling factor, q_s is the reciprocal of the screening length.

The polar optical phonon scattering is expressed as [30]:

$$\tau_{po}(k) = \frac{f_0(E)}{W_0 \left[n(\omega) + 1\right] f_0(E + \hbar\omega)} \cdot \left(\frac{E}{\hbar\omega}\right)^{1/2} \cdot \sinh\left(\frac{E}{\hbar\omega}\right)^{1/2}, \tag{4-13}$$

where ω is the optical phonon frequency, $n(\omega)$ is the Boson factor and

$$W_0 = \frac{e^2}{4\pi\hbar}\cdot\left(\frac{2m_{eff}\omega}{\hbar}\right)^{1/2}\cdot\left(\frac{1}{\varepsilon_\infty}-\frac{1}{\varepsilon_s}\right). \tag{4-14}$$

The non-polar optical phonon scattering is expressed as [25]:

$$\tau_{npo}(k) = \frac{\sqrt{2}\cdot\pi\cdot\rho\cdot\hbar^3\cdot\omega\cdot f_0(E)}{D_0 m^{*\frac{3}{2}} n_0}\cdot\left[(E+\hbar\omega)^{\frac{1}{2}} + H(E-\hbar\omega)\frac{n_0+1}{n_0}(E-\hbar\omega)^{\frac{1}{2}}\right]^{-1}. \tag{4-15}$$

The total relaxation time is then obtained as:

$$\tau_{total}^{-1}(k) = \tau_{dis}^{-1}(k) + \tau_{ii}^{-1}(k) + \tau_{dp}^{-1}(k) + \tau_{pe}^{-1}(k) + \tau_{po}^{-1}(k) + \tau_{npo}^{-1}(k). \tag{4-16}$$

Thus, based on the total relaxation time, the thermoelectric properties such as electrical conductivity σ, the Seebeck coefficient S, and the electronic thermal conductivity K_e can be obtained as:

$$\sigma = e^2\int\left(-\frac{\partial f_0}{\partial E}\right)\tau_{total}(k)v^2(k)\frac{dk^3}{4\pi^3}, \tag{4-17}$$

$$S = -\frac{e}{\sigma T}\int\left(-\frac{\partial f_0}{\partial E}\right)\tau_{total}(k)v^2(k)(E-E_f)\frac{dk^3}{4\pi^3}, \tag{4-18}$$

$$\kappa_e = \frac{e}{T^2}\int\left(-\frac{\partial f_0}{\partial E}\right)\tau_{total}(k)v^2(k)(E-E_f)^2\frac{dk^3}{4\pi^3} - \sigma S^2 T. \tag{4-19}$$

4.4.3 Virtual Crystal Model and Phonon Scatterings

The lattice thermal conductivity, which is the major contribution for the total thermal conductivity, is calculated by the use of virtual crystal model in order to account for the interfacial disorder [26]. In this model, the III-Nitride alloys are considered as virtual crystals which consist of homogenized crystal regions.

By Vegard's law, the virtual atomic weight M is obtained as

$$M = xM_{InN} + (1-x)M_{GaN}. \tag{4-20}$$

The virtual atomic volume can be expressed as

$$V^{1/3} = xV_{InN}^{1/3} + (1-x)V_{GaN}^{1/3}. \tag{4-21}$$

In III-Nitride bulk alloys and thin films, the resistive phonon scatterings are dominant and the lattice thermal conductivity can be obtained by Callaway's approximation [31],

$$\kappa_{ph} = \frac{k_B}{2\pi^2 v}\left(\frac{k_B T}{\hbar}\right)^3 \int_0^{\Theta/T} \frac{x^4 e^x}{\left(e^x - 1\right)^2} \tau_R dx \,, \tag{4-22}$$

where v is the average phonon group velocity, Θ is the Debye temperature, and the term x is defined as:

$$x = \frac{\hbar\omega}{k_B T} \,, \tag{4-23}$$

where ω is the phonon frequency.

The three major resistive scatterings of phonons are taken into account: 1) the scattering on point defects, 2) the Umklapp scattering, and 3) the scattering on rough boundary. Both the impurities and alloy components are considered as point defects in this model. The scattering rate can be calculated as:

$$\tau_{PD}^{-1} = \frac{V\Gamma\omega^4}{4\pi v^3} \,, \tag{4-24}$$

where V is the virtual atomic volume, v is the average phonon group velocity.

The scattering factor can be expressed as:

$$\Gamma = \Gamma_{imp} + \Gamma_{alloy} \,, \tag{4-25}$$

where

$$\Gamma_{imp} = \sum_i x_i \Gamma_i \,, \tag{4-26}$$

with x_i as the mass fraction of each component crystal, and

$$\Gamma_{alloy} = \sum_i x_i \left[\left(M_i - M\right)/M\right]^2 \cdot \tag{4-27}$$

Secondly, the Umklapp scattering rate can be expressed as:

$$\tau_{UK}^{-1} = \frac{\hbar\gamma^2 T\omega^2}{M v^2 \Theta} \exp\left(-\frac{\Theta}{3T}\right), \tag{4-28}$$

where γ is the Gruneisen anharmonicity constant.

Then, the third scattering (rough boundary scattering) relaxation time is obtained as:

$$\tau_{RB}^{-1} = \frac{v}{L}, \tag{4-29}$$

where L is the dimension of the sample.

Thus, the total resistive scattering rate of phonon can be obtained by summation of the individual scattering rate, as follow:

$$\tau_R^{-1} = \tau_{PD}^{-1} + \tau_{UK}^{-1} + \tau_{RB}^{-1}. \tag{4-30}$$

Therefore, the lattice thermal conductivity K_{ph} can be obtained by substituting the equation (4-30) back into equation (4-22).

4.4.4 Theoretical Results of Thermoelectric Properties of III-Nitride Materials

In order to verify the accuracy of the simulation model based on the Boltzmann transport equation and the virtual crystal model, the simulated electrical and thermoelectric properties of Nitride materials are compared with the experimental measurements.

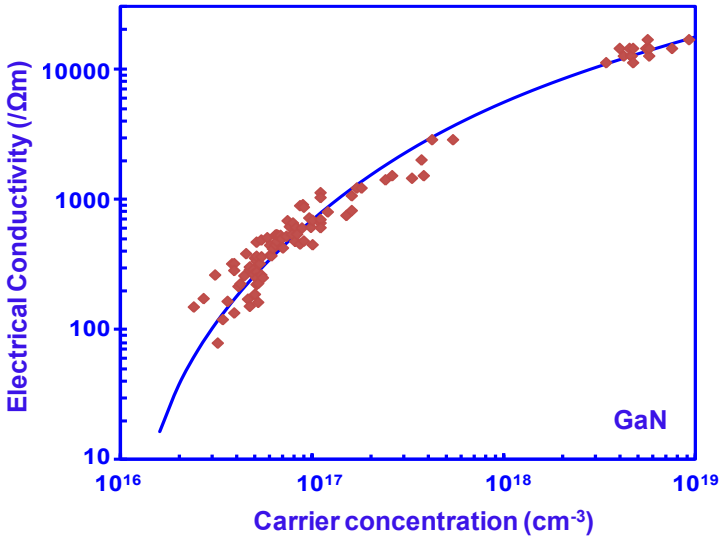

Figure 4-15: *The simulated electrical conductivities as a function of carrier concentration in comparison with experimental measurement data for GaN.*

Figure 4-15 shows the simulated electrical conductivity (σ) as a function of carrier concentration (n) (solid curve) for GaN, in comparison with the experimental measurement data (red dots) obtained from the MOCVD-grown GaN alloys grown in house. From the curve, it shows that the simulated curve matches well with the experimental measurements.

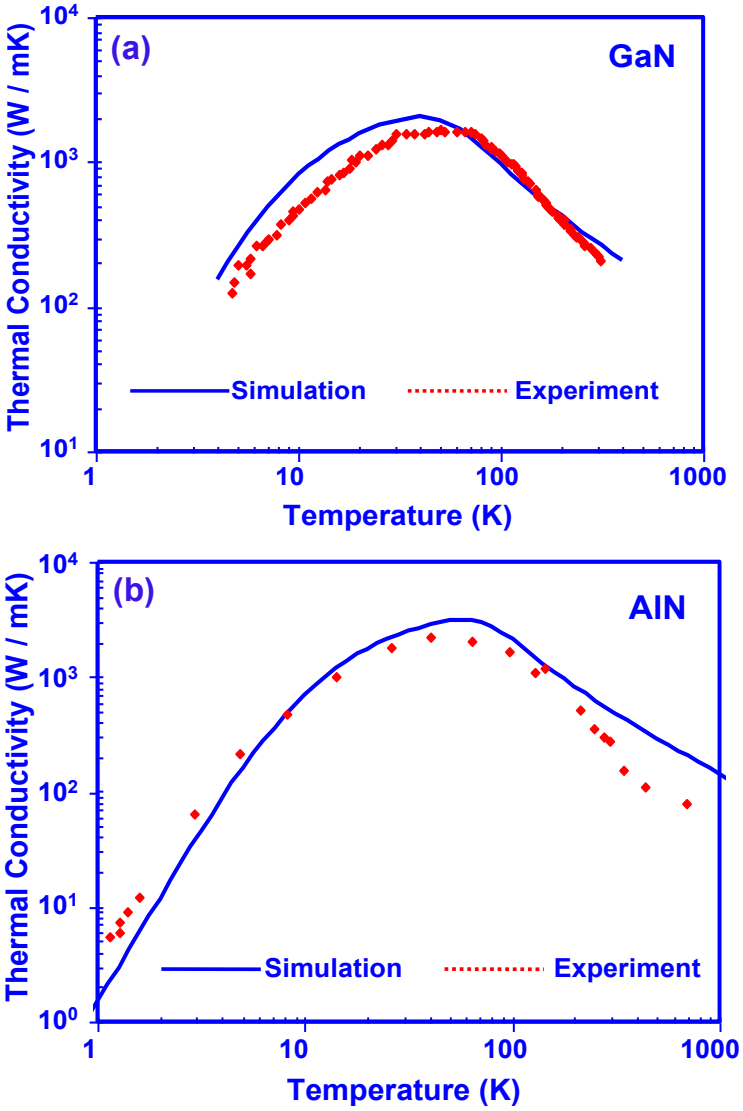

Figure 4-16: *The simulated thermal conductivities as a function of temperature in comparison with experimental measurement data [32, 33] for (a) GaN and (b) AlN.*

Figure 4-16 shows the comparison of the simulated thermal conductivity (solid cuve) and experimental measurement data (red dots) as a function of temperature for (a) GaN and (b) AlN. Good agreement is obtained between simulated thermal conductivity and measured thermal conductivity for both GaN and AlN materials for the temperature range from 10 K up to 1000 K.

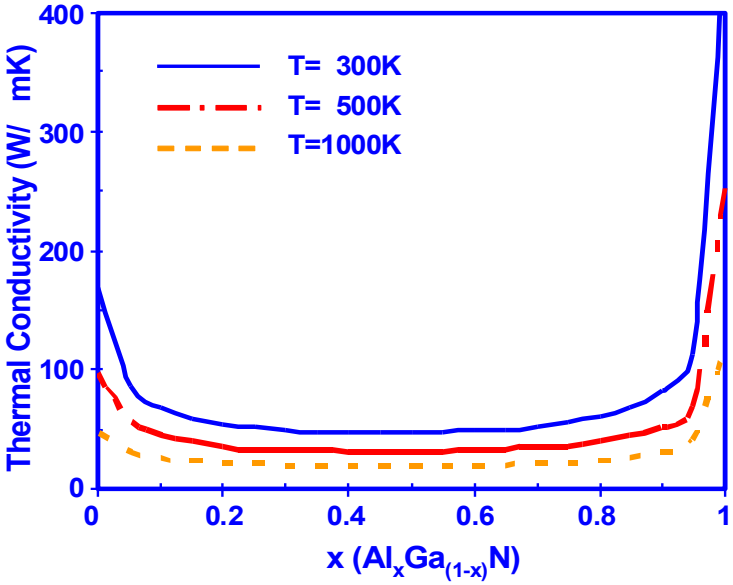

Figure 4-17: *The simulated thermal conductivities as a function of Al-content for ternary $Al_xGa_{1-x}N$ alloy with temperature range of 300-1000 K.*

Therefore, based on the verified simulation model, figure 4-17 shows the calculated thermal conductivity as a function of Al-content (*x*) at different temperatures for $Al_xGa_{1-x}N$ alloys. The thermal conductivity for ternary AlGaN alloys are much lower in comparison to those of binary GaN (170 W/mK) and binary AlN (400 W/mK). The lowest thermal conductivity is achieved by the use of $Al_{0.4}Ga_{0.6}N$ alloy, which is with the value of ~60 W/mK at room temperature. In addition, the thermal conductivity of $Al_xGa_{1-x}N$ alloys decrease with increasing temperature.

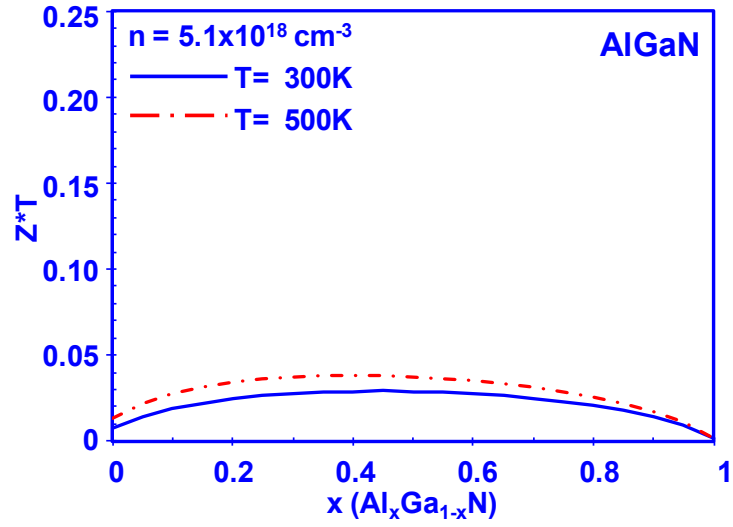

Figure 4-18: *The simulated Z*T values as a function of Al-content for ternary $Al_xGa_{1-x}N$ alloy with temperature range of 300-500 K.*

The simulation of the electrical conductivity and the Seebeck coefficient can be obtained by the Boltzmann transport equation and relaxation time approximation approach [37, 38]. Thus, after obtaining the thermal conductivity, as well as the electrical conductivity and the Seebeck coefficient, the thermoelectric figure of merit Z^*T values can be simulated, which are shown in figure 6 for $Al_xGa_{1-x}N$ alloys for temperature range from 300 K up to 500 K, with carrier density n = $5.1x10^{18}$ cm^{-3}.

From figure 4-18, the figure of merits Z^*T values of $Al_xGa_{1-x}N$ ternary alloys are higher than that of the binary GaN alloy (x = 0) or binary AlN alloy (x = 1). The optimum simulated Z^*T for $Al_xGa_{1-x}N$ alloy is achieved at Al-content of approximately 40%. The improved figure of merit from ternary $Al_xGa_{1-x}N$ alloys can be attributed to the reduced thermal conductivity from alloying effect.

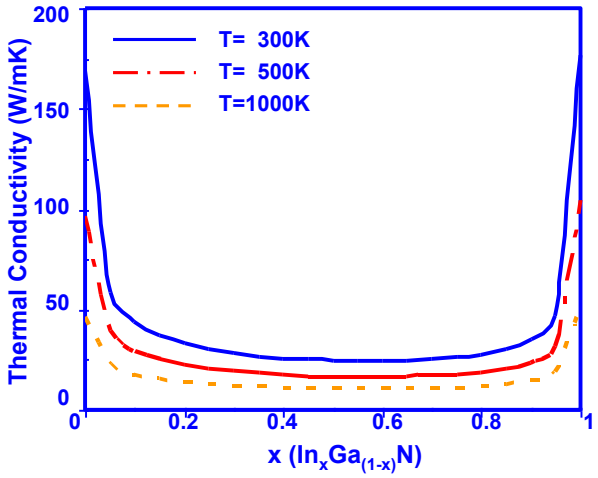

Figure 4-19: *The simulated thermal conductivities as a function of In-content for ternary $In_xGa_{1-x}N$ alloy with temperature range of 300-1000 K.*

Similarly, figure 4-19 shows the simulated thermal conductivities of the ternary $In_xGa_{1-x}N$ alloys as a function of In-content (x) for different temperatures, which are lower than those of GaN (x = 0) and InN (x = 1) alloys. The lowest thermal conductivity can be obtained by the use of $In_xGa_{1-x}N$ with In-contents in the range of 55% up to 65%, resulting in thermal conductivity of approximately 30 W/mK at room temperature.

Figure 4-20 shows the Z^*T values of as a function of In-contents for $In_xGa_{1-x}N$ alloys at temperatures of 300K- 500K, with the carrier density n = $5.1x10^{18}$ cm^{-3}. From the simulation

results, the optimized Z^*T for $In_xGa_{1-x}N$ alloy is obtained for the In-content of 65%, which leads to the figure of merit Z^*T ~ 0.15, which are higher than those of AlGaN alloys.

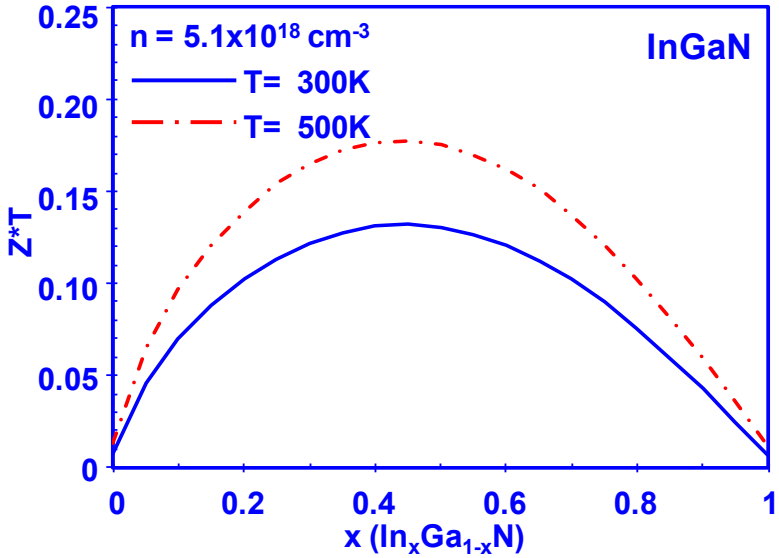

Figure 4-20: *The simulated Z*T values as a function of In-content for ternary $In_xGa_{1-x}N$ alloy with temperature range of 300-500 K.*

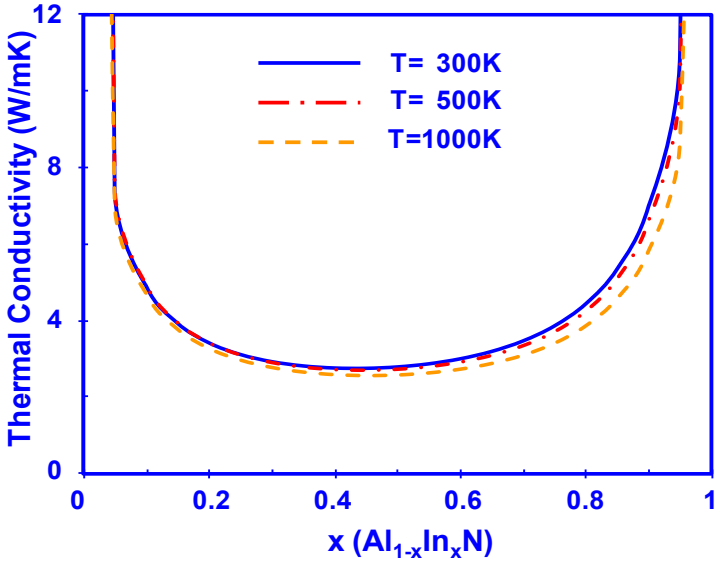

Figure 4-21: *The simulated thermal conductivities as a function of In-content for ternary $Al_{1-x}In_xN$ alloy with temperature range of 300-1000 K.*

Figure 4-21 shows the simulated thermal conductivities of the ternary $Al_{1-x}In_xN$ alloys as a function of In-content (x) for different temperatures, which are lower than those of AlN (x = 0) and InN (x = 1) alloys. The lowest thermal conductivity can be obtained by the use of $Al_{1-x}In_xN$ with In-

contents in the range of 55% up to 70%, resulting in thermal conductivity of approximately 4 W/mK at room temperature, which are lower than that of the AlGaN and InGaN alloys.

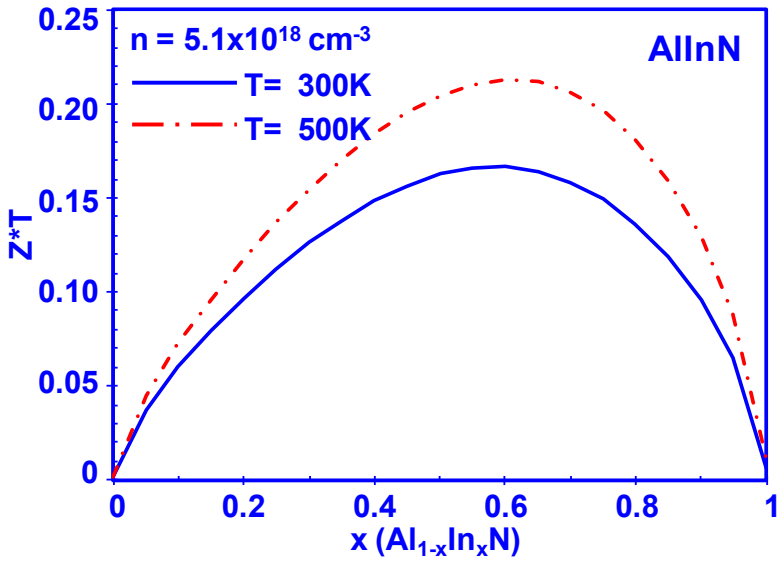

Figure 4-22: *The simulated Z*T values as a function of In-content for ternary $Al_{1-x}In_xN$ alloy with temperature range of 300-500 K.*

Figure 4-22 shows the *Z*T* values of as a function of In-contents for $Al_{1-x}In_xN$ alloys at temperatures of 300K- 500K, with the carrier density n = $5.1x10^{18}$ cm^{-3}. From the simulation results, the optimized *Z*T* for the $Al_{1-x}In_xN$ alloy is obtained for the In-content of ~55% - 70%, which leads to higher figure of merit *Z*T* than those of AlGaN alloys and InGaN alloys, attributed from the further reduced thermal conductivity, as well as the enhanced electrical conductivity and Seebeck coefficients.

4.5 Summary

In summary, the thermoelectric properties of MOVPE-grown n-$Al_{1-x}In_xN$ (*x*=0.11-0.2134) alloys are presented. The record *Z*T* values of the $Al_{1-x}In_xN$ alloys were measured as high as 0.391 up to 0.532 at *T*=300 K, which show significant improvement from the RF-sputtered AlInN (*Z*T*=0.005, *T*=300 K) [4] and MOVPE-grown InGaN (*Z*T*=0.08, T=300 K) [12, 13]. The improvement observed from the MOVPE-grown AlInN alloys can be attributed to the increase in the Seebeck coefficient and electrical conductivity resulting in higher power factor, in comparison

to those measured from MOVPE-grown InGaN and RF-sputtered AlInN. The use of high In-content (x = 21.34%) AlInN alloys leads to significant reduction in thermal conductivity [K = 1.62 W/(mK)] due to the increased alloy scattering, however, the use of high In-content AlInN alloys leads to slight reduction in power factor. To optimize the high Z*T value in AlInN material system, it is important to employ crack-free AlInN thin film with large carrier concentration in order to obtain high power factor, while minimizing the thermal conductivity by employing AlInN alloy with In-content in the range of x = 17% - 22%. The finding indicates that MOVPE-grown AlInN alloy as excellent thermoelectric material for III-Nitride device integration.

The numerical simulations of thermoelectric properties of n-type $Al_xGa_{1-x}N$ and $In_xGa_{1-x}N$ alloys are presented. The electronic properties such as electrical conductivities, electronic thermal conductivities, Seebeck coefficients in semiconductor were solved by using Boltzmann transport equation under relaxation time approximation, and each individual relaxation times due to five dominant electron scatterings were computed. Phonon scattering mechanisms are considered in the virtual crystal model. The figure of merits (Z*T) are computed for both AlGaN and InGaN alloys, by using the computed electron transport and phonon scattering properties. The simulation model presented in this work show very good agreement with the experimental data obtained for GaN and AlN binary alloys. The optimum Z*T values for AlGaN alloy is obtained for Al-content of 40%, resulting in Z*T value of 0.06 at 1000K. For the case of InGaN alloy, the optimum Z*T value of 0.15 at 1000 K is obtained for In-content of 65%. The findings presented here indicate that ternary AlGaN or InGaN alloys as promising candidates for thermoelectric cooling application in nitride-based high power LEDs, lasers, and electronics.

References for Chapter 4

[1] G. Chen and A. Shakouri, J. Heat Transfer, **124**, 242 (2002).

[2] G. Chen, M.S. Dresselhaus, G. Dresselhaus, J.-P. Fleurial, and T. Caillat, Int. Mater. Rev., **48**, 45 (2003).

[3] S. Yamaguchi, Y. Iwamura, and A. Yamamoto, Appl. Phys. Lett., **82**, 2065 (2003).

[4] S. Yamaguchi, R. Izaki, K. Yamagiwa, K. Taki, Y. Iwamura, and A. Yamamoto, Appl. Phys. Lett., **83**, 5398 (2003).

[5] S. Yamaguchi, R. Izaki, N. Kaiwa, S. Sugimura and A. Yamamoto, Appl. Phys. Lett., **84**, 5344 (2004).

[6] S. Yamaguchi, R. Izaki, Y. Iwamura, and A. Yamamoto, Physica Stat. Solidi (a), **201**, 225 (2004).

[7] R. Izaki, N. Kaiwa, M. Hoshino, T. Yaginuma, S. Yamaguchi, and A. Yamamoto, Appl. Phys. Lett., **87**, 243508 (2005).

[8] S. Yamaguchi, R. Izaki, N. Kaiwa, and A. Yamamoto, Appl. Phys. Lett., **86**, 252102 (2005).

[9] A. Sztein, H. Ohta, J. Sonoda, A. Ramu, J. E. Bowers, S. P. DenBaars, and S. Nakamura, Appl. Phys. Exp., **2**, 111003 (2009).

[10] W. Liu, and A. A. Balandin, J. Appl. Phys., **97**, 073710 (2005).

[11] W. Liu, and A. A. Balandin, J. Appl. Phys., **97**, 123705 (2005).

[12] B. N. Pantha, R. Dahal, J. Li, J. Y. Lin, H. X. Jiang, and G. Pomrenke, Appl. Phys. Lett., **92**, 042112 (2008).

[13] B. N. Pantha, R. Dahal, J. Li, J. Y. Lin, H. X. Jiang, and G. Pomrenke, J. Electro. Mater., **38**, 1132 (2009).

[14] H. Tong, J. Zhang, G. Liu, J. A. Herbsommer, G. S. Huang, and N. Tansu, Appl. Phys. Lett., **97**, 112105 (2010).

[15] S.-M. Lee, and D. G. Cahill, J. App. Phys., **81**, 2590 (1997).

[16] Z. Bian, M. Zebarjadi, R. Singh, Y. Ezzahri, A. Shakouri, G. Zeng, J.-H. Bahk, J. E. Bowers, J. M. O. Zide, and A. C. Gossard, Physical Review B, **76**, 205311 (2007).

[17] R. Butte, J. F. Carlin, E. Feltin, M. Gonschorek, S. Nicolay, G. Christmann, D. Simeonov, A. Castiglia, J. Dorsaz, H. J. Buehlmann, S. Christopoulos, G. Baldassarri Hoger von Hogersthal, A. J. D. Grundy, M. Mosca, C. Pinquier, M. A. Py, F. Demangeot, J. Frandon, P. G. Lagoudakis, J. J. Baumberg, and N. Grandjean, J. Phys. D: Appl. Phys., **40**, 6328 (2007).

[18] W. Gee, and M. Green, J. Phys. E: Sci. Instrum., **3**, 135 (1970).

[19] D. G. Cahill, and R. O. Pohl, Phys. Rev. B, **35**, 4067 (1987).

[20] D. G. Cahill, Rev. Sci. Instrum. **61**, 802 (1990).

[21] D. G. Cahill, Rev. Sci. Instrum. **73**, 3701 (2002).

[22] D. G. Cahill, M. Katiyar, and J. R. Abelson, Phys. Rev. B **50**, 6077 (1994).

[23] F. P. Incropera and D. P. De Witt, *Fundamentals of Heat and Mass Transfer (5th ed.)*, New York, (Wiley, 2001).

[24] Snyder, G. J., and Toberer, E. S., "Complex thermoelectric materials", Nature Materials, 7, 105 (2008).

[25] Pantha, B. N., Dahal, R., Li, J., Lin, J. Y., Jiang, H. X. and Pomrenke, G., "Thermoelectric properties of InxGa1-xN alloys", App. Phys. Lett., 92, 042112 (2008).

[26] Nag, B. R., "Electron Transport in Compound Semiconductors", Springer-Verlag Berlin Heidelberg New York, 99 (1980).

[27] Liu, W., and Balandin, A. A., "Thermal conduction in AlxGa1-xN alloys and thin films", J. Appl. Phys., 97, 073710 (2005).

[28] Look, D. C., and Sizelove, J. R., "Dislocation Scattering in GaN", Phys. Rev. Lett., 82, 1237 (1999).

[29] Look, D. C., "Electrical Characterization of GaAs Materials and Devices", John Wiley & Sons, 77, (1989).

[30] Ridley, B. K., "Quantum processes in semiconductors", Oxford University Press, 98, (1982).

[31] Ridley, B. K., Foutz, B. E., and Eastman, L. F., "Mobility of electrons in bulk GaN and AlxGa1-xN/GaN heterostructures", Phys. Rev. B, 61, 16862, (2000).

[32] Callaway, J., "Model for Lattice Thermal Conductivity at Low Temperatures", Phys. Rev., 113, 1046 (1959).

[33] Jezowski, A., Danilchenko, B. A., Bockowski, M., Grzegory, I., Krukowski, S., Suski, T., and Paszkiewicz, T., "Thermal conductivity of GaN crystals in 4.2 – 300 K range", Solid State Commun., 128, 69 (2003).

[34] Slack, G. A., Tanzilli, R. A., Pohl, R. O., and Vandersande, J. W., "The intrinsic thermal conductivity of AlN", J. Phys. Chem. Solids, 48, 641 (1987).

[35] J. Zhang, H. Tong, G. Y. Liu, J. A. Herbsommer, G. S. Huang, and N. Tansu, "Characterizations of Seebeck Coefficients and Thermoelectric Figures of Merit for AlInN Alloys with Various In-Contents," J. Appl. Phys., 109(5), 053706, (2011).

[36] G. Y. Liu, J. Zhang, X. H. Li, G. S. Huang, T. Paskova, K. R. Evans, H. P. Zhao, and N. Tansu, "Metalorganic Vapor Phase Epitaxy and Characterizations of Nearly-Lattice-Matched AlInN Alloys on GaN / Sapphire Templates and Free-Standing GaN Substrates," J. Crys. Growth, 340 (1), 66-73, (2012).

[37] H. Tong, H. P. Zhao, Y. K. Ee, V. A. Handara, J. A. Herbsommer, and N. Tansu, "Analysis of Thermoelectric Characteristics of InGaN Semiconductors," in Proc. of the SPIE Photonics West 2009, Physics and Simulation of Optoelectronics Devices XVII, San Jose, CA, Jan 2009.

[38] H. Tong, J. Zhang, J. A. Herbsommer, and N. Tansu, "Analysis of Thermoelectric Properties of AlInN Semiconductor Alloys," in Proc. of the SPIE Photonics West 2011, Physics and Simulation of Optoelectronics Devices XIX, San Francisco, CA, Jan 2011.

[39] H. Tong, Thermoelectric Characteristics and Measurements of Ternary III-Nitride Semiconductors, Ph.D. Dissertation, Lehigh University, Sep. 2010.

Chapter 5: Thermal Conductivity Measurement Methods for III-Nitride Semiconductors

In chapter 4, the thermal conductivity of AlInN alloys grown by metalorganic chemical vapor deposition (MOCVD) with various In-contents were characterized by the differential technique of the 3 omega (3ω) measurement method.

In this chapter, we present a brief summary on the thermal conductivity measurement methods for both bulk materials and thin film materials. Specifically, the 2D multilayer thermal diffusion model was developed and the extended slope technique based on this model was proposed to accurately extract the thin film thermal conductivity which is higher than that of the substrate. The thermal conductivities are measured for MOCVD-grown GaN thin film on sapphire substrate and InN thin film on GaN/ sapphire substrate in order to verify the validity and accuracy of the proposed 2D multilayer thermal diffusion model and the extended slope technique [1, 2]. Those works regarding the thermal conductivity measurement methods are in collaboration with H. Tong [1].

5.1 The Conventional Three Omega (3ω) Method

Conventionally, several measurement methods [21] have been employed to characterize the thermal conductivity of materials, such as steady-state method (absolute or comparative), radial heat flow method, and laser flash method. Note that all these methods require either direct or indirect determination of the heat flux and temperature differences between two points of the material under characterization. Other than using optical heating and sensing, electrical heating and sensing based on micro-heaters and sensors have the advantage of precisely controlled heat transfer and accurately determined temperature rise. The 3ω method is a well-established technique for measuring the thermal conductivity of both bulk materials [22-24] and thin films [15, 25-26].

Figure 5-1 shows the schematic of four point configuration of the metal heater and experiment setup for the 3ω measurement [5-6]. The sample under test was prepared with 200 nm SiO_2

insulation layer, which was deposited by plasma-enhanced chemical vapor deposition. The metal heater contacts of 20 nm Ti / 130 nm Au were deposited by using electron beam evaporator. In the 3ω measurement set up, a digital lock-in amplifier SR830 was employed to supply the driving AC current (Iω) with sweeping frequency ω and collect the voltage (Vω) as well as the third harmonic voltage ($V_{3\omega}$) of the metal stripe. A digital multimeter HP 34401A was used to measure the current in order to obtain the metal heater resistance. The measured frequency of the driving current ($\omega/2\pi$) ranged from 100 Hz to 1000 Hz. The selection of the frequency range is to ensure the thermal penetration depth smaller than the thickness of the substrate while larger than the thickness of thin films. All the 3ω measurements were performed at room temperature. The 3ω measurement set up was calibrated by measuring the thermal conductivities of sapphire and SiO_2 using differential [15, 16] and slope [22-25] methods. For calibration purpose, the thermal conductivities of sapphire and SiO_2 (T = 300K) were obtained as 41 W/(mK) and 1.1 W/(mK), respectively, in good agreement with reported values [15, 21].

The flowchart of the 3ω measurement process has been shown in figure 4-7. The strip metal (with length of 680 μm, and width of 30 μm) is used as heater and temperature sensor at the same time to obtain the thermal conductivity information of the sample under test. By depositing the metal strip heater on the top surface of the sample, an AC current oscillating at frequency ω (I_{AC}) is applied to the ends of the metal heater. An AC heat flow at frequency 2ω is generated from Joule heating and diffusing into the underneath sample. The parameter T_{AC} refers to the temperature variation at frequency 2ω caused by the AC heat flow, which results in a resistance variation (R_{AC}) of the metal heater at frequency 2ω. Consequently, the R_{AC} combined with I_{AC} creates a voltage variation ($V_{3\omega}$) at frequency 3ω. Thus, the $V_{3\omega}$ is a function of the thermal conductivity of the sample under test from the heat diffusion theory, and the in-phase component of $V_{3\omega}$ has a linear relationship with the logarithm of the driving current frequency ω. By measuring the $V_{3\omega}$ as a function of frequency ω in logarithm scale, the thermal conductivity of the material under test can be determined.

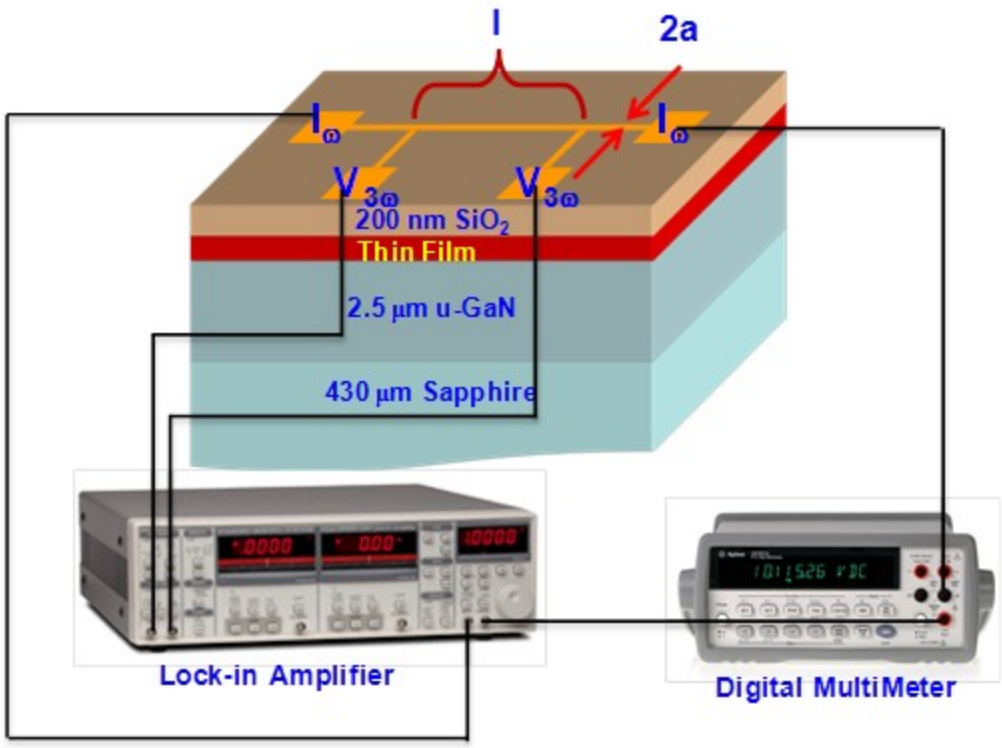

Figure 5-1: *The cross sectional schematic of four-probe 3ω measurement setup for thin films grown on GaN/sapphire template prepared with SiO_2 insulation layer.*

5.1.1 The Slope Technique for Bulk Thermal Conductivity Measurement and Differential Technique for Thin Film Thermal Conductivity Measurement [1-2, 15-16, 22-25]

For the analysis of bulk material, the thermal conductivity is determined by using the slope $dV_{3\omega}/d\ln\omega$ from the 3ω method [22-25]. The thermal conductivity of bulk can be extracted by the following relation:

$$\kappa = \frac{a}{\pi \dfrac{d(T_{AC}/q)_{in\_phase}}{d\ln\omega}} = \frac{V^3 \dfrac{dR}{dT}}{4\pi R^2 \dfrac{dV_{3\omega\_in\_phase}}{d\ln\omega}} \qquad (5\text{-}1).$$

For the analysis of thin film on substrate with $K_f < K_{substrate}$, the thermal conductivity of the thin film can be obtained by employing the differential technique [15, 16]. The differential technique allows the measurement of the temperature oscillation amplitudes (T_{AC}) of two samples: the

reference substrate sample and the thin film-on-substrate sample. By measuring T_{AC} of these two samples and calculating the differences between them, the thermal conductivity of the thin film layer can be determined.

$$\Delta T_{AC} = T_{AC}(sample) - T_{AC}(reference) \quad (5\text{-}2),$$

$$\kappa_f = \frac{b_f}{\Delta T_{AC} / q} \quad (5\text{-}3).$$

Note that for the condition that the thermal conductivity of the thin film is much smaller than the substrate, the temperature variation of the thin film-on-substrate sample is higher than the reference substrate sample, and the differences of the variations are independent of frequency.

5.2 The Extended Slope Technique and 2D Thermal Diffusion Model [1-2]

Note that the conventional differential technique is only accurate and applicable under the condition that the thermal conductivity of the thin film is much smaller than the substrate. Thus, in order to measure the thermal conductivity of thin films which have a higher thermal conductivity than that of the substrate material, the 2D multilayer thermal diffusion model is developed in this work and the extended slope technique based on this model is proposed to extract the thermal conductivity of the thin films.

5.2.1 The 2D Thermal Diffusion Model

Figure 5-2 shows the schematic of the 2D multilayer thermal diffusion model. In this model, we assume the following conditions: 1) the bottom surface of the substrate is thermal insulating, 2) the interface thermal conductances are infinite (perfect thermal contacts), and 3) the nonisotropic aspects are ignored. The 2D heat conduction equation in each layer is written as:

$$\frac{1}{\alpha_i}\frac{\partial T_i}{\partial t} = \frac{\partial^2 T_i}{\partial x^2} + \frac{\partial^2 T_i}{\partial z_i^{\,2}}, i = s, f_1, f_2, f_3 \cdots \quad (5\text{-}4),$$

where s, f_1, f_2, f_3 … denote the substrate and thin film layers. The parameter Ti is the temperature oscillation amplitude and α_i is the thermal diffusivity of each layer. For simplicity, we only focus on two layer structure in the following discussions.

The boundary conditions for a film-on-substrate structure can be written as follow:

$$-\kappa_{f1}\left.\frac{\partial T_{f1}}{\partial z_{f1}}\right|_{z_{f1}=0} = f(x)\cos(2\omega t) \tag{5-5},$$

$$\kappa_{f1}\left.\frac{\partial T_{f1}}{\partial z_{f1}}\right|_{z_{f1}=b_{f1}} = \kappa_s\left.\frac{\partial T_s}{\partial z_s}\right|_{z_s=0} \tag{5-6},$$

$$\left.T_{f1}\right|_{z_{f1}=b_{f1}} = \left.T_s\right|_{z_s=0} \tag{5-7},$$

$$\left.\frac{\partial T_s}{\partial z_s}\right|_{z_s=b_s} = 0 \tag{5-8},$$

where κ_i (i = s, f_1) is the thermal conductivity of each layer, b_i (i = s, f_1) is the layer thickness, and f(x) is a rectangular function denoting the heating spatial distribution.

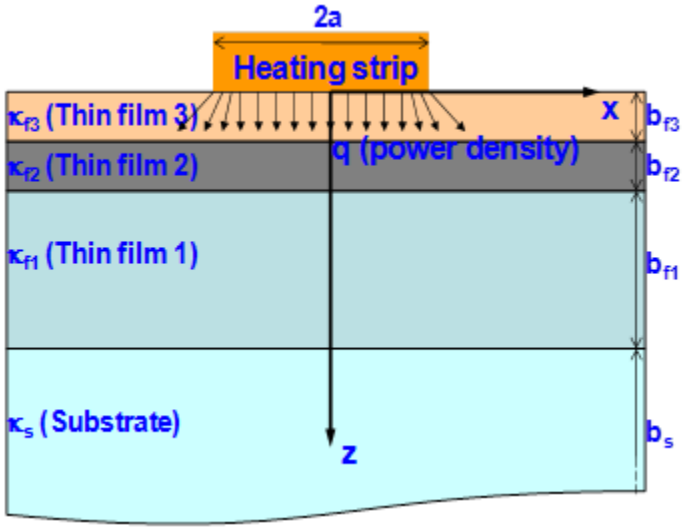

Figure 5-2: *The schematic of the 2D multilayer thermal diffusion model.*

To simplify the derivation, the parameters are normalized as follow. The above equations are normalized for simple derivations based on the following defined parameters and variables:

$$\tau = b_{f1}^2 / \alpha_s \tag{5-9},$$

$$T_{ref} = q \cdot b_{f1} / \kappa_s \tag{5-10},$$

$$t' = t / \tau \tag{5-11},$$

$$\omega' = \omega\tau \tag{5-12},$$

$$x' = x / a \tag{5-13},$$

$$z_i' = z_i / b_{f1} \tag{5-14},$$

$$T_i' = T_i / T_{ref} \tag{5-15},$$

$$K = \kappa_{f1} / \kappa_s \tag{5-16},$$

where q is the heating power density, a is half of the heater linewidth.

By employing the normalized parameters and variables listed above, the heat equations and boundary conditions can be re-written as follow:

$$\frac{\alpha_s}{\alpha_{f1}} \frac{\partial T_{f1}'}{\partial t'} = \frac{b_{f1}^2}{a^2} \frac{\partial^2 T_{f1}'}{\partial x'^2} + \frac{\partial^2 T_{f1}'}{\partial z_{f1}'^2} \tag{5-17},$$

$$\frac{\partial T_s'}{\partial t'} = \frac{b_{f1}^2}{a^2} \frac{\partial^2 T_s'}{\partial x'^2} + \frac{\partial^2 T_s'}{\partial z_s'^2} \tag{5-18},$$

$$-K \left. \frac{\partial T_{f1}'}{\partial z_{f1}'} \right|_{z_{f1}'=0} = u(x')\cos(2\omega' t'), u(x') = \begin{cases} 1 & x' \in [-1,1], \\ 0 & otherwise. \end{cases} \tag{5-19},$$

$$K \left. \frac{\partial T_{f1}'}{\partial z_{f1}'} \right|_{z_{f1}'=1} = \left. \frac{\partial T_s'}{\partial z_s'} \right|_{z_s'=0} \tag{5-20},$$

$$\left. T_{f1}' \right|_{z_{f1}'=1} = \left. T_s' \right|_{z_s'=0} \tag{5-21},$$

$$\left. \frac{\partial T_s'}{\partial z_s'} \right|_{z_s'=b_s / b_{f1}} = 0 \tag{5-22}.$$

Under the alternating excitation at frequency 2ω, the general solution of the temperature field T' can be expressed as:

$$T_i' = X(x')Z_i(z_i')\exp(-j2\omega' t') \tag{5-23}.$$

By performing a Fourier transform for the x' axis, the equations can be written as:

$$\frac{\partial^2 Z_{f1}}{\partial z_{f1}'^2} - \frac{b_{f1}^2}{a^2}\lambda^2 Z_{f1} + j2\omega' \frac{\alpha_s}{\alpha_{f1}} Z_{f1} = 0 \quad (5\text{-}24),$$

$$\frac{\partial^2 Z_s}{\partial z_s'^2} - \frac{b_{f1}^2}{a^2}\lambda^2 Z_s + j2\omega' Z_s = 0 \quad (5\text{-}25),$$

$$-K \left.\frac{\partial Z_{f1}}{\partial z_{f1}'}\right|_{z_{f1}'=0} = \frac{\sin(\lambda)}{\lambda} \quad (5\text{-}26),$$

$$K \left.\frac{\partial Z_{f1}}{\partial z_{f1}'}\right|_{z_{f1}'=1} = \left.\frac{\partial Z_s}{\partial z_s'}\right|_{z_s'=0} \quad (5\text{-}27),$$

$$Z_{f1}\big|_{z_{f1}'=1} = Z_s\big|_{z_s'=0} \quad (5\text{-}28),$$

$$\left.\frac{\partial Z_s}{\partial z_s'}\right|_{z_s'=b_s/b_{f1}} = 0 \quad (5\text{-}29).$$

In practice, the thermal conductivity of the reference substrate needs to be known or measured first (e.g. by using the 3ω slope method for bulk material). Then by measuring the $V_{3\omega}$ vs. ω curve for the film-on-substrate sample, solving the above equations and fitting the experimental data, the ratio of the thermal conductivity of thin film over substrate (*K*) can be obtained. Thus, the thermal conductivity of thin film can be calculated by using the relation $\kappa_f = K \times \kappa_s$.

5.2.2 The Extended Slope Technique

The extended slope technique combines the conventional 3ω slope technique with 2D thermal diffusion model, which can be applicable in analyzing thin film with thermal conductivity either smaller or larger than that of the substrate ($\kappa_f < \kappa_s$ and $\kappa_f > \kappa_s$).

The 2D thermal diffusion model shows that for the case of thermal conductivity ratio $K < 1$, which is the condition where the thermal conductivity of the thin film is smaller than the substrate ($\kappa_f < \kappa_s$), the in-phase T' vs. ln(ω) curve of the film-on-substrate sample is parallel to the curve of the substrate sample, which results in a temperature raise $T'_{f1} - T'_s$ independent of the frequency.

As an example, figures 5-3(a) and 5-3(b) illustrate the temperature difference ($T'_{f1} - T'_s$) as a function of frequency in logarithm scale for the cases of K = 0.05 and K = 0.5, and the temperature difference is independent with frequency.

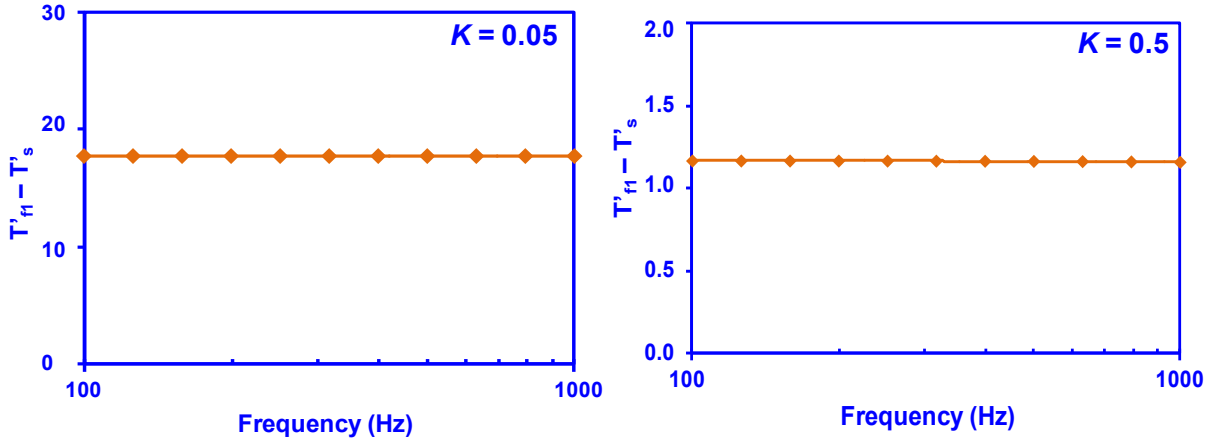

Figure 5-3: *The simulated temperature difference ($T'_{f1} - T'_s$) between thin film sample and substrate sample as a function of frequency in logarithm scale for (a) thermal conductivity ratio K = 0.05, and (b) thermal conductivity ratio K = 0.5, by using 2D thermal diffusion model.*

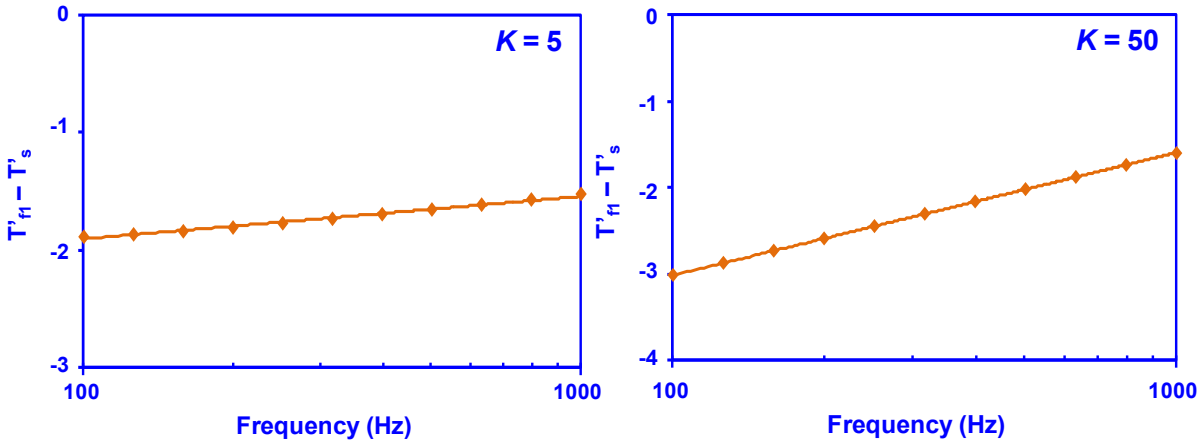

Figure 5-4: *The simulated temperature difference ($T'_{f1} - T'_s$) between thin film sample and substrate sample as a function of frequency in logarithm scale for (a) thermal conductivity ratio K = 5, and (b) thermal conductivity ratio K = 50, by using 2D thermal diffusion model.*

In contrast, for the case of thermal conductivity ratio $K > 1$ ($\kappa_f > \kappa_s$), the slope dT'/ dln(ω) of the film-on-substrate sample is different from the slope of the substrate sample. Thus, the in-phase T' vs. ω curves of the thin film and the substrate are not parallel. As an illustration, figures 5-4(a) and 5-4(b) show the temperature difference ($T'_{f1} - T'_s$) as a function of frequency in logarithm scale for the cases of K = 5 and K = 50, and the temperature difference has a linear relation with

ln(ω). Moreover, the reflection from the interface between the thin film and the substrate cannot be ignored, which will cause the temperature oscillation out of phase which results in a lower temperature of the thin film than that of the substrate.

Thus, as the slope dT'/dln(ω) of the film-on-substrate sample is dependent with the thermal conductivity of the thin film κ_f, and $K = \frac{k_f}{k_s}$ (κ_s is known), the relationship of the slope dT'/dln(ω) as a function of thermal conductivity ratio *K* can be obtained. Figure 5-5 shows the slope of dT'/dln(ω) increases as a monotonic function of the thermal conductivity ratio *K*. The monotonic relationship between slope dT'/dln(ω) and the thermal conductivity ratio *K* indicates that the ratio *K* can be obtained by fitting the slope with experimental data.

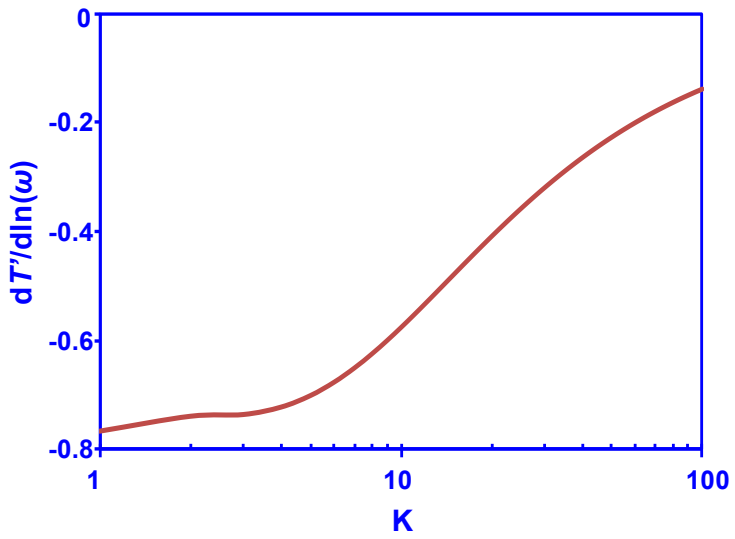

Figure 5-5: *The Monotonic relationship of the slope dT'/dlnω as a function of thermal conductivity ratio K, simulated by 2D thermal diffusion model.*

Note that when the thin film and substrate are the same material, then relation *K*=1 will be obtained, which in turn transforms the slope technique into the conventional slope method for bulk material thermal conductivity measurement. Thus, the generality of the approach developed in this work is referred as the extended slope technique for thin film thermal conductivity measurement.

Figure 5-6 presents the procedure of extended slope technique analysis, which is the combination of a 2D thermal diffusion model and original slope technique. First, the 2D thermal

diffusion model is employed to obtain the relation of slope dT'/ dln(ω) and thermal conductivity ratio *K*. Then the $V_{3\omega}$ as a function of ln(ω) will be measured for the film-on-substrate sample from the 3ω measurement. By combining the results from the measurements and 2D thermal diffusion model, the thermal conductivity of thin film (κ_f) can be obtained by $\kappa_f = K \times \kappa_s$, where κ_s is known.

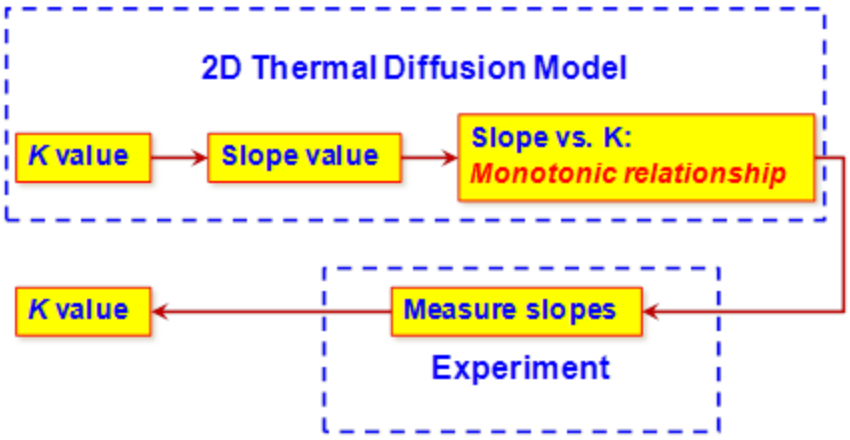

Figure 5-6: *The flow chart of thermal conductivity determination of thin film materials using extended slope technique and 2D thermal diffusion model.*

In order to verify the validity and accuracy of the 2D multilayer thermal diffusion model and the extended slope technique, the thermal conductivities were measured for MOCVD-grown GaN thin film on sapphire substrate, and the MOCVD-grown InN thin film on GaN/ Sapphire substrate, which were also compared with other reported thermal conductivity values.

5.2.3 Thermal Conductivity Measurement of GaN Thin Film

The undoped GaN thin film with thickness of 2.5 μm is grown on c-plane sapphire substrate (430 μm) by MOCVD [13, 14]. The thermal conductivity value of the sapphire reference sample ($\kappa_{sapphire}$) is obtained using the conventional slope technique, which is determined by using equation (5-1). The $V_{3\omega}$ as a function of frequency in logarithm scale for sapphire is shown in figure 5-7, and the $\kappa_{sapphire}$ is measured as 41 W/(mK), within the range of reported 35 – 42 W/(mK) [21].

Both curves of $V_{3\omega}$ as a function of frequency in logarithm scale for sapphire reference sample and GaN/sapphire sample were measured and shown in figure 5-7 with good linearity.

Thus, as shown in figure 5-8, the temperature oscillation amplitude T_{AC} can be obtained for both sapphire reference sample and GaN/sapphire sample by using the following relation [5, 6, 14-15]:

$$T_{AC} = 2\frac{V_{3\omega}}{V_{\omega}}\frac{dT}{dR}R \qquad (5\text{-}30).$$

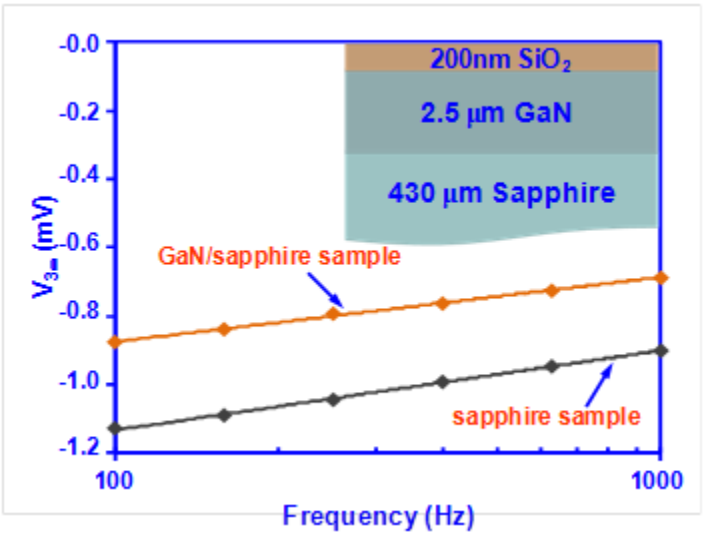

Figure 5-7: *The measured in-phase $V_{3\omega}$ as a function of frequency in logarithm scale for both GaN thin film on sapphire substrate sample and sapphire substrate sample at 300 K.*

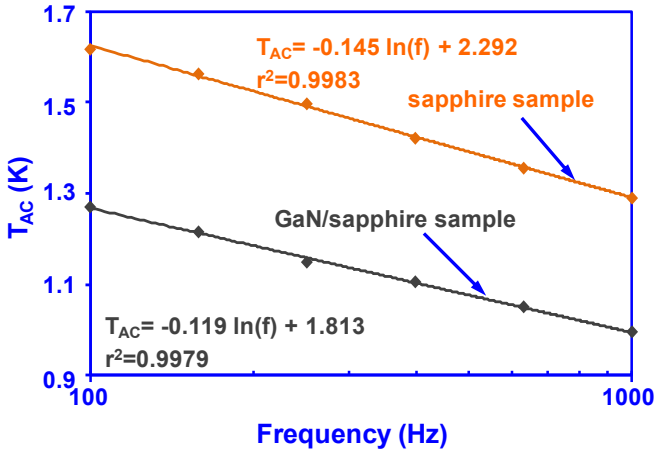

Figure 5-8: *The measured in-phase temperature oscillation amplitude (T_{AC}) as a function of frequency in logarithm scale for GaN thin film on sapphire substrate sample and sapphire substrate sample at 300 K.*

Note that the two curves of T_{AC} as a function of ln(ω) are not parallel, which confirms the inapplicability of conventional 3ω differential technique for characterization of thin film thermal conductivity which is higher than that of the substrate.

Thus, the extended slope technique and the 2D thermal diffusion model are required in order to measure the thermal conductivity of the GaN sample. The slope of dT'/ dln(ω) for the GaN/ sapphire was measured as -0.73606. After substituting the measured slope of the GaN/ sapphire sample into the 2D thermal diffusion model, the value of thermal conductivity ratio *K* = 2.63 is obtained to match the experimental slope, as shown in figure 5-9. Thus, the thermal conductivity value for GaN thin film (κ_{GaN}) is obtained as 41×2.63 = 108 W/(mK) at room temperature, which is in good agreement with reported values [17, 18].

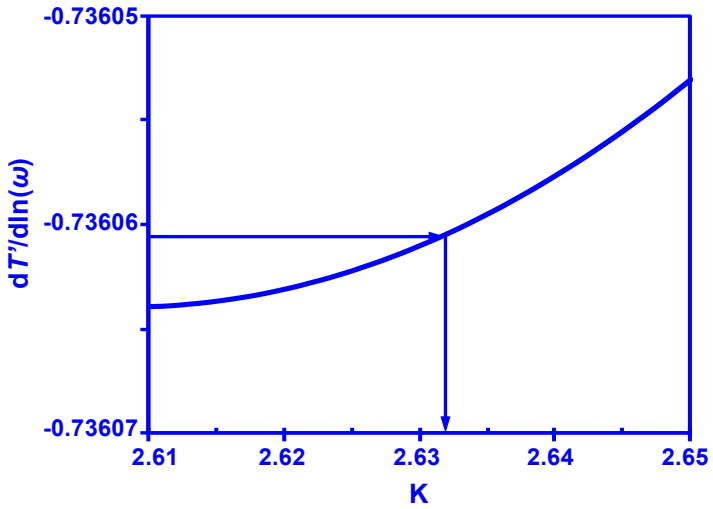

Figure 5-9: *The determination of thermal conductivity ratio K from normalized in-phase slope dT'/dln(ω) for GaN thin film on sapphire substrate using 2D thermal diffusion model.*

5.2.1 Thermal Conductivity Measurement of InN Thin Film

The extended slope technique and the 2D thermal diffusion model were also employed to measure the thermal conductivity of InN alloys. The 220 nm InN alloy was grown on undoped GaN (2.5 μm) / sapphire (430 μm) substrate, which also serves as reference sample. The inset of figure 11 shows the schematic of the structures employed in the measurements for InN thin film. The InN material was grown by employing pulsed MOCVD technique [13, 14], which resulted in

high quality narrow-bandgap InN semiconductor with bandgap of 0.77 eV. The background carrier density of the InN alloy was measured as 1.5 × 10^{19} cm^{-3}, and the electron mobility was measured as 681 $cm^2/(Vs)$ [13, 14]. The use of pulsed MOCVD technique was instrumental to realize droplet-free InN film with excellent optical properties.

Figure 5-10 shows the measured $V_{3\omega}$ as a function of ln(ω) for the InN thin film on GaN/ sapphire substrate sample. The GaN/ sapphire reference sample exhibited an effective thermal conductivity of 44.5 W/(mK), which was measured by the conventional slope method. The slope $dT/d\ln(\omega)$ of InN thin film on GaN/ sapphire substrate sample was measured as -0.73575 by 3ω measurement. After substituting the measured slope into the 2D thermal diffusion model, the thermal conductivity ratio K was obtained as K = 2.83 as shown in figure 5-11. Thus, the thermal conductivity of InN thin film was determined as κ_{InN} = 44.5 × 2.83 = 126 W/(mK) for the high-quality pulsed-MOCVD grown InN thin film at room temperature.

The measured thermal conductivity of MOCVD-grown InN alloy (κ_{InN} = 126 W/(mK)) shows very good agreement with the measured thermal conductivity of MBE-grown InN alloy (κ_{InN} = 120 W/(mK) [19]), which also confirms the validity and accuracy of the proposed extended slope technique and the 2D thermal diffusion model for thermal conductivity characterization for thin film material with thermal conductivity higher than that of the substrate material.

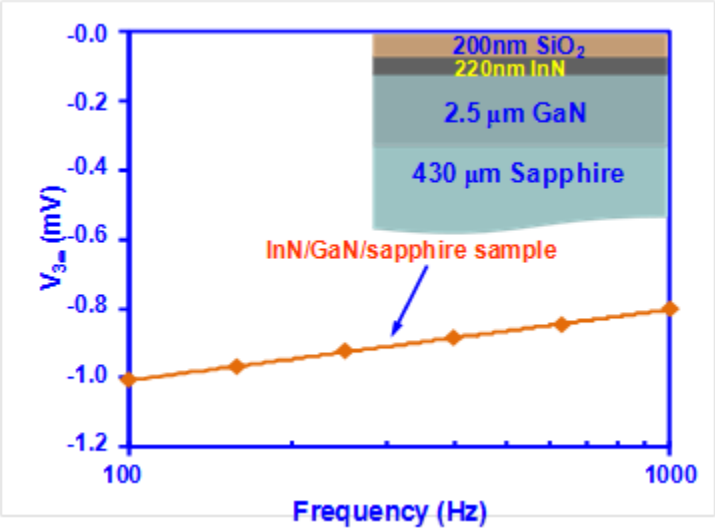

Figure 5-10: *The measured in-phase $V_{3\omega}$ as a function of frequency in logarithm scale for the 220 nm InN thin film on GaN/sapphire substrate at 300 K.*

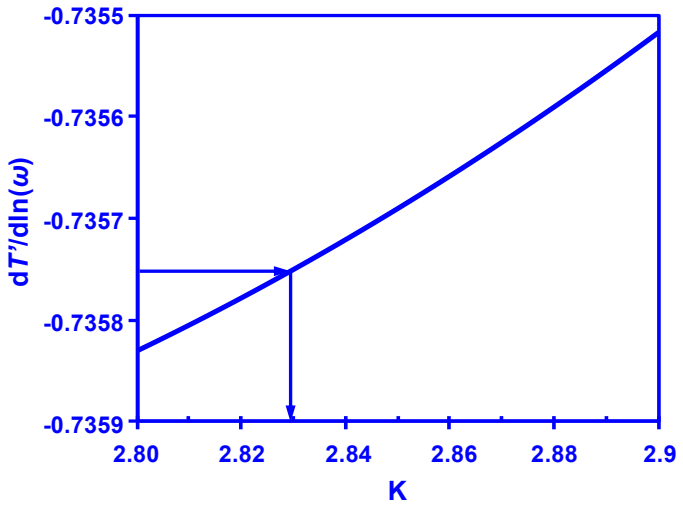

Figure 5-11: *The determination of ratio K from normalized in-phase slope dT'/dln(ω) for InN thin film on GaN/sapphire substrate using 2D thermal diffusion model.*

Note that the measured thermal conductivity of MOCVD-grown InN thin film is much higher in comparison to the previously reported value of 45 W/(mK) for porous InN obtained by nitrogen plasma method [27] and 17 W/(mK) for porous InN obtained by hot-press method [28], while in good trend with the theoretical value of 176 W/(mK) – 180 W/(mK) based on phonon scattering [20, 27]. The thermal conductivity values of crystalline InN material are of great interest for thermal management and thermoelectric materials based on InN-containing alloys, such as MOVPE-grown InGaN alloys [3, 4, 9], AlInN alloys [5, 6, 8, 10], or AlInGaN alloys [7].

5.3 Summary

In summary, the 2D multilayer thermal diffusion model was developed and the extended slope technique based on this model was proposed to accurately extract the thin film thermal conductivity which is higher than that of the substrate ($\kappa_f > \kappa_s$). The thermal conductivities are measured for MOCVD-grown GaN thin film on sapphire substrate and MOCVD-grown InN thin film on GaN/ sapphire substrate in order to verify the validity and accuracy of the 2D multilayer thermal diffusion model and the extended slope technique. The measured thermal conductivity of GaN (κ_{GaN} = 108 W/(mK)) is in good agreement with reported values [17, 18]. For the case of MOCVD-grown InN thin film, the measured thermal conductivity (κ_{InN} = 126 W/(mK)) agrees very

well with the reported value of MBE-grown InN thin film [19]. The thermal conductivity value of MOCVD-grown InN thin film will be of great interest in order to understand thermoelectric characteristics of InN-based ternary and quaternary materials. Therefore, the proposed extended slope method and the 2D multilayer thermal diffusion model will serve as an alternative method in order to accurately characterize thermal conductivity of thin film materials.

References for Chapter 5

[1] H. Tong, Thermoelectric Characteristics and Measurements of Ternary III-Nitride Semiconductors, Ph.D. Dissertation, Lehigh University, Sep. 2010.

[2] H. Tong, J. A. Herbsommer, V. A. Handara, H. P. Zhao, G. Y. Liu, and N. Tansu, "Thermal Conductivity Measurement of Pulsed-MOVPE InN Alloy Grown on GaN / Sapphire by 3ω Method," Proc. of the SPIE Photonics West 2010, Gallium Nitride Materials and Devices V, San Francisco, CA, (2010).

[3] B. N. Pantha, R. Dahal, J. Li, J. Y. Lin, H. X. Jiang, and G. Pomrenke, Appl. Phys. Lett., 92, 042112 (2008).

[4] B. N. Pantha, R. Dahal, J. Li, J. Y. Lin, H. X. Jiang, and G. Pomrenke, J. Electro. Mater., 38, 1132 (2009).

[5] H. Tong, J. Zhang, G. Liu, J. A. Herbsommer, G. S. Huang, and N. Tansu, Appl. Phys. Lett., 97, 112105 (2010).

[6] J. Zhang, H. Tong, G. Liu, J. A. Herbsommer, G. S. Huang, and N. Tansu, J. Appl. Phys., 109, 053706 (2011).

[7] B. N. Pantha, I. Feng, K. Aryal, J. Li, J. Y. Lin, and H. X. Jiang, Applied Physics Express, 4, 051001 (2011).

[8] J. Zhang, S. Kutlu, G.Y.Liu, and N. Tansu, J. Appl. Phys., 110, 043710 (2011).

[9] A. Sztein, H. Ohta, J. E. Bowers, S. P. DenBaars, and S. Nakamura, J. Appl. Phys. 110, 123709 (2011).

[10] A. Sztein, J. E. Bowers, S. P. DenBaars, and S. Nakamura, J. Appl. Phys. 112, 083716 (2012).

[11] W. Gee, and M. Green, J. Phys. E: Sci. Instrum., 3, 135 (1970).

[12] R. E. Bentley, Theory and Practice of Thermoelectric Thermometry, Chapter 2, page 60, Springer, Springer, 1998.

[13] M. Jamil, H. Zhao, J. Higgins, and N. Tansu, J. Crys. Growth, 310, 4947 (2008).

[14] M. Jamil, H. Zhao, J. Higgins and N. Tansu, Physica Status Solidi (a), 205, 2886 (2008).

[15] S.-M. Lee and D. G. Cahill, J. App. Phys., 81, 2590 (1997).

[16] Z. Bian, M. Zebarjadi, R. Singh, Y. Ezzahri, A. Shakouri, G. Zeng, J.-H. Bahk, J. E. Bowers, J. M. O. Zide, and A. C. Gossard, Phys. Rev. B 76, 205311 (2007).

[17] C.-Y. Luo, H. Marchand, D. R. Clarke, and S. P. DenBaars, Appl. Phys. Lett. 75, 4151 (1999).

[18] D.I. Florescu, V.M. Asnin, F.H. Pollak, a.M. Jones, J.C. Ramer, M.J. Schurman, and I. Ferguson, Appl. Phys. Lett. 77, 1464 (2000).

[19] A. X. Levander, T. Tong, K. M. Yu, J. Suh, D. Fu, R. Zhang, H. Lu, W. J. Schaff, O. Dubon, W. Walukiewicz, D. G. Cahill, and J. Wu, Appl. Phys. Lett. 98, 012108 (2011).

[20] H.-H. Huang, I.-L. Lu, and Y.-R. Wu, Phys. Status Solidi A, 208, 1562 (2011).

[21] F. P. Incropera and D. P. De Witt, Fundamentals of Heat and Mass Transfer (5th ed.), New York, (Wiley, 2001).

[22] D. G. Cahill and R. O. Pohl, Phys. Rev. B. 35, 4067 (1987).

[23] D. G. Cahill, Rev. Sci. Instrum. 61, 802 (1990).

[24] D. G. Cahill, Rev. Sci. Instrum. 73, 3701 (2002).

[25] D. G. Cahill, M. Katiyar, and J. R. Abelson, Phys. Rev. B. 50, 6077 (1994).

[26] D. Cahill, H. Fischer, T. Klitsner, and E. Swartz, Science & Technology A: Vacuum, Surfaces, and Films, 1989.

[27] S. Krukowski, Journal of Physics and Chemistry of Solids, 59, 289 (1998).

[28] A. Yamamoto and S. Yamaguchi, Materials Research Society Symposium Proceedings, 793, 283 (2004).

Chapter 6: High Temperature Thermoelectric Characterizations for Nitride Materials

In chapter 4, the thermoelectric characterizations of AlInN alloys grown by metalorganic chemical vapor deposition (MOCVD) with various In-contents were presented and discussed in details.

In this chapter, we present the detailed discussions on characterizations of the Seebeck coefficients for n-type $Al_{1-x}In_xN$ alloys (x = 0.0038 - 0.2134) in the temperature range from room temperature (T = 300 K) up to high temperature (T = 382 K) [31]. The Seebeck coefficients of the binary AlN and InN alloys were also characterized, in order to provide comparison to those measured from the n-type AlInN ternary alloys. All the n-type $Al_{1-x}In_xN$ alloys with various In-contents, as well as the AlN and InN alloys, were grown by MOCVD. The thermal gradient method was employed for the Seebeck coefficient measurements. The details of the high temperature thermoelectric characterizations will be presented in the following sections.

6.1 Metalorganic Chemical Vapor Deposition (MOCVD) of AlInN Alloys

Our recent work [15, 16] reported the epitaxy and thermoelectric characteristics of AlInN alloys with various In-contents at room temperature (T = 300 K). All the n-type AlInN films were grown by MOCVD on undoped-GaN (thickness = 2.8 μm; $n_{background}$ ~ 5 x 10^{16} cm^{-3}) template on c-plane sapphire substrates. The growth temperatures of the n-type $Al_{1-x}In_xN$ alloys (~200 nm thick) ranged between 750- 860 °C with growth pressure of 20 Torr. The measured In-contents (x) of $Al_{1-x}In_xN$ epilayers were x = 0.0038, 0.11, 0.17, and 0.2134, respectively. For $Al_{0.83}In_{0.17}N$ alloys, which are lattice-matched to GaN, the growth temperature and V/III ratio were 780 ^{0}C and 9300, respectively. For $Al_{0.9962}In_{0.0038}N$, $Al_{0.89}In_{0.11}N$ and $Al_{0.79}In_{0.21}N$ alloys, the growth temperatures were 860 ^{0}C, 790 ^{0}C and 750 ^{0}C, respectively. The background carrier concentrations of n-type $Al_{1-x}In_xN$ alloys were measured by the Hall method. The background n-type carrier concentrations for two lattice-matched $Al_{0.83}In_{0.17}N$ samples were measured as 5.1×$10^{18}$$cm^{-3}$ and 1.6×$10^{18}$$cm^{-3}$, respectively. For $Al_{0.89}In_{0.11}N$ and $Al_{0.79}In_{0.21}N$ alloys, the background n-type carrier concentrations

were measured as $1.1x10^{18}cm^{-3}$ and $2.2\times10^{18}cm^{-3}$, respectively. The details of the growth conditions of the AlInN alloys were presented in reference 16.

High Z^*T values were reported at T= 300 K for MOCVD-grown n-type AlInN alloys [15, 16], which were measured as high as 0.391 up to 0.532. The highest Z^*T value (T= 300K) was achieved as 0.532 for lattice-matched n-type $Al_{0.83}In_{0.17}N$ with carrier concentration $n = 5.1\times10^{18}$ cm^{-3}. The Z^*T values of the MOVPE-grown $Al_{1-x}In_xN$ alloys are significantly higher than the RF-sputtered AlInN (Z^*T= 0.005, T= 300 K) [8] and MOCVD-grown InGaN (Z^*T= 0.08, T= 300 K) [13, 14]. The improvement observed from MOCVD-grown AlInN alloys are primarily attributed to the larger Seebeck coefficient and electrical conductivity resulting in higher power factor, in comparison to those measured from MOCVD-grown InGaN [13] and RF-sputtered AlInN [8].

Large Seebeck coefficients obtained from the MOCVD-grown AlInN alloys directly contributed to the enhancement of the thermopower and Z^*T values [16]. Therefore, the characteristics of Seebeck coefficients of MOCVD-grown AlInN alloys are important in order to understand the contribution of Seebeck coefficients for improved Z^*T values. However, the investigation of thermoelectric characteristics of MOCVD-grown AlInN alloys at higher temperatures is relatively lacking, which play important roles in higher temperature thermoelectric device operations. Further investigations of the thermoelectric characteristics for MOCVD-grown AlInN alloys at higher temperatures are of great interest for improved understanding of the improvement of Z^*T values at higher temperatures in this material system.

6.2 High-Temperature Characterizations of Seebeck Coefficients for AlInN Alloys

The thermal gradient method, which is similar to the method employed in references 13-17, was employed to determine the Seebeck coefficients, and the experimental set up is shown in figure 6-1. When a temperature gradient was created in the sample (figure 6-1), both the voltage difference and temperature difference were collected at the same time. Two type-K thermocouples were attached to the top surface of AlInN samples via indium (In) metal contacts to measure temperature difference. The positive chromel electrodes of the thermocouples were

utilized to collect the Seebeck voltage, which was measured by a digital multimeter HP 34401A. The Seebeck voltages (ΔV) for all the $Al_{1-x}In_xN$ samples show good linearity with the measured temperature difference (ΔT) from room temperature up to high temperatures. The total Seebeck coefficient was determined by using - $\Delta V/\Delta T$ relation for all the n-type $Al_{1-x}In_xN$ samples, which refer to the total Seebeck coefficients of n-type $Al_{1-x}In_xN$ alloys combined with that of the chromel electrode. The corresponding absolute Seebeck coefficients for n-type $Al_{1-x}In_xN$ films need to be compensated by the Seebeck coefficient of chromel (21.5 μV/K) at room temperature (T= 300 K) [18], which changes minimally (~ 0.3 μV/K) [19] for temperature range (T = 300-382 K) used in our experiments.

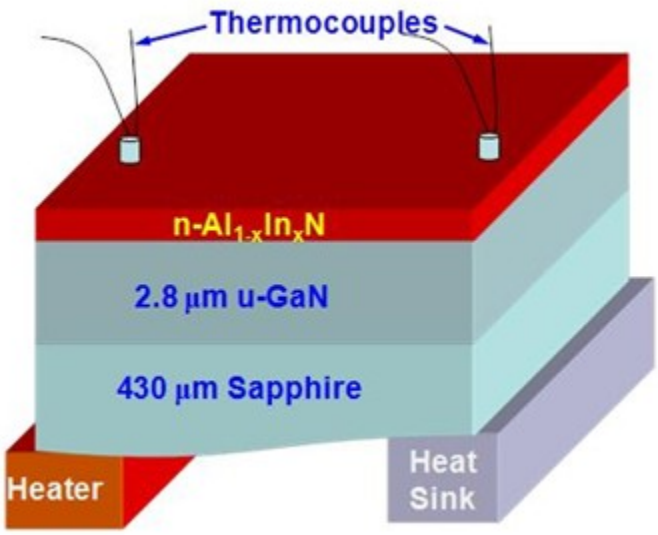

Figure 6-1: *The set up for the thermal gradient method for Seebeck voltage measurements.*

6.2.1 High-Temperature Seebeck Coefficients of $Al_{1-x}In_xN$ (x=0.0038, 0.11) Tensile Films

The measured Seebeck voltages (ΔV) as a function of the temperature difference (ΔT) for $Al_{1-x}In_xN$ (x=0.0038, 0.11) alloys from T=300 K up to T=382 K are shown in figures 6-2(a) and 6-3(a), respectively. The absolute Seebeck coefficients of $Al_{1-x}In_xN$ (x= 0.0038, 0.11) alloys at various temperatures are shown in figure 6-2(b) and 6-3(b), respectively.

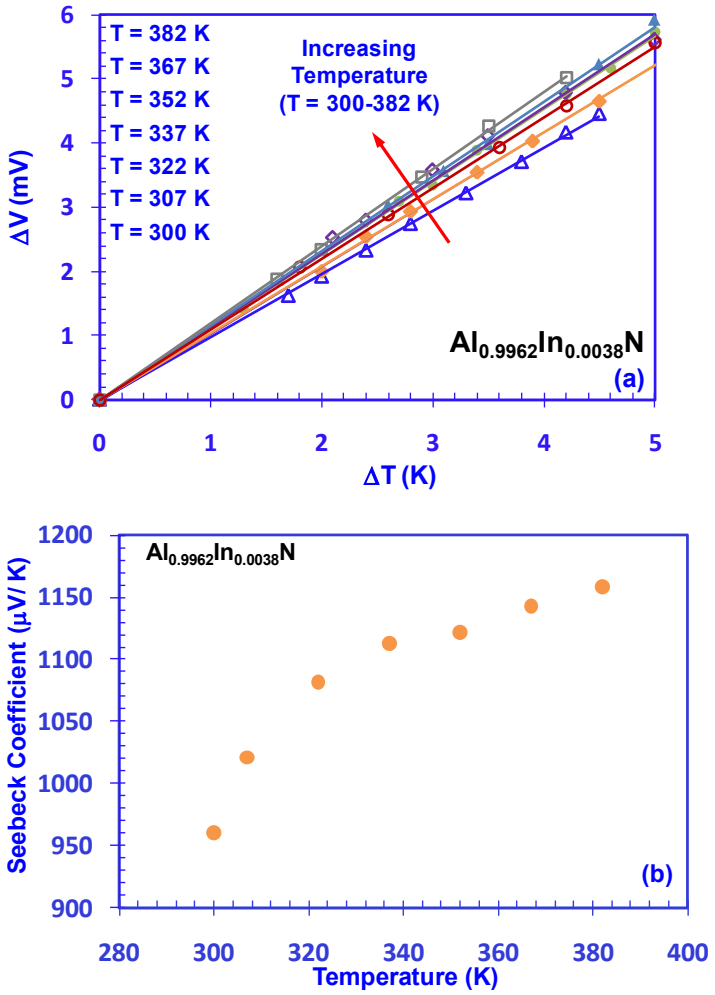

Figure 6-2: *(a) Seebeck voltage as a function of the temperature difference, and (b) measured Seebeck coefficients for n-type $Al_{0.9962}In_{0.0038}N$ alloy from T=300K up to T=382K.*

The absolute Seebeck coefficients for both $Al_{1-x}In_xN$ (x=0.0038, 0.11) tensile films show increasing trend with raising temperatures. For the $Al_{0.9962}In_{0.0038}N$ sample with lowest In-content, the absolute Seebeck coefficients were measured as high as 960.3 μV/K –1143.0 μV/K for temperatures range from 300 K up to 382 K. For the $Al_{0.89}In_{0.11}N$ sample, the absolute Seebeck coefficients were measured as 323.2 μV/K – 401.6 μV/K for temperatures range from 300 K up to 382 K. Note that both $Al_{0.9962}In_{0.0038}N$ and $Al_{0.89}In_{0.11}N$ samples have cracks in the films, which are related to the dislocation density of the tensile films grown on GaN templates. The cracking of the tensile films will reduce the relaxation time of the carriers, which will lead to lower Seebeck coefficients of the films [16].

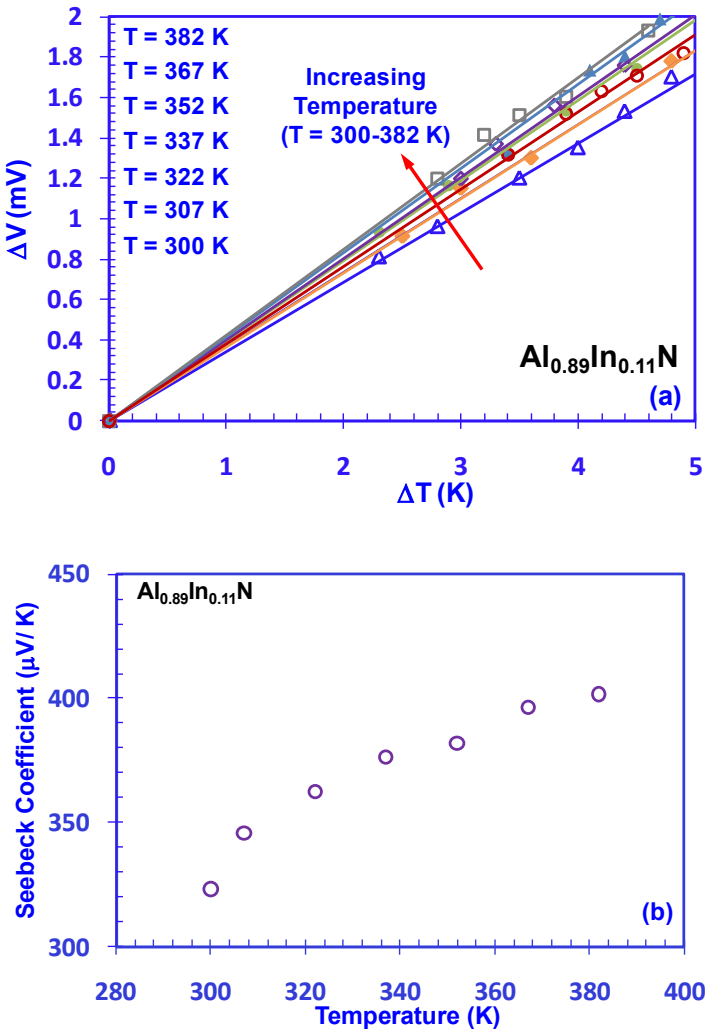

Figure 6-3: *(a) Seebeck voltage as a function of the temperature difference, and (b) measured Seebeck coefficients for n-type $Al_{0.89}In_{0.11}N$ alloy from T=300K up to T=382K.*

6.2.2 High-Temperature Seebeck Coefficients of $Al_{0.79}In_{0.21}N$ Compressive Film

Figure 6(a) and 6(b) show the measured Seebeck voltages (ΔV) as a function of the temperature difference (ΔT) and the absolute Seebeck coefficients for $Al_{0.79}In_{0.21}N$ alloy from T=300 K up to T=382 K, respectively. As the $Al_{0.79}In_{0.21}N$ sample was grown on GaN template with compressive strain, the thin film was crack-free. The absolute Seebeck coefficients for the compressive $Al_{0.79}In_{0.21}N$ film show increasing trend with raising temperatures, which were measured as 386.4 μV/K – 460.7 μV/K for temperatures range from T = 300 K up to T = 382 K.

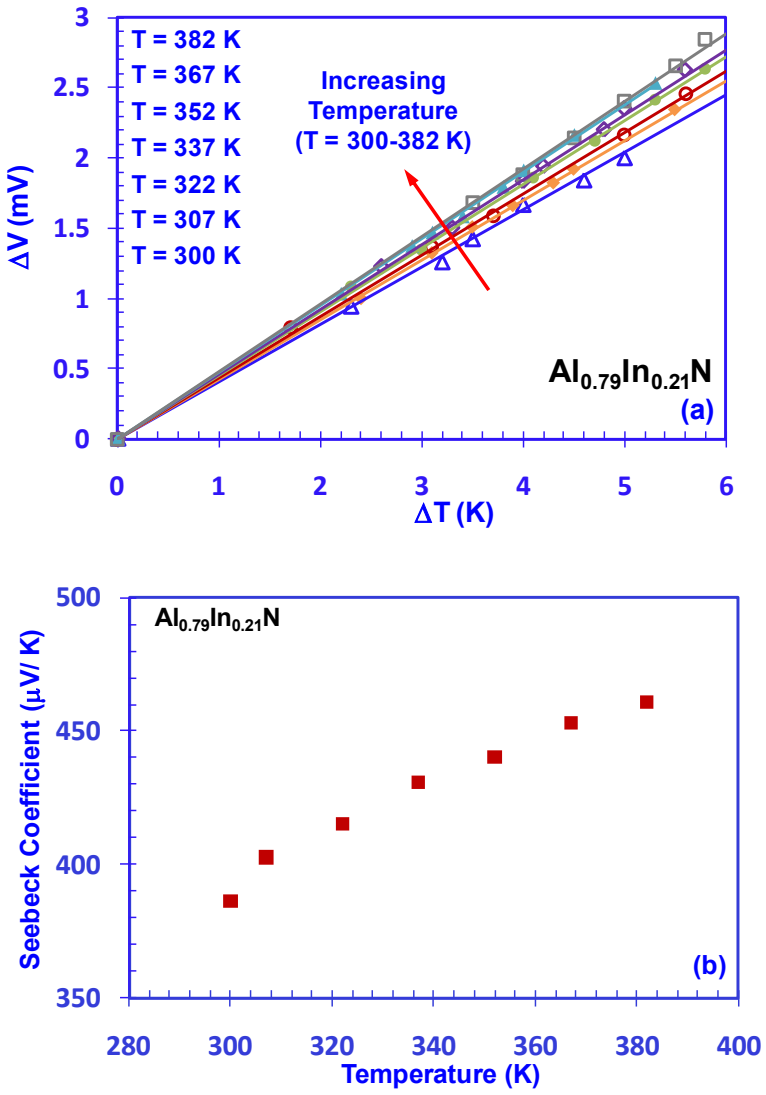

Figure 6-4: *(a) Seebeck voltage as a function of the temperature difference, and (b) measured Seebeck coefficients for n-type $Al_{0.79}In_{0.21}N$ alloy from T=300K up to T=382K.*

6.2.3 High-Temperature Seebeck Coefficients of Lattice-Matched $Al_{0.83}In_{0.17}N$ Alloys with Different Background Concentrations

Figure 6-5(a) and 6-5(b) show the measured Seebeck voltages (ΔV) as a function of the temperature difference (ΔT) for both lattice-matched $Al_{0.83}In_{0.17}N$ (n = 5.1×10^{18} cm^{-3}) and $Al_{0.83}In_{0.17}N$ (n = 1.6×10^{18} cm^{-3}) samples from T=300 K up to T=382 K, respectively. The absolute Seebeck coefficients for both $Al_{0.83}In_{0.17}N$ (n = 5.1×10^{18} cm^{-3}) and $Al_{0.83}In_{0.17}N$ (n = 1.6×10^{18} cm^{-3}) samples are shown in figure 5-5(c). Both the lattice-matched $Al_{0.83}In_{0.17}N$ samples exhibit large

Seebeck coefficients for various temperatures. The absolute Seebeck coefficients were measured as high as 602.0 μV/K – 1233.2 μV/K and 446.3 μV/K – 592.3 μV/K from 300 K up to 382 K for $Al_{0.83}In_{0.17}N$ (n = 5.1×10^{18} cm^{-3}) and $Al_{0.83}In_{0.17}N$ (n = 1.6×10^{18} cm^{-3}) samples, respectively. Therefore, higher background doping level of the lattice-matched $Al_{0.83}In_{0.17}N$ sample shows larger enhancement of the Seebeck coefficient with increasing temperature. In addition, the lattice-matched $Al_{0.83}In_{0.17}N$ sample with higher doping level exhibits larger Seebeck coefficient for the temperature range of 300 K up to 382 K, which can be attributed to larger relaxation time of carriers that results from better crystalline epitaxial material quality [11, 12, 16]. Further, larger Seebeck coefficient of the higher background doping level $Al_{0.83}In_{0.17}N$ sample can also be attributed to the hopping conductance [3]. Specifically, as the hopping conductance leads to the decrease of resistivity for increasing carrier concentration, the Seebeck coefficient increases with higher carrier concentration [3].

Therefore, the high-temperature Seebeck coefficient characteristics of the n-type $Al_{1-x}In_xN$ alloys show that with higher In-content, the Seebeck coefficients are reduced for the n-type $Al_{1-x}In_xN$ thin films for the temperature ranges from T = 300 K up to T = 382 K. The $Al_{0.9962}In_{0.0038}N$ sample with the lowest In-content exhibits the largest absolute Seebeck coefficient at various temperatures. The absolute Seebeck coefficients of the lattice-matched $Al_{0.83}In_{0.17}N$ samples are larger than that of the tensile $Al_{0.89}In_{0.11}N$ alloy and the compressive $Al_{0.79}In_{0.21}N$ alloy. Despite its lower In-content of the $Al_{0.89}In_{0.11}N$ sample, the Seebeck coefficient is lower than the lattice-matched $Al_{0.83}In_{0.17}N$ samples and the $Al_{0.79}In_{0.21}N$ sample, which can be attributed to the cracking of the tensile film that will reduce the relaxation time of the carriers.

The Seebeck coefficients of the n-type $Al_{1-x}In_xN$ alloys show increasing trend with raising temperatures, which are significantly higher in comparison with those for RF-sputtered AlInN (20-50 μV/K, T = 300- 400 K) [8] and MOVPE-grown InGaN (150- 180 μV/K, T=300-400 K) [13, 14]. Therefore, the increase of Seebeck coefficients of the MOVPE-grown n-type $Al_{1-x}In_xN$ alloys at higher temperatures can potentially lead to ~1.5-4 times enhancement of the thermopower at higher temperature up to T = 382 *K*.

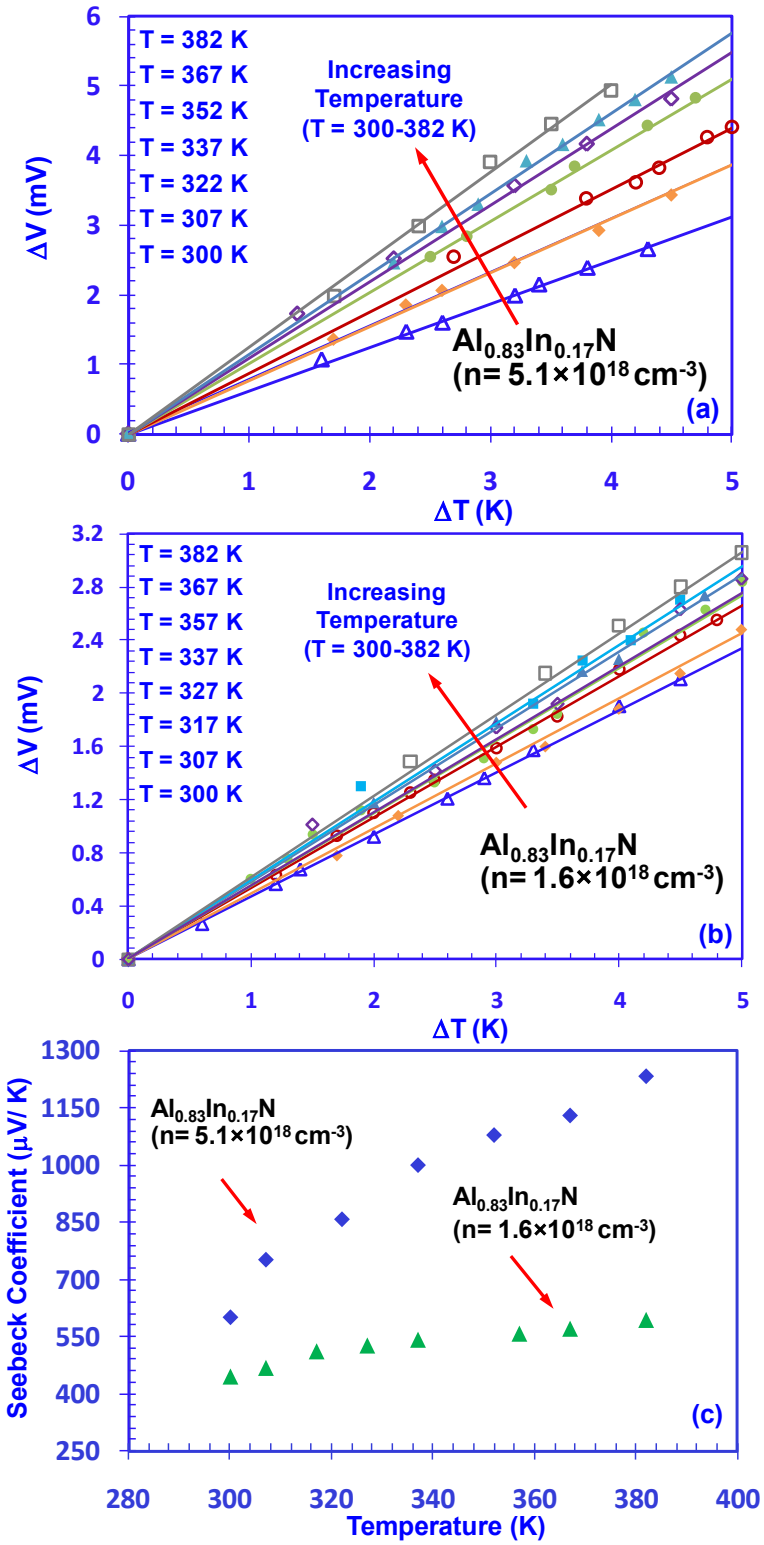

Figure 6-5: *(a) Seebeck voltage as a function of the temperature difference for n-type $Al_{0.83}In_{0.17}N$ ($n=5.1\times10^{18}cm^{-3}$) alloy, (b) Seebeck voltage as a function of the temperature difference for n-type $Al_{0.83}In_{0.17}N$ ($n=1.6\times10^{18}cm^{-3}$) alloy, and (c) measured Seebeck coefficients for n-type $Al_{0.83}In_{0.17}N$ ($n=5.1\times10^{18}cm^{-3}$ and $n=1.6\times10^{18}cm^{-3}$) alloys from T=300K up to T=382K.*

6.3 Seebeck Coefficients of InN and AlN Binary Alloys

6.3.1 MOCVD Growths of InN and AlN Binary Alloys

For comparison purpose, the Seebeck coefficients were characterized for InN and AlN binary alloys at various temperatures as supplementary to the characterizations for the ternary n-type $Al_{1-x}In_xN$ thin films. The AlN binary alloy growth was performed by MOVPE on undoped-GaN (2.8 μm) / sapphire substrate for the purpose of Seebeck coefficient characterization. TMAl was used as group III precursors, and NH_3 was used as group V precursor, and the V/III molar ratio was 2222. The growth temperature was 1075 °C with growth pressure of 100 Torr. The growth rate was measured as 3.7 nm/min, and the thickness of the AlN film was 190 nm.

The InN binary alloy was grown on undoped-GaN (2.8 μm) / sapphire substrate by pulsed growth MOVPE method [20]. TMIn was used as group III precursors, and NH_3 was used as group V precursor, and the V/III molar ratio was 12460. The growth temperature for the growth of InN layer was 575 °C with growth pressure of 200 Torr, and the thickness of the n-type InN film was 200 nm with carrier concentration n ~ 3.2 x 10^{19} cm^{-3}.

6.3.2 High-Temperature Seebeck Coefficients of AlN Alloy

The Seebeck coefficients of the binary n-type AlN alloy were determined by the thermal gradient method at various temperatures range from T = 300 K up to T = 322 K. The measured Seebeck voltages (ΔV) as a function of the temperature difference (ΔT) for AlN alloy at various temperatures are shown in figure 6-6(a). The Seebeck voltages (ΔV) show good linearity with the measured temperature difference (ΔT) at various temperatures for the binary AlN sample. The measured absolute Seebeck coefficients of n-type AlN alloy after the correction from the Seebeck coefficient of chromel are shown in figure 5-6(b). The absolute Seebeck coefficients for the n-type AlN alloy were measured as high as 992.5 μV/K up to 1004.7 μV/K from room temperature up to T = 322 K. The measured Seebeck coefficients of the AlN binary alloy are larger than the $Al_{1-x}In_xN$ (x = 11%- 21%) ternary alloys at similar temperatures. Further, the Seebeck coefficients of

the AlN binary alloy are measured as very similar with those for $Al_{0.9962}In_{0.0038}N$ alloy with the lowest In-content at various temperatures, within the experimental error.

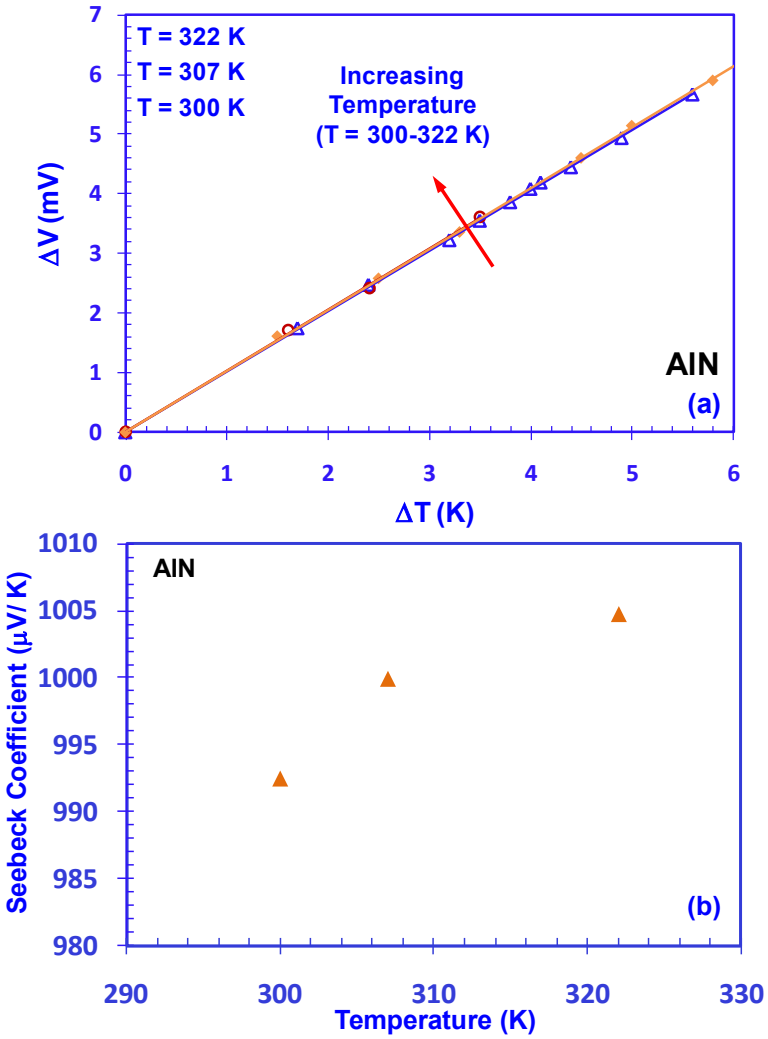

Figure 6-6: *(a) Seebeck voltage as a function of the temperature difference, and (b) measured Seebeck coefficients for n-type AlN alloy from T=300K up to T=322K.*

6.3.3 High-Temperature Seebeck Coefficients of InN Alloy

The measured Seebeck voltages (ΔV) for binary n-type InN alloy as a function of the temperature difference (ΔT) for InN alloy at various temperatures are shown in figure 6-7(a). The Seebeck voltages (ΔV) for the InN sample also show good linearity with the measured temperature difference (ΔT) at various temperatures from T = 300 *K* up to T = 382 *K* for the binary InN sample. The absolute Seebeck coefficients of n-type InN alloy were measured as 33.2 μV/K

up to 81.2 μV/K for T=300K up to T=382 K, after the correction from the Seebeck coefficient of chromel [figure 5-7(b)].

The Seebeck coefficients of the binary n-type InN alloy are found to be an order of magnitude lower than those of n-type $Al_{1-x}In_xN$ (x = 0.38%- 21%) ternary alloys at various temperatures. In addition, the lower Seebeck coefficients of the InN samples can partially be attributed to the much higher doping concentration of the InN alloy (n ~ 3.2×10^{19} cm^{-3}), which is in agreement with the theoretical simulation of the relationship between Seebeck coefficient and background carrier concentration [11, 12].

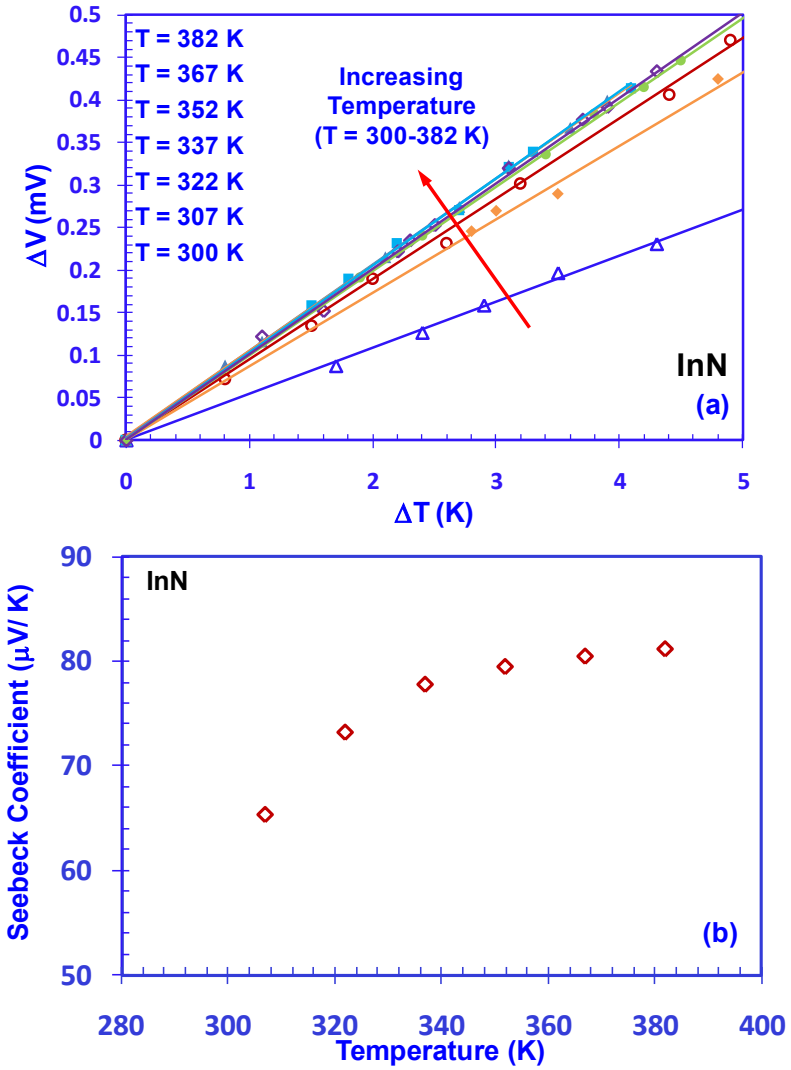

Figure 6-7: *(a) Seebeck voltage as a function of the temperature difference, and (b) measured Seebeck coefficients for n-type InN alloy from T=300K up to T=382K.*

6.3.4 Comparison for Seebeck Coefficients of Ternary and Binary Alloys

For non-crack $Al_{1-x}In_xN$ alloys, the Seebeck coefficients are expected to be in the range between that of AlN and InN. For the low In-content $Al_{1-x}In_xN$ alloy (ie. x ~ 0.38%), the Seebeck coefficient is expected to be very similar to that measured for AlN alloy, which is in agreement with the comparison in figures 6-2(b) and 6-6(b). To the best of our knowledge, there has been no prior reported theoretical value in the literature for the Seebeck coefficients of AlInN alloys. Future theoretical studies by using Boltzman transport equation [12] or iterative method [21] are important to extract the Seebeck coefficients of the AlInN alloys, in order to provide directions for optimization of AlInN alloys as thermoelectric materials.

The findings presented here are important for providing the useful thermoelectric parameters of III-Nitride and AlInN alloys in the literature [22-24]. Future works include the comprehensive measurements of the thermal conductivities of these n-type AlInN alloys with various In-contents up to high temperature, in order to obtain the Z^*T values of these materials at high temperature operation. The measurements of the thermal conductivities of these alloys can be carried out by employing the 3ω measurement set up with differential [25, 26] and slope [27-30] methods, similar to the approaches used in references 13-17.

6.4 Summary

In summary, the Seebeck coefficient characteristics of MOVPE-grown n-type $Al_{1-x}In_xN$ (x=0.0038-0.2134) alloys are presented from T=300 K up to T=382 K. The Seebeck coefficients were also characterized for InN and AlN binary alloys for comparison purpose. The Seebeck coefficients show significant enhancement at higher temperatures for the n-type $Al_{1-x}In_xN$ alloys. In addition, the Seebeck coefficients for n-type n-$Al_{1-x}In_xN$ alloy show decreasing trend with increasing In-content in the alloy. The Seebeck coefficients for the lattice-matched $Al_{0.83}In_{0.17}N$ (n = 5.1×10^{18} cm^{-3}) sample were measured as high as 602.0 μV/K – 1233.2 μV/K in the temperature range of T=300 K up to T = 382 K, which are significantly higher in comparison with those measured for RF-sputtered AlInN (20- 50 μV/K, T = 300- 400 K) [3] and MOVPE-grown InGaN

(150- 180 μV/K, *T*=300- 400 K) [13, 14]. The enhancement of the Seebeck coefficients can be attributed to longer relaxation time of carriers of the MOVPE-grown AlInN alloys with better crystalline quality. The increase of Seebeck coefficients of the n-type $Al_{1-x}In_xN$ alloys at elevated temperature (*T* = 382 K) can lead to ~1.5-4 times enhancement of the thermopower over those obtained at room temperature, which indicates that n-type AlInN materials as promising thermoelectric materials at high device operating temperature.

References for Chapter 6

[1] G. Chen and A. Shakouri, J. Heat Transfer, **124**, 242 (2002).

[2] G. Chen, M.S. Dresselhaus, G. Dresselhaus, J.-P. Fleurial, and T. Caillat, Int. Mater. Rev., **48**, 45 (2003).

[3] S. Yamaguchi, Y. Iwamura, and A. Yamamoto, Appl. Phys. Lett., **82**, 2065 (2003).

[4] S. Yamaguchi, R. Izaki, K. Yamagiwa, K. Taki, Y. Iwamura, and A. Yamamoto, Appl. Phys. Lett., **83**, 5398 (2003).

[5] S. Yamaguchi, R. Izaki, N. Kaiwa, S. Sugimura and A. Yamamoto, Appl. Phys. Lett., **84**, 5344 (2004).

[6] S. Yamaguchi, R. Izaki, Y. Iwamura, and A. Yamamoto, Physica Stat. Solidi (a), **201**, 225 (2004).

[7] R. Izaki, N. Kaiwa, M. Hoshino, T. Yaginuma, S. Yamaguchi, and A. Yamamoto, Appl. Phys. Lett., **87**, 243508 (2005).

[8] S. Yamaguchi, R. Izaki, N. Kaiwa, and A. Yamamoto, Appl. Phys. Lett., **86**, 252102 (2005).

[9] A. Sztein, H. Ohta, J. Sonoda, A. Ramu, J. E. Bowers, S. P. DenBaars, and S. Nakamura, Appl. Phys. Exp., **2**, 111003 (2009).

[10] E. N. Hurwitz, M. Asghar, A. Melton, B. Kucukgok, L. Su, M. Orocz, M. Jamil, N. Lu, I. T. Ferguson, J. Elec. Materials, **40**, 513 (2011).

[11] W. Liu, A. A. Balandin, J. Appl. Phys., **97**, 073710 (2005).

[12] W. Liu, and A. A. Balandin, J. Appl. Phys., **97**, 123705 (2005).

[13] B. N. Pantha, R. Dahal, J. Li, J. Y. Lin, H. X. Jiang, and G. Pomrenke, Appl. Phys. Lett., **92**, 042112 (2008).

[14] B. N. Pantha, R. Dahal, J. Li, J. Y. Lin, H. X. Jiang, and G. Pomrenke, J. Electro. Mater., **38**, 1132 (2009).

[15] H. Tong, J. Zhang, G. Liu, J. A. Herbsommer, G. S. Huang, and N. Tansu, Appl. Phys. Lett., **97**, 112105 (2010).

[16] J. Zhang, H. Tong, G. Liu, J. A. Herbsommer, G. S. Huang, and N. Tansu, J. Appl. Phys., **109**, 053706 (2011).

[17] B. N. Pantha, I. Feng, K. Aryal, J. Li, J. Y. Lin, and H. X. Jiang, Applied Physics Express, **4**, 051001 (2011).

[18] W. Gee, and M. Green, J. Phys. E: Sci. Instrum., **3**, 135 (1970).

[19] R. E. Bentley, Theory and Practice of Thermoelectric Thermometry, Chapter 2, page 60, Springer, Springer, 1998.

[20] M. Jamil, H. Zhao, J. Higgins, and N. Tansu, J. Crys. Growth, **310**, 4947 (2008).

[21] A. T. Ramu, L. E. Cassels, N. H. Hackman, H. Lu, J. M. O. Zide, J. E. Bowers, J. Appl. Phys., 107, 083707 (2010).

[22] I. Vurgaftman, and J.R. Meyer, *J. Appl. Phys.*, **94**, 3675 (2003).

[23] E. Sakalauskas, H. Behmenburg, P. Schley, G. Gobsch, C. Giesen, H. Kalisch, R. H. Jansen, M. Heuken, and R. Goldhahn, Phys. Stat. Sol. A, 208, 1517 (2011). DOI: 10.1002/pssa.201000931

[24] R. Butte, J. F. Carlin, E. Feltin, M. Gonschorek, S. Nicolay, G. Christmann, D. Simeonov, A. Castiglia, J. Dorsaz, H. J. Buehlmann, S. Christopoulos, G. Baldassarri Hoger von Hogersthal, A. J. D. Grundy, M. Mosca, C. Pinquier, M. A. Py, F. Demangeot, J. Frandon, P. G. Lagoudakis, J. J. Baumberg, and N. Grandjean, J. Phys. D: Appl. Phys., **40**, 6328 (2007).

[25] S.-M. Lee and D. G. Cahill, J. App. Phys., 81, 2590 (1997).

[26] Z. Bian, M. Zebarjadi, R. Singh, Y. Ezzahri, A. Shakouri, G. Zeng, J.-H. Bahk, J. E. Bowers, J. M. O. Zide, and A. C. Gossard, Phys. Rev. B 76, 205311 (2007).

[27] D. G. Cahill and R. O. Pohl, Phys. Rev. B. 35, 4067 (1987).

[28] D. G. Cahill, Rev. Sci. Instrum. 61, 802 (1990).

[29] D. G. Cahill, Rev. Sci. Instrum. 73, 3701 (2002).

[30] D. G. Cahill, M. Katiyar, and J. R. Abelson, Phys. Rev. B. 50, 6077 (1994).

[31] J. Zhang, S. Kutlu, G.Y.Liu, and N. Tansu, J. Appl. Phys., 110, 043710, (2011).

Chapter 7: Three-Layer Superlattice Design for Thermoelectric Applications

In this chapter, the cross-plane thermal conductivity of three-layer superlattices is calculated by a numerical method, which is developed from the lattice dynamical theory. The phonon mean free path is included into the calculation, thus the minimum thermal conductivity occurs at the crossover of the particle-like model and wave-like model of the phonons. The studies focus on the effect of mass ratio, layer thickness, and mean free path on the minimum thermal conductivity of the three-layer superlattice design.

7.1 Theory and Numerical Methods

7.1.1 Analytical Method for Superlattice Thermal Conductivity Calculation

The thermal conductivity of semiconductor superlattices plays important roles in various device applications [1-9]. For solid-state refrigeration and heat recycling for electric power generation, the thermal conductivity of the material needs to be reduced as low as possible in order to achieve higher thermoelectric efficiency of devices, as the device efficiency depends on the thermoelectric figure of merit (Z^*T): $Z^*T = S^2 \sigma / \kappa \times T$ [10, 11], where S is the Seebeck coefficient, σ is the electrical conductivity, κ is the thermal conductivity and T is the temperature. Both theoretical and experimental data show that the cross-plane thermal conductivity of superlattices is much lower than that of the bulk materials [12-18].

Simkin and Mahan [19] developed an analytical approach to calculate the thermal conductivity of superlattices composed of two layers with identical thicknesses, taking into account the phonon mean free path (MFP). By taking into account the phonon MFP, a minimum superlattice thermal conductivity occurs at the crossover of the particle and wave-interference types of phonon transport.

The thermal conductivity is calculated by the following formula in d dimensions:

$$\mathrm{K}(T) = \sum_{\lambda} \int \frac{d^d k}{(2\pi)^d} \hbar \omega_\lambda(k) \left| v_z(k) \right| \ell_\lambda(k) \frac{\partial n(\omega, T)}{\partial T} \qquad (7\text{-}1).$$

Where $n(\omega,T)$ is the Bose-Einstein distribution function, λ is the band index, $\ell_\lambda(k)$ is the MFP. At high temperatures, $n \sim k_B T/\hbar\omega_\lambda(k)$, so (7-1) becomes:

$$\mathrm{K}(T) = k_B \sum_\lambda \int \frac{d^d k}{(2\pi)^d} |v_z(k)| \ell_\lambda(k) \tag{7-2}.$$

Consider two important special cases: constant relaxation time $\mathrm{K}_\tau(T)$ and constant MFP $\mathrm{K}_\ell(T)$:

$$\mathrm{K}_\tau(T) = k_B \tau \sum_\lambda \int \frac{d^d k}{(2\pi)^d} v_z(k)^2 \tag{7-3},$$

$$\mathrm{K}_\ell(T) = k_B \ell \sum_\lambda \int \frac{d^d k}{(2\pi)^d} |v_z(k)| \tag{7-4}.$$

Where (7-3) and (7-4) are related to the distribution $P(v_z)$ of phonon velocities perpendicular to the layers:

$$P(v_z) = \sum_\lambda \int \frac{d^d k}{(2\pi)^d} \delta(v_z - |v_z(k)|) \tag{7-5},$$

$$\mathrm{K}_\tau(T) = k_B \tau \int dv_z P(v_z) {v_z}^2 \tag{7-6},$$

$$\mathrm{K}_\ell(T) = k_B \ell \int dv_z P(v_z) v_z \tag{7-7}.$$

As wave interference leads to band folding, band folding leads to reduction of phonon velocities. Thus $\mathrm{K}_\tau(T)$ and $\mathrm{K}_\ell(T)$ are reduced by wave interferences. The case of constant MFP in one dimension then is reduced to a simple formula:

$$\mathrm{K}_\ell = \frac{k_B \ell}{2\pi} \sum_\lambda \int dk \left| \frac{d\omega}{dk} \right| \tag{7-8},$$

$$= \frac{k_B \ell}{2\pi} \sum_\lambda [\omega_\lambda^{\max} - \omega_\lambda^{\min}] \tag{7-9}.$$

Then use one dimension atomic chain model to illustrate above assertions, and assume all spring constants identical, and layers differ in their masses. The first layer has $N/2$ atoms with mass m_1 and the second layer has $N/2$ atoms with mass m_2.

The next step is to obtain the characteristic matrix. For example, when $N=6$, suppose that at a particular time the nth atom in the chain has a displacement u_n from its equilibrium, then the equation of motion for this atom is:

$$m\frac{d^2u_n}{dt^2}=\Lambda[(u_{n+1}-u_n)+(u_{n-1}-u_n)] \tag{7-10}.$$

Here m is the mass of the atom and Λ is the nearest-neighbor force constant. The solution then has following format:

$$u_n=A\exp[i(kx-\omega t)] \tag{7-11}.$$

Here A represents the amplitude of the motion of the nth atom, then:

$$\frac{d^2u_n}{dt^2}=-A\omega^2u_n \tag{7-12}.$$

Substitute (7-12) into (7-10):

$$\frac{Am}{\Lambda}\omega^2u_n=-u_{n-1}+2u_n-u_{n+1} \tag{7-13}.$$

Then in the case $N=6$, based on (7-13), a 6×6 characteristic matrix can be given as follows:

$$\frac{Am}{\Lambda}\omega^2\begin{bmatrix}u_1\\u_2\\u_3\\u_4\\u_5\\u_6\end{bmatrix}=\begin{bmatrix}2&-1&0&0&0&-\exp(-ikN)\\-1&2&-1&0&0&0\\0&-1&2&-1&0&0\\0&0&-\alpha&2\alpha&-\alpha&0\\0&0&0&-\alpha&2\alpha&-\alpha\\-\alpha\exp(ikN)&0&0&0&-\alpha&2\alpha\end{bmatrix}\begin{bmatrix}u_1\\u_2\\u_3\\u_4\\u_5\\u_6\end{bmatrix} \tag{7-14}.$$

So the 6×6 characteristic matrix is defined as M matrix, setting the determinant $\left\|M-\omega^2 1\right\|$ to zero gives the characteristic equation:

$$\cos(kN) = \cos(k_1 N/2)\cos(k_2 N/2) - \frac{1-\cos(k_1)\cos(k_2)}{\sin(k_1)\sin(k_2)} \times \sin(k_1 N/2)\sin(k_2 N/2) \quad \text{(7-15)}.$$

Where $\cos(k_1) = 1-\omega^2/2$, $\cos(k_2) = 1-\omega^2/(2\alpha)$ define the wave vectors (k_1, k_2) in the individual layers in dimensionless units.

Based on equation 7-15, the dispersion relation of the superlattice can be obtained. Then the thermal conductivity can be calculated by formula (7-9), which is divided by $2k_B\ell$, and in dimensionless units.

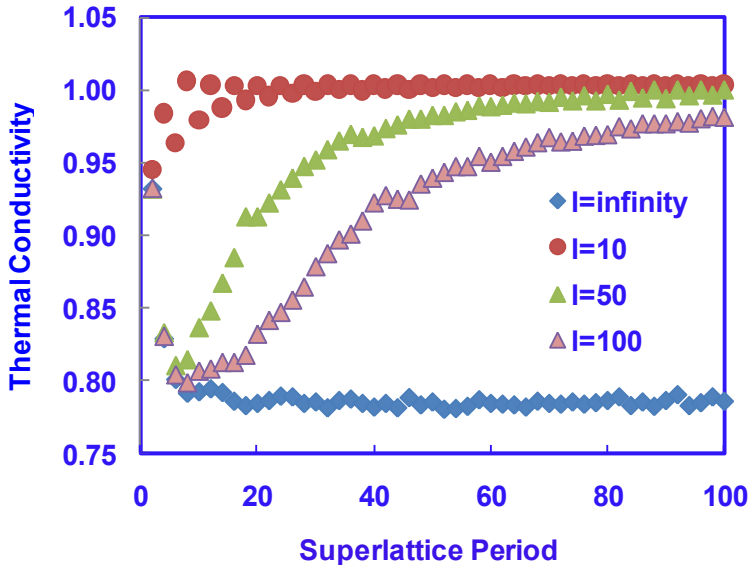

Figure 7-1: *Thermal conductivity in one dimension as a function of period thickness with different values of the phonon mean free path [19].*

However, superlattice design does not have to be composed of merely two materials with identical thicknesses [20]. By intentionally introducing some disorder into the conventional two-layer superlattice structure, the cross-plane thermal conductivity can be further reduced, which will lead to the further enhancement of the *Z*T* value of the superlattices.

7.1.2 Thermal Conductivity Calculation Based on Matrix Method

In this chapter, we present the cross-plane thermal conductivity of three-layer superlattices based on a numerical method, which is developed from lattice dynamical theory. The phonon

MFP is included into the calculation similar to the treatment in reference 19. The minimum thermal conductivity of the three-layer superlattices is approximately half of that of the corresponding conventional two-layer superlattice structure, which implies that the *Z*T* can be further enhanced by ~2-times by employing the three-layer superlattice design.

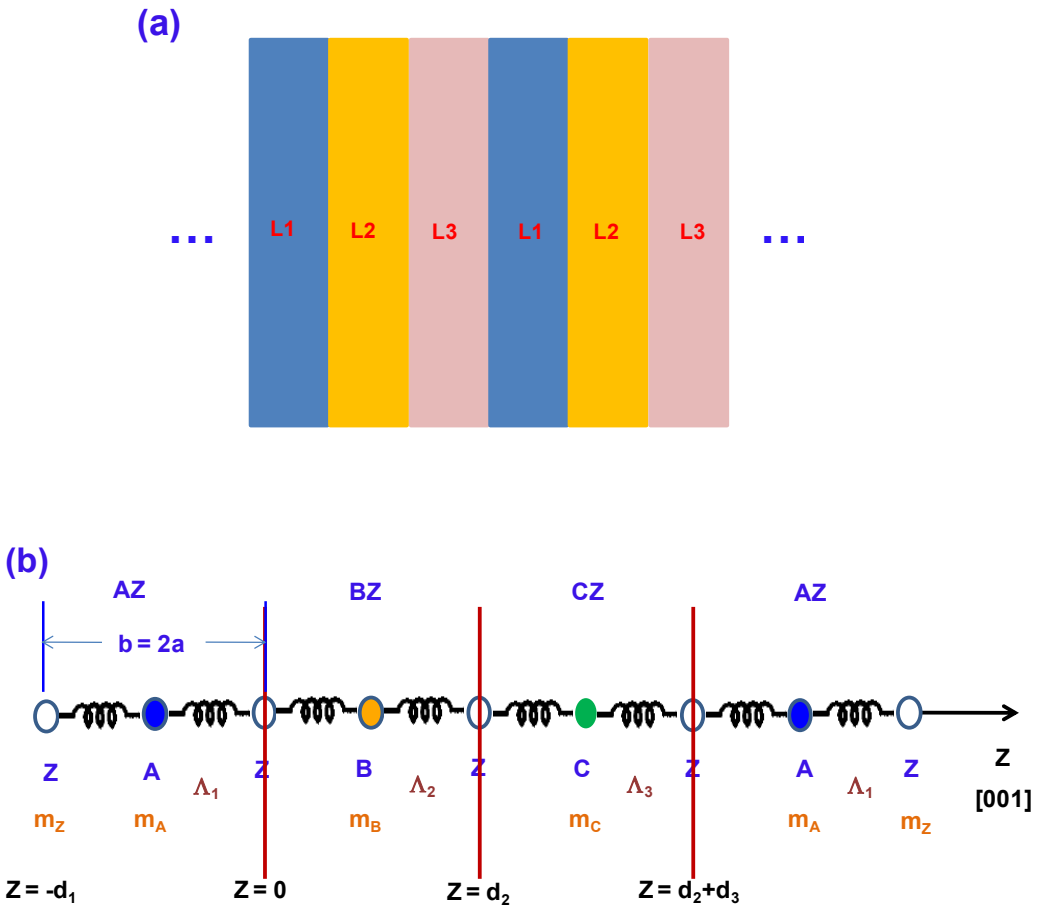

Figure 7-2: *(a) Schematics of the lattice dynamical linear chain model and (b) the three-layer superlattice structure.*

Numerical method based on lattice dynamical theory of phonons is developed to calculate the cross-plane thermal conductivity of the three-layer superlattices. The schematic of a three-layer superlattice design with L_1 / L_2 / L_3 layers is shown in figure 7-2(a). As shown in figure 7-2(a), the L_1 / L_2 / L_3 superlattice layers repeat the periodicity along [001] direction, and these layers correspond to N_1 layers of material AZ / N_2 layers of material BZ / N_3 layers of material CZ,

respectively. All the AZ, BZ, and CZ materials are assumed as zincblende materials. In the analysis here, all materials are assumed to have same lattice constant a, and the thickness of a monolayer is $b = 2a$. The schematic of the linear chain model is shown in figure 7-2(b). The thicknesses of layers AZ, BZ, and CZ are $d_1 = N_1 \cdot b$, $d_2 = N_2 \cdot b$ and $d_3 = N_3 \cdot b$, respectively. Thus, the superlattice periodicity is $d = d_1 + d_2 + d_3 = (N_1 + N_2 + N_3) \cdot b$. The parameters m_A, m_B, m_C and m_Z are the masses of the atoms A, B, C and Z respectively. The parameters u_A, u_B, u_C and u_Z are the displacements of atoms A, B, C and Z respectively.

Therefore, within layer AZ, at $z = jb$, the solutions to the equations of motion for j^{th} atom A, and the j^{th} atom Z are defined in the following form [35]:

$$u_{A\_1}(jb) = A_1 \exp\left[i(k_1 jb - \omega t)\right] \quad (7\text{-}16),$$

$$u_{Z\_1}(jb) = A_2 \exp\left[i(k_1 jb - \omega t)\right] \quad (7\text{-}17),$$

where the parameter k_1 corresponds to the wave vector in layer 1 (AZ). The parameters A_1 and A_2 represent the atomic vibration amplitudes for the atoms A and Z in the layer 1 (AZ), respectively, and the parameter ω corresponds to the frequency. Thus, the ratios of the amplitudes (γ_+ and γ_-) for atomic vibrations in the layer AZ can be defined as follow:

$$\gamma_\pm = \frac{A_2}{A_1} = \frac{\Lambda_1(1 + \exp(\pm ik_1 b))}{(2\Lambda_1 - m_Z \cdot \omega^2)} \quad (7\text{-}18),$$

where Λ_1 corresponds to the force constant of the AZ material. Similarly, the amplitude ratios in layer BZ (δ_+ and δ_-) and layer CZ (β_+ and β_-) can be obtained as follow:

$$\delta_\pm = \frac{B_2}{B_1} = \frac{\Lambda_2(1 + \exp(\pm ik_2 b))}{(2\Lambda_2 - m_Z \cdot \omega^2)} \quad (7\text{-}19),$$

$$\beta_\pm = \frac{C_2}{C_1} = \frac{\Lambda_3(1 + \exp(\pm ik_3 b))}{(2\Lambda_3 - m_Z \cdot \omega^2)} \quad (7\text{-}20),$$

where Λ_2 and Λ_3 refer to the force constants of the BZ and CZ materials, respectively. The parameters k_2 and k_3 are the wave vectors in layer 2 (BZ) and layer 3 (CZ), respectively.

The solutions for atomic vibrations in the superlattice layers can be written as follow: in layer 1 (AZ), the solutions are $u_{A\_1}(z) = (Ae^{ik_1 z} + Be^{-ik_1 z})e^{-i\omega t}$ and $u_{Z\_1}(z) = (\gamma_+ Ae^{ik_1 z} + \gamma_- Be^{-ik_1 z})e^{-i\omega t}$; in layer 2 (BZ), the solutions are $u_{B\_2}(z) = (Ce^{ik_2 z} + De^{-ik_2 z})e^{-i\omega t}$ and $u_{Z\_2}(z) = (\delta_+ Ce^{ik_2 z} + \delta_- De^{-ik_2 z})e^{-i\omega t}$; in layer 3 (CZ), the solutions are $u_{C\_3}(z) = (Ee^{ik_3 z} + Fe^{-ik_3 z})e^{-i\omega t}$ and $u_{Z\_3}(z) = (\beta_+ Ee^{ik_3 z} + \beta_- Fe^{-ik_3 z})e^{-i\omega t}$.

The solutions should satisfy the boundary conditions at the interface: (1) stress continuity $\Lambda_1 \frac{\partial u_1}{\partial z} = \Lambda_2 \frac{\partial u_2}{\partial z}$ and (2) displacement continuity $u_1 = u_2$. In addition, from the periodicity of the superlattice, the displacement continuity will require: $u(z+d) = u(z)e^{ikz}$, where k is the z component, which is along the [001] direction of the phonon vector $\vec{k}$ of the superlattice.

At interface $z = 0$, we define the parameters G and H as $G_\pm = \Lambda_1(e^{\pm ik_1 b} - 1)$ and $H_\pm = \Lambda_2(e^{\pm ik_2 b} - 1)$ to simplify the calculation. By applying the boundary conditions, the following relation can be obtained:

$$\begin{bmatrix} C \\ D \end{bmatrix} = \begin{bmatrix} \dfrac{\dfrac{\gamma_+}{\delta_-} - \dfrac{G_+}{H_-}}{\dfrac{\delta_+}{\delta_-} - \dfrac{H_+}{H_-}} & \dfrac{\dfrac{\gamma_-}{\delta_-} - \dfrac{G_-}{H_-}}{\dfrac{\delta_+}{\delta_-} - \dfrac{H_+}{H_-}} \\ \dfrac{\dfrac{\gamma_+}{\delta_+} - \dfrac{G_+}{H_+}}{\dfrac{\delta_-}{\delta_+} - \dfrac{H_-}{H_+}} & \dfrac{\dfrac{\gamma_-}{\delta_+} - \dfrac{G_-}{H_+}}{\dfrac{\delta_-}{\delta_+} - \dfrac{H_-}{H_+}} \end{bmatrix} \times \begin{bmatrix} A \\ B \end{bmatrix} \qquad \text{(7-21).}$$

The above 2×2 matrix can be written as M_1, which can be expressed as:

$$\begin{bmatrix} C \\ D \end{bmatrix} = M_1 \times \begin{bmatrix} A \\ B \end{bmatrix} \qquad \text{(7-22).}$$

Similarly, at the boundary $z = d_2$, we define the parameter I as $I_{\pm} = \Lambda_3(e^{\pm ik_3 b} - 1)$, and the following relation can be obtained:

$$\begin{bmatrix} E \\ F \end{bmatrix} = \begin{bmatrix} \left(\dfrac{\dfrac{\delta_+}{\beta_-} - \dfrac{H_+}{I_-}}{\dfrac{\beta_+}{\beta_-} - \dfrac{I_+}{I_-}} \right) \cdot e^{i(k_2 - k_3)\cdot d_2} & \left(\dfrac{\dfrac{\delta_-}{\beta_-} - \dfrac{H_-}{I_-}}{\dfrac{\beta_+}{\beta_-} - \dfrac{I_+}{I_-}} \right) \cdot e^{-i(k_2 + k_3)\cdot d_2} \\ \left(\dfrac{\dfrac{\delta_+}{\beta_+} - \dfrac{H_+}{I_+}}{\dfrac{\beta_-}{\beta_+} - \dfrac{I_-}{I_+}} \right) \cdot e^{i(k_2 + k_3)\cdot d_2} & \left(\dfrac{\dfrac{\delta_-}{\beta_+} - \dfrac{H_-}{I_+}}{\dfrac{\beta_-}{\beta_+} - \dfrac{I_-}{I_+}} \right) \cdot e^{i(k_3 - k_2)\cdot d_2} \end{bmatrix} \times \begin{bmatrix} C \\ D \end{bmatrix} \quad (7\text{-}23).$$

The above 2×2 matrix can be defined as M_2, which can be rewritten as:

$$\begin{bmatrix} E \\ F \end{bmatrix} = M_2 \times \begin{bmatrix} C \\ D \end{bmatrix} \quad (7\text{-}24).$$

By combining equations (6-22) and (6-24), the following relation can be obtained:

$$\begin{bmatrix} E \\ F \end{bmatrix} = M_2 \cdot M_1 \times \begin{bmatrix} A \\ B \end{bmatrix} \quad (7\text{-}25).$$

At interface $z = d_2 + d_3$, the following relation can be obtained:

$$\begin{bmatrix} A \\ B \end{bmatrix} = \begin{bmatrix} \left(\dfrac{\dfrac{\beta_+}{\gamma_-} - \dfrac{I_+}{G_-}}{\dfrac{\gamma_+}{\gamma_-} - \dfrac{G_+}{G_-}} \right) \cdot e^{i(k_1 d_1 + k_3(d_2+d_3))} \cdot e^{-ikd} & \left(\dfrac{\dfrac{\beta_-}{\gamma_-} - \dfrac{I_-}{G_-}}{\dfrac{\gamma_+}{\gamma_-} - \dfrac{G_+}{G_-}} \right) \cdot e^{i(k_1 d_1 - k_3(d_2+d_3))} \cdot e^{-ikd} \\ \left(\dfrac{\dfrac{\beta_+}{\gamma_+} - \dfrac{I_+}{G_+}}{\dfrac{\gamma_-}{\gamma_+} - \dfrac{G_-}{G_+}} \right) \cdot e^{i(k_3(d_2+d_3) - k_1 d_1)} \cdot e^{-ikd} & \left(\dfrac{\dfrac{\beta_-}{\gamma_+} - \dfrac{I_-}{G_+}}{\dfrac{\gamma_-}{\gamma_+} - \dfrac{G_-}{G_+}} \right) \cdot e^{-i(k_1 d_1 + k_3(d_2+d_3))} \cdot e^{-ikd} \end{bmatrix} \times \begin{bmatrix} E \\ F \end{bmatrix}$$

(7-26).

The above 2×2 matrix can be defined as M_3, the relation can be expressed as:

$$\begin{bmatrix} E \\ F \end{bmatrix} = M_3^{-1} \times \begin{bmatrix} A \\ B \end{bmatrix} \quad (7\text{-}27).$$

By subtracting equation (7-27) from equation (7-25), the following relation can be obtained:

$$\begin{bmatrix} 0 \\ 0 \end{bmatrix} = \left[M_2 \cdot M_1 - M_3^{-1} \right] \times \begin{bmatrix} A \\ B \end{bmatrix} \quad (7\text{-}28).$$

For non-trivial solutions of the equation (6-28), the following expression must be satisfied:

$$\left| M_2 \cdot M_1 - M_3^{-1} \right| = 0 \quad (7\text{-}29).$$

The equation (7-29) gives the dispersion relation of the superlattice. Assume the masses of unit cell in layer 1, 2 and 3 are m_1, m_2 and m_3, respectively, where $m_1 = m_A + m_Z$, $m_2 = m_B + m_Z$ and $m_3 = m_C + m_Z$. The mass ratios α_1 and α_2 are defined as $\alpha_1 = m_1 / m_2$, $\alpha_2 = m_1 / m_3$. To be more specific, the equation (14) contains the relationship between k and k_1, k_2, k_3. Note that the k_1, k_2 and k_3 are defined the same way in the analytical model as follow: $\cos(k_1) = 1 - \omega^2 / 2$, $\cos(k_2) = 1 - \omega^2 / (2\alpha_1)$, and $\cos(k_3) = 1 - \omega^2 / (2\alpha_2)$. Based on the superlattice dispersion, the thermal conductivity can be calculated as follow:

$$\mathrm{K}_\ell = \frac{k_B \ell}{2\pi} \sum_\lambda \int dk \left| \frac{d\omega}{dk} \right| \quad (7\text{-}30).$$

In this work, we assume $\Lambda_1 = \Lambda_2$ for the simplicity of the calculation. For the case of calculation of the thermal conductivity K_l in three dimensions, the wave vectors k_1, k_2 and k_3 are expressed as:

$$\cos(k_1) = 3 - \cos(q_x) - \cos(q_y) - \omega^2 / 2 \quad (7\text{-}31),$$

$$\cos(k_2) = 3 - \cos(q_x) - \cos(q_y) - \omega^2 / (2\alpha_1) \quad (7\text{-}32),$$

$$\cos(k_3) = 3 - \cos(q_x) - \cos(q_y) - \omega^2 / (2\alpha_2) \quad (7\text{-}33),$$

which follow the same formulation in the analytical model [19], where the q_x, q_y are the wave vectors within the planes for the three-dimension integration.

7.2 Thermal Conductivity Calculation Characteristics Based on Matrix Method

Figure 7-3(a) shows the cross-plane phonon dispersions in extended zone representation for (a) two-layer superlattice with α = 2, and (b) three-layer superlattice with α_1 = 2 and α_2 = 0.5. The superlattice periodicity (*N*) equals to 6 in both cases. In the extended zone representation, it is clearer to observe the phonon frequency gaps that appear at the center and edge of the Brillouin zone. In both cases, the phonon bands are flattened for higher frequency regimes, which indicate that high-frequency phonons contribute little to the superlattice thermal conductivity. A low-frequency cutoff (ω_{cutoff}) is suggested in the spectrum of phonons that transport heat [15]. For phonons with frequencies lower than the ω_{cutoff}, which are the main heat-conducting phonons, the transmission is inhibited. However, for phonons with frequencies higher than the ω_{cutoff}, the transmission is allowed in the superlattices. For the two-layer superlattices, the ω_{cutoff} is ~ 2.20 from the dispersion curve, which is consistent with results in reference 19. For the three-layer superlattices, the ω_{cutoff} is reduced to ~1.57, which represents effective deduction of the cutoff frequency by the use of the three-layer superlattice design.

Figure 7-3(b) and 7-3(c) show the comparison of the thermal conductivities for conventional two-layer superlattice and three-layer superlattice structures as a function of superlattice period (*N*) in one-dimension and three-dimension, respectively. The results are normalized in dimensionless units similar to the approach in reference 19. The phonon MFP (*l*) is given in terms of lattice periods, which equals to 50 in both cases. In order to verify the accuracy and validity of the numerical model based on the matrix method developed in this work, the calculation results of the two-layer superlattice structure are compared to the analytical method that developed by Simkin and Mahan [19], which shows identical results from both methods and confirms the accuracy of the numerical model.

For the three-layer structure, the ω_{cutoff} is lower than that of the two-layer structure, which corresponds to less low-frequency heat-conducting phonons and reduced thermal conductivity in the three-layer superlattice. As shown in figure 7-3(b), the calculation results in 1D show that the minimum thermal conductivity of three-layer superlattice is reduced to ~0.6 times of that of the two-layer structure. For more practical and representative comparison, the calculation results in 3D (figure 7-3(c)) show that the minimum thermal conductivity obtained from the three-layer

superlattice is reduced to ~0.25 times of that of the conventional two-layer structure. Thus, from the 3D calculation results comparison, the *Z*T* values from the use of three-layer structure can be potentially enhanced by ~3-4 times compared to the conventional two-layer structure.

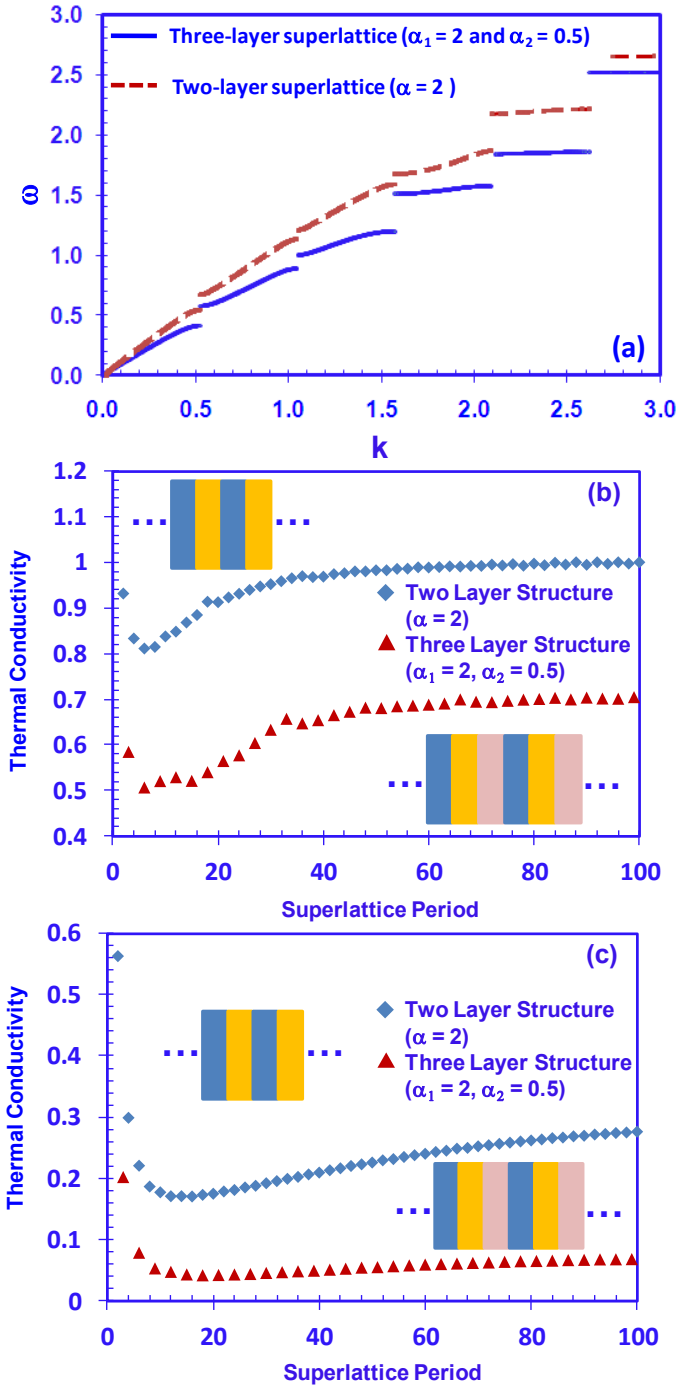

Figure 7-3: *(a) The cross-plane phonon dispersion relation of two-layer superlattices and three-layer superlattices in extended zone representation. Comparison of cross-plane dimensionless superlattice thermal conductivity calculation as a function of superlattice period for conventional two-layer structure with three-layer structure (b) in one dimension, and (c) in three dimensions.*

Figures 7-4(a) and 7-4(b) show the thermal conductivities for three-layer superlattice as a function of period thickness for various phonon MFPs (l = 10, 50, 100, and infinity) in 1D and 3D, respectively. The mass ratios are chosen as α_1 = 2, and α_2 = 0.5 for the three-layer structure. For small period regime, the phonons are considered incoherent and treated as particles. The phonons frequency gaps exist for all the small period values, thus the thermal conductivity will decrease with increasing period. However, for large period regime, the phonons are considered coherent and treated as wave. Part of the phonon low-frequency gaps will vanish when the period becomes larger, which leads to the increase of thermal conductivity in large period regime. The combination of the particle-like and wave-like models will predict the minimum superlattice thermal conductivity [19, 22-24].

As shown in both cases of 1D calculation (figure 7-4(a)) and 3D calculation (figure 7-4(b)), when the MFP is infinity, the thermal conductivity first falls with the period, and then it will remain as a constant. For the case with MFP of 10 for both 1D and 3D calculations, the thermal conductivity increases in small period values, which then shows no dependency with the period. For the case with phonon MFP of 50 or 100 for both 1D and 3D calculations, the thermal conductivity first decreases with the period and reaches minimum, and then it will start to increase for larger period. The minimum superlattice thermal conductivity occurs when the period is in the range from 10 to 30, which is shorter than the phonon MFP, as observed in for both 1D and 3D calculations.

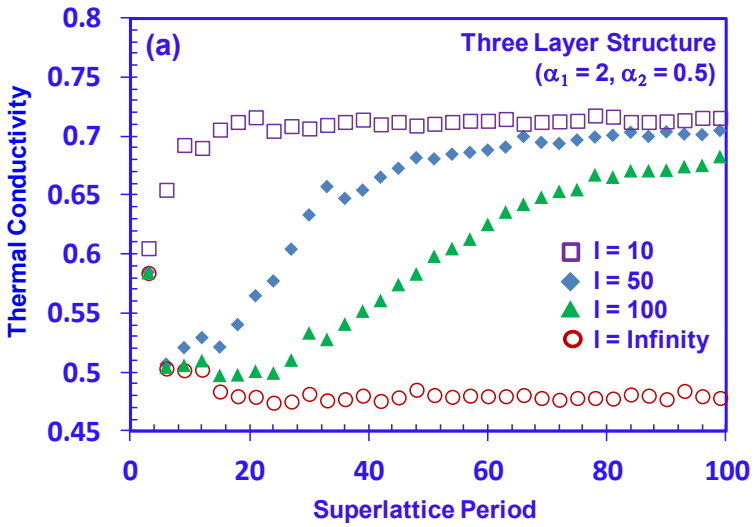

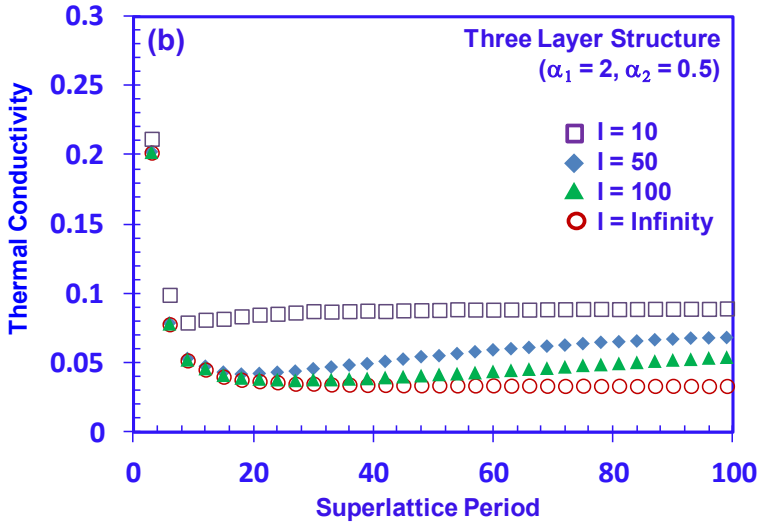

Figure 7-4: *Cross-plane dimensionless superlattice thermal conductivity as a function of superlattice period of three-layer structure with different values of phonon MFPs (a) calculated in one dimension, and (b) calculated in three dimensions.*

Figures 7-5(a) and 7-5(b) show the three-layer superlattice thermal conductivities with different mass ratios (case #1: α_1 = 2 and α_2 = 1.5; case #2: α_1 = 2 and α_2 = 0.5; case #3: α_1 = 3 and α_2 = 0.5) calculated in 1D and 3D, respectively. The layer thicknesses are kept the same for each layer. As shown in both figure 7-5(a) and figure 7-5(b), the thermal conductivities for both cases #2 and #3 are much lower than that of case #1. This finding indicates that the larger difference between the mass ratios α_1 and α_2 leads to further reduction in thermal conductivity in the three-layer superlattice. For more accurate comparison in 3D integration, figure 7-5(b) shows that the minimum thermal conductivity of the case #3 (α_1 = 3 and α_2 = 0.5) is ~7 times smaller than that of the case #1 (α_1 = 2 and α_2 = 1.5).

Therefore, engineering the choice of the materials in the three layer design can further reduce the superlattice thermal conductivity. The further reduction by employing layers with more different mass ratios can be attributed to the Anderson localization of the phonons [15, 25]. By introducing more nonlinearity into the superlattice structure, the localization of low-frequency phonons is more severe, which results in the further reduction of thermal conductivity.

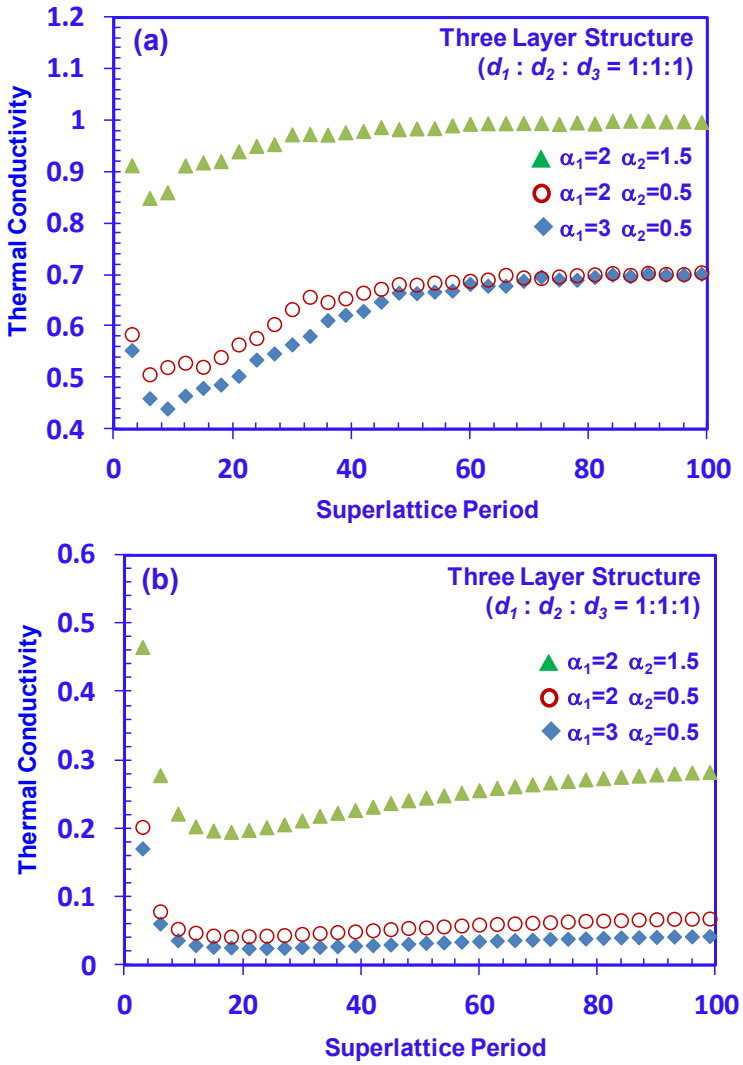

Figure 7-5: *Cross-plane dimensionless superlattice thermal conductivity as a function of superlattice period of three-layer structure with different values of mass ratios (a) calculated in one dimension, and (b) calculated in three dimensions.*

Figures 7-6(a) and 7-6(b) show three-layer superlattice thermal conductivities with different thicknesses for each layer (case #1: d_1:d_2:d_3 = 1:1:1; case #2: d_1:d_2:d_3 = 3:2:1; case #3: d_1:d_2:d_3 = 4:2:1) calculated in 1D and 3D, respectively. The mass ratios are kept the same for the three cases, which are chosen as α_1 = 2, and α_2 = 0.5. For both calculations in 1D and 3D, the curves show that the minimum thermal conductivities vary slightly for the three different cases with different layer thicknesses. However, for large period regime, the thermal conductivities are relatively independent of different layer thicknesses. Therefore, the layer thicknesses variation of the three-layer superlattices contributes minimally to the heat-conducting phonons localization.

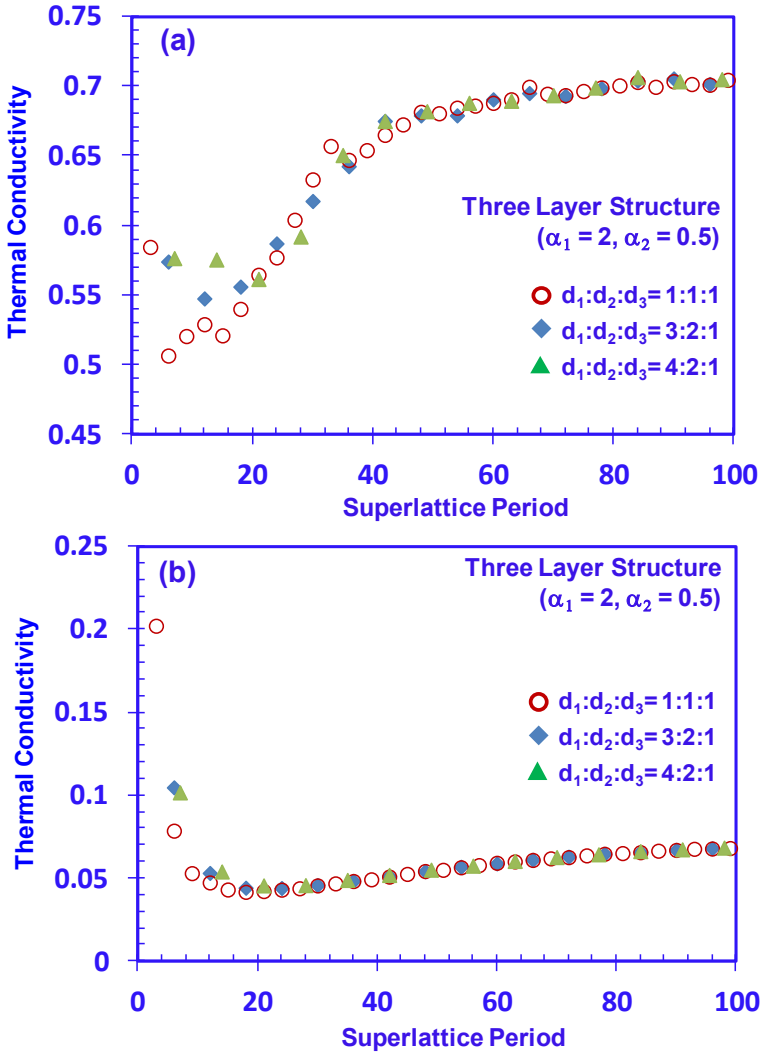

Figure 7-6: *Cross-plane dimensionless superlattice thermal conductivity as a function of superlattice period of three-layer structure with different values of layer thicknesses (a) calculated in one dimension, and (b) calculated in three dimensions.*

7.3 Summary

In summary, the use of three-layer superlattices structure results in further reduction of cross-plane thermal conductivity. The numerical method is developed to calculate the thermal conductivity of the three-layer superlattices with varying phonon MFPs, mass ratios and layer thicknesses. By using the three-layer superlattice, low-frequency phonons which mainly conduct the heat are reduced compared to the two-layer superlattice. At the same time, the localization of those low-frequency phonons is enhanced by using the three-layer superlattice. Both effects lead

to the reduction of the superlattice thermal conductivity. The minimum thermal conductivity of three-layer structure superlattice is approximately 25% of that the conventional two-layer superlattice, which leads to further increase in Z^*T by up to ~4-times with the three-layer superlattice.

References for Chapter 7

[1] G. Chen, M.S. Dresselhaus, G. Dresselhaus, J.-P. Fleurial, and T. Caillat, Int. Mater. Rev., **48**, 45 (2003).

[2] H. Tong, J. Zhang, G. Liu, J. A. Herbsommer, G. S. Huang, and N. Tansu, Appl. Phys. Lett., **97**, 112105 (2010).

[3] J. Zhang, H. Tong, G. Y. Liu, J. A. Herbsommer, G. S. Huang, and N. Tansu, J. Appl. Phys., 109, 053706 (2011).

[4] R. Venkatasubramanian, E. Siivola, T. Colptiis, and B. O'Quinn, Nature (London) **413**, 597 (2001).

[5] T. C. Harman, P. J. Taylor, M. P. Walsh, B. E. LaForge, Science **297**, 2229 (2002).

[6] L. D. Hicks and M. S. Dresselhaus, Phys. Rev. B **47**, 12727 (1993).

[7] G. D. Mahan and H. B. Lyon, J. Appl. Phys., **76**, 1899 (1994).

[8] J. O. Sofo and G. D. Mahan, Appl. Phys. Lett., **65**, 2690 (1994).

[9] G. Chen and A. Shakouri, J. Heat Transfer, J. Heat Transfer, **124 (2)**, 242 (2002).

[10] G. D. Mahan, and J. O. Sofo, Proc. Natl. Acad. Sci. USA, **93**, 7436 (1996).

[11] H. J. Goldsmid, *Thermoelectric Refrigeration* (Plenum, New York, 1964).

[12] G. Chen, Phys. Rev. B **57**, 14958 (1998).

[13] T. Yao, Appl. Phys. Lett., **51**, 1798 (1987).

[14] P. Hyldgaard and G. D. Mahan, Phys. Rev. B **56**, 10 754 (1997).

[15] R. Venkatasubramanian, Phys. Rev. B **61**, 3091 (2000).

[16] S. -M. Lee, D. G. Cahill, and R. Venkatasubramanian, Appl. Phys. Lett. **70**, 2957 (1997).

[17] W. S. Capinski, H. J. Maris, T. Ruf, M. Cardona, K. Ploog, and D. S. Katzer, Phys. Rev. B **59**, 8105 (1999).

[18] S. T. Huxtable, A. R. Abramson, C. L. Tien, A. Majumdar, C. LaBounty, X. Fan, G. Zeng, J. E. Bowers, A. Shakouri, and E. T. Croke, Appl. Phys. Lett. **80**, 1737 (2002).

[19] M. V. Simkin and G. D. Mahan, Phys. Rev. Lett., **84**, 927 (2000).

[20] G. D. Mahan, in *Thermal Conductivity, Theory, Properties and Applications*, edited by T. M. Tritt (Kluwer Academic / Plenum Publishers, 2004), p. 153.

[21] G.P. Srivastava, *The Physics of Phonons*, (Adam Hilger, Bristol, Philadelphia and New York, 1990), p. 267.

[22] B. Yang and G. Chen, Phys. Rev. B **67**, 195311 (2003).

[23] G. Chen, *Nanoscale energy transport and conversion*, (Oxford University Press, 2005), p. 215.

[24] G. D. Mahan, *Condensed Matter in a Nutshell*, (Princeton University Press, 2010), p. 365.

[25] M. J. McKenna, R. L. Stanley, and J. D. Maynard, Phys. Rev. Lett., **69**, 1807 (1992).

Chapter 8: Numerical Simulation and Material Parameters for Optical Properties of III-Nitride Semiconductors

8.1 Band Structure and Wave Function Calculations Based on the 6-Band *k·p* Method

The calculations of the semiconductor band structures including the energy bands and the corresponding wavefunctions are very important in order to provide thorough understanding and useful guidance for optical and photonic devices based on semiconductors. As direct band gap semiconductors are mostly used for optical and photonic devices, the physical understanding near the band edges are of great interest. In this section, the 6-band ***k·p*** method will be introduced with details, which is of great importance for the conduction and valence band structures near the band edges. [3]

8.1.1 The 6×6 *k·p* Hamiltonian Matrix with Spin-Orbit Coupling

The calculations of the band structures and electron and hole wave functions are based on the 6-band ***k·p*** formalism for wurtzite semiconductors, which takes into account the valence band mixing, strain effect, spontaneous and piezoelectric polarization, as well as the carrier screening effect. The spin-orbit interaction is taken into account in the 6-band ***k·p*** method.

For the self-consistent 6-band ***k·p*** formalism, the six bands correspond to the heavy hole, the light hole, and the crystal-field split-off bands, which have double degeneracy with their spin counterparts. In the calculation, the electron energy bands are assumed to be parabolic. The hole energy bands are computed via the 6×6 diagonalized Hamiltonian matrix.

The Kane's model was employed to obtain important physical parameters for direct bandgap semiconductors such as the band-edge energies and optical momentum-matrix elements [3, 4]. The Kane's model takes into account the spin-orbit interaction. The conduction band, the heavy hole, the light hole, and the crystal-field split-off bands are considered, which have double degeneracy with their spin counterparts.

Consider the Schrodinger equation for the periodic part $u_{n\mathbf{k}}(\mathbf{r})$ of the Bloch function and the energy $E_n(\mathbf{k})$ near the band edge $\mathbf{k}_0 = 0$ can be written as:

$$Hu_{nk}(r) = (H_0 + \frac{\hbar^2 k^2}{2m_0} + \frac{\hbar}{m_0} k \cdot p + H_{SO}) u_{nk}(r)$$

$$= E_n(k) u_{nk}(r). \tag{8-1}$$

The Hamiltonian near $\mathbf{k}_0 = 0$ is:

$$H = H_0 + \frac{\hbar^2 k^2}{2m_0} + \frac{\hbar}{m_0} k \cdot p + H_{SO}, \tag{8-2}$$

where $H_0 = \frac{p^2}{2m_0} + V(r)$, (8-3)

$$H_{SO} = \frac{\hbar}{4m_0^2 c^2} \nabla V \times p \cdot \sigma. \tag{8-4}$$

The term H_{SO} accounts for the spin-orbit interaction, and σ is the Pauli spin matrix with components:

$$\sigma_x = \begin{bmatrix} 0 & 1 \\ 1 & 0 \end{bmatrix} \qquad \sigma_y = \begin{bmatrix} 0 & -i \\ i & 0 \end{bmatrix} \qquad \sigma_z = \begin{bmatrix} 1 & 0 \\ 0 & -1 \end{bmatrix}, \tag{8-5}$$

when operating with spins,

$$\uparrow \equiv \begin{bmatrix} 1 \\ 0 \end{bmatrix} \qquad \downarrow \equiv \begin{bmatrix} 0 \\ 1 \end{bmatrix}. \tag{8-6}$$

Thus, the matrix product by (8-5) and (8-6) is:

$$\sigma_x \uparrow = \downarrow \qquad \sigma_y \uparrow = i \downarrow \qquad \sigma_z \uparrow = \uparrow$$

$$\sigma_x \downarrow = \uparrow \qquad \sigma_y \downarrow = i \uparrow \qquad \sigma_z \downarrow = \downarrow. \tag{8-7}$$

The set of basis band edge functions $u_{n\mathbf{0}}(\mathbf{r})$ are:

for conduction band: $\left| iS \uparrow \right\rangle$, $\left| iS \downarrow \right\rangle$,

for valence band: $u_1 = \left| -\frac{(X + iY)}{\sqrt{2}} \uparrow \right\rangle$, $u_2 = \left| \frac{(X - iY)}{\sqrt{2}} \uparrow \right\rangle$, $u_3 = \left| Z \uparrow \right\rangle$,

$$u_4 = \left| \frac{(X - iY)}{\sqrt{2}} \downarrow \right\rangle,\ u_5 = \left| -\frac{(X + iY)}{\sqrt{2}} \downarrow \right\rangle,\ u_6 = \left| Z \downarrow \right\rangle. \tag{8-8}$$

The 8×8 Hamiltonian matrix can be written as:

$$H_{8\times 8} = \frac{\hbar^2 k^2}{2m_0} + \begin{bmatrix} E_c & -\frac{k+P_2}{\sqrt{2}} & \frac{k-P_2}{\sqrt{2}} & k_z P_1 & 0 & 0 & 0 & 0 \\ -\frac{k-P_2}{\sqrt{2}} & E_v + \Delta_1 + \Delta_2 & 0 & 0 & 0 & 0 & 0 & 0 \\ \frac{k+P_2}{\sqrt{2}} & 0 & E_v + \Delta_1 - \Delta_2 & 0 & 0 & 0 & 0 & \sqrt{2}\Delta_3 \\ k_z P_1 & 0 & 0 & E_v & 0 & 0 & \sqrt{2}\Delta_3 & 0 \\ 0 & 0 & 0 & 0 & E_c & \frac{k-P_2}{\sqrt{2}} & -\frac{k+P_2}{\sqrt{2}} & k_z P_1 \\ 0 & 0 & 0 & 0 & \frac{k+P_2}{\sqrt{2}} & E_v + \Delta_1 + \Delta_2 & 0 & 0 \\ 0 & 0 & 0 & \sqrt{2}\Delta_3 & -\frac{k-P_2}{\sqrt{2}} & 0 & E_v + \Delta_1 - \Delta_2 & 0 \\ 0 & 0 & \sqrt{2}\Delta_3 & 0 & k_z P_1 & 0 & 0 & E_v \end{bmatrix}$$

(8-9)

where $k_{\pm} = k_x \pm i k_y$ (8-10)

and the definitions for the energies are:

$$\langle S|H_0|S\rangle = E_c\ ,$$

$$\langle X|H_0|X\rangle = \langle Y|H_0|Y\rangle = E_v + \Delta_1\ ,$$

$$\langle Z|H_0|Z\rangle = E_v\ ,$$

$$\langle X|H_{SZ}|Y\rangle = -i\Delta_2\ ,$$

$$\langle Y|H_{sx}|Z\rangle = \langle Z|H_{SY}|X\rangle = -i\Delta_3\ , \tag{8-11}$$

the two Kane's parameters P_1 and P_2, which are related to the interband momentum matrix elements, are defined as:

$$\left\langle iS\left|\frac{\hbar}{i}\frac{\partial}{\partial z}\right|Z\right\rangle = \frac{m_0}{\hbar}P_1\ ,$$

$$\left\langle iS\left|\frac{\hbar}{i}\frac{\partial}{\partial x}\right|X\right\rangle = \left\langle iS\left|\frac{\hbar}{i}\frac{\partial}{\partial y}\right|Y\right\rangle = \frac{m_0}{\hbar}P_2 \ . \tag{8-12}$$

For wurtzite semiconductor crystals, the three components of the **k** vector are considered. The sixfold symmetry on the x-y plane was used for the derivations of the optical matrix element.

At the zone center (k_x = k_y = k_z =0), the band edge energies with corresponding basis functions can be obtained from the eigenvalues and eigenvectors from the Hamiltonian in (8-9):

for conduction band: E_c, $\left|iS\uparrow\right\rangle$, $\left|iS\downarrow\right\rangle$,

for valence bands: $E_1 = E_v + \Delta_1 + \Delta_2$, u_1, u_4,

$$E_2 = E_v + \frac{\Delta_1 - \Delta_2}{2} + \sqrt{(\frac{\Delta_1 - \Delta_2}{2})^2 + 2\Delta_3^2}\ ,\ au_2 + bu_6\ ,\ bu_3 + au_5\ ,$$

$$E_3 = E_v + \frac{\Delta_1 - \Delta_2}{2} - \sqrt{(\frac{\Delta_1 - \Delta_2}{2})^2 + 2\Delta_3^2}\ ,bu_2 - au_6\ ,\ -au_3 + bu_5\ ,$$

where $a = \dfrac{E_2}{\sqrt{E_2^2 + 2\Delta_3^2}}$, $b = \dfrac{\sqrt{2}\Delta_3}{\sqrt{E_2^2 + 2\Delta_3^2}}$. (8-13)

The spin-orbit interaction leads to energy bands splitting, as illustrated in figure 8-1.

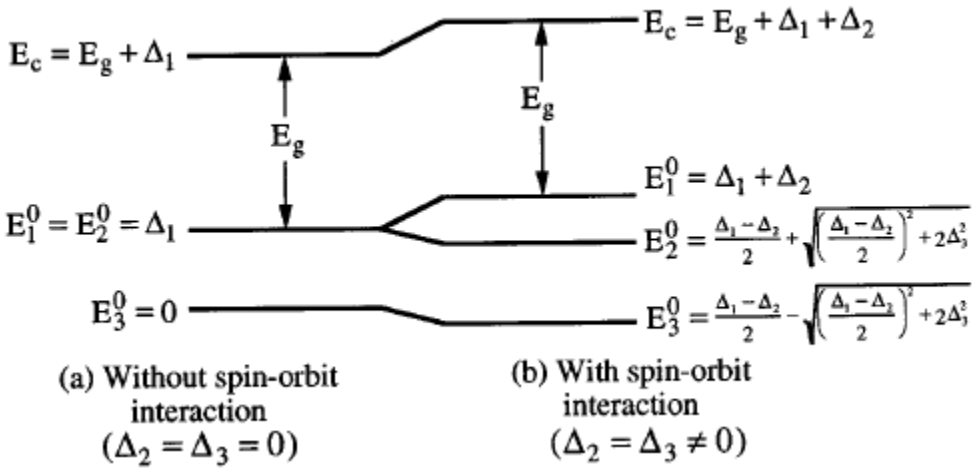

Figure 8-1: *The comparison of band edge energies (a) without spin-orbit interaction, and (b) with spin-orbit interaction. [4]*

The Lowdin's perturbation method provides the Hamiltonian to the second order in the ***k·p*** contributions, which was employed to treat the coupling of the degenerate valence bands. Then, the Hamiltonian was written as:

$$H = H_0 + \frac{\hbar^2 k^2}{2m_0} + \frac{\hbar}{m_0} k \cdot p + H_{SO} + H', \tag{8-14}$$

where $H' = \frac{\hbar}{m_0} k \cdot \Pi$, $\Pi = p + \frac{\hbar}{4m_0 c^2} \sigma \times \nabla V$. (8-15)

Therefore, the 6×6 Hamiltonian matrix for the valence bands can be obtained as the sum of a band edge contribution and a ***k***-dependent contribution:

$$H_{6\times6,jj'}(k) = H_{6\times6,jj'}(k=0) + D_{jj'}, \tag{8-16}$$

where the ***k***-dependent matrix is: $D_{jj'} = \sum_{\alpha,\beta} D_{jj'}^{\alpha\beta} \kappa_\alpha \kappa_\beta$,

$$D_{jj'}^{\alpha\beta} = \frac{\hbar^2}{2m_0}\left[\delta_{jj'}\delta_{\alpha\beta} + \sum_{\gamma}^{B} \frac{p_{j\gamma}^{\alpha} p_{\gamma j'}^{\beta} + p_{j\gamma}^{\beta} p_{\gamma j'}^{\alpha}}{m_0 (E_0 - E_\gamma)}\right]. \tag{8-17}$$

Thus, the band edge Hamiltonian matrix obtained from the Kane's model can be written as (8-18):

$$H_{6\times6}(k=0) = \begin{bmatrix} E_v + \Delta_1 + \Delta_2 & 0 & 0 & 0 & 0 & 0 \\ 0 & E_v + \Delta_1 - \Delta_2 & 0 & 0 & 0 & \sqrt{2}\Delta_3 \\ 0 & 0 & E_v & 0 & \sqrt{2}\Delta_3 & 0 \\ 0 & 0 & 0 & E_v + \Delta_1 + \Delta_2 & 0 & 0 \\ 0 & 0 & \sqrt{2}\Delta_3 & 0 & E_v + \Delta_1 - \Delta_2 & 0 \\ 0 & \sqrt{2}\Delta_3 & 0 & 0 & 0 & E_v \end{bmatrix}.$$

Then, the D matrix can be obtained by the Luttinger-Kohn model, which can be written as:

$$D_{6\times6} = \begin{bmatrix} D_{11} & D_{21}^* & -D_{23}^* & & & \\ D_{21} & D_{11} & D_{23} & & 0 & \\ -D_{23} & D_{23}^* & D_{ZZ} & & & \\ & & & D_{11} & D_{21} & D_{23} \\ & 0 & & D_{21}^* & D_{11} & -D_{23}^* \\ & & & D_{23}^* & -D_{23} & D_{ZZ} \end{bmatrix}, \tag{8-19}$$

where $D_{11} = (\frac{L_1 + M_1}{2})(k_x^2 + k_y^2) + M_2 k_z^2$,

$$D_{zz} = M_3(k_x^2 + k_y^2) + L_2 k_z^2,$$

$$D_{21} = -\frac{1}{2}\left[(L_1 - M_1)(k_x^2 - k_y^2) + 2iN_1 k_x k_y\right] = -\frac{1}{2}N_1(k_x + ik_y)^2,$$

$$D_{23} = \frac{1}{\sqrt{2}}N_2(k_x + ik_y)k_z,$$

$$L_1 - M_1 = N_1. \tag{8-20}$$

Therefore, the full Hamiltonian $H_{6\times6,jj'}(k) = H_{6\times6,jj'}(k=0) + D_{jj'}$ can be obtained:

$$H = \begin{bmatrix} F & -K^* & -H^* & 0 & 0 & 0 \\ -K & G & H & 0 & 0 & \Delta \\ -H & H^* & \lambda & 0 & \Delta & 0 \\ 0 & 0 & 0 & F & -K & H \\ 0 & 0 & \Delta & -K^* & G & -H^* \\ 0 & \Delta & 0 & H^* & -H & \lambda \end{bmatrix} \begin{matrix} |u_1\rangle \\ |u_2\rangle \\ |u_3\rangle \\ |u_4\rangle \\ |u_5\rangle \\ |u_6\rangle \end{matrix}. \tag{8-21}$$

where $F = \Delta_1 + \Delta_2 + \lambda + \theta$,

$$G = \Delta_1 - \Delta_2 + \lambda + \theta,$$

$$\lambda = \frac{\hbar^2}{2m_0}\left[A_1 k_z^2 + A_2(k_x^2 + k_y^2)\right],$$

$$\theta = \frac{\hbar^2}{2m_0}\left[A_3 k_z^2 + A_4(k_x^2 + k_y^2)\right],$$

$$K = \frac{\hbar^2}{2m_0}A_5(k_x + ik_y)^2,$$

$$H = \frac{\hbar^2}{2m_0}A_6(k_x + ik_y)k_z,$$

$$\Delta = \sqrt{2}\Delta_3. \tag{8-22}$$

8.1.2 The Incorporation of Strain Effect and Polarization Fields

The strained-layer superlattices or quantum wells (QWs) are very important in order to engineer the semiconductor material properties such as lattice constant, band gap, and

perpendicular transport by the use of ternary strained-layer superlattices or QWs, which lead to application such as strained QW laser diodes. [3, 4]

For a strained-layer wurtzite crystalline semiconductor material grown pseudomorphically along the (0001) (z axis) direction, the strain tensor can be obtained as:

$$\varepsilon_{xx} = \varepsilon_{yy} = \frac{a_0 - a}{a},$$

$$\varepsilon_{zz} = -\frac{2C_{13}}{C_{33}}\varepsilon_{xx},$$

$$\varepsilon_{xy} = \varepsilon_{yz} = \varepsilon_{zx} = 0, \tag{8-23}$$

where a_0 and a are the lattice constants of the substrate material and the layer material, C_{13} and C_{33} are the elastic stiffness constants.

There are two types of strain effects, namely, tensile strain and compressive strain, as illustrated in figure 7-2(a) and 7-2(b).

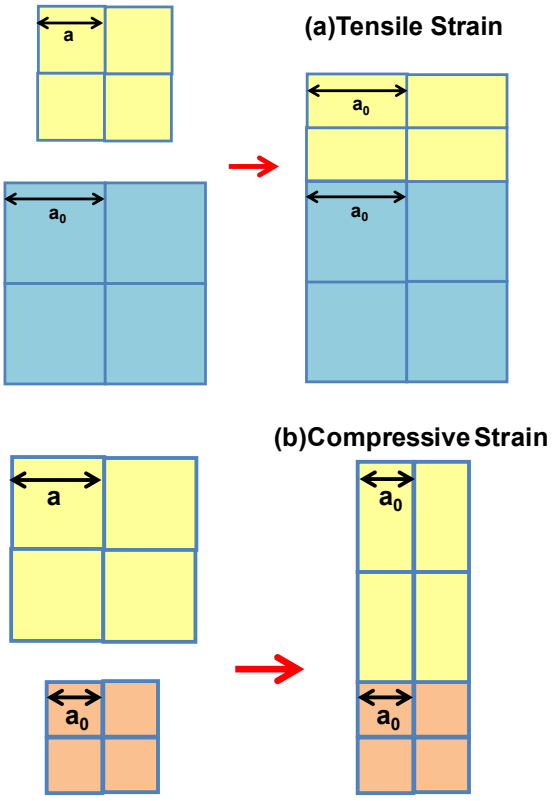

Figure 8-2: *Illustration of (a) tensile strain, and (b) compressive strain.*

Thus, the strain effect should be included to the total Hamiltonian obtained in 8.1.1. Besides, the 6×6 Hamiltonian matrix can be block diagonalized with the final expression as following:

$$H_{6\times6}=\begin{bmatrix} F & K_t & -iH_t & 0 & 0 & 0 \\ K_t & G & \Delta-iH_t & 0 & 0 & 0 \\ iH_t & \Delta+iH_t & \lambda & 0 & 0 & 0 \\ 0 & 0 & 0 & F & K_t & iH_t \\ 0 & 0 & 0 & K_t & G & \Delta+iH_t \\ 0 & 0 & 0 & -iH_t & \Delta-iH_t & \lambda \end{bmatrix}, \tag{8-24}$$

where

$$F=\Delta_1+\Delta_2+\lambda+\theta,$$

$$G=\Delta_1-\Delta_2+\lambda+\theta,$$

$$\lambda=\frac{\hbar^2}{2m_0}\left[A_1k_z^2+A_2k_t^2\right]+D_1\varepsilon_{zz}+D_2(\varepsilon_{xx}+\varepsilon_{yy}),$$

$$\theta=\frac{\hbar^2}{2m_0}\left[A_3k_z^2+A_4k_t^2\right]+D_3\varepsilon_{zz}+D_4(\varepsilon_{xx}+\varepsilon_{yy}),$$

$$K_t=\frac{\hbar^2}{2m_0}A_5k_t{}^2,$$

$$H_t=\frac{\hbar^2}{2m_0}A_6k_tk_z,$$

$$\Delta=\sqrt{2}\Delta_3. \tag{8-25}$$

The electrostatic field resulting from the spontaneous polarization field (P_{sp}) and piezoelectric polarization field (P_{pz}) is also taken into account in the numerical calculation model [5]. The calculation of spontaneous polarization uses linear interpolation following the treatment in reference [10]. Specifically,

for $In_XGa_{1-x}N$: $P^{sp}=x\cdot P^{sp}_{InN}+(1-x)\cdot P^{sp}_{GaN}$,

for $Al_XGa_{1-x}N$: $P^{sp}=x\cdot P^{sp}_{AlN}+(1-x)\cdot P^{sp}_{GaN}$,

for $Al_XIn_{1-x}N$: $P^{sp}=x\cdot P^{sp}_{AlN}+(1-x)\cdot P^{sp}_{InN}$,

for $Al_XIn_yGa_{1-x-y}N$: $P^{sp} = x \cdot P^{sp}_{AlN} + y \cdot P^{sp}_{InN} + (1-x-y) \cdot P^{sp}_{GaN}$. (8-26)

The calculation of piezoelectric polarization field uses linear interpolation for the piezoelectric coefficients and elastic stiffness coefficients with appropriate bowing parameters similar to the widely-used treatment in reference [11], and this method had been implemented in various works for analyzing the InGaN QW LEDs and lasers. However, the piezoelectric polarization field is linearly dependent with the strain, which does not include the non-linear term with respect to the strain [8, 11]. It is important to note that the use of nonlinear piezoelectric polarization fields had also been reported in analyzing the QDs systems with complex strain distributions [12, 13], and recent works had also clarified the importance on nonlinear piezoelectric effect in nitride semiconductors [14].

Specifically, the piezoelectric polarization field can be expressed as:

$$P_{pz} = 2d_{31}(C_{11} + C_{12} - \frac{2C_{13}^2}{C_{33}})\varepsilon_{xx}, \quad (8\text{-}27)$$

where d_{31} is piezoelectric coefficient, and C's are the elastic stiffness coefficients.

Therefore, as a result of both spontaneous and piezoelectric polarization fields, the electrostatic fields in each layer (j_{th}) can be written as:

$$E_j = \frac{\sum_k l_k p_k / \varepsilon_k - P_j \sum_k l_k / \varepsilon_k}{\varepsilon_j \sum_k l_k / \varepsilon_k}, \quad (8\text{-}28)$$

where P is the total macroscopic polarization, ε is the static dielectric constant, and l is the thickness of each layer (kth, jth). The electrostatic field needs to satisfy the periodic boundary conditions in order to ensure zero average electric field in the layers:

$$\sum_k l_k E_k = 0, \quad (8\text{-}29)$$

where the summation sums up all layers including the multiple QWs, including the QW active regions and barrier regions.

8.1.3 The Carrier Screening Effect and Calculation Flowchart

The carrier screening effect has been taken into account in the numerical model, and the calculation for the eigen energies and wave functions are based on a self-consistent model by solving the Poisson equation [3, 5]:

$$\frac{\partial}{\partial z}(\varepsilon \frac{\partial V_{sc}}{\partial z}) = -\rho(z), \tag{8-30}$$

where the potential V_{sc} includes both the effects of spontaneous and piezoelectric polarizations.

The charge distribution is given by:

$$\rho(z) = |e|[p(z) - n(z)], \tag{8-31}$$

where p(z) and n(z) are hole and electron concentrations, which are related to the wave functions of the n_{th} conduction subband and the m_{th} valence subband:

$$n(z) = \sum_n |\phi_n(z)|^2 N_n \ ,$$

$$p(z) = \sum_m |g_m(z)|^2 P_m \ . \tag{8-32}$$

The surface electron concentration in the n_{th} conduction band (N_n) and surface hole concentration in the m_{th} valence band (P_m) are expressed as:

$$N_n = 2\int_0^\infty \frac{2\pi k_t}{(2\pi)^2} \frac{1}{1+e^{[E_{en}(k_t)-F_c]/K_BT}} dk_t \ ,$$

$$P_m = 2\int_0^\infty \frac{2\pi k_t}{(2\pi)^2} \frac{1}{1+e^{[F_v-E_{hm}(k_t)]/K_BT}} dk_t \ . \tag{8-33}$$

Thus, the total potential profiles for electrons and holes will be modified by the inclusion of self-consistent electrostatic potential:

$$U_e(z) = U_0^e(z) - |e|V_{sc}(z),$$

$$U_h(z) = U_0^h(z) - |e|V_{sc}(z). \tag{8-34}$$

The self-consistent Schrodinger equations which take into account the carrier screening effect for electrons and holes can be expressed as:

$$\left[-\frac{\hbar^2}{2m_e^*}\frac{d^2}{dz^2}+U_e(z)\right]\phi(z)=E_e\phi(z),$$

$$\left[-\frac{\hbar^2}{2m_h^*}\frac{d^2}{dz^2}+U_h(z)\right]g(z)=E_hg(z). \tag{8-35}$$

The finite difference method is employed to solve the Schrödinger effective-mass equations with the spatial interval of 1 Å, similar to the treatment in references 2 and 5.

In the finite difference method, all the differential operators can be expressed as $A(z)\frac{\partial^2}{\partial z^2}$ or $B(z)\frac{\partial}{\partial z}$, where A and B represent the position (z)-dependent (QW or barrier) inverse effective-mass parameters. Then, the Hermitian properties of the Hamiltonian and boundary conditions can be obtained by the finite-difference formulae as follow:

$$A(z)\frac{\partial^2}{\partial z^2}\Big|_{z=z_i}=\frac{\partial}{\partial z}\left(A(z)\frac{\partial g}{\partial z}\right)\Big|_{z=z_i}$$

$$\approx\frac{A(z_{i+1})+A(z_i)}{2(\Delta z)^2}g(z_{i+1})-\frac{A(z_{i-1})+2A(z_i)+A(z_{i-1})}{2(\Delta z)^2}g(z_i)+\frac{A(z_i)+A(z_{i-1})}{2(\Delta z)^2}g(z_{i-1}),$$

$$B(z)\frac{\partial}{\partial z}\Big|_{z=z_i}=\frac{1}{2}\left(B(z)\frac{\partial g}{\partial z}+\frac{\partial(Bg)}{\partial z}\right)\Big|_{z=z_i}$$

$$\approx\frac{B(z_{i+1})+B(z_i)}{4\Delta z}g(z_{i+1})-\frac{B(z_i)+B(z_{i-1})}{4\Delta z}g(z_{i-1}), \tag{8-36}$$

where $\Delta z=z_{i+1}-z_i=z_i-z_{i-1}$ is the difference interval, which is employed as 1 Å in the numerical model.

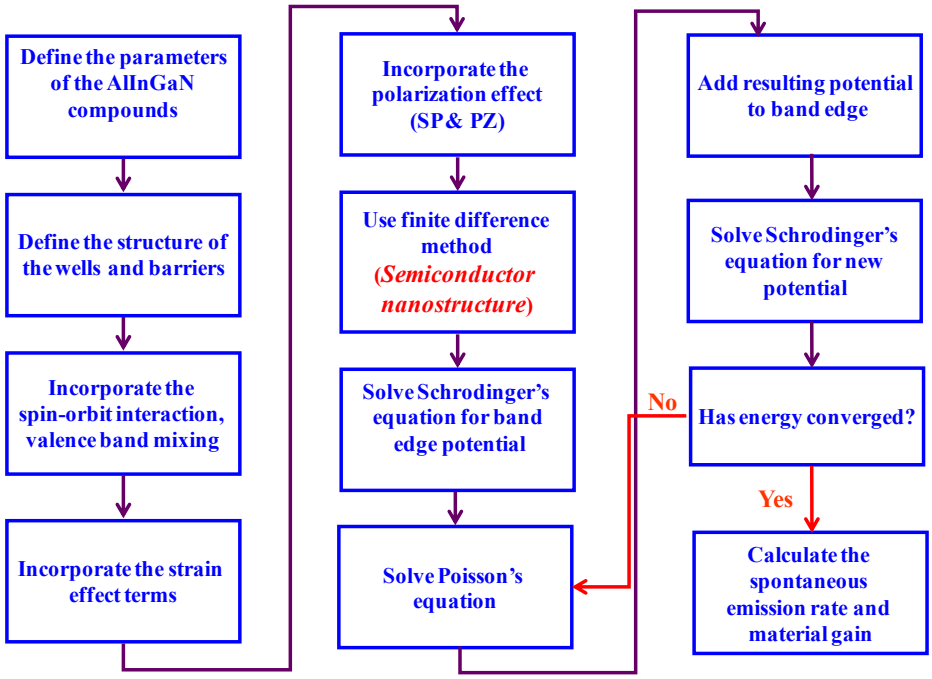

Figure 8-3: *Numerical flowchart of the simulation process for self-consistent 6-band* ***k·p*** *method for wurtzite semiconductor QW active region [5].*

Attributed from the interdependence of the carrier distribution and the band-edge potential, the band-edge potential has to be solved self-consistently using a close loop in order to solve the Schrödinger equations and Poisson equation alternately until the eigen energy converges (errors of the eigen energy converge to less than 0.1%), while the wave functions are simultaneously solutions for both Schrödinger and Poisson equations. The convergence condition in the self-consistent calculation requires 15 up to 20 iterations for each carrier density computation. The details of the numerical flowchart of the simulation process for self-consistent model of 6-band ***k·p*** method for wurtzite semiconductor QW active region is illustrated in figure 8-3 [5].

8.2 Spontaneous Radiative Recombination Rate and Optical Gain Calculation

The Hamiltonian obtained from 8.1.2 can be expressed as:

$$H^{v}_{6\times6}(k)=\begin{bmatrix} H^{U}_{3\times3}(k) & 0 \\ 0 & H^{L}_{3\times3}(k) \end{bmatrix}, \tag{8-37}$$

Where the 3×3 matrices are defined as:

$$H^U = \begin{bmatrix} F & K_t & -iH_t \\ K_t & G & \Delta - iH_t \\ iH_t & \Delta + iH_t & \lambda \end{bmatrix},$$

$$H^L = \begin{bmatrix} F & K_t & iH_t \\ K_t & G & \Delta + iH_t \\ -iH_t & \Delta - iH_t & \lambda \end{bmatrix}. \tag{8-38}$$

The optical transition matrix element relating n_{th} state in conduction band and m_{th} state in valence band can be obtained by using the calculated envelop functions:

for Transverse Electric (TE)-polarization ($\hat{e} = \hat{x}$ or $\hat{y}$, $\perp c$ axis):

$$\left|(M_x)_{nm}^{\sigma}(k_t)\right|^2 = \frac{\left|\left\langle S|p_x|X\right\rangle\right|^2}{4}\left\{\left\langle \phi_n \middle| g_m^{(1)}\right\rangle^2 + \left\langle \phi_n \middle| g_m^{(2)}\right\rangle^2\right\}, \text{ for } \sigma = U$$

$$= \frac{\left|\left\langle S|p_x|X\right\rangle\right|^2}{4}\left\{\left\langle \phi_n \middle| g_m^{(4)}\right\rangle^2 + \left\langle \phi_n \middle| g_m^{(5)}\right\rangle^2\right\}, \text{ for } \sigma = L \tag{8-39}$$

for Transverse Magnetic (TM)-polarization ($\hat{e} = \hat{z}$, $// c$ axis):

$$\left|(M_z)_{nm}^{\sigma}(k_t)\right|^2 = \frac{\left|\left\langle S|p_z|Z\right\rangle\right|^2}{2}\left\langle \phi_n \middle| g_m^{(3)}\right\rangle^2, \text{ for } \sigma = U$$

$$= \frac{\left|\left\langle S|p_z|Z\right\rangle\right|^2}{2}\left\langle \phi_n \middle| g_m^{(6)}\right\rangle^2, \text{ for } \sigma = L, \tag{8-40}$$

where the ϕ_n is the n_{th} conduction band confined state, and g_m is the m_{th} valence band confined state.

Then, the optical gain calculation is obtained based on the Fermi's Golden rule, including a Lorentzian line-shape function [1, 5]. The upper and lower 3×3 Hamiltonian blocks from the 6×6 diagonalized Hamiltonian matrix are denoted as σ =U and σ = L, respectively. The spontaneous emission rate for TE-polarization ($\hat{e} = \hat{x}$ or $\hat{y}$) or TM polarization ($\hat{e} = \hat{z}$)can be obtained by taking into account all inter-band transitions between n^{th} conduction subbands and m^{th} valence

subbands. The optical gain calculation formula is listed below, which similar to the treatment in references 1 and 5:

$$g_{sp}^{e}(\hbar\omega) = \frac{2q^2\pi}{n_r c\varepsilon_0 m_0^2 \omega L_w} \sum_{\sigma=U,L} \sum_{n,m} \int \frac{k_t dk_t}{2\pi} \left|(M_e)_{nm}^{\sigma}(k_t)\right|^2 \cdot \frac{f_n^c(k_t)(1-f_{\sigma m}^v(k_t))(\gamma/\pi)}{(E_{\sigma,nm}^{cv}(k_t)-\hbar\omega)^2+\gamma^2} \quad .$$

(8-41)

where q is the magnitude of the electron charge, m_0 is the electron mass in free space, c and ε_0 are the velocity of light and permittivity in free space, respectively. The $\hat{e}$ is the polarization vector of the optical electric field; the n_r and L_w are the refractive index and thickness of the QW, respectively.

The term $\hbar\gamma$ is the half line width of the Lorentzian function, and the linewidth broadening time τ_s = 0.1 ps (γ = (0.1 ps)$^{-1}$) is used in our calculation, which is similar to the value used in references 44 and 47. The inhomogeneous broadening is not taken into account in this work, as there has been no clear experimental data on the inhomogeneous broadening value from growths of InGaN on ternary substrates. The term $(M_e)_{nm}^{\sigma}(k_t)$ is the momentum matrix element for transitions between the n^{th} conduction-band state and the m^{th} valence-band state, and the details for the calculation of the matrix element are from equations (8-39) and (8-40).

The optical gain with TE and TM polarizations are related to the spontaneous emission rate, which can be expressed as:

$$g^{TE}(\hbar\omega) = g_{sp}^{x}(\hbar\omega)\left[1-\exp(\frac{\hbar\omega-\Delta F}{k_B T})\right],$$

$$g^{TM}(\hbar\omega) = g_{sp}^{z}(\hbar\omega)\left[1-\exp(\frac{\hbar\omega-\Delta F}{k_B T})\right], \qquad (8\text{-}42)$$

where the ΔF represents the separation between the quasi-Fermi levels of electrons (F_c) and holes (F_v): $\Delta F = F_c - F_v$.

The Fermi-Dirac distributions for the electrons in the conduction bands and valence bands are expressed as:

$$f_n^c(k_t) = \frac{1}{1+\exp(\frac{E_n^c(k_t)-F_c}{k_BT})},$$

$$f_{\sigma m}^v(k_t) = \frac{1}{1+\exp(\frac{E_{\sigma,m}^v(k_t)-F_v}{k_BT})}. \quad (8\text{-}43)$$

Thus, the electron concentration *n* and the hole concentration *p* are related to the quasi-Fermi levels of electrons (F_c) and holes (F_v):

$$n = \frac{2}{L_w}\sum_n \int \frac{k_t dk_t}{2\pi} f_n^c(k_t)$$

$$= \frac{k_B T m_e^t}{\pi\hbar^2 L_w}\sum_n \ln\left[1+\exp(\frac{F_c - E_n^c(0)}{k_BT})\right],$$

$$p = \frac{1}{L_w}\sum_{\sigma=U,L}\sum_m \int \frac{k_t dk_t}{2\pi}(1-f_{\sigma m}^v(k_t)). \quad (8\text{-}44)$$

Since the momentum matrix element of the total spontaneous emission is the angular average of two TE-polarization components and one TM-polarization component:

$$\left|M_{sp}\right|^2 = \frac{1}{3}(2\left|M_x\right|^2 + \left|M_z\right|^2), \quad (8\text{-}45)$$

the total spontaneous emission rate per energy interval per unit volume ($s^{-1}eV^{-1}cm^{-3}$) is given by:

$$r_{sp}(\hbar\omega) = \frac{n_e^2\omega^2}{\pi^2\hbar c^2}\frac{(2g_{sp}^x + g_{sp}^z)}{3}. \quad (8\text{-}46)$$

The total spontaneous emission rate per unit volume ($s^{-1}cm^{-3}$) can be obtained by summing up the average of three polarizations ($\frac{2\times TE + TM}{3}$), and then integrate over the emission spectrum:

$$R_{sp} = \int_0^\infty r^{spon}(\hbar\omega)d(\hbar\omega). \quad (8\text{-}47)$$

The radiative current density (A/cm^2) can be obtained as:

$$J_{rad} = q \cdot d \cdot R_{sp}, \tag{8-48}$$

where $q = 1.6 \times 10^{-19} C$ is the unit charge of electron, and d is the thickness of the QW active region where the injection current provides the electrons and holes for radiative recombination.

8.3 Carrier Lifetime and Radiative Efficiency Calculation Formulations

The external quantum efficiency (η_{external}) of III-Nitride photonic devices depends on three important parameters: 1) current injection efficiency (η_{inj}), 2) radiative efficiency (η_{Rad}), and 3) light extraction efficiency ($\eta_{\text{extraction}}$) [6, 7]:

$$\eta_{external} = \eta_{inj} \cdot \eta_{Rad} \cdot \eta_{extraction}. \tag{8-49}$$

The current injection efficiency (η_{inj}) represents the fraction of the injected current that recombines in the QW active region.

The radiative efficiency (η_{Rad}) represents the fraction of recombination current in the QW active region that recombines radiatively leading to generation of photons.

The light extraction efficiency ($\eta_{\text{extraction}}$) represents the fraction of the generated photons in the QW active region which can be extracted out from the semiconductor cavity into free space.

The total recombination current in the QW active region consists of radiative recombination current and non-radiative recombination current:

$$\eta_{inj} \cdot J = J_{QW} = q \cdot d_{QW} \cdot (A \cdot N + R_{sp} + C \cdot N^3), \tag{8-50}$$

where J is the injected current density, and d_{QW} is the QW active region thickness. The J_{QW} represents the total recombination current in the QW, which includes both the radiative recombination current and non-radiative recombination current. The parameters *A* and *C* represent the monomolecular recombination rate and Auger recombination rate coefficients, respectively, and the parameter N is the carrier density in the QW active region. The R_{sp} is the total radiative recombination rate from the QW active region.

Thus, the total carrier recombination rate (R_{total}) in the QW active region is:

$$R_{total} = A \cdot N + R_{sp} + C \cdot N^3 , \tag{8-51}$$

where the non-radiative recombination rate (R_{non_rad}) in the QW active region can be expressed as:

$$R_{non\_rad} = A \cdot N + C \cdot N^3 . \tag{8-52}$$

Then, the radiative efficiency (η_{Rad}) is obtained as:

$$\eta_{Rad} = \frac{R_{sp}}{R_{total}} = \frac{R_{sp}}{R_{non\_rad} + R_{sp}} . \tag{8-53}$$

For GaN-based wide bandgap materials, the Auger recombination rate can be negligible due to the low value of the Auger recombination rate (C_{Auger}~10^{-32} cm^6/sec) in InGaN [17, 18]. Thus, the radiative efficiency (η_{Rad}) can be expressed as:

$$\eta_{Rad} = \frac{R_{sp}}{A \cdot N + R_{sp}} . \tag{8-54}$$

It is important to point out the large discrepancy on the C_{Auger} for InGaN QWs reported in the literatures [17-20]. The C_{Auger} of 3.5x10^{-34} cm^6/sec up to 1x10^{-32} cm^6/sec had been reported for InGaN QWs [17, 18], while values of 1.4-2x10^{-30} cm^6/sec had been reported in the bulk system [19, 20]. Further conclusive studies are still required for determining the C_{Auger} in InGaN QWs [17-20].

Then, the total carrier recombination rate (R_{total}) can be written as a function of total carrier lifetime (τ_{total}) and carrier density in the QW (N):

$$R_{total} = R_{sp} + R_{non\_rad} = \frac{N}{\tau_{total}} . \tag{8-55}$$

Similarly, the total carrier lifetime (τ_{total}) includes both the radiative carrier lifetime (τ_{rad}) and non-radiative carrier lifetime (τ_{non_rad}):

$$\frac{1}{\tau_{total}} = \frac{1}{\tau_{rad}} + \frac{1}{\tau_{non\_rad}} , \tag{8-56}$$

where the radiative carrier lifetime (τ_{rad}) and non-radiative carrier lifetime (τ_{non_rad}) can be expressed:

$$\frac{1}{\tau_{rad}} = \frac{R_{sp}}{N},$$

$$\frac{1}{\tau_{non\_rad}} = \frac{R_{non\_rad}}{N}. \tag{8-57}$$

8.4 Material Parameters for Optical Properties of III-Nitride Semiconductors

The material parameters for GaN, AlN and InN alloys are taken from references 5, 8-9, which are all listed in the Table 8-I below:

Parameters	**GaN**	**AlN**	**InN**
Lattice constant			
a (Å)	3.189	3.112	3.545
c (Å)	5.185	4.982	5.703
Energy parameters			
E_g (eV) at 300 K	3.437	6.00	0.6405
$\Delta_1(=\Delta_{cr})$ (eV)	0.01	-0.227	0.024
$\Delta_2=\Delta_3=\Delta_{SO}/3$ (eV)	0.00567	0.012	0.00167
Conduction-band effective masses			
$m_{//}^*/m_0$ at 300 K	0.21	0.32	0.07
$m_{\perp}^*/m_0$ at 300 K	0.2	0.3	0.07
Valence-band effective mass parameters			
A_1	-7.21	-3.86	-8.21
A_2	-0.44	-0.25	-0.68
A_3	6.68	3.58	7.57
A_4	-3.46	-1.32	-5.23

A_5	-3.4	-1.47	-5.11
A_6	-4.9	-1.64	-5.96
Deformation potentials			
a_{cz} (eV)	-7.1	-3.4	-4.2
a_{ct} (eV)	-9.9	-11.8	-4.2
D_1 (eV)	-3.6	-2.9	-3.6
D_2 (eV)	1.7	4.9	1.7
D_3 (eV)	5.2	9.4	5.2
D_4 (eV)	-2.7	-4	-2.7
Elastic stiffness constants			
C_{11} (GPa)	390	396	223
C_{12} (GPa)	145	137	115
C_{13} (GPa)	106	108	92
C_{33} (GPa)	398	373	224
Piezoelectric coefficients			
d_{13} (pmV^{-1})	-1	-2.1	-3.5
d_{33} (pmV^{-1})	1.9	5.4	7.6
Spontaneous polarization			
P_{sp} (C/m^2)	-0.034	-0.09	-0.042

Table 8-1: *Material parameters for GaN, AlN and InN. The Parameters are taken from references 5, 8-9.*

8.5 Summary

In summary, the numerical model for the calculations of the band structures and electron and hole wave functions based on the 6-band ***k·p*** formalism for wurtzite semiconductors, which takes

into account the valence band mixing, strain effect, spontaneous and piezoelectric polarization, as well as the carrier screening effect has been reviewed in details in this chapter. Specifically, the spin-orbit interaction and the incorporation of strain effect and polarization fields were reviewed with detailed formulism. The carrier screening effect and calculation flowchart of the self-consistent 6-band ***k·p*** method were also presented.

The calculation formulations of the spontaneous radiative recombination rate and optical gain were then reviewed for III-Nitride semiconductors. The carrier lifetime and radiative efficiency calculation formulations, as well as the material parameters for optical properties of III-Nitride semiconductors were presented at the end of the section.

References for Chapter 8

[1] S. L. Chuang, "Optical Gain of Strained Wurtzite GaN Quantum-Well Lasers," IEEE J. Quantum Electron., vol. **32**, no. 10, pp. 1791-1800, Oct. 1996.

[2] S. L. Chuang and C. S. Chang, "A band-structure model of strained quantum-well wurtzite semiconductors," Semicond. Sci. Technol., vol. **12**, no. 3, pp. 252-263, Mar. 1997.

[3] S. L. Chuang, Physics of Photonic Devices 2nd ed. Wiley, New York, 2009, Chap. 4, Chap. 9 and Chap. 11.

[4] S. L. Chuang and C. S. Chang, "***k·p*** method for strained wurtzite semiconductors," Phys. Rev. B., vol. 54, pp. 2491–2504, Jul. 1996.

[5] H. Zhao, R. A. Arif, Y. K. Ee, and N. Tansu, "Self-Consistent Analysis of Strain-Compensated InGaN–AlGaN Quantum Wells for Lasers and Light-Emitting Diodes," IEEE J. Quantum Electron., vol. **45**, no. 1, pp. 66-78, Jan. 2009.

[6] H. P. Zhao, R. A. Arif, and N. Tansu, "Design Analysis of Staggered InGaN Quantum Wells Light-Emitting Diodes at 500-540 nm," IEEE J. Sel. Top. Quantum Electron., vol. 15 (4), pp. 1104-1114, July 2009.

[7] N. Tansu and L. J. Mawst, "Current injection efficiency of 1300-nm InGaAsN quantum-well lasers," J. Appl. Phys., vol. 97, no. 5, Art. 054502, Mar. 2005.

[8] I. Vurgaftman and J.R. Meyer, Chapter 2 in Nitride Semiconductor Devices, J. Piprek (Editor), Wiley, 2007.

[9] I. Vurgaftman and J.R. Meyer, “Band parameters for nitrogen-containing semiconductors,” J. Appl. Phys., vol. **94**, no. 6, pp. 3675-3696, Sep. 2003.

[10] F. Bernardini and V. Fiorentini, “Spontaneous versus piezoelectric polarization in III–V Nitrides: Conceptual aspects and practical consequences,” Phys. Stat. Sol. (b), vol. 216, pp. 391–398, Nov. 1999.

[11] O. Ambacher, J.Majewski, C. Miskys, A. Link, M. Hermann, M. Eickhoff, M. Stutzmann, F. Bernardini, V. Fiorentini, V. Tilak, W. J. Schaff, and L. F. Eastman, “Pyroelectric properties of Al(In)GaN/GaN heteroand quantum well structures,” J. Phys.: Condens. Matter, vol. 14, pp. 3399–3434, Mar. 2002.

[12] G. Bester, X. Wu, D. Vanderbilt, and A. Zunger, “Importance of Second-Order Piezoelectric Effects in Zinc-Blende Semiconductors,” Phys. Rev. Lett., vol. 96, pp. 187602-1– 187602-4, May 2006.

[13] G. Bester, A. Zunger, X. Wu and D. Vanderbilt, “Effects of linear and nonlinear piezoelectricity on the electronic properties of InAs/GaAs quantum dots,” Phys. Rev. B, vol. 74, pp. 081305-1-081305-4, Aug. 2006.

[14] J. Pal, G. Tse, V. Haxha, M. A. Migliorato, and S. Tomic, “Importance of non linear piezoelectric effect in Wurtzite III-N semiconductors,” Opt. Quant. Electron., vol. 44, no. 3-5, pp. 195-203, June 2012.

[15] H. Y. Ryu, K. H. Ha, S. N. Lee, T. Jang, J. K. Son, H. S. Paek, Y. J. Sung, H. K. Kim, K. S. Kim, O. H. Nam, Y. J. Park, and J. I. Shim, “High-performance blue InGaN lase diodes with single-quantum-well active layers.” IEEE Photon. Technol. Lett., vol. 19, no. 21, pp. 1717-1719, Nov. 2007.

[16] W. W. Chow, M. Kneissl, “Laser gain properties of AlGaN quantum wells,” J. Appl. Phys., vol. **98**, no. 11, pp. 114502-1–114502-6, Dec. 2005.

[17] J. Hader, J. V. Moloney, A. Thranhardt, and S. W. Koch, in Nitride Semiconductor Devices, edited by J. Piprek (Wiley-CCH, Weinheim, 2007), Chap. 7.

[18] J. Hader, J. V. Moloney, B. Pasenow, S. W. Koch, M. Sabathil, N. Linder, and S. Lutgen, “On the importance of radiative and Auger losses in GaN-based quantum wells,” Appl. Phys. Lett., vol. 92, Art. 261103, July 2008.

[19] Y. C. Shen, G. O. Mueller, S. Watanabe, N. F. Gardner, A. Munkholm, and M. R. Krames, “Auger recombination in InGaN measured by photoluminescence,” Appl. Phys. Lett., vol. 91, Art. 141101, Oct. 2007.

[20] K. T. Delaney, P. Rinke, and C. G. Van de Walle, “Auger recombination rates in nitrides from first principles,” Appl. Phys. Lett., vol. 94, Art. 191109, May 2009.

Chapter 9: Physics on Gain Characteristics of AlGaN Quantum Wells (QWs) UV Lasers

In Chapter 2, the current status of AlGaN QWs UV lasers has been reviewed, which includes the challenges to achieve high-efficiency UV lasers, as well as the state-of-the-art AlGaN QW lasers emitting in mid- and deep-UV spectral regimes. In this chapter, a comprehensive study is carried out for the optical gain and threshold characteristics of both high and low Al-content AlGaN QWs active regions for deep- and mid-UV lasers. The polarization properties of optical gain and spontaneous emission characteristics, as well as the threshold properties of the $Al_xGa_{1-x}N$ QWs with AlN barriers are calculated and analyzed for mid- and deep-UV lasers. The carrier lifetimes and differential gain properties are analyzed and compared for high Al-content AlGaN QWs. The effect of the QW thickness on the valence subbands crossover is studied for AlGaN QWs deep-UV active regions. The band structures and wave functions for AlGaN QWs with AlN barriers are calculated by employing self-consistent 6-band ***k·p*** formalism for wurtzite semiconductor taking into account the valence band mixing, strain effect, spontaneous and piezoelectric polarization fields, and carrier screening effect [35-38]. The band parameters for the III-Nitride semiconductors in this work are obtained from references 38-41. The calculation details and band parameters can be found in Chapter 8.

9.1 Introduction and Band Structure Analysis for $Al_xGa_{1-x}N$ QWs

Attributed to the challenges discussed in Chapter 2, the improved understanding in the physics of optical gain of AlGaN QW is important in identifying the limitations and potential solutions for achieving low-threshold and high-efficiency lasers in the deep- and mid-UV spectral regimes (λ ~ 220-300 nm).

9.1.1 Valence Band Crossovers in AlGaN Alloys

The valence band structures for bulk GaN and bulk AlN are presented in figure 9-1 in order for improved physics understanding of AlGaN materials. For bulk GaN material, the heavy hole (HH)

band and light hole (LH) band are with higher energy levels than that of the crystal-field split-off hole (CH) band. In contrast, the energy level of CH band is higher compared to that of the HH and LH bands for bulk AlN. Thus, there will exist a valence crossover in the ternary AlGaN alloy.

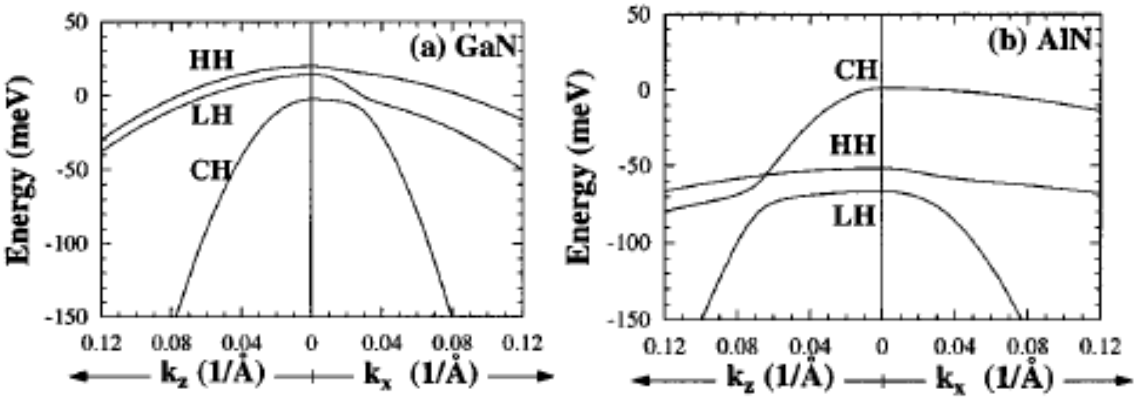

Figure 9-1: *Valence band structures for wurtzite (a) GaN and (b) AlN.(from reference 34)*

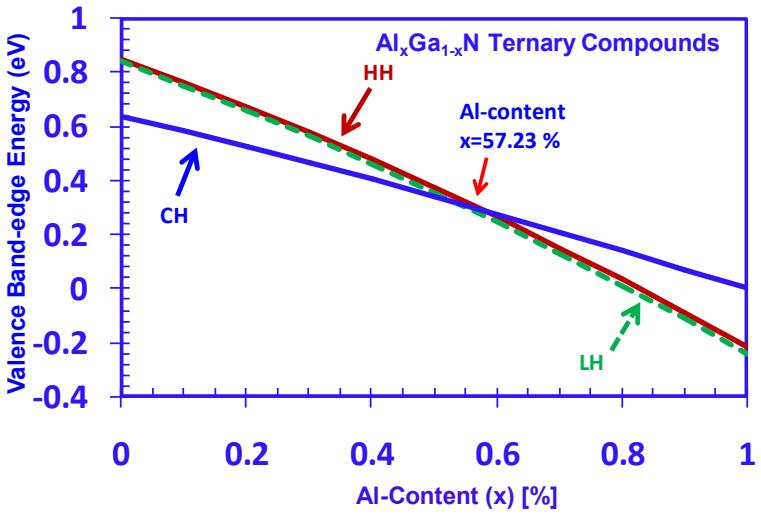

Figure 9-2: *Energy band edges of the HH, LH and CH bands as a function of Al-content (x) for $Al_xGa_{1-x}N$ ternary compounds.*

The valence band-edge energy levels (HH, LH, and CH) for $Al_xGa_{1-x}N$ alloys with Al-contents (x) [x = 0%-100%] are shown in figure 9-2. For $Al_xGa_{1-x}N$ with x < 57.2%, the band-edge energy levels for HH and LH bands are larger than that of the CH band. The band-edge energy separations between HH / LH bands and CH band reduces with increasing Al-content, and the HH / LH and CH bands have a crossover at x = 57.2%. For $Al_xGa_{1-x}N$ with x > 57.2%, the band-edge energy level of CH band becomes larger than those of HH / LH bands, and this energy separation further increases as the Al-content in AlGaN alloy increases. The HH and CH bands

crossover is important, as the transition between conduction and CH bands is transverse magnetic (TM)-polarized component.

9.1.2 Valence Band Structures for $Al_xGa_{1-x}N$ QWs with AlN Barriers

Figures 9-3(a) and 9-3(b) show the band-edge valence band structures for both conventional 30-Å $Al_{0.2}Ga_{0.8}N$ QW and 30-Å $Al_{0.2}Ga_{0.8}N$ QW at carrier density (n) of $n = 5\times10^{19}$ cm^{-3} at T = 300 K. For conventional low Al-content $Al_{0.2}Ga_{0.8}N$ QW with AlN barriers, the energy levels of HH1 and LH1 subbands are closely separated at Γ-point, which are much higher than the energy level of the CH1 subband, as shown in figure 9-3(a). The energy separation between the HH1 and CH1 subbands is relatively large (~340 meV) at Γ-point, which ensures the dominant C1-HH1 transition in the gain media up to high carrier density. In contrast, for conventional high Al-content $Al_{0.8}Ga_{0.2}N$ QW with AlN barriers, the valence subband energy level of CH1 band is higher than that of the HH1 and LH1 subbands. In addition, the energy separation between the HH1 and LH1 subbands is relatively larger (~20 meV) at Γ-point. Thus, the dominant transition in the gain media becomes the C1-CH1 transition, which leads to TM-polarized optical gain.

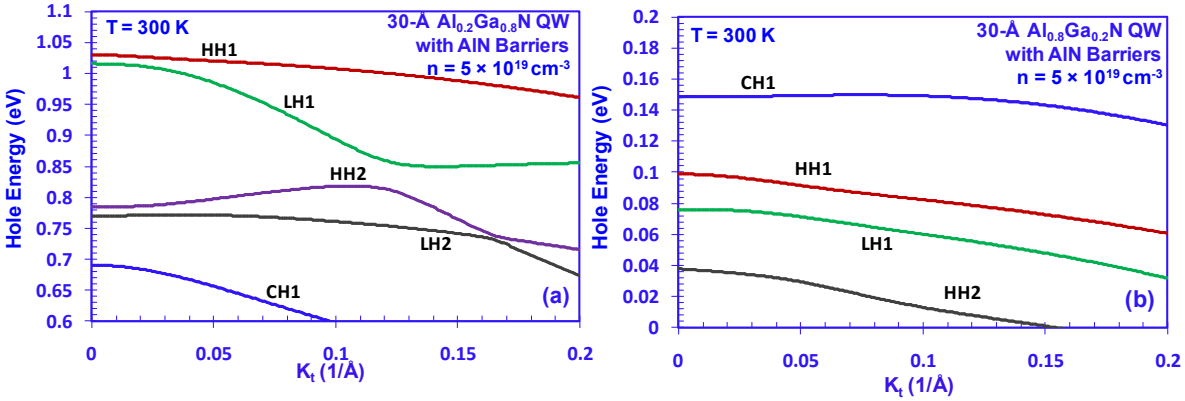

Figure 9-3: *Valence band structures for (a) 3-nm $Al_{0.2}Ga_{0.8}N$ QW and (b) 3-nm $Al_{0.8}Ga_{0.2}N$ QW with AlN barriers at carrier density 5×10^{19} cm^{-3} at room temperature.*

9.2 Momentum Matrix Element Characteristics

The square of momentum matrix elements are shown as a function of in-plane wave vector k_t for 3-nm $Al_{0.2}Ga_{0.8}N$ QW (figure 9-4(a)), and 3-nm $Al_{0.8}Ga_{0.2}N$ QW (figure 9-4(b)) with AlN barriers with carrier density 5×10^{19} cm^{-3} at room temperature. The insets are the schematics of the AlGaN

QW structures for both (a) 3-nm low Al-content $Al_{0.2}Ga_{0.8}N$ QW and (b) 3-nm high Al-content $Al_{0.8}Ga_{0.2}N$ QW.

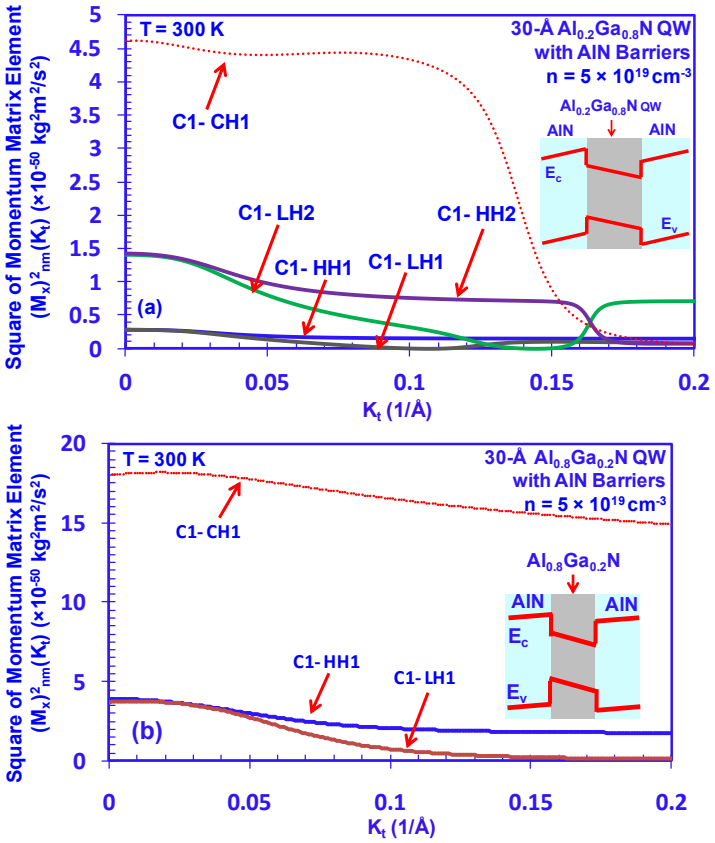

Figure 9-4: *Square of momentum matrix elements as a function of in-plane wave vector k_t for (a) 3-nm $Al_{0.2}Ga_{0.8}N$ QW and (b) 3-nm $Al_{0.8}Ga_{0.2}N$ QW with AlN barriers at carrier density 5×10^{19} cm^{-3} at room temperature. The insets are the schematics of the AlGaN QW structures.*

For the 3-nm low Al-content $Al_{0.2}Ga_{0.8}N$ QW, the optical matrix element of C1-CH1 transition is relatively stronger than those of C1-HH1 and C1-LH1 transitions. However, as the carriers are mainly populating the HH1 and LH1 subbands, weaker C1-HH1 and C1-LH1 transitions will lead to low transverse electric (TE)-polarized spontaneous emission and optical gain. Attributed from the low population of carriers in CH1 subband, the TM-polarized gain will be low despite its large C1-CH1 matrix element. In contrast, for 3-nm high Al-content $Al_{0.8}Ga_{0.2}N$ QW, the C1-CH1 transition is dominant compared to the C1-HH1 and C1-LH1 transitions. As the carriers are mainly populating the CH subband, strong C1-CH1 transition will lead to large TM-polarized spontaneous emission and optical gain.

9.3 Spontaneous Emission and Optical Gain Characteristics of $Al_xGa_{1-x}N$ QW Lasers

To illustrate the effect of the valence subbands crossover for the AlGaN QWs active regions, the spontaneous emission recombination rate per unit volume (R_{sp}) and optical gain characteristics were studied and analyzed. The R_{sp} as a function of Al-contents for the 3-nm thick $Al_xGa_{1-x}N$ QW is presented in figure 9-5(a) with $n = 3\times10^{19}$ cm^{-3} at T = 300 K.

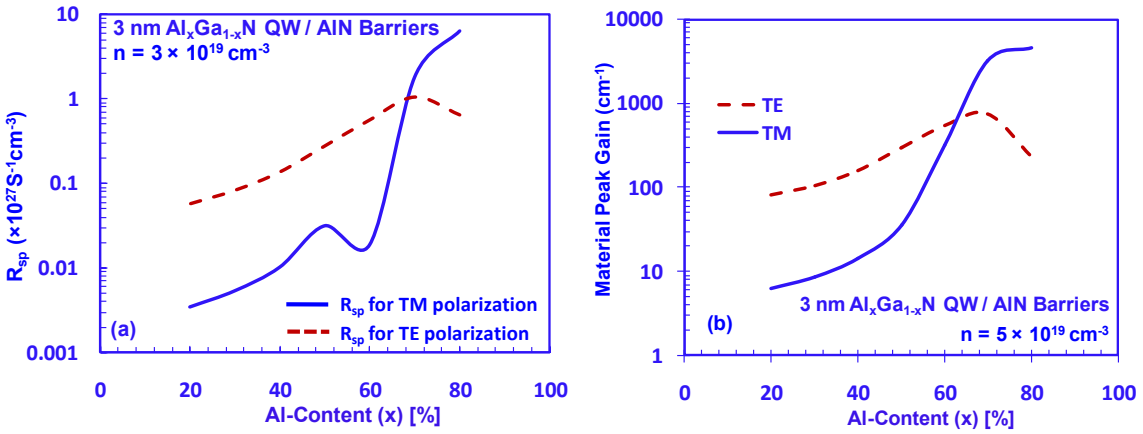

Figure 9-5: *TE-polarized and TM-polarized (a) spontaneous emission rate (R_{sp}) and (b) peak material gain for 3-nm thick $Al_xGa_{1-x}N$ QWs with AlN barriers as a function of Al-contents (x).*

The analysis is carried out for AlGaN QW with Al-contents from 20% up to 80%. The spontaneous emission rates (R_{sp}) for low Al-content AlGaN QW show dominant TE polarization, which is an order of magnitude or higher in comparison to that for the TM polarization. Both the TE-polarized and TM-polarized R_{sp} show increasing trend for increasing Al-content, while the TM-polarized R_{sp} starts to exhibit large increase for x > ~ 58%. For AlGaN QW with Al-content of 68%, both TE- and TM-polarized components are similar. For high Al-content above 68%, the TM-polarized spontaneous emission is significantly enhanced attributing to the strong transition between conduction band and CH band. The reduction in the TE-spontaneous emission for high Al-content AlGaN QW can be attributed to the significantly lower carrier density populating the HH and LH bands from the increasing energy separation between CH and HH / LH bands.

Both TE-polarized (g^{TE}_{peak}) and TM-polarized material peak gains (g^{TM}_{peak}) as a function of Al-content for the 3-nm $Al_xGa_{1-x}N$ QW with AlN barriers calculated for $n = 5\times10^{19}$ cm^{-3} at T = 300 K

were shown in figure 9-5(b). For low Al-content AlGaN QW (x < 68%), both the TE- and TM-polarized gains are relatively low (g_{peak} < 500 cm^{-1}), however the TE-polarized gain is relatively larger than the TM-polarized gain. For AlGaN QW with Al-content above ~68%, the TM-polarized peak material gain is dominant resulting in significantly higher peak gain (g^{TM}_{peak} = 3280 cm^{-1} for x = 70%, and g^{TM}_{peak} = 4690 cm^{-1} for x = 80%). The gain analysis indicates that the carriers in the high Al-content AlGaN QW are dominantly confined in the CH band after the crossover of the HH/ LH and CH bands, resulting in higher than one-order of magnitude ratio of g^{TM}_{peak} / g^{TE}_{peak} ratio.

Note that experimentally, the CH and HH/ LH subbands crossover has also been confirmed for AlGaN QWs by G. A. Garrett and co-authors very recently [32], which is consistent with our theoretical analysis.

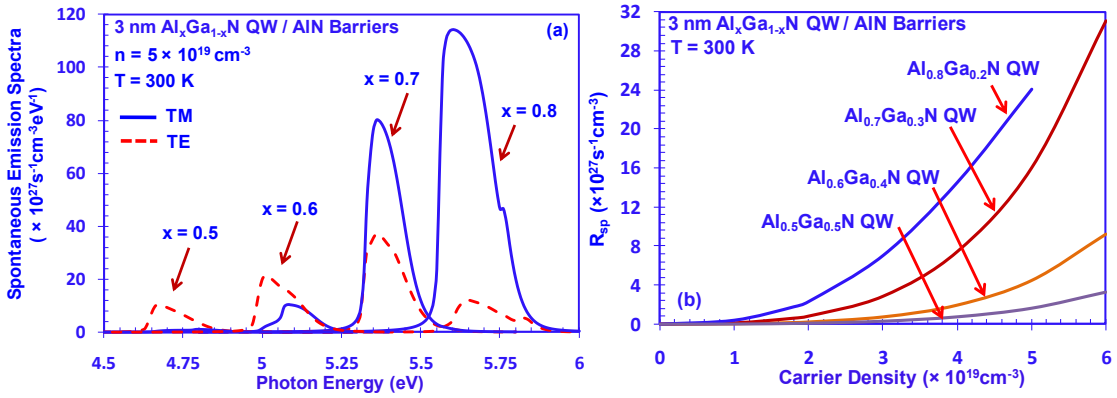

Figure 9-6: *(a) TE-polarized and TM-polarized spontaneous emission spectra, and (b) spontaneous emission rate (R_{sp}) as a function of carrier density for 3-nm thick $Al_xGa_{1-x}N$ QWs (x = 50% - 80%) with AlN barriers at T = 300 K.*

Figure 9-6(a) shows both TE- and TM-polarized spontaneous emission spectra for 3-nm thick $Al_xGa_{1-x}N$ QWs (x = 50% - 80%) with AlN barriers calculated with n = 5×10^{19} cm^{-3} at T = 300 K. For lower Al-content $Al_xGa_{1-x}N$ QWs (x = 50%, 60%), which are with the Al-contents before the valence-bands crossover, the TE-polarized peak spontaneous emission spectra is higher than the TM-polarized peak spontaneous emission spectra as major carriers are populating the HH1 and LH1 valence subbands. In contrast, for higher Al-content $Al_xGa_{1-x}N$ QWs (x = 70%, 80%) after the valence-bands crossover, higher TM-polarized peaks are obtained from the spontaneous emission spectra, attributed from the dominant C1-CH1 transition.

The total R_{sp} as a function of carrier density up to n = 6×10^{19} cm^{-3} is shown in figure 9-6(b) for $Al_xGa_{1-x}N$ (x = 50% - 80%) QWs. The total R_{sp} shows increasing trend with higher carrier density for all the $Al_xGa_{1-x}N$ (x = 50% - 80%) QWs, as the matrix elements are enhanced with larger *n*. Attributed from the significantly increased TM-polarized R_{sp} for high Al-content $Al_xGa_{1-x}N$ QWs (x = 70%, 80%) after the valence subbands crossover, the enhancement of total R_{sp} for $Al_{0.7}Ga_{0.3}N$ QW and $Al_{0.8}Ga_{0.2}N$ QW are higher than that of $Al_{0.5}Ga_{0.5}N$ QW and $Al_{0.6}Ga_{0.4}N$ QW. Specifically, for the $Al_{0.7}Ga_{0.3}N$ QW (or $Al_{0.8}Ga_{0.2}N$ QW), the increase of the R_{sp} as a function of carrier density ranges between 3.4 - 3.9 times (or 5.4 - 10.5 times) higher compared to that of the $Al_{0.6}Ga_{0.4}N$ QW.

Figure 9-7(a) shows both TE-polarized and TM-polarized optical gain spectra for 3-nm thick $Al_xGa_{1-x}N$ QWs (x = 20% - 50%) with AlN barriers at n = 5×10^{19} cm^{-3} at T = 300 K. All the $Al_xGa_{1-x}N$ QWs (x = 20% - 50%) are with Al-contents before the valence-bands crossover. The peak gain wavelengths (λ_{peak}) for AlGaN QW with Al-contents of 20%, 30%, 40%, 50% are 334.2 nm, 308.5 nm, 285.7 nm and 265.5 nm, respectively. For all the low Al-content $Al_xGa_{1-x}N$ QWs (x = 20% - 50%), both the TE- and TM-polarized gains are low (below g_{peak} ~ 300 cm^{-1}). The TM-polarized gain is almost negligible compared to the TE-polarized gain for low Al-content $Al_xGa_{1-x}N$ QWs (x = 20% - 50%), as there are significantly less carriers populating the CH1 subband.

Both the TE-polarized and TM-polarized optical gain spectra for $Al_xGa_{1-x}N$ QWs (*x* = 60% - 80%) are analyzed at carrier density 5×10^{19} cm^{-3} in figure 9-7(b). For the $Al_xGa_{1-x}N$ QWs (*x* = 60% - 80%), the corresponding peak gain wavelengths (λ_{peak}) are ranging from λ_{peak} ~ 221.8 nm up to λ_{peak} ~ 247.5 nm in deep-UV spectral regime. Both the TE- and TM-polarized gains are relatively low (g_{peak} ~ 400-500 cm^{-1}) for $Al_{0.6}Ga_{0.4}N$ QW, with the Al-content before the valence subbands crossover. For $Al_xGa_{1-x}N$ QWs (x= 70%, 80%) with higher Al-contents after the valence subbands crossover, significantly enhanced TM-polarized gains are obtained with λ_{peak} ~ 221.8-231.3 nm, as major carriers are populating the CH1 subband, and the C1-CH1 transition becomes dominant after the crossover.

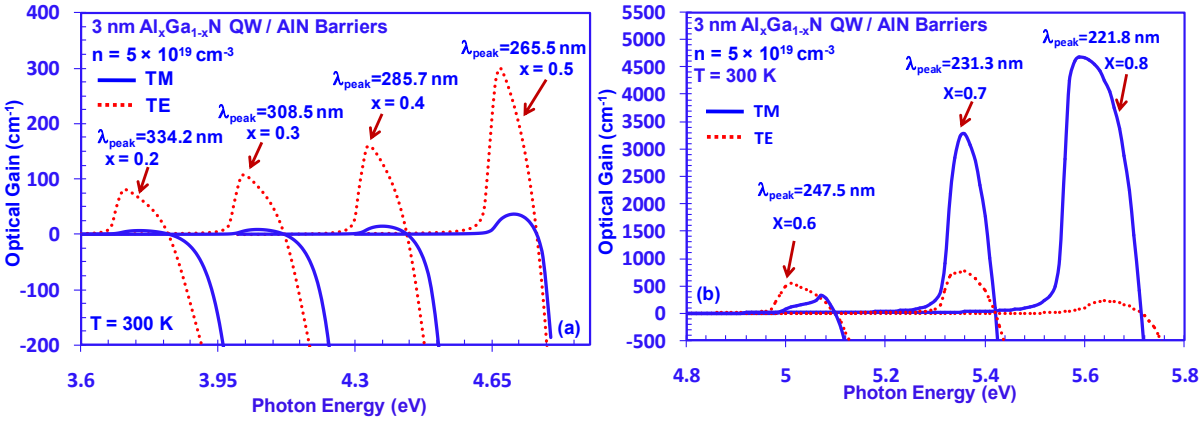

Figure 9-7: *TE-polarized and TM-polarized optical gain spectra for 3-nm thick (a) $Al_xGa_{1-x}N$ QWs (x = 20% - 50%), and (b) $Al_xGa_{1-x}N$ QWs (x = 60% - 80%) with AlN barriers with n = 5×10^{19} cm^{-3}.*

The TM-polarized and TE-polarized peak material gains are analyzed and compared in figures 9-8(a) and 9-8(b) for 3-nm thick $Al_xGa_{1-x}N$ QWs with Al-content ranging from x = 50% up to x = 80% as a function of carrier density up to n = 7×10^{19} cm^{-3}. For the low Al-content $Al_{0.5}Ga_{0.5}N$ QW with Al-contents before the valence subbands crossover, larger g^{TE}_{peak} are obtained than that of the g^{TM}_{peak}, as the carriers are mainly populating the HH and LH bands. Specifically, the g^{TE}_{peak} and g^{TM}_{peak} of the $Al_{0.5}Ga_{0.5}N$ QW at n= 7×10^{19} cm^{-3} are 833.5 cm^{-1} and 186.5 cm^{-1}, respectively. For $Al_{0.6}Ga_{0.4}N$ QW with Al-content close to the crossover, stronger mixing effect is expected for the valence subbands. The separation between the HH band and CH band is closer than that of $Al_{0.5}Ga_{0.5}N$ QW, due to the use of higher Al-content. Thus, similar g^{TE}_{peak} and g^{TM}_{peak} are obtained for the $Al_{0.6}Ga_{0.4}N$ QW. Specifically, with relatively high carrier density of n= 7×10^{19} cm^{-3}, the g^{TE}_{peak} and g^{TM}_{peak} of the $Al_{0.6}Ga_{0.4}N$ QW are 1425 cm^{-1} and 1610 cm^{-1}, respectively.

For the high Al-content $Al_{0.7}Ga_{0.3}N$ QW and $Al_{0.8}Ga_{0.2}N$ QW with Al-contents after the valence subbands crossover, significantly increased TM-polarized material peak gains are obtained in comparison with TE-polarized gains, which are attributed from the larger energy separation of the CH and HH / LH bands at Γ-point that ensures the dominant C-CH transition. Specifically, with carrier density of n = 5×10^{19} cm^{-3}, the g^{TM}_{peak} of $Al_{0.8}Ga_{0.2}N$ QW and $Al_{0.7}Ga_{0.3}N$ QW are 4690 cm^{-1} and 3280 cm^{-1}; the g^{TE}_{peak} of $Al_{0.8}Ga_{0.2}N$ QW and $Al_{0.7}Ga_{0.3}N$ QW are 230 cm^{-1} and 765 cm^{-1}, respectively. Therefore, TM-polarized lasing is feasible for high Al-content AlGaN QW deep UV lasers emitting in 220-230 nm spectral regime.

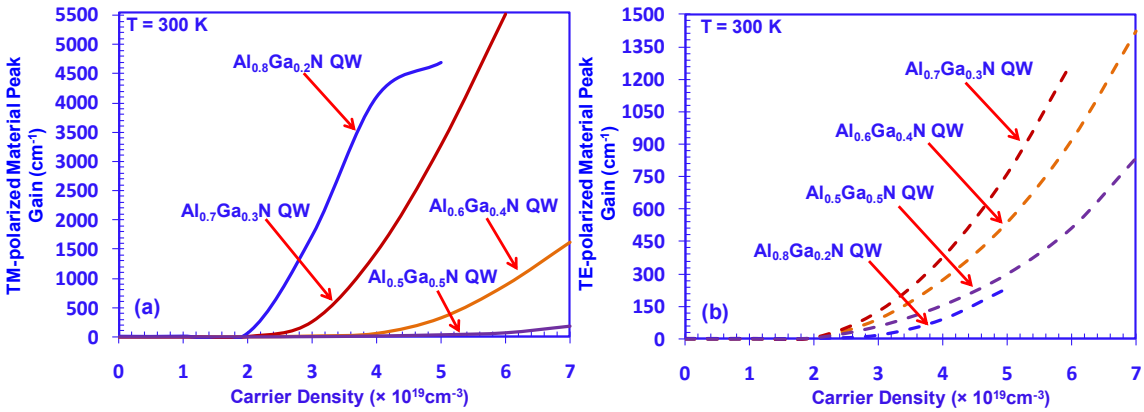

Figure 9-8: *(a) TM-polarized peak optical material gain and (b) TE-polarized peak optical material gain as a function of carrier density for 3-nm thick $Al_xGa_{1-x}N$ QWs (x = 50% - 80%) with AlN barriers.*

Figure 9-9 illustrates the ratio of TM-polarized peak optical material gain and TE-polarized peak optical material gain as a function of Al-content (*x*) for $Al_xGa_{1-x}N$ QWs with n = 5×10^{19} cm^{-3}. For AlGaN QWs with Al-content below x ~ 68%, which are before the valence-bands crossover, the g^{TM}_{peak} / g^{TE}_{peak} ratios are ~ 0.08-0.6. In contrast, for high Al-content AlGaN QWs after the valence-bands crossover, the g^{TM}_{peak} / g^{TE}_{peak} ratios increase dramatically, which are ~ 4.3 for $Al_{0.7}Ga_{0.3}N$ QW and ~ 20.2 for $Al_{0.8}Ga_{0.2}N$ QW. The increase of the g^{TM}_{peak} / g^{TE}_{peak} ratio indicates that the C1-CH1 transition is dominant after the valence subbands crossover for higher Al-content AlGaN QWs.

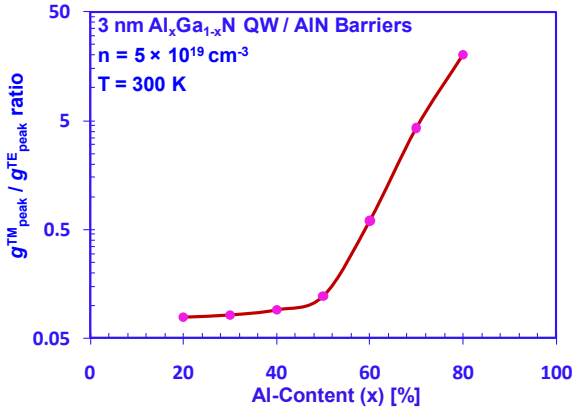

Figure 9-9: *The ratio of g^{TM}_{peak} and g^{TE}_{peak} as a function of Al-content (x) for $Al_xGa_{1-x}N$ QWs with n = 5×10^{19} cm^{-3} at T = 300 K.*

9.4 Carrier Lifetime and Differential Gain for High Al-Content AlGaN QWs

The understanding of the carrier lifetime for AlGaN QWs active region for various carrier density levels are of great importance in optimizing the current injection for deep-UV and mid-UV

lasers. The current injection efficiency for QW lasers, which is defined as the fraction of the injected current density that recombine in the QW at threshold condition, depends on the carrier recombination lifetime in the QW at threshold condition. Thus, the complete understanding of the carrier lifetime in the AlGaN QW enables the elucidation in the device physics of AlGaN QW for understanding the radiative recombination lifetime and radiative efficiency in the QW, as well as for optimizing to reduce the threshold current density in the QW lasers.

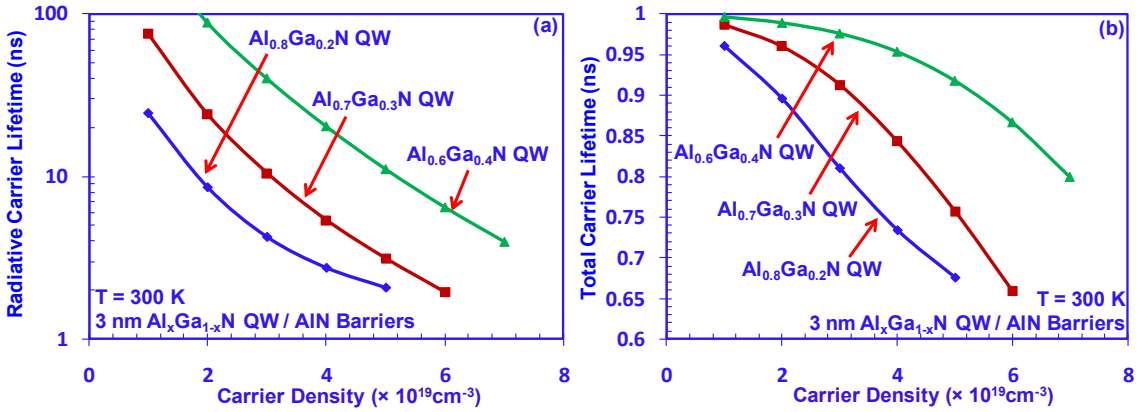

Figure 9-10: *(a) Radiative carrier lifetime, and (b) total carrier lifetime as a function of carrier density for 3-nm $Al_xGa_{1-x}N$ (x =0.6, 0.7, 0.8) QW with AlN barriers at room temperature.*

Figure 9-10(a) shows the radiative carrier lifetime (τ_{rad}) as a function of carrier density for 3-nm $Al_xGa_{1-x}N$ (x =0.6, 0.7, 0.8) QW with AlN barriers at room temperature. The calculation details and formulas can be found in Chapter 8. The τ_{rad} decreases with increasing carrier density for these three cases. For $Al_xGa_{1-x}N$ QWs with Al-contents of 70% and 80%, the radiative carrier life time is reduced compared to the $Al_{0.6}Ga_{0.4}N$ QW, which is attributed from the larger spontaneous emission radiative recombination rate for high Al-content $Al_xGa_{1-x}N$ QWs after the valence subbands crossover.

The total carrier lifetime (τ_{total}) is obtained the same way as in reference 33, which has been covered in Chapter 8. The monomolecular recombination rate (A) employed here is $A = 1\times10^9\ s^{-1}$ [20]. Figure 8-10(b) shows the total carrier life time as a function of carrier density for 3-nm $Al_xGa_{1-x}N$ (x =0.6, 0.7, 0.8) QW with AlN barriers at room temperature. The τ_{total} are reduced for the $Al_{0.8}Ga_{0.2}N$ and $Al_{0.7}Ga_{0.3}N$ QWs, in comparison with the $Al_{0.6}Ga_{0.4}N$ QW before the valence

subbands crossover. Thus, high Al-content $Al_xGa_{1-x}N$ QWs can lead to lower total carrier lifetimes.

The differential gain is an important parameter determining the high speed modulation bandwidth and relaxation frequency in QW lasers. The relaxation frequency and modulation bandwidth for QW lasers are proportional to the square root of the differential gain at a particular threshold carrier density. Note that the large differential gain for QW lasers is also important for enabling low threshold carrier density operation, which will in turn lead to significant reduction in non-radiative recombination current density at threshold condition. [37, 42-46].

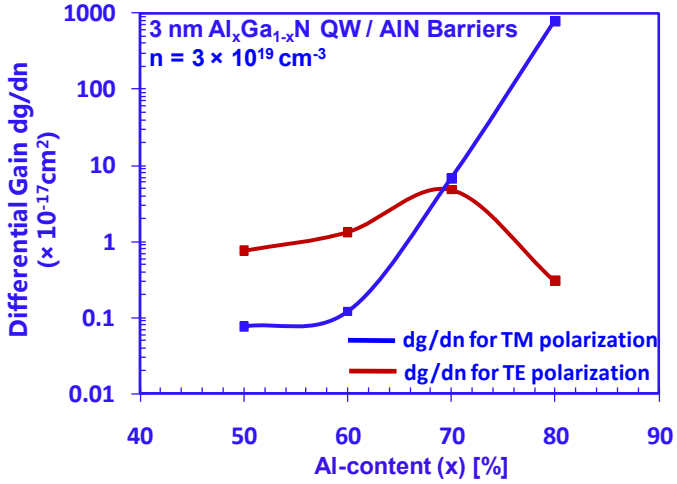

Figure 9-11: *Differential gain as a function of Al-content (x = 50%- 80%) for 3-nm $Al_xGa_{1-x}N$ QW with AlN barriers at carrier density of 3 × 10^{19} cm^{-3} at room temperature.*

Figure 9-11 shows the TE- and TM-polarized differential gains (dg/dn^{TE}, and dg/dn^{TM}) as a function of Al-content (x = 50%- 80%) for 3-nm $Al_xGa_{1-x}N$ QW with AlN barriers with n = 3 × 10^{19} cm^{-3} at room temperature. The TM-polarized differential gain increases with increasing Al-content of the $Al_xGa_{1-x}N$ QW; while the differential gain for TE polarization first increases with Al-content, reaches maximum, then decreases with higher Al-content. Before the valence subbands crossover, for the $Al_{0.5}Ga_{0.5}N$ QW and $Al_{0.6}Ga_{0.4}N$ QW, the TE-polarized differential gains (dg/dn^{TE} = 0.766 × 10^{-17} cm^2 for $Al_{0.5}Ga_{0.5}N$ QW, and dg/dn^{TE} = 1.346 × 10^{-17} cm^2 for $Al_{0.6}Ga_{0.4}N$ QW) are higher than the TM-polarized gains. For higher Al-content $Al_xGa_{1-x}N$ QWs (x = 70%, 80%) after the valence subbands crossover, TM-polarized differentials gains become higher than TE-polarized differential gains. For $Al_{0.7}Ga_{0.3}N$ QW, the TM-polarized differential gain (dg/dn^{TM} =

6.791 × 10^{-17} cm^2) is ~ 1.4 times of the TE-polarized differential gain (dg/dn^{TE} = 4.835 × 10^{-17} cm^2). For $Al_{0.8}Ga_{0.2}N$ QW, the TM-polarized differential gain becomes significantly higher (dg/dn^{TM} = 785.064 × 10^{-17} cm^2), while the TE-polarized differential gain (dg/dn^{TE} = 0.304 × 10^{-17} cm^2) is almost negligible. This finding indicates that the use of high Al-content AlGaN QW for deep UV lasers could potentially lead to improved modulation bandwidth and reduced threshold carrier density attributing to the significant larger differential gain, in comparison to those for mid UV lasers employing lower Al-content AlGaN QW.

9.5 Threshold Analysis of $Al_xGa_{1-x}N$ QW Deep UV Lasers

The threshold properties are analyzed for $Al_xGa_{1-x}N$ QW mid- and deep- UV lasers with Al-contents ranging from x = 50% up to x = 80%. The optical confinement factor (Γ_{opt}) is employed as 0.02 [20] in the analysis. The internal losses (α_i) are used as from 14 cm^{-1} [14] up to 50 cm^{-1} [20] for typical AlGaN QW lasers. The laser cavity length is assumed as 500 μm [14, 20]. The end-facet reflectivities are assumed as 95% and 35%, which correspond to mirror loss (α_m) of 11 cm^{-1}. By using the equation $\Gamma_{opt} g_{th} = \alpha_i + \alpha_m$, the threshold gains ($g_{th}$) are estimated as ~1250 cm^{-1} (α_i = 14 cm^{-1}) and ~3050 cm^{-1} (α_i = 50 cm^{-1}), respectively.

The threshold carrier densities (n_{th}) can be estimated from the TM-polarized material peak gain and carrier density relation in figure 8-8(a). For the lasers with the threshold gain g_{th} ~ 1250 cm^{-1}, the threshold carrier densities (n_{th}) are 2.8×10^{19} cm^{-3}, 3.9×10^{19} cm^{-3} and 6.5×10^{19} cm^{-3} for $Al_{0.8}Ga_{0.2}N$ QW (λ_{peak} = 221.8 nm), $Al_{0.7}Ga_{0.3}N$ QW (λ_{peak} = 231.3 nm) and $Al_{0.6}Ga_{0.4}N$ QW (λ_{peak} = 247.5 nm), respectively. For the lasers with g_{th} ~ 3050 cm^{-1}, the threshold carrier densities (n_{th}) of 3.5×10^{19} cm^{-3} and 4.9×10^{19} cm^{-3} are obtained for $Al_{0.8}Ga_{0.2}N$ QW and $Al_{0.7}Ga_{0.3}N$ QW, respectively.

Figures 9-12(a), 9-12 (b) and 9-12 (c) show TM- and TE-polarized material peak gains as a function of radiative current density (J_{rad}) for 3-nm thick $Al_xGa_{1-x}N$ QWs (x = 60%, 70% and 80%) with AlN barriers, respectively. The J_{rad} is obtained the same way as in reference 33. Note that the threshold carrier density for the $Al_{0.6}Ga_{0.4}N$ QW is larger than the $Al_{0.7}Ga_{0.3}N$ QW and

$Al_{0.8}Ga_{0.2}N$ QW. However, the transparency radiative current density is smaller compared to the $Al_{0.7}Ga_{0.3}N$ QW and $Al_{0.8}Ga_{0.2}N$ QW. Moreover, the transparency radiative current density of $Al_{0.7}Ga_{0.3}N$ QW is similar with $Al_{0.8}Ga_{0.2}N$ QW. Before the valence subbands crossover, for $Al_{0.6}Ga_{0.4}N$ QW, the material peak gain versus J_{rad} relations are similar for both TE and TM polarizations. After the valence subbands crossover, for $Al_{0.7}Ga_{0.3}N$ QW and $Al_{0.8}Ga_{0.2}N$ QWs, the J_{rad} for TE-polarized material peak gain become significantly smaller than that of the TM-polarized material peak gain.

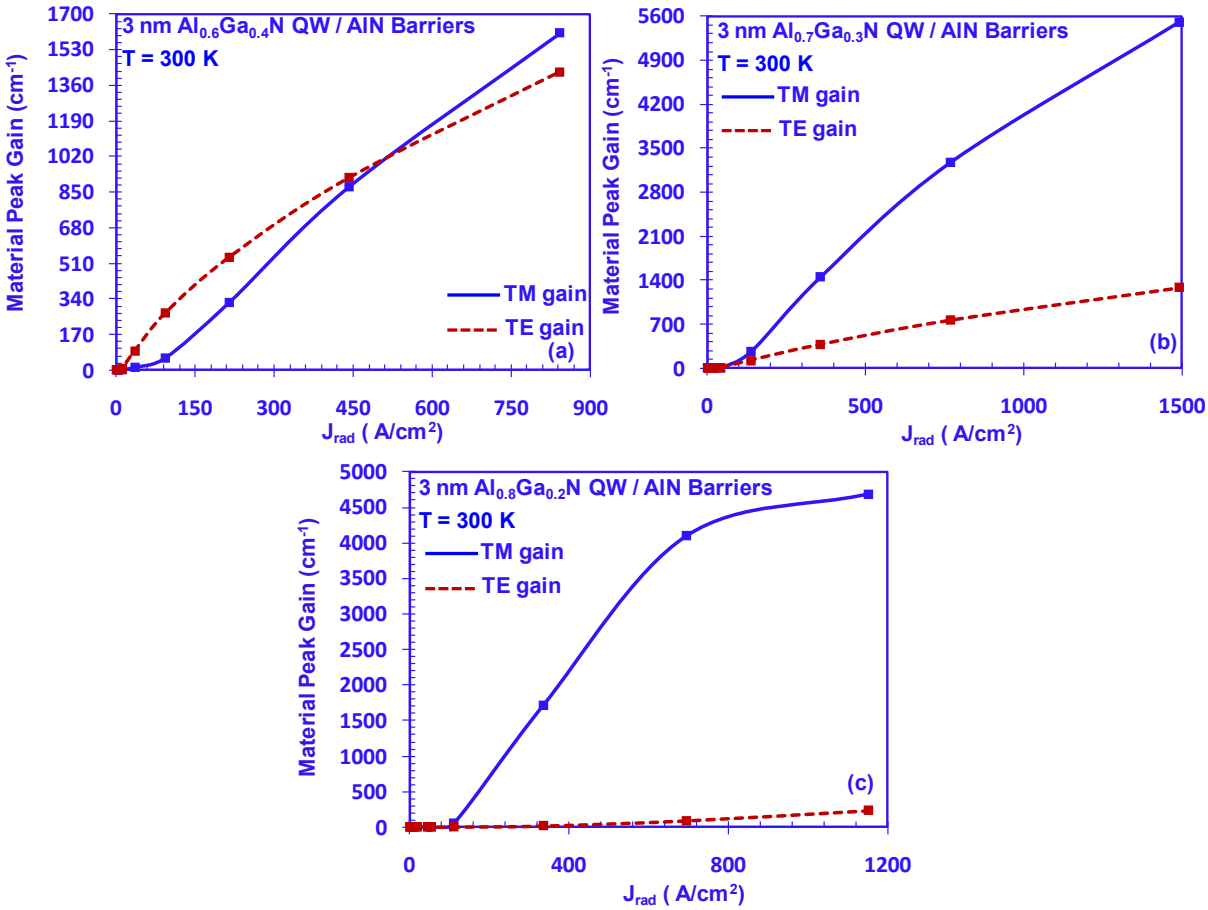

Figure 9-12: *TM- and TE-polarized material peak gain as a function of radiative current density for 3-nm thick (a) $Al_{0.6}Ga_{0.4}N$ QWs, (b) $Al_{0.7}Ga_{0.3}N$ QWs, (c) $Al_{0.8}Ga_{0.2}N$ QWs with AlN barriers.*

Figures 9-13(a) and 9-13(b) show both the TE- and TM-polarized material peak gain (g^{TE}_{peak} and g^{TM}_{peak}) as a function of total current density (J_{tot}) for 3-nm thick $Al_xGa_{1-x}N$ QWs (x = 50% - 80%) with AlN barriers. The monomolecular recombination rates employed here is $A = 2\times10^9\ s^{-1}$. Note that the J_{tot} includes both the radiative current density and nonradiative current density (J_{tot} =

J_{rad}+ J_{nr}). In our analysis, the monomolecular current density as the nonradiative term (J_{mono} ~ $A{\cdot}n$) has only been considered. The Auger current density (J_{Auger}) component is neglected, as this recombination is negligible for wide bandgap AlGaN QWs [47-51]. For low Al-content $Al_xGa_{1-x}N$ QWs (x = 50%, 60%), both the TE- and TM- polarized material peak gains are low, even at high J_{tot} of ~7000 A/cm^2, which can be attributed to the low matrix element for the $Al_xGa_{1-x}N$ QWs before the valence subbands crossover. For high Al-content $Al_xGa_{1-x}N$ QWs (x = 70%, 80%), larger TM-polarized material peak gains are achieved in comparison with the TE-polarized material peak gains at the same J_{tot}.

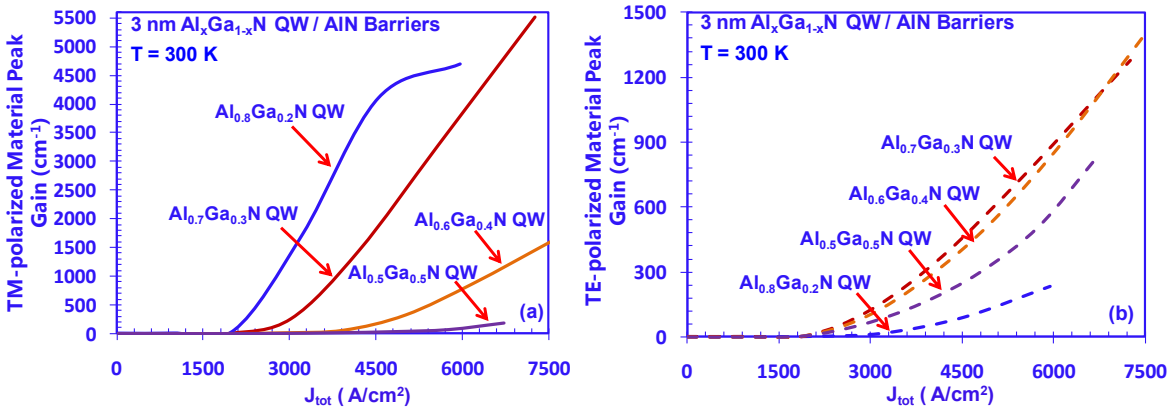

Figure 9-13: *(a) TM-polarized material peak gain (g^{TM}_{peak}) and (b) TE-polarized material peak gain (g^{TE}_{peak}) as a function of total current density for 3-nm thick $Al_xGa_{1-x}N$ QWs (x = 50% - 80%) with AlN barriers. The monomolecular recombination rate is with A = 2×10^9 s^{-1}.*

Figure 9-14 shows TM-polarized material peak gain as a function of total current density for 3-nm thick $Al_xGa_{1-x}N$ QWs (x = 70%, 80%) with AlN barriers. The monomolecular recombination rates are with A = 6×10^8 s^{-1}, 1×10^9 s^{-1}, and 2×10^9 s^{-1}, respectively. For the laser structure with g_{th} ~ 3050 cm^{-1}, the threshold current density calculated for $Al_{0.8}Ga_{0.2}N$ QW and $Al_{0.7}Ga_{0.3}N$ QWs are 1525 A/cm^2 and 2100 A/cm^2 for A = 6×10^8 s^{-1}, 2200 A/cm^2 and 3050 A/cm^2 for A = 1×10^9 s^{-1}, 3900 A/cm^2 and 5400 A/cm^2 for A = 2×10^9 s^{-1}, respectively. For the laser structure with g_{th} ~ 1250 cm^{-1}, the threshold current density calculated for $Al_{0.8}Ga_{0.2}N$ QW and $Al_{0.7}Ga_{0.3}N$ QWs are 1075 A/cm^2 and 1350 A/cm^2 for A = 6×10^8 s^{-1}, 1600 A/cm^2 and 2175 A/cm^2 for A = 1×10^9 s^{-1}, 2925 A/cm^2 and 4050 A/cm^2 for A = 2×10^9 s^{-1}, respectively.

Note that the threshold carrier densities of the $Al_{0.8}Ga_{0.2}N$ and $Al_{0.7}Ga_{0.3}N$ QWs are reduced by 57% and 40% compared to the $Al_{0.6}Ga_{0.4}N$ QW, which in turn lead to reduced threshold current

densities. Specifically, the threshold current densities of the $Al_{0.8}Ga_{0.2}N$ and $Al_{0.7}Ga_{0.3}N$ QWs are reduced by 58% and 41% compared to the $Al_{0.6}Ga_{0.4}N$ QW.

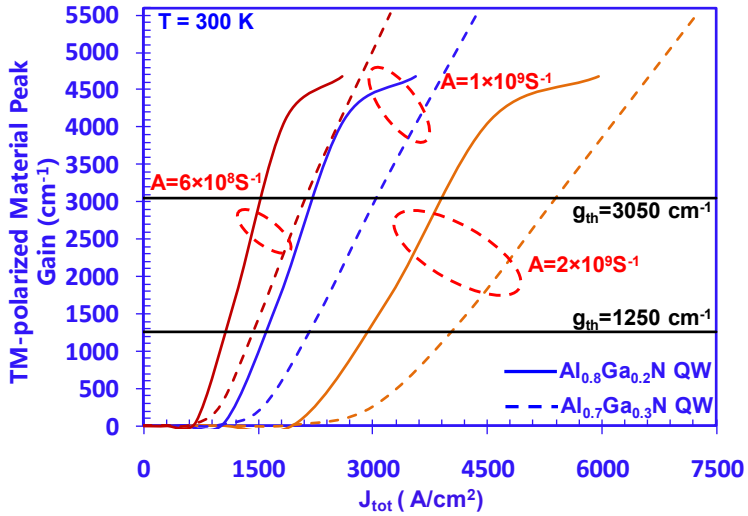

Figure 9-14: *TM-polarized material peak gain as a function of total current density for 3-nm thick $Al_xGa_{1-x}N$ QWs (x = 70%, 80%) with AlN barriers. The monomolecular recombination rates are with A = 6×10^8 s^{-1}, 1×10^9 s^{-1}, and 2×10^9 s^{-1}.*

9.6 Effect of AlGaN QW Thickness on the Valence Subbands Crossover

In order to illustrate the effect of AlGaN QW thickness on the valence subbands crossover, figure 9-15 shows the Al-contents for the valence subbands crossover for AlGaN QWs with thicknesses ranging from 0.5 nm up to 4 nm with n = 5×10^{19} cm^{-3}. As shown in figure 9-2, the valence subbands crossover is estimated around 57.2% for bulk AlGaN alloy. For the 4-nm AlGaN QW, the valence subbands crossover is obtained as ~51.9%, after taking into account the effect of strain and polarization fields.

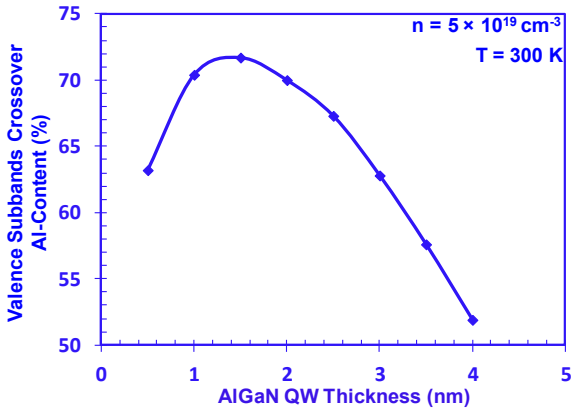

Figure 9-15: *The Al-contents for the valence subbands crossover of the AlGaN QWs with thicknesses ranging from 0.5 nm up to 4 nm with n = 5×10^{19} cm^{-3}.*

For thinner AlGaN QWs with thicknesses less than 4 nm, the Al-contents of the valence subbands crossover increase with the reducing QW thickness, which can be attributed to the quantum size effect. For AlGaN QWs with further reduced thicknesses of 0.5 nm or 1 nm, as the wavefunctions extend to the AlN barriers more than that of the thicker AlGaN QWs, thus the valence subbands crossovers require lower Al-contents, attributed from the barrier states from the thin QWs.

9.7 Summary

In summary, the optical gain and threshold characteristics are analyzed for high and low Al-content AlGaN QWs active regions for mid- and deep-UV lasers in this chapter. The effect of CH and HH/ LH valence subbands crossover is comprehensively analyzed for the optical gain and threshold characteristics of high and low Al-content AlGaN QWs with AlN barriers. The use of low Al-content AlGaN QWs results in low optical gain in mid-UV spectral regime due to the low optical matrix element of C-HH transition. The use of high Al-content AGaN QWs active regions after the valence subbands crossover leads to large TM-polarized optical gain at λ ~ 220-230 nm, as the large energy separation of the CH and HH / LH bands at Γ-point ensures the dominant C-CH transition. Shorter carrier lifetime and larger differential gains are also obtained by the high Al-content AlGaN QWs. Reduced threshold carrier densities and current densities are achieved by the high Al-content AlGaN QWs gain media. The effect of the AlGaN QW thickness on the valence subbands crossover is also clarified. The Al-contents of the crossover are higher for the thinner AlGaN QWs, while for QWs with thicknesses less than 1 nm, the crossovers happen with lower Al-contents, attributing from the increased AlN barrier states.

References for Chapter 9

[1] A. Yasan, R. McClintock, K. Mayes, D. Shiell, L. Gautero, S. R. Darvish, P. Kung, and M. Razeghi, Appl. Phys. Lett., **83**, 4701 (2003).

[2] A. J. Fischer, A. A. Allerman, M. H. Crawford, K. H. A. Bogart, S. R. Lee, R. J. Kaplar, W. W. Chow, S. R. Kurtz, K. W. Fullmer, and J. J. Figiel, Appl. Phys. Lett., **84**, 4762 (2004).

[3] V. Adivarahan, S. Wu, J. P. Zhang, A. Chitnis, M. Shatalov, V. Mandavilli, R. Gaska, and M. A. Khan, Appl. Phys. Lett., **84**, 3394 (2004).

[4] Z. Ren, Q. Sun, S. Y. Kwon, J. Han, K. Davitt, Y. K. Song, A. V. Nurmikko, H. K. Cho, W. Liu, J. A. Smart, and L. J. Schowalter, Appl. Phys. Lett., **91**, 051116 (2007).

[5] A. V. Sampath, M. L. Reed, C. Chua, G. A. Garrett, G. Dang, E. D. Readinger, H. Shen, A. Usikov, O. Kovalenkov, L. Shapovalova, V. A. Dmitriev, N.M. Johnson, and M. Wraback, M. L. Reed M. Wraback, Physica Status Solidi C, 5, 2303 (2008).

[6] C. G. Moe, M. L. Reed, G. A. Garrett, A. V. Sampath, T. Alexander, H. Shen, M. Wraback, Y. Bilenko, M. Shatalov, J. Yang, W. Sun, J. Deng, and R. Gaska, Appl. Phys. Lett., **96**, 213512 (2010).

[7] Y. Sakai, Y. Zhu, S. Sumiya, M. Miyoshi, M. Tanaka, and T. Egawa, Jpn. J. Appl. Phys., **49**, 022102 (2010).

[8] Y. Taniyasu and M. Kasu, Appl. Phys. Lett., **96**, 221110 (2010).

[9] H. Hirayama, N. Noguchi, N. Kamata, Applied Physics Express, **3**, 032102 (2010).

[10] T. Takano, Y. Narita, A. Horiuchi, and H. Kawanishi, Appl. Phys. Lett., **84**, 3567 (2004).

[11] M. Kneissl, Z. Yang, M. Teepe, C. Knollenberg, O. Schmidt, P. Kiesel, and N. M. Johnson, S. Schujman, and L. J. Schowalter, J. Appl. Phys., **101**, 123103 (2007).

[12] V. N. Jmerik, A. M. Mizerov, A. A. Sitnikova, P. S. Kop'ev, S. V. Ivanov, E. V. Lutsenko, N. P. Tarasuk, N. V. Rzheutskii, and G. P. Yablonskii, Appl. Phys. Lett., **96**, 141112 (2010).

[13] H. Yoshida, M. Kuwabara, Y. Yamashita, K. Uchiyama, and H. Kan, Appl. Phys. Lett., **96**, 211122 (2010).

[14] H. Yoshida, M. Kuwabara, Y. Yamashita, Y. Takagi, K. Uchiyama, and H. Kan, New Journal of Physics, **11**, 125013 (2009).

[15] M. Kneissl, D. W. Treat, M. Teepe, N. Miyashita, and N. M. Johnson, Appl. Phys. Lett. **82**, 25 (2003).

[16] C. Chen, M. Shatalov, E. Kuokstis, V. Adivarahan, M. Gaevski, S. Rai, and M. Asif Khan, Jpn. J. Appl. Phys., **43**, L1099 (2004).

[17] T. M. Al Tahtamouni, N. Nepal, J. Y. Lin, H. X. Jiang, and W. W. Chow, Appl. Phys. Lett. **89**, 131922 (2006).

[18] K. B. Nam, J. Li, M. L. Nakarmi, J. Y. Lin, and H. X. Jiang, Appl. Phys. Lett., **84**, 25 (2004).

[19] W. W. Chow, M. Kneissl, J. E. Northrup and N. M. Johnson, Appl. Phys. Lett. **90**, 101116 (2007).

[20] W. W. Chow, M. Kneissl, J. Appl. Phys., **98**, 114502 (2005).

[21] S. H. Park, S. L. Chuang, Appl. Phys. A **78**, 107–111 (2004).

[22] S. H. Park, Semicond. Sci. Technol., **24**, 035002 (2009).

[23] J. Zhang, H. Zhao, and N. Tansu, *Appl. Phys. Lett.*, **97**, 111105 (2010).

[24] T. Kolbe, A. Knauer, C. Chua, Z. Yang, S. Einfeldt, P. Vogt, N. M. Johnson, M. Weyers, and M. Kneissl, *Appl. Phys. Lett.*, **97**, 171105 (2010).

[25] T. K. Sharma, and E. Towe, J. Appl. Phys. **109**, 086104 (2011).

[26] J. Zhang, H. Zhao, and N. Tansu, Appl. Phys. Lett., **98**, 171111 (2011).

[27] T. K. Sharma, D. Naveh, and E. Towe, "Strain-driven light-polarization switching in deep ultraviolet nitride emitters", Physical Review B, **84**, 035305 (2011).

[28] T. Kolbe, A. Knauer, C. Chua, Z. Yang, V. Kueller, S. Einfeldt, P. Vogt, N. M. Johnson, M. Weyers, and M. Kneissl, "Effect of temperature and strain on the optical polarization of (In)(Al)GaN ultraviolet light emitting diodes," Appl. Phys. Lett. **99**, 261105 (2011).

[29] Y. Taniyasu, and M. Kasu, "Polarization property of deep-ultraviolet light emission from C-plane AlN/GaN short-period superlattices," Appl. Phys. Lett. **99**, 251112 (2011).

[30] E. F. Pecora, W. Zhang, A. Y. Nikiforov, L. Zhou, D. J. Smith, J. Yin, R. Paiella, L. D. Negro, and T. D. Moustakas, "Sub-250 nm room-temperature optical gain from AlGaN/AlN multiple quantum wells with strong band-structure potential fluctuations," Appl. Phys. Lett. **100**, 061111 (2012).

[31] E. F. Pecora, W. Zhang, J. Yin, R. Paiella, L. D. Negro, and T. D. Moustakas, “Polarization Properties of Deep-Ultraviolet Optical Gain in Al-Rich AlGaN Structures,” Appl. Phys. Express **5**, 032103 (2012).

[32] G. A. Garrett, P. Rotella, H. Shen, M. Wraback, T. Wunderer, C. L. Chua, Z. Yang, J. E. Northrup, and N. M. Johnson, "Sub-Threshold Time-Resolved Spectroscopy of Mid-UV AlGaN Laser Diode Structures Pseudomorphically Grown on Bulk AlN," in CLEO: Applications and Technology, OSA Technical Digest (online) (Optical Society of America, 2012), paper JTh1L.5.

[33] H. Zhao, G. Liu, X. H. Li, R. A. Arif, G. S. Huang, J. D. Poplawsky, S. Tafon Penn, V. Dierolf, and N. Tansu, “Design and Characteristics of Staggered InGaN Quantum Well Light-Emitting Diodes in the Green Spectral Regimes,” IET Optoelectron., vol. 3, no. 6, pp. 283-295, Dec. 2009.

[34] S. L. Chuang and C. S. Chang, Appl. Phys. Lett. 68, 1657 (1996).

[35] S. L. Chuang, IEEE J. Quantum Electron., **32**, 1791 (1996).

[36] S. L. Chuang and C. S. Chang, Semicond. Sci. Technol., **12**, 252 (1997).

[37] S. L. Chuang, Physics of Photonic Devices 2nd ed. Wiley, New York, 2009, Chap. 4.

[38] H. Zhao, R. A. Arif, Y. K. Ee, and N. Tansu, IEEE J. Quantum Electron., **45**, 66 (2009).

[39] I. Vurgaftman and J.R. Meyer, Chapter 2 in Nitride Semiconductor Devices, J. Piprek (Editor), Wiley, 2007.

[40] I. Vurgaftman and J.R. Meyer, J. Appl. Phys. **94**, 3675 (2003).

[41] M. Bass, C. Decusatis, G. Li, V. Lakshminarayanan, E. V. Stryland and V. N. Mahajan, Vol. 2, Handbook of optics, McGraw-Hill, 1994.

[42] L. A. Coldren and S. W. Corzine, Diode lasers and photonic integrated circuits. Wiley, New York, 1995.

[43] S. C. Kan, D. Vassilovski, T. C. Wu, and K. Y. Lau, “Quantum Capture and Escape in Quantum-Well Lasers – Implications on Direct Modulation Bandwidth Limitations,“ IEEE Photon. Technol. Lett., vol. 4, no. 5, pp. 428-431, May 1992.

[44] R. Nagarajan, M. Ishikawa, T. Fukushima, R. S. Geels, J. E. Bowers, “High-Speed Quantum Well Lasers and Carrier Transport Effects,” IEEE J. Quantum Electron., vol. 28, no. 10, pp. 1990-2008, Oct. 1992.

[45] R. Nagarajan, J. E. Bowers, “Effects of Carrier Transport on Injection Efficiency and Wavelength Chirping in Quantum-Well Lasers,“ IEEE J. Quantum Electron., vol. 29, no. 6, pp. 1601-1608, Jun. 1993.

[46] N. Tansu, and L. J. Mawst, “Current Injection Efficiency of 1300-nm InGaAsN Quantum-Well Lasers,” J. Appl. Phys., vol. 97, no. 5, pp. 054502-1 - 054502-18, Mar. 2005.

[47] J. Hader, J. V. Moloney, A. Thranhardt, and S. W. Koch, “Interband transitions in InGaN quantum wells,” in Nitride Semiconductor Devices, J. Piprek, Ed. Weinheim, Germany: Wiley-VCH, 2007, ch. 7, p. 164.

[48] J. Hader, J. V. Moloney, B. Pasenow, S.W. Koch, M. Sabathil, N. Linder, and S. Lutgen, “On the importance of radiative and Auger losses in GaNbased quantum wells,” Appl. Phys. Lett., vol. 92, Art. 261103, Jul. 2008.

[49] Kris T. Delaney, P. Rinke, and C. G. Van de Walle, “Auger recombination rates in nitrides from first principles,” Appl. Phys. Lett., vol. 94, Art. 191109, May. 2009.

[50] J. C. Zhang, Y. Sakai, and T. Egawa, “Low-temperature electroluminescence quenching of AlGaN deep ultraviolet light-emitting diodes,” Appl. Phys. Lett. 96, 013503 (2010).

[51] J. Piprek and S. Nakamura, “Physics of high-power InGaN/GaN lasers,” IEE Proc.: Optoelectron. 149, 145 (2002).

Chapter 10: Enhanced Gain by Novel Nanostructure Engineering of AlGaN-based UV Lasers

As discussed in the Chapter 9, our previous work [2] has revealed the valence subbands crossover in high Al-content AlGaN QWs. In high Al-content AlGaN QWs, the valence subbands crossover leads to strong conduction (C) -crystal-field split-off hole (CH) transition, which results in large transverse-magnetic (TM)-polarized optical gain for λ ~220-230 nm. Recent experimental works have also confirmed the dominant TM-polarized emission dominant for shorter wavelength with higher Al-content of AlGaN QWs LEDs [4, 5], which is in agreement with our theoretical prediction [2]. The subsequent paper has also studied about the temperature and barrier effect on the polarization properties of AlGaN QWs [6]. Recently, theoretical work by Sharma and co-authors [7] has also confirmed the valence subbands crossover for AlGaN alloys on $Al_{0.85}Ga_{0.15}N$ substrate, in agreement with previous finding [2]. Furthermore, subsequent theoretical work [8] has discussed the strain effect by using various AlGaN substrates or templates on the crossover of AlGaN alloys. Very recent study by G. A. Garrett and co-authors has experimentally confirmed our theoretical prediction of the CH and heavy hole (HH) bands crossover for AlGaN QWs by showing that the dominant photoluminescence polarization switched from transverse-electric (TE) polarized (λ ~ 253 nm) to TM-polarized (λ ~ 237 nm) emissions [9].

In contrast to the potential large material gain from high Al-content AlGaN QW in the deep-UV spectral regime, the use of conventional AlGaN QW for gain media emitting in the mid-UV spectral regime results in low material gain. Thus, approaches based on novel AlGaN-based QW wth large material gain in the mid-UV regime are of great interest. In order to address the issue of low optical gain at λ ~ 250-300 nm, we have proposed several novel nanostructure engineering approaches for AlGaN-based UV Lasers, which will be discussed in details in this chapter.

10.1 Design of AlGaN-Delta-GaN QW

Although large TM-polarized gain can be achieved by high Al-content conventional AlGaN QWs after the valence subbands crossover, it is still very challenging to obtain large optical gain

at λ ~220-300 nm. As shown in figure 10-1, the material gains were calculated for 3-nm conventional $Al_xGa_{1-x}N$ QW with AlN barriers with x = 20% - 80%. From our studies, large TM-polarized material gains (g^{TM}_{peak}) is achievable for $Al_xGa_{1-x}N$ QWs with x = 70% and 80% corresponding to λ_{peak} ~220-230 nm. The g^{TM}_{peak} values for $Al_{0.8}Ga_{0.2}N$ QW and $Al_{0.7}Ga_{0.3}N$ QW are ~ 4700 cm^{-1} and ~ 3300 cm^{-1} for carrier density (*n*) of 5×10^{19} cm^{-3}, respectively, while the corresponding TE-polarized gains are relatively low (g^{TE}_{peak} ~ 200-700 cm^{-1}).

In addition, the conventional $Al_xGa_{1-x}N$ QWs in the 250-320 nm spectral range are limited to relatively low gain for Al-contents below 60% (figure 10-1). For *n* = 5×10^{19} cm^{-3}, the g^{TE}_{peak} and g^{TM}_{peak} for $Al_{0.6}Ga_{0.4}N$ QW are ~550 cm^{-1} and ~330 cm^{-1}, respectively. The low optical gain for the conventional AlGaN QW in the ~250-320 nm spectral regime is attributed to the significant band filling for the heavy-hole (HH) / light-hole (LH) and CH subbands, which leads to challenges in obtaining high gain active material in this wavelength range [2]. Thus, the pursuit of AlGaN-based QW gain media with large optical gain in the mid-UV spectral regime is of great importance for laser applications. In addition, the availability of large TE-polarized deep-UV gain media is also important for laser structures that require high TE-polarized gain media.

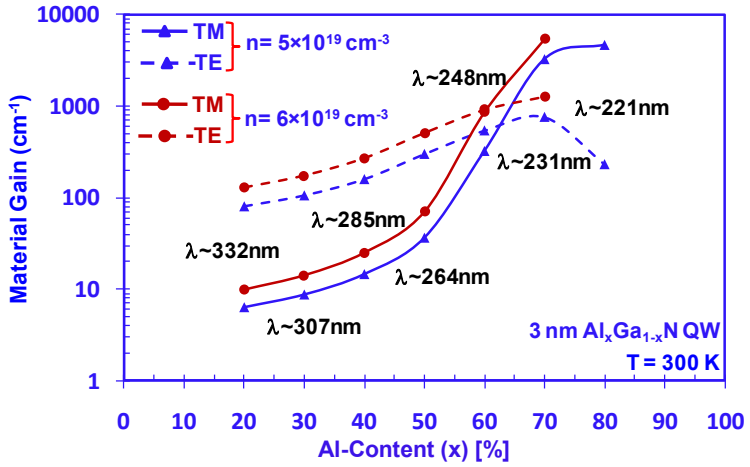

Figure 10-1: *TE- and TM-polarized material peak gain as a function of Al-content (x) for 3-nm $Al_xGa_{1-x}N$ QW with AlN barriers at carrier densities (n) of $5\times10^{19}cm^{-3}$ and $6\times10^{19}cm^{-3}$. The peak emission wavelengths (λ_{peak}) for different Al-contents are shown for n= $5\times10^{19}cm^{-3}$.*

10.1.1 Concept and Valence Band Structures of AlGaN-Delta-GaN QW

The delta QW is realized by the insertion of GaN delta-layer (3Å-9Å) in high Al-content AlGaN QWs. By employing the AlGaN-delta-GaN QW structure [inset in figure 10-2(b)], the strong

valence band mixing results in the valence subband rearrangement, which in turn leads to 1) higher HH1 and LH1 subband energy levels in comparison to that of the CH1 subband, 2) splitting of the HH1 and LH1 subbands, and 3) dominant C1-HH1 transition leading to large TE-polarized gain. Thus, large TE-polarized gains in the deep- and mid-UV spectral regimes are achievable for the AlGaN-delta-GaN QW gain media.

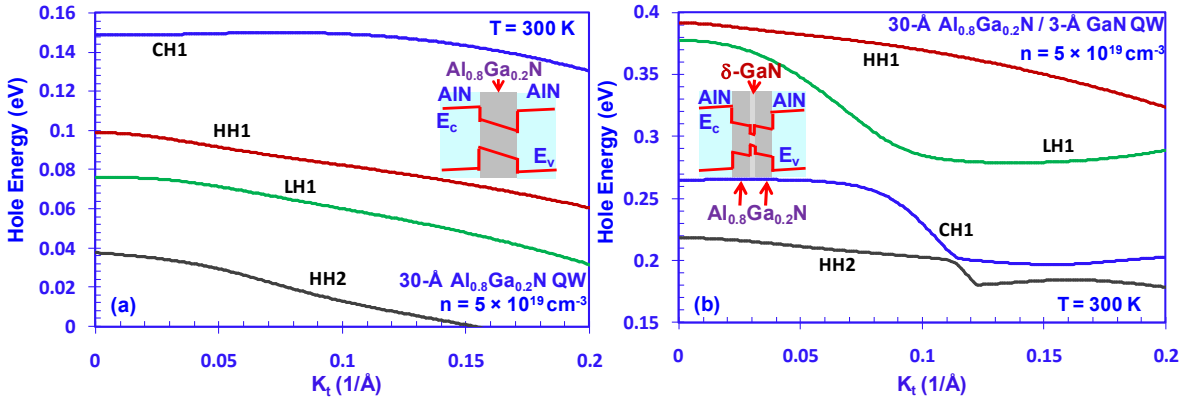

Figure 10-2: *The schematics and the valence band structures of (a) conventional 30-Å $Al_{0.8}Ga_{0.2}N$ QW and (b) 30-Å $Al_{0.8}Ga_{0.2}N$ / 3-Å GaN QW with AlN barriers.*

Figures 10-2(a) and 10-2(b) show the valence band structures for both conventional 30-Å $Al_{0.8}Ga_{0.2}N$ QW and 30-Å $Al_{0.8}Ga_{0.2}N$ / 3-Å GaN QW, respectively, for n=5×10^{19} cm^{-3} at T = 300 K. All structures studied here employed AlN barriers. For conventional $Al_{0.8}Ga_{0.2}N$ QW, the CH1 subband energy is much larger than those of the HH1 and LH1 subbands [figure 9-2(a)]. In contrast, the HH1 and LH1 subbands are re-arranged into higher subband energy levels than that of the CH1 subband for the 30-Å $Al_{0.8}Ga_{0.2}N$ / 3-Å GaN QW (delta-QW). The energy separation between the HH1 and CH1 subbands for the $Al_{0.8}Ga_{0.2}N$ / 3-Å GaN QW is relatively large (~140 meV) at Γ-point [figure 9-2(b)], which results in dominant C1-HH1 transition.

10.1.2 Polarization Engineering by the Use of AlGaN-Delta-GaN QW

Figure 10-3(a) shows both the TE- and TM-polarized optical gain spectra for 30-Å $Al_xGa_{1-x}N$ / 3-Å GaN QW (x = 0.7, 0.8) with n=5×10^{19} cm^{-3} at T = 300 K. Attributing to the insertion of the GaN delta-layer into $Al_xGa_{1-x}N$ QW, the band energies of HH and LH subbands are increased significantly than that of the CH subband. Thus, the TE-polarized gains for both 30-Å $Al_{0.7}Ga_{0.3}N$ / 3-Å GaN QW and 30-Å $Al_{0.8}Ga_{0.2}N$ / 3-Å GaN QW become dominant (g^{TE}_{peak} = 4442 cm^{-1} for x =

0.7, and g^{TE}_{peak} = 3537 cm^{-1} for x = 0.8), while the TM-polarized gains are negligible as compared to the TE-polarized gains.

Figure 10-3(b) shows the comparison of the TE-polarized optical gains for 30-Å $Al_xGa_{1-x}N$ / 3-Å GaN QW (x= 0.7, 0.8) and conventional 30-Å $Al_xGa_{1-x}N$ QW (x= 0.6, 0.7, 0.8) for $n = 5\times10^{19}$ cm^{-3} at T = 300 K. For conventional $Al_xGa_{1-x}N$ QW, relatively low TE-polarized gains (g^{TE}_{peak} = 539 cm^{-1} for x = 0.6; g^{TE}_{peak} = 763 cm^{-1} for x = 0.7; g^{TE}_{peak} = 232 cm^{-1} for x = 0.8) were obtained with λ_{peak} ~220-250 nm. In contrast, large TE-polarized gains were obtained with λ_{peak} ~245-255 nm for gain media employing $Al_xGa_{1-x}N$ delta-GaN QWs. For $Al_{0.7}Ga_{0.3}N$ / 3-Å GaN and $Al_{0.8}Ga_{0.2}N$ / 3-Å GaN QW, the TE-polarized gains are 4442 cm^{-1} and 3537 cm^{-1} for λ_{peak} ~ 253.6 nm and λ_{peak} ~ 245.1 nm, respectively.

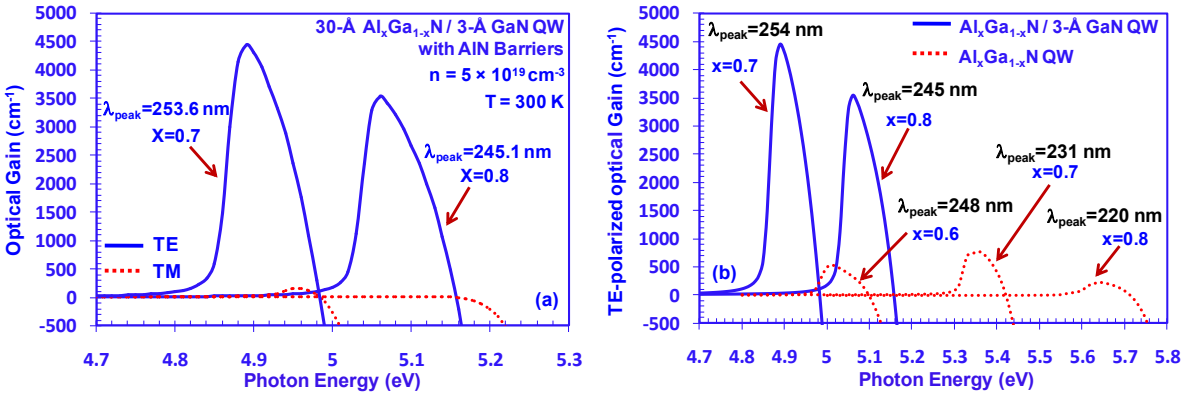

Figure 10-3: *(a) TE-polarized and TM-polarized gain spectra for 30-Å $Al_{0.8}Ga_{0.2}N$ / 3-Å GaN QW and (b) TE-polarized gain spectra for both 30-Å $Al_xGa_{1-x}N$ / 3-Å GaN QW and conventional $Al_xGa_{1-x}N$ QW with AlN barriers.*

10.1.3 Gain Characteristics of AlGaN-Delta-GaN QWs Structures

Figure 10-4(a) shows the TE-polarized gain spectra for AlGaN-delta-GaN QW as a function of GaN delta-layer thickness (d) with $n = 5\times10^{19}cm^{-3}$ at T= 300K. For GaN delta-layer thickness ≤ 9-Å (as delta layer), high TE-polarized gain can be obtained from the insertion of the delta layer attributed to the HH / CH band realignment in the QW. The use of the delta layer in the QW pushes the CH1 subband further away from the valence band edge (figure 10-2(b)), which leads to the C1-HH1 dominant transition. For GaN layer thickness > 9-Å, the TE-polarized gain decreases severely with larger GaN thickness, which indicates that the GaN layer behaves as

single QW-like active region. This finding indicates that the use of AlGaN-delta-GaN QW leads to high optical gain material for λ_{peak} ~240-300 nm, as well as large TE-polarized gain in the deep UV spectral regime.

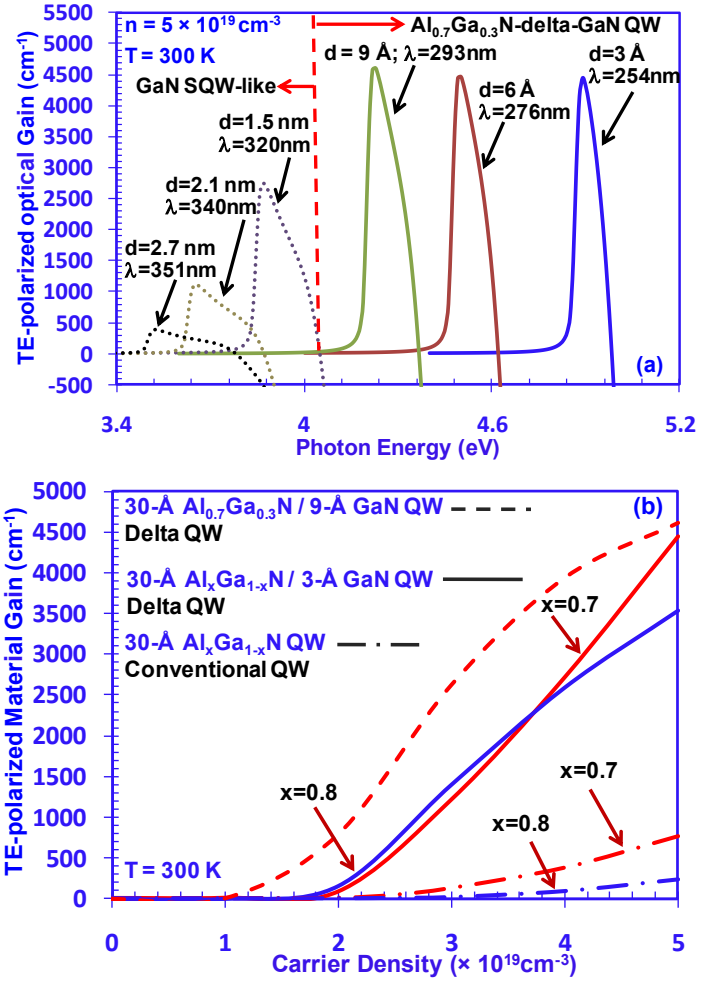

Figure 10-4: *(a) TE-polarized optical gain for 30-Å $Al_{0.7}Ga_{0.3}N$ / d-Å GaN QW at n = 5 × 10^{19} cm^{-3} and (b) TE-polarized material gain as a function of carrier density for 30-Å $Al_{0.7}Ga_{0.3}N$ / 9-Å GaN QW, 30-Å $Al_xGa_{1-x}N$ / 3-Å GaN QW (x=0.7, 0.8), and conventional 30-Å $Al_xGa_{1-x}N$ QW (x=0.7, 0.8).*

Figure 10-4(b) shows the TE-polarized material gain as a function of carrier density up to n = 5×10^{19} cm^{-3} at T = 300 K for 30-Å $Al_{0.7}Ga_{0.3}N$ / 9-Å GaN QW, 30-Å $Al_xGa_{1-x}N$ / 3-Å GaN QW (x=0.7, 0.8), and conventional 30-Å $Al_xGa_{1-x}N$ QW (x=0.7, 0.8). The 30-Å $Al_{0.7}Ga_{0.3}N$ / 9-Å GaN QW shows transparency carrier density (n_{tr}) at n_{tr} ~ 1.0×10^{19} cm^{-3}, and the n_{tr} ~ 1.8×10^{19} cm^{-3} are obtained for both 30-Å $Al_{0.7}Ga_{0.3}N$ / 3-Å GaN QW and 30-Å $Al_{0.8}Ga_{0.2}N$ / 3-Å GaN QW. All the delta QW gain media exhibit significantly higher TE-polarized materials gains, in comparison to

those of conventional AlGaN QWs (figure 9-4(b)). For $n > 4\times10^{19}$ cm^{-3}, the TE-polarized material gain for $Al_{0.7}Ga_{0.3}N$ / 3-Å GaN QW is ~1.05-1.26 times of the $Al_{0.8}Ga_{0.2}N$ / 3-Å GaN QW, which is attributed from better carrier confinement that leads to larger momentum matrix element. In comparison to the conventional 30-Å $Al_{0.7}Ga_{0.3}N$ QW, the insertion of 3-Å and 9-Å GaN delta-layer in the 30-Å $Al_{0.7}Ga_{0.3}N$ QW active regions lead to increase in TE-polarized gain up to ~ 5.8 times and ~6.0 times, while the increase in TE-polarized gain is ~15.3 times for 30-Å $Al_{0.8}Ga_{0.2}N$ / 3-Å GaN QW in comparison to that of conventional 30-Å $Al_{0.8}Ga_{0.2}N$ QW.

10.1.4 Threshold Analysis of AlGaN-Delta-GaN QW Mid- and Deep-UV Lasers

The threshold properties of AlGaN-delta-GaN QW for mid- and deep-UV lasers were analyzed. The laser structure (L_{cav} = 500 μm) with optical confinement factor of 0.02 [1] and mirror loss of 11 cm^{-1} were used, and the internal loss was assumed as 50 cm^{-1} [1]. The threshold gain (g_{th}) was estimated as ~3050 cm^{-1}. From figure 4(b), the threshold carrier densities (n_{th}) are $4.4\times10^{19}cm^{-3}$ and $4.2\times10^{19}cm^{-3}$ for $Al_{0.8}Ga_{0.2}N$ / 3-Å GaN QW (λ ~ 245nm) and $Al_{0.7}Ga_{0.3}N$ / 3-Å GaN QW (λ ~ 254nm), respectively. For mid UV lasers (λ ~ 293nm) using $Al_{0.7}Ga_{0.3}N$ / 9-Å GaN QW, the threshold carrier density is 3.3×10^{19} cm^{-3}.

In summary, the gain characteristics of high Al-content AlGaN-delta-GaN QWs were calculated and analyzed for mid- and deep-UV lasers. The insertion of the ultra-thin GaN layer in high Al-content AlGaN QW leads to the strong rearrangement of the valence subbands of the QW. Attributing to the strong transition between the C1-HH1 subbands, high TE-polarized optical gain is achievable for high Al-content AlGaN-delta-GaN QWs as active regions for mid- and deep-UV lasers emitting at λ ~ 250-300 nm. Recent experimental work by Taniyasu and co-authors [11] has reported the polarization properties of the deep-UV emission from AlN/GaN short-period superlattices. The study revealed that stronger TE-polarized deep-UV emission can be obtained by inserting a very thin GaN layer into AlN active region, similar with our prediction based on high Al-content $Al_xGa_{1-x}N$-delta-GaN QW structure [10].

10.2 Engineering of AlGaN-Delta-GaN QW

In this section, we present a comprehensive optimization study on the optical gain and threshold characteristics of AlGaN-delta-GaN QWs with varying delta-GaN positions and AlGaN QWs compositions for the mid- and deep-UV spectral regimes.

10.2.1 Concept of Asymmetric AlGaN-Delta-GaN QWs

Figure 9-5 shows the schematics of the AlGaN-delta-GaN QW structure. Our previous work [10] revealed that the use of symmetric structure of the high Al-content AlGaN-delta-GaN QWs led to large TE-polarized optical gain at λ ~240-300 nm. Here, we present the comprehensive optimization study of the asymmetric AlGaN-delta-GaN QWs. The asymmetric QWs can be introduced by engineering the thicknesses of the AlGaN layers (d_1, d_2) and / or the Al-contents of the AlGaN layers (x_1, x_2) surrounding the delta-GaN layer.

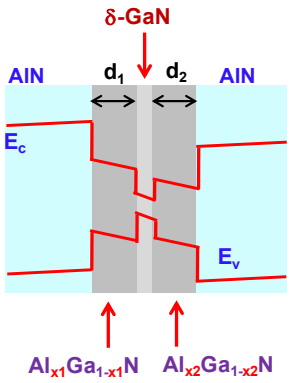

Figure 10-5: *The schematics energy band lineups of the $Al_{x1}Ga_{1-x1}N$/ delta-GaN/ $Al_{x2}Ga_{1-x2}N$ QW structure with AlN barriers.*

For the AlGaN-delta-GaN QWs, the energy levels of the HH and light hole (LH) subbands are higher than that of the CH subband, which leads to the dominant C-HH transition. Note the difference in the effective masses of the electrons and holes in III-Nitride alloys leads to different spreading of the wave functions for electrons and holes in III-Nitride based QWs. In the case of identical effective masses for both electrons and holes, the optimized overlap will occur with the delta position at the center of the QWs. However, the effective masses for holes are larger than those of electrons in nitride-based QWs, thus the optimization of the electron-hole wavefunction

overlap can be achieved by using engineering of the delta layer position (d_1, d_2) [figures 10-6(a) and 10-6(b)] or by using different compositions of AlGaN QW sub-layers (x_1, x_2) [figures 10-7(a) and 10-7(b)]. The optimized overlap function leads to improved spontaneous emission rate and material gain in the asymmetric QW structures.

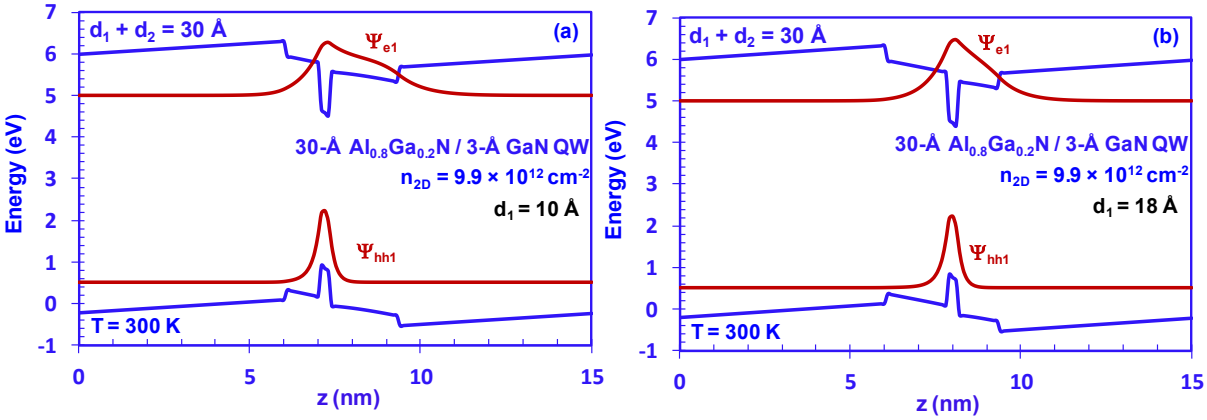

Figure 10-6: *Energy lineups with electron wavefunction EC1 and hole wave function HH1 for the 30-Å $Al_{0.8}Ga_{0.2}N$ / 3-Å GaN QW with (a) d_1 = 10 Å, and (b) d_1 = 18 Å.*

Figures 10-6(a) and 10-6(b) show the energy lineups with electron wavefunction EC1 and hole wave function HH1 for the 30-Å $Al_{0.8}Ga_{0.2}N$ / 3-Å GaN QW with different d_1 thicknesses and sheet carrier density (n_{2D}) of 9.9×10^{12} cm^{-2} at room temperature. For comparison purpose, the total thicknesses of d_1 and d_2 are maintained as 30Å for both cases. For the 30-Å $Al_{0.8}Ga_{0.2}N$ / 3-Å GaN QW structure with d_1 = 10 Å in figure 2(a), the electron-hole wavefunction overlap (Γ_{e_hh}) is obtained as ~ 63.51%. By engineering the delta QW structure with d_1 = 18 Å, as shown in figure 2(b), the electron and hole wavefunctions are strongly localized toward the center of the QW active region, attributing to the engineered spreading of the wavefunctions, which leads to the enhancement of the Γ_{e_hh} ~ 73.92%.

Figures 10-7(a) and 10-7(b) show the energy band lineups with electron wavefunction EC1 and hole wave function HH1 for the 30-Å $Al_{0.75}Ga_{0.25}N$ / 3-Å GaN / $Al_{0.65}Ga_{0.35}N$ QW and $Al_{0.75}Ga_{0.25}N$ / 3-Å GaN / $Al_{0.85}Ga_{0.15}N$ QW with n_{2D} = 1.65×10^{13} cm^{-2} at T = 300 K, and the thickness of d_1 is maintained the same with the thickness of d_2. For the 30-Å $Al_{0.75}Ga_{0.25}N$ / 3-Å GaN / $Al_{0.65}Ga_{0.35}N$ QW, as the bandgap of $Al_{0.75}Ga_{0.25}N$ QW is larger than that of $Al_{0.65}Ga_{0.35}N$ QW, which leads to the Γ_{e_hh} ~ 60.31%. By engineering the Al-contents of the AlGaN layers as x_1

= 0.75, and x_2 = 0.85, as shown in figure 3(b), the electron and hole wavefunctions are pushed toward the center of the QW active region, as the bandgap of $Al_{0.85}Ga_{0.15}N$ is larger than that of $Al_{0.75}Ga_{0.25}N$, which results in the improvement of the Γ_{e_hh} ~ 78.83%. Therefore, the matrix element will be enhanced attributing to the improved Γ_{e_hh}, which will contribute to the optical gain by using the optimized asymmetric AlGaN-delta-GaN QW structures.

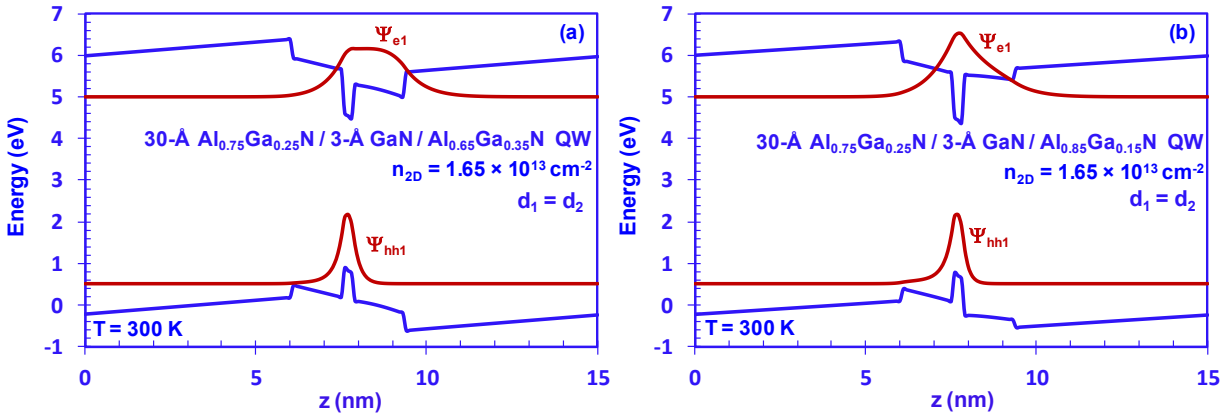

Figure 10-7: *Energy lineups with electron wavefunction EC1 and hole wave function HH1 for (a) the 30-Å $Al_{0.75}Ga_{0.25}N$ / 3-Å GaN / $Al_{0.65}Ga_{0.35}N$ QW, and (b) the 30-Å $Al_{0.75}Ga_{0.25}N$ / 3-Å GaN / $Al_{0.85}Ga_{0.15}N$ QW.*

10.2.2 Optical Gain for AlGaN-Delta-GaN QWs with Different Delta-Layer Positions

Figure 10-8 shows the TE-polarized optical gain spectra for 30-Å $Al_{0.8}Ga_{0.2}N$ / 3-Å GaN QW with n_{2D} = 1.65×10^{13} cm^{-2} at T = 300 K with varying d_1 thicknesses. For the asymmetric QW with d_1 = 18 Å, the TE-polarized optical gain is larger than that of the symmetric QW with d_1 = 15 Å, attributing to the enhanced Γ_{e_hh} from the optimized AlGaN-delta-GaN QW structure. For the asymmetric QW with d_1 = 10 Å, the optical gain is slightly lower due to the weaker confinement of the electron and hole wavefunctions. Note that the peak emission wavelengths (λ_{peak}) for the asymmetric QWs with d_1 = 10 Å and 18 Å are ~ 246 nm, and ~245 nm, respectively, which are very similar with the symmetric QW. In comparison with the conventional $Al_{0.6}Ga_{0.4}N$ QW with similar emission wavelength, the optimized asymmetric 30-Å $Al_{0.8}Ga_{0.2}N$ / 3-Å GaN QW with d_1 = 18 Å show ~ 6 times enhancement in the TE-polarized optical gain at mid-UV spectra regime.

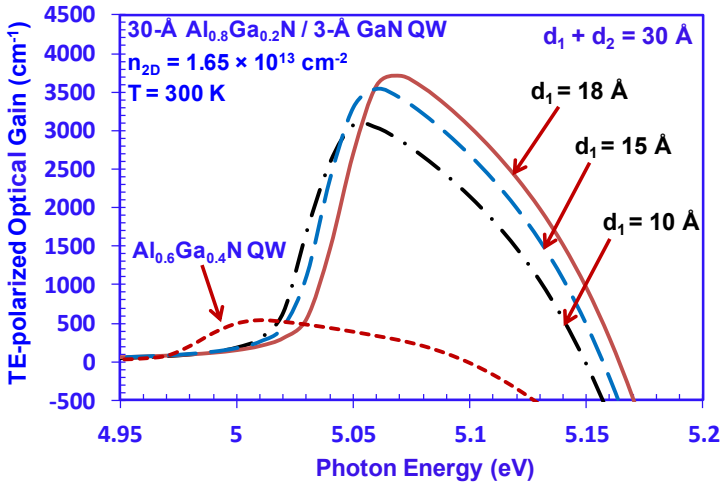

Figure 10-8: *TE-polarized optical gain spectra for 30-Å $Al_{0.8}Ga_{0.2}N$ / 3-Å GaN QW with n_{2D} = 1.65×10^{13} cm^{-2} at T = 300 K with varying d_1 thicknesses.*

Figure 10-9 shows the TE-polarized material peak gain (g^{TE}_{peak}) as a function of the d_1 thickness for the 30-Å $Al_{0.8}Ga_{0.2}N$ / 3-Å GaN QW with n_{2D} = 1.65×10^{13} cm^{-2} at T = 300 K. With the d_1 thicknesses ranging from 5 Å up to 20 Å, the TE-polarized material gain varies from ~3078 cm^{-1} (d_1 = 10 Å) up to ~3703 cm^{-1} (d_1 = 18 Å). Therefore, very large optical gain can be maintained for emission wavelength ~245 nm for the asymmetric AlGaN-delta-GaN QW structures with different delta-GaN positions.

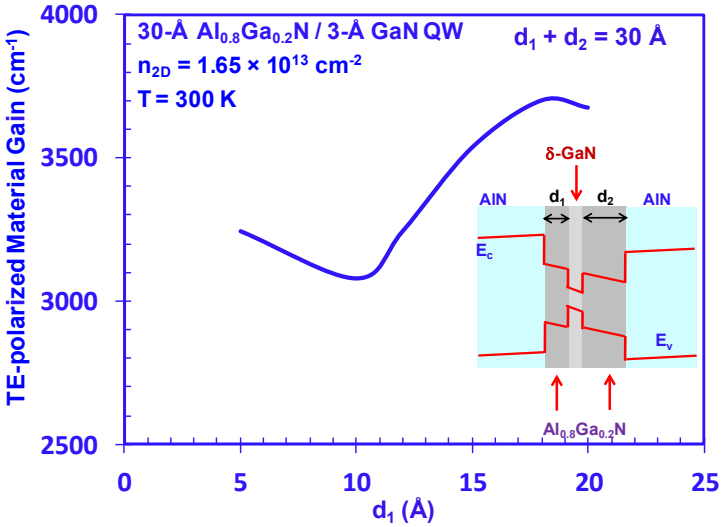

Figure 10-9: *TE-polarized material peak gain as a function of the d_1 thickness for the 30-Å $Al_{0.8}Ga_{0.2}N$ / 3-Å GaN QW with n_{2D} = 1.65×10^{13} cm^{-2} at T = 300 K.*

10.2.3 Optical Gain for AlGaN-Delta-GaN QWs with Different Al-Content AlGaN QWs

Figure 10-10 illustrates the TE-polarized optical gain spectra for 30-Å $Al_{x1}Ga_{1-x1}N$ / 3-Å GaN / $Al_{x2}Ga_{1-x2}N$ QW with n_{2D} = 1.65×10^{13} cm^{-2} at T = 300 K with varying combinations of the Al-contents x_1 and x_2 of the AlGaN QWs. For the optimized delta QW with Al-contents of x_1 = 0.75 and x_2 = 0.85, very large TE-polarized optical gain (g^{TE}_{peak} ~3967 cm^{-1}) can be obtained at λ_{peak} ~ 244 nm, attributing to the improved Γ_{e_hh} from the asymmetric QW structure. For the asymmetric cases of $Al_{0.85}Ga_{0.15}N$ / 3-Å GaN / $Al_{0.75}Ga_{0.25}N$ QW (x_1 = 0.85, x_2 = 0.75) and $Al_{0.8}Ga_{0.2}N$ / 3-Å GaN / $Al_{0.7}Ga_{0.3}N$ QW (x_1 = 0.8, x_2 = 0.7), large optical gain can be obtained with emission wavelength ranging from ~244-252 nm, which are ~6-7 times larger than that of the conventional $Al_{0.6}Ga_{0.4}N$ QW emitting at similar wavelengths.

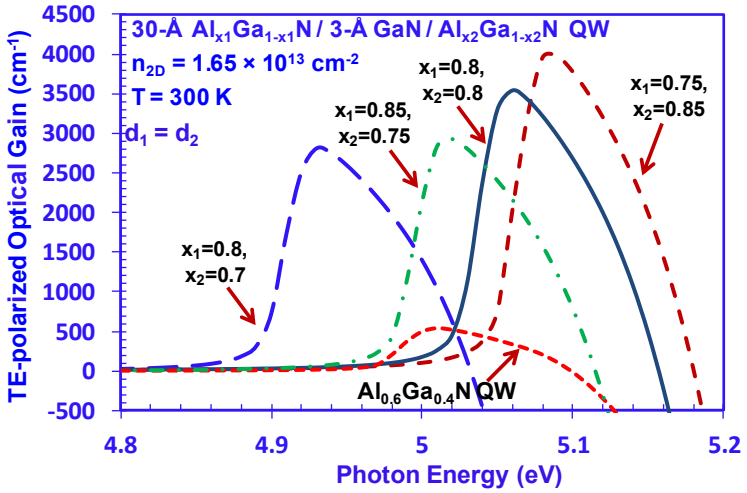

Figure 10-10: *TE-polarized optical gain spectra for 30-Å $Al_{x1}Ga_{1-x1}N$ / 3-Å GaN / $Al_{x2}Ga_{1-x2}N$ QW with n_{2D} = 1.65×10^{13} cm^{-2} at T = 300 K with varying combinations of the Al-contents x_1 and x_2.*

Figure 10-11 shows the TE-polarized material peak gain for the 30-Å $Al_{x1}Ga_{1-x1}N$ / 3-Å GaN / $Al_{x2}Ga_{1-x2}N$ QW with n_{2D} = 1.65×10^{13} cm^{-2} at T = 300 K. By varying the Al-contents of the AlGaN layers surrounding the delta-GaN layer, the TE-polarized material peak gains are ranged from ~2700 cm^{-1} up to ~4000 cm^{-1}. Therefore, the optimized asymmetric QW structures with different Al-contents can lead to enhanced optical gain. Also, large TE-polarized gain can be maintained by different combinations of the Al-contents of the AlGaN QWs, which will provide flexibility in the

experimental realizations of the AlGaN-delta-GaN QWs lasers emitting in mid- and deep-UV spectral regimes.

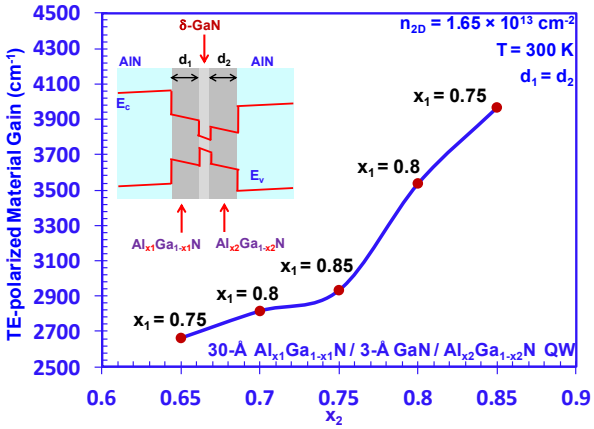

Figure 10-11: *TE-polarized material peak gain for the 30-Å $Al_{x1}Ga_{1-x1}N$ / 3-Å GaN / $Al_{x2}Ga_{1-x2}N$ QW with n_{2D} = 1.65×10^{13} cm^{-2} at T = 300 K.*

10.2.4 Threshold Properties and Differential Gains of AlGaN-Delta-GaN QWs

Figure 10-12 shows the TE-polarized material gain as a function of sheet carrier density for both 30-Å $Al_{0.8}Ga_{0.2}N$ / 3-Å GaN QW with varying d_1 thicknesses, and conventional 30 Å $Al_xGa_{1-x}N$ QW (x = 0.7, 0.8) at T = 300 K. The g^{TE}_{peak} for the AlGaN-delta-GaN QWs structures (~3100-3700 cm^{-1}) are found to be significantly larger than that of the conventional high Al-content AlGaN QWs (~200-800 cm^{-1}) at relatively high sheet carrier density n_{2D} = 1.65×10^{13} cm^{-2}. The optimized structure asymmetric QW with d_1 = 18 Å achieves ~1.2 times larger material gain than that of the symmetric QW structure, attributing to its improved matrix element.

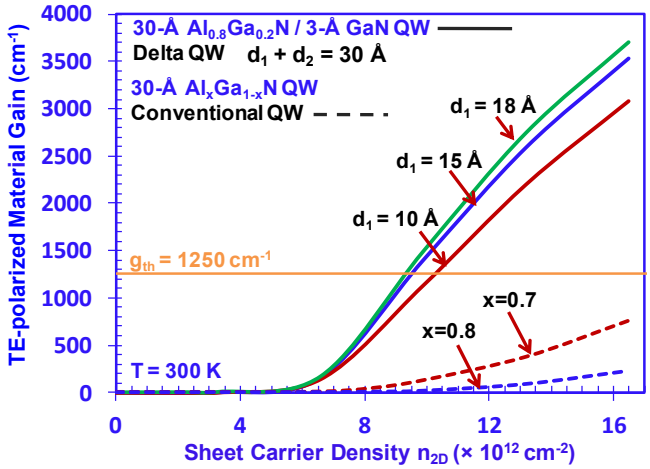

Figure 10-12: *TE-polarized material gain as a function of sheet carrier density for both 30-Å $Al_{0.8}Ga_{0.2}N$ / 3-Å GaN QW with varying d_1 thicknesses, and conventional 30 Å $Al_xGa_{1-x}N$ QW (x = 0.7, 0.8).*

Similarly, in order to illustrate the effect of different Al-contents of the AlGaN QWs, figure 10-13 shows the TE-polarized material gain as a function of sheet carrier density for both 30-Å $Al_{x1}Ga_{1-x1}N$ / 3-Å GaN / $Al_{x2}Ga_{1-x2}N$ QWs, and conventional 30 Å $Al_xGa_{1-x}N$ QW (x = 0.7, 0.8) at T = 300 K. Attributing to the reduced charge separation effect, the optimized structure asymmetric 30-Å $Al_{0.75}Ga_{0.25}N$ / 3-Å GaN / $Al_{0.85}Ga_{0.15}N$ QW achieves ~1.4 times larger material gain than that of the symmetric QW structure. Therefore, the TE- polarized lasing is feasible for asymmetric AlGaN-delta-GaN QW lasers emitting in the 240-250 nm spectral range.

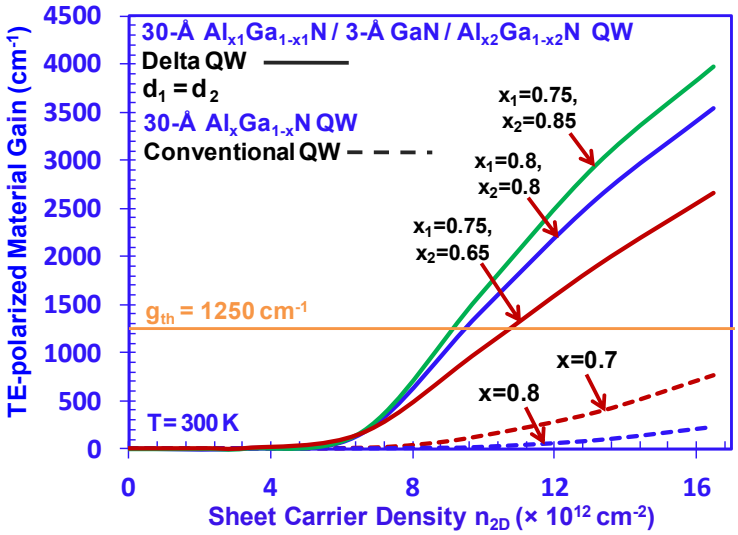

Figure 10-13: *TE-polarized material gain as a function of sheet carrier density for both 30-Å $Al_{0.8}Ga_{0.2}N$ / 3-Å GaN QW with varying d_1 thicknesses, and conventional 30 Å $Al_xGa_{1-x}N$ QW (x = 0.7, 0.8).*

To analyze the threshold properties of mid- and deep-UV lasers, AlGaN QWs lasers with optical confinement factor (Γ_{opt}) of 0.02 [1] were employed in the analysis. Note that the modal gain for the QW structures is an important parameter in laser device design. Based on transfer matrix method, the optical confinement factors for the asymmetric and symmetric QW structures are calculated as almost identical with negligible variations. Thus, the modal gain comparison for the QW structures will be primarily governed by the difference in the material gain comparison. The internal loss (α_i) in typical AlGaN lasers is 14 cm^{-1} [23]. The laser cavity length is assumed as 500 μm [1, 23] with end-facet reflectivities of 95% and 35%, which correspond to mirror loss (α_m) of 11 cm^{-1}. By employing the relation $\Gamma_{opt} g_{th} = \alpha_i + \alpha_m$, the threshold gain ($g_{th}$) is estimated as ~1250 cm^{-1}. The threshold sheet carrier density (n_{2D}^{th}) is 9.273×10^{12} cm^{-2} for the symmetric 30-Å

$Al_{0.8}Ga_{0.2}N$ / 3-Å GaN QW. For the optimized structure with d_1 = 18 Å from figure 9-12, the n_{2D}^{th} is 9.042×10^{12} cm^{-2}. Similarly, for optimized 30-Å $Al_{0.75}Ga_{0.25}N$ / 3-Å GaN / $Al_{0.85}Ga_{0.15}N$ QW, the n_{2D}^{th} is 8.976×10^{12} cm^{-2}. Thus, the threshold carrier densities for both optimized AlGaN-delta-GaN QW structures with different delta-GaN positions and varying Al-contents are reduced compared to the symmetric QW, which are applicable for mid- and deep-UV semiconductor lasers.

In order to analyze the spontaneous emission properties for both symmetric and asymmetric AlGaN-Delta-GaN QWs, the spontaneous recombination rates per unit volume (R_{sp}) as a function of sheet carrier density are presented in figures 9-14(a) and 9-14(b). By comparing the R_{sp} for different delta-layer positions, as shown in figure 9-14(a), the asymmetric delta QW structure with d_1 = 18 Å shows higher R_{sp} (~2.07×10^{28} $s^{-1}cm^{-3}$ with n_{2D} = 1.65×10^{13} cm^{-2}) than that of the other structures, attributed from the improved electron and hole wavefunction overlap (Γ_{e_hh} ~ 73.92%). For the case of delta QW structure with d_1 = 10 Å, the lower C-HH wavefunction overlap (Γ_{e_hh} ~ 63.51%) leads to ~ 22.9% lower R_{sp} (~1.68×10^{28} $s^{-1}cm^{-3}$ with n_{2D} = 1.65×10^{13} cm^{-2}) than that of the optimized structure with d_1 = 18 Å. Figure 9-14(b) compares the R_{sp} for AlGaN-Delta-GaN QWs with different Al-contents of AlGaN QW sub-layers. The enhanced C-HH wavefunction overlap (Γ_{e_hh} ~ 78.83%) obtained from the $Al_{0.75}Ga_{0.25}N$ / 3-Å GaN / $Al_{0.85}Ga_{0.15}N$ QW results in ~ 68.4 % increase in the R_{sp} at n_{2D} = 1.65×10^{13} cm^{-2}, in comparison with the $Al_{0.75}Ga_{0.25}N$ / 3-Å GaN / $Al_{0.65}Ga_{0.35}N$ QW with lower C-HH Γ_{e_hh} ~ 60.31%. Therefore, the improved C-HH Γ_{e_hh} that attributed from the use of optimized delta QW structures leads to ~22.9%- 68.4% increase in R_{sp}.

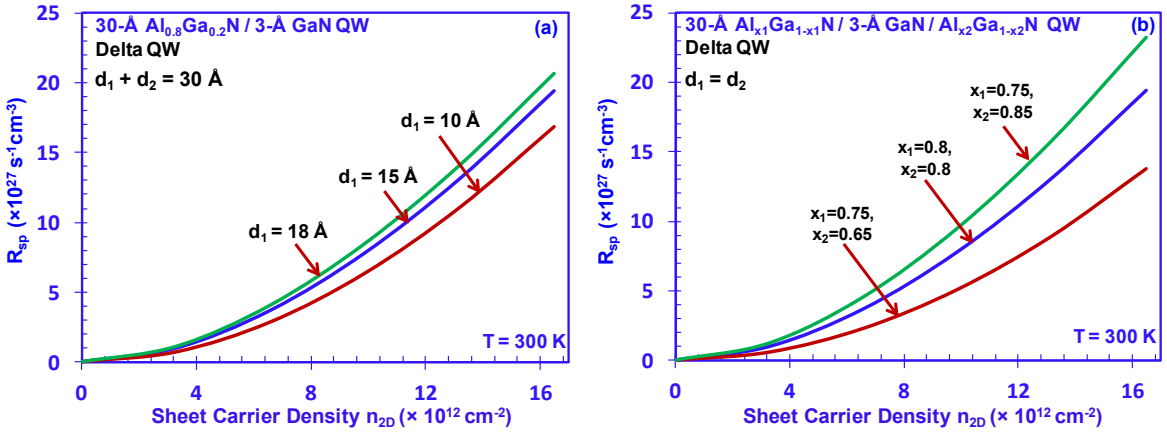

Figure 10-14: *R_{sp} as a function of sheet carrier density for both symmetric and asymmetric AlGaN-Delta-GaN QWs to illustrate (a) effect of delta positions, and (b) effect of Al-contents of AlGaN QWs.*

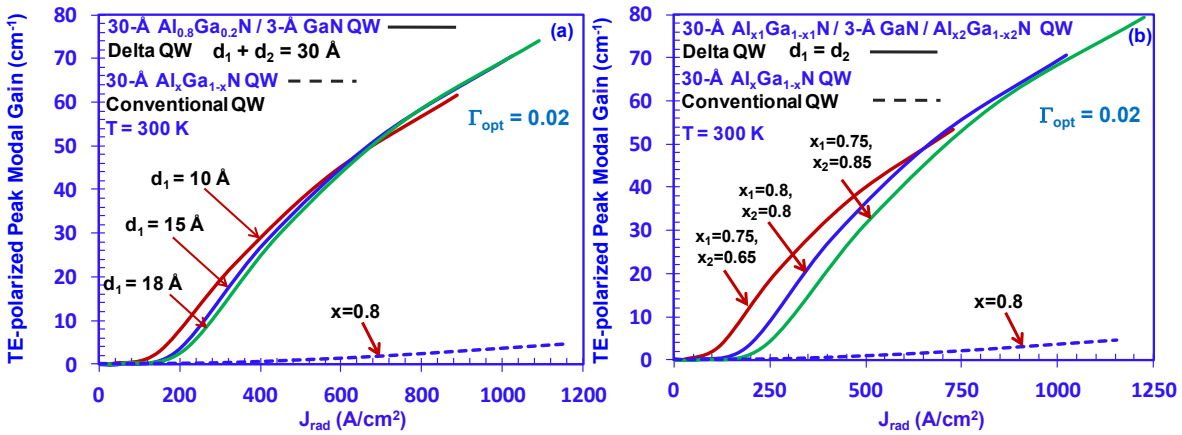

Figure 10-15: *The peak modal gain as a function of radiative current density for AlGaN-Delta-GaN QWs and conventional $Al_xGa_{1-x}N$ QW (x = 0.8) with (a) different delta positions, and (b) different Al-contents of AlGaN QWs.*

The peak modal gains (with Γ_{opt} = 0.02 [1]) a function of J_{rad} are compared for AlGaN-Delta-GaN QWs and conventional $Al_{0.8}Ga_{0.2}N$ QW for the studies on the delta layer position (d_1, d_2) and different AlGaN QW sub-layers compositions are shown in figures 10-15(a) and 10-15(b), respectively. The delta QWs exhibited significantly higher peak modal gain for any radiative current density injection level, in comparison to that of conventional QW. Note that the total recombination current density J_{tot} in the QW active region includes both the radiative and non-radiative current densites ($J_{tot} = J_{rad} + J_{non\text{-}rad}$) [17], and the $J_{non\text{-}rad}$ ($\sim A \cdot n_{th} + C \cdot n_{th}^3$) represents the dominant part of the J_{tot} in AlGaN-based QW [1, 17]. Thus, the reduction in threshold carrier density is important for suppressing monomolecular ($\sim A \cdot n_{th}$) and Auger ($\sim C \cdot n_{th}^3$) recombination currents at threshold.

The differential gain properties are also analyzed for both symmetric and asymmetric AlGaN-Delta-GaN QWs to illustrate effect of delta positions (figure 10-16(a)), as well as effect of Al-contents (figure 10-16(b)). For both cases, the differential gains first increase with higher carrier densities, which can be attributed to the carrier screening effect. After reaching the maximum, the differential gains start to decrease with further increased carrier densities, which is due to the band filling effect. In figures 10-16(a) and 10-16(b), the peak differential gains of the optimized asymmetric AlGaN-delta-GaN QW structures are higher than that of the symmetric AlGaN-delta-GaN QW structures, which indicates that the optimized AlGaN-delta-GaN QW structures will be applicable for high speed modulation lasers.

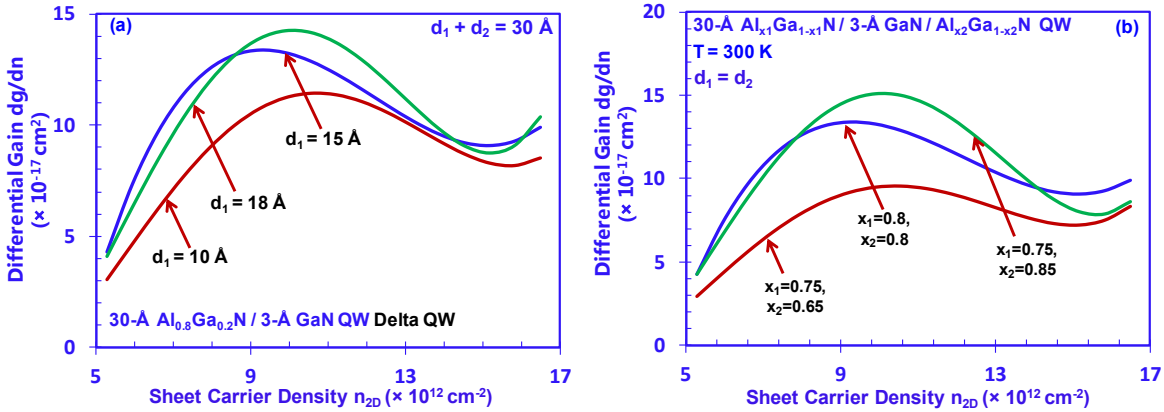

Figure 10-16: *The differential gain as a function of sheet carrier density for both symmetric and asymmetric AlGaN-Delta-GaN QWs to illustrate (a) effect of delta positions, and (b) effect of Al-contents of AlGaN QWs.*

10.3 Design of Staggered AlGaN QW

In order to achieve large optical gain in deep UV spectral regime, the most important aspect is to surpass the valence subbands crossover, so that the dominant C-CH transition will lead to high TM-polarized optical gain. Secondly, instead of using conventional high Al-content AlGaN QWs after the crossover, the optical gain at deep UV spectral regimes can be further improved by engineering the QW structure with staggered AlGaN QW design. In this section, we are focusing on the two main effects by employing the staggered QW structures: (1) further enhanced TM-polarized gain with engineered optical matrix element by broadening the concept from the InGaN QW system with large electron-hole wave function overlap (Γ_{e_hh}) design [24-34], and (2) polarization engineering of AlGaN QW system to achieve high TE-polarized optical gain from dominant C-HH transition.

10.3.1 Concept of Staggered AlGaN QW

The schematics of conventional $Al_zGa_{1-z}N$ QW and two-layer staggered $Al_xGa_{1-x}N$/ $Al_yGa_{1-y}N$ QW structures are shown in figures 10-17(a) and 10-17(b), respectively. The QW thickness is maintained as 3 nm for conventional $Al_zGa_{1-z}N$ QW. The two-layer $Al_xGa_{1-x}N$/ $Al_yGa_{1-y}N$ QW is composed of Al-content profile in the QW as follows: (1) lower Al-content of x, and (2) higher Al-

content. The thicknesses are maintained the same for the two layers for the $Al_xGa_{1-x}N$/ $Al_yGa_{1-y}N$ QW.

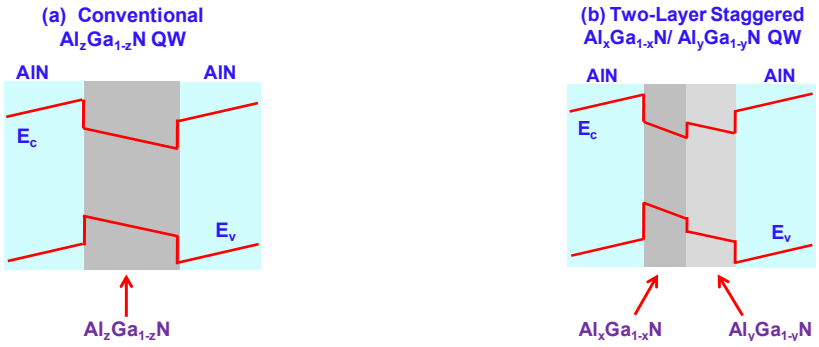

Figure 10-17: *Schematics of the (a) conventional $Al_zGa_{1-z}N$ QW; (b) two-layer staggered $Al_xGa_{1-x}N$/ $Al_yGa_{1-y}N$ QW structures.*

10.3.2 Momentum Matrix Element Characteristics

Figures 10-18(a) and 10-18(b) show square of momentum matrix elements as a function of in-plane wave vector k_t for 3-nm conventional $Al_{0.75}Ga_{0.25}N$ QW (figure 10-18(a)), and 3-nm two-layer staggered $Al_{0.75}Ga_{0.25}N$/ $Al_{0.85}Ga_{0.15}N$ QW (figure 10-18(b)) at carrier density 5×10^{19} cm^{-3} at room temperature. By inserting one layer of 1.5-nm $Al_{0.85}Ga_{0.15}N$ sub QW to the conventional $Al_{0.75}Ga_{0.25}N$ QW layer with identical thickness, the Γ_{e_hh} increases to 72.8%, which is ~13% higher than that of conventional 3-nm $Al_{0.75}Ga_{0.25}N$ QW (Γ_{e_hh} ~ 64.29%). The dominant transition is between C1 band to CH1 band, which will lead to TM-polarized emission. For the two-layer staggered $Al_{0.75}Ga_{0.25}N$/ $Al_{0.85}Ga_{0.15}N$ QW, the C1-CH1 transition is stronger than that of the conventional $Al_{0.75}Ga_{0.25}N$ QW, which will contribute to the TM-polarized emission.

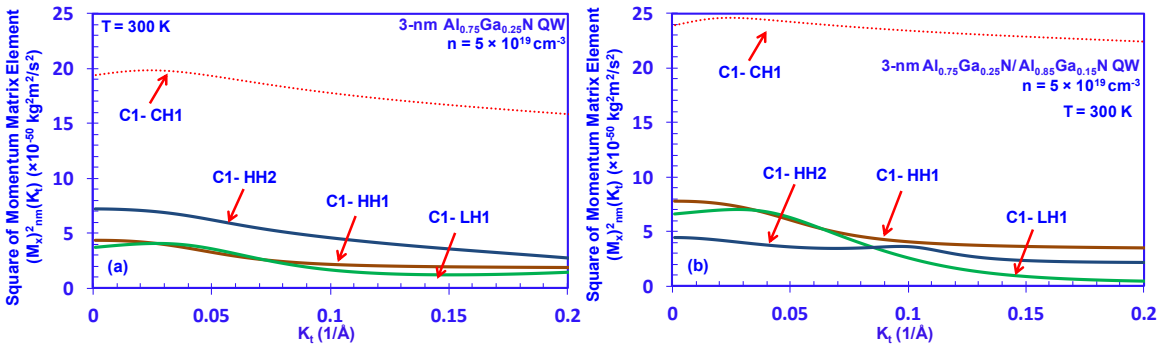

Figure 10-18: *Square of momentum matrix elements as a function of in-plane wave vector k_t for (a) 3-nm $Al_{0.75}Ga_{0.25}N$ QW and (b) 3-nm $Al_{0.75}Ga_{0.25}N$/ $Al_{0.85}Ga_{0.15}N$ QW at carrier density 5×10^{19} cm^{-3} at room temperature.*

Figures 10-19(a) and 10-19(b) show square of momentum matrix elements as a function of in-plane wave vector k_t for 3-nm two-layer staggered $Al_{0.7}Ga_{0.3}N$/ $Al_{0.8}Ga_{0.2}N$ QW (figure 10-19(a)), and 2-nm two-layer staggered $Al_{0.7}Ga_{0.3}N$/ $Al_{0.8}Ga_{0.2}N$ QW (figure 9-19(b)) at carrier density 5×10^{19} cm^{-3}. For the 3-nm two-layer staggered $Al_{0.7}Ga_{0.3}N$/ $Al_{0.8}Ga_{0.2}N$ QW, the valence subbands are rearranged due to the use of relatively lower Al-content $Al_{0.7}Ga_{0.3}N$ sub QW as the first layer of the staggered structure, which is close to the Al-composition of crossover. The HH1 band has been arranged into higher energy level; while mixed states of LH and CH bands are obtained at lower energy levels. It can be seen from figure 10-19(a) that the dominant transitions occur between the C1 band to the mixed states, which will contribute to both the TE- and TM-polarized emissions.

By using thinner QW thickness (d_{QW} = 1 nm) for both $Al_{0.7}Ga_{0.3}N$ and $Al_{0.8}Ga_{0.2}N$ sub QW layers, stronger rearrangement of the valence subbands is obtained for the 2-nm two-layer staggered $Al_{0.7}Ga_{0.3}N$/ $Al_{0.8}Ga_{0.2}N$ QW, as shown in figure 10-19(b). The carriers are dominantly populating the HH1 and LH1 bands, which have been arranged to higher energy levels. Although the C1-CH1 transition is stronger at the Γ-point, the TM-polarized emission will be reduced due to the low population of carriers.

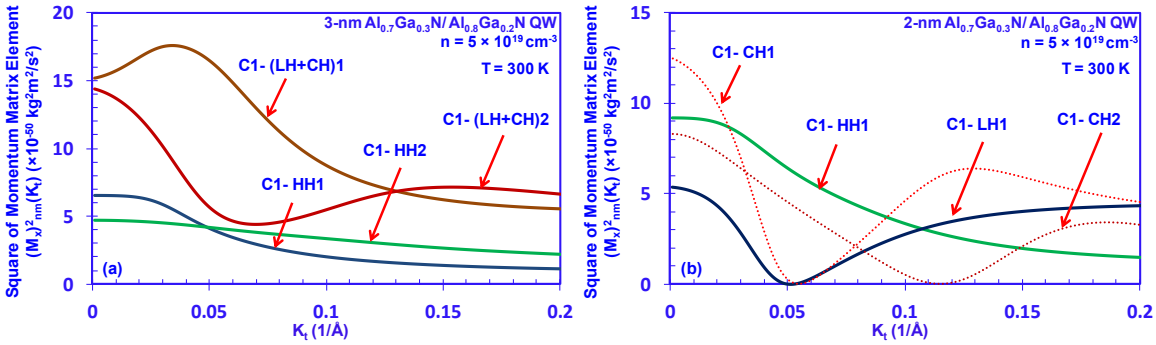

Figure 10-19: *Square of momentum matrix elements as a function of in-plane wave vector k_t for (a) 3-nm $Al_{0.7}Ga_{0.3}N$/ $Al_{0.8}Ga_{0.2}N$ QW and (b) 2-nm $Al_{0.7}Ga_{0.3}N$/ $Al_{0.8}Ga_{0.2}N$ QW at carrier density 5×10^{19} cm^{-3} at room temperature.*

10.3.3 Enhanced Optical Gain and Spontaneous Emission

Figure 10-20(a) shows both the TE-polarized and TM-polarized optical gain spectra for 3-nm thick conventional $Al_{0.75}Ga_{0.25}N$ QW, and two-layer staggered $Al_{0.75}Ga_{0.25}N$/ $Al_{0.85}Ga_{0.15}N$ QW at

carrier density 5×10^{19} cm^{-3} at room temperature. Similar emission wavelengths are obtained from both the conventional $Al_{0.75}Ga_{0.25}N$ QW (λ_{peak} ~ 226 nm), and the two-layer staggered $Al_{0.75}Ga_{0.25}N$/ $Al_{0.85}Ga_{0.15}N$ QW (λ_{peak} ~ 222 nm). The TE-polarized optical gains are lower than that of TM-polarized optical gains for both high Al-content conventional $Al_{0.75}Ga_{0.25}N$ QW and staggered $Al_{0.75}Ga_{0.25}N$/ $Al_{0.85}Ga_{0.15}N$ QW, attributed from the dominant C1-CH1 transition, as well as less carriers populating the HH1 and LH1 bands. The peak TM-polarized optical gain of two-layer staggered $Al_{0.75}Ga_{0.25}N$/ $Al_{0.85}Ga_{0.15}N$ QW (g^{TM}_{peak} ~ 6470.3 cm^{-1}) is ~21.5% higher than that of the conventional $Al_{0.75}Ga_{0.25}N$ QW (g^{TM}_{peak} ~ 5323.1 cm^{-1}), attributed from the suppressed charge separation effect by the use of larger overlap QW design.

The TE- and TM-polarized spontaneous emission spectra are also compared for the 3-nm thick conventional $Al_{0.75}Ga_{0.25}N$ QW, and two-layer staggered $Al_{0.75}Ga_{0.25}N$/ $Al_{0.85}Ga_{0.15}N$ QW at carrier density 5×10^{19} cm^{-3} at room temperature, as shown in figure 10-20(b). From the spontaneous emission spectra, the peak emission wavelength for the $Al_{0.75}Ga_{0.25}N$ QW is λ_{peak} ~ 226 nm, and λ_{peak} ~ 222 nm for the two-layer staggered $Al_{0.75}Ga_{0.25}N$/ $Al_{0.85}Ga_{0.15}N$ QW. The use of two-layer staggered $Al_{0.75}Ga_{0.25}N$/ $Al_{0.85}Ga_{0.15}N$ QW leads to enhanced TM-polarized spontaneous emission from the improved TM-polarized optical matrix element, which is applicable for deep-UV LEDs.

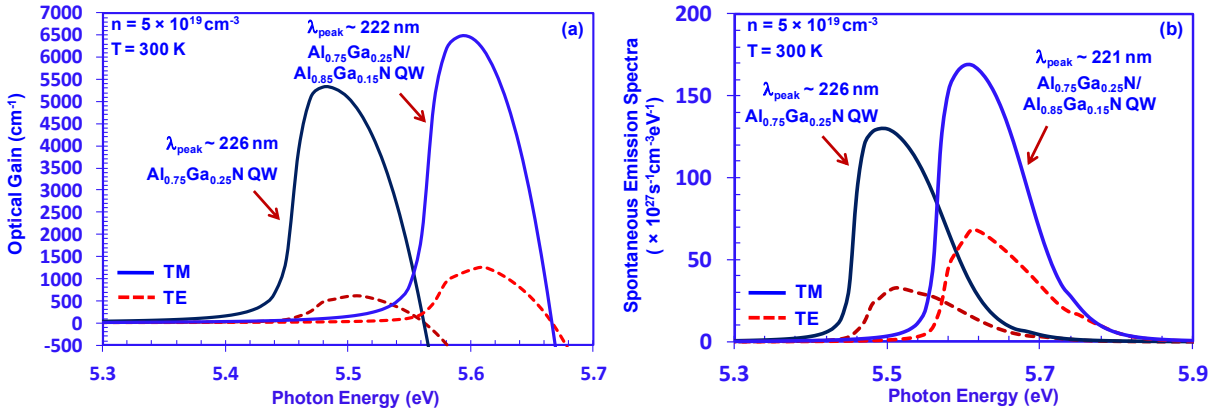

Figure 10-20: *TE-polarized and TM-polarized (a) spontaneous emission spectra, and (b) optical gain spectra for 3-nm thick $Al_{0.75}Ga_{0.25}N$ QW, and $Al_{0.75}Ga_{0.25}N$/ $Al_{0.85}Ga_{0.15}N$ QW with AlN barriers at carrier density 5×10^{19} cm^{-3} at room temperature.*

10.3.4 Polarization Engineering by Staggered AlGaN QW

The polarization properties of spontaneous emission and optical gain can also be engineered by employing the staggered AlGaN QW structure. Figure 10-21 shows the TE-polarized and TM-polarized spontaneous emission spectra for both the 3-nm thick $Al_{0.7}Ga_{0.3}N$/ $Al_{0.8}Ga_{0.2}N$ QW and the 2-nm thick $Al_{0.7}Ga_{0.3}N$/ $Al_{0.8}Ga_{0.2}N$ QW with carrier density 5×10^{19} cm^{-3} at room temperature. For the3-nm thick $Al_{0.7}Ga_{0.3}N$/ $Al_{0.8}Ga_{0.2}N$ QW, as the dominant transitions occur between the C1 band to the mixed states of LH and CH bands, the ratio of TE-polarized spontaneous emission peak to TM-polarized spontaneous emission peak is increased. However, which can be attributed from the stronger C1-CH transition. By using thinner 2-nm thick $Al_{0.7}Ga_{0.3}N$/ $Al_{0.8}Ga_{0.2}N$ QW, as majority carriers are populating the HH1 and LH1 bands, the TE-polarized spontaneous becomes stronger than that of TM-polarized spontaneous emission.

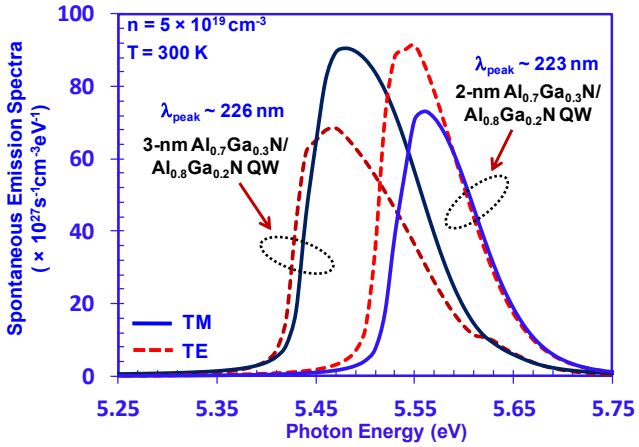

Figure 10-21: *TE-polarized and TM-polarized spontaneous emission spectra for 3-nm thick $Al_{0.7}Ga_{0.3}N$/ $Al_{0.8}Ga_{0.2}N$ QW, and 2-nm thick $Al_{0.7}Ga_{0.3}N$/ $Al_{0.8}Ga_{0.2}N$ QW with AlN barriers at carrier density 5×10^{19} cm^{-3} at room temperature.*

Figure 10-22 compares the TE- and TM-polarized optical gain spectra for (a) 3-nm thick $Al_{0.7}Ga_{0.3}N$/ $Al_{0.8}Ga_{0.2}N$ QW, and (b) 2-nm thick $Al_{0.7}Ga_{0.3}N$/ $Al_{0.8}Ga_{0.2}N$ QW with carrier density 5×10^{19} cm^{-3}. In figure 9-22(a), for the3-nm thick $Al_{0.7}Ga_{0.3}N$/ $Al_{0.8}Ga_{0.2}N$ QW, higher TM-polarized optical (g^{TM}_{peak} ~ 3416.1 cm^{-1}) is obtained at λ_{peak} ~ 227 nm. In figure 9-22(b), due to the valence subbands rearrangement, the use of thinner 2-nm $Al_{0.7}Ga_{0.3}N$/ $Al_{0.8}Ga_{0.2}N$ QW results in higher TE-polarized optical gain (g^{TE}_{peak} ~ 1239 cm^{-1}) at λ_{peak} ~ 224 nm from the stronger C1-HH1 and C1-LH1 transitions.

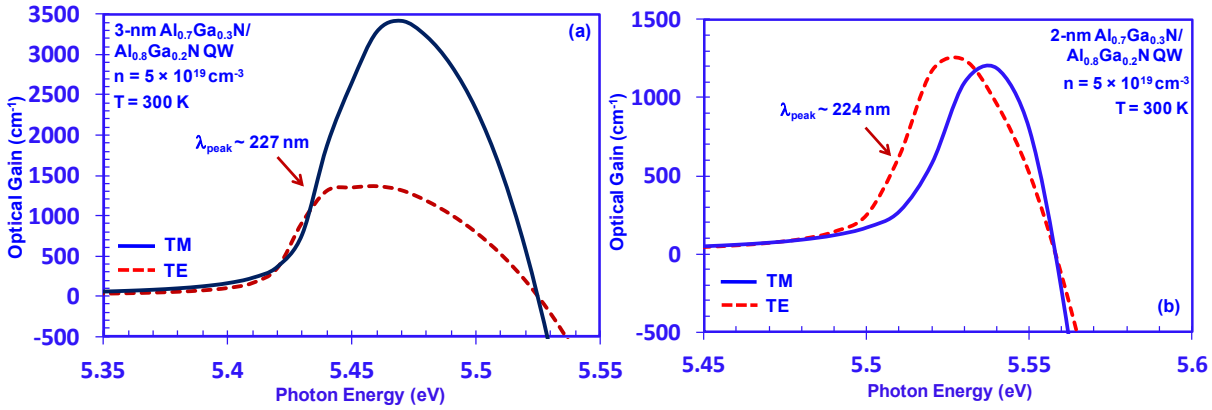

Figure 10-22: *TE-polarized and TM-polarized optical gain spectra for (a) 3-nm thick $Al_{0.7}Ga_{0.3}N$/ $Al_{0.8}Ga_{0.2}N$ QW, and (b) 2-nm thick $Al_{0.7}Ga_{0.3}N$/ $Al_{0.8}Ga_{0.2}N$ QW with AlN barriers at carrier density 5×10^{19} cm^{-3} at room temperature.*

10.4 Summary

In summary, in order to address the issue of low optical gain at λ ~ 250-300 nm, we have proposed the AlGaN-delta-GaN QW structure by inserting an ultra-thin GaN layer into high Al-content (x) $Al_xGa_{1-x}N$-delta-GaN QW active region. The use of AlGaN-delta-GaN QWs resulted in strong valence subbands mixing, which led to large TE-polarized gain at λ ~ 240-300 nm, attributing to the dominant C-HH transition.

The comprehensive optimization studies on the gain characteristics of AlGaN-delta-GaN QWs with various delta-GaN positions and Al-content AlGaN QW compositions are analyzed for the mid- and deep-UV spectral regimes. Attributing to the valence subband rearrangement and enhanced electron and hole wavefunction overlap, the use of optimized asymmetric AlGaN-delta-GaN QWs structures result in ~7 times increase in material gain, in comparison to that of conventional AlGaN QW. Recent works had also reported the TE-polarized gain from the $Al_{0.7}Ga_{0.3}N$ / AlN multiple QWs with low Al-content nanocluster-like 'quantum dot' features within the $Al_{0.7}Ga_{0.3}N$ QW layers [21, 22], which is consistent with the dominant TE-polarized gain from the prediction of high Al-content AlGaN QWs consisting of low bandgap material in the center of the active layer [10]. Large material gains can be maintained at λ ~ 240-250 nm for the asymmetric AlGaN-delta-GaN QWs structures. Despite the improved material gain for the asymmetric QW structures, the finding shows that large material gain can be obtained for both

symmetric and asymmetric AlGaN-delta-GaN QWs, which indicates the flexibility and robustness in the experimental implementations of this concept in device structures. The reduced threshold carrier densities obtained from the optimized delta QWs structures are important for the suppression of the non-radiative recombination current densities, which reduces the threshold current densities. Therefore, by employing asymmetric QW design, with optimized GaN delta layer position and asymmetric AlGaN-composition layers, the optimized optical gain and lower threshold carrier densities are achievable for the AlGaN-delta-GaN QW structures with realistic design applicable for mid- and deep-UV lasers.

The staggered AlGaN QW structure is proposed to lead to two major effects: 1) further enhanced TM-polarized gain from the improved electron- crystal-field split-off hole wave function overlap, 2) larger TE-polarized optical gain in deep-UV spectral regime from the engineered valence subbands structure.

References for Chapter 10

[1] W. W. Chow, M. Kneissl, "Laser gain properties of AlGaN quantum wells," J. Appl. Phys., vol. **98**, no. 11, pp. 114502-1–114502-6, Dec. 2005.

[2] J. Zhang, H. Zhao, and N. Tansu, "Effect of crystal-field split-off hole and heavy-hole bands crossover on gain characteristics of high Al-content AlGaN quantum well lasers," Appl. Phys. Lett., vol. **97**, no. 11, pp. 111105-1–111105-3, Sep. 2010.

[3] S. H. Park, "Theoretical study of optical properties in deep ultraviolet Al-rich AlGaN/AlN quantum wells," Semicond. Sci. Technol., vol. **24**, no. 3, pp. 035002-1–035002-4 , Feb. 2009.

[4] T. Kolbe, A. Knauer, C. Chua, Z. Yang, S. Einfeldt, P. Vogt, N. M. Johnson, M. Weyers, and M. Kneissl, "Optical polarization characteristics of ultraviolet (In)(Al)GaN multiple quantum well light emitting diodes," Appl. Phys. Lett., vol. **97**, no. 17, pp. 171105-1–171105-3, Oct. 2010.

[5] T. M. Al tahtamouni, J. Y. Lin, and H. X. Jiang, “Optical polarization in c-plane Al-rich AlN/$Al_xGa_{1-x}N$ single quantum wells,” Appl. Phys. Lett., vol. 101, no. 4, pp. 042103-1–042103-3, Jul. 2012.

[6] T. Kolbe, A. Knauer, C. Chua, Z. Yang, V. Kueller, S. Einfeldt, P. Vogt, N. M. Johnson, M. Weyers, and M. Kneissl, “Effect of temperature and strain on the optical polarization of (In)(Al)GaN ultraviolet light emitting diodes,” Appl. Phys. Lett., **vol. 99**, no. 26, pp. 261105-1–261105-4, Dec. 2011.

[7] T. K. Sharma, and E. Towe, “Impact of strain on deep ultraviolet nitride laser and light-emitting diodes,” J. Appl. Phys., vol. **109**, no. 8, pp. 086104-1–086104-3, Apr. 2011.

[8] T. K. Sharma, D. Naveh, and E. Towe, “Strain-driven light-polarization switching in deep ultraviolet nitride emitters”, Physical Review B, vol. **84**, no. 3, pp. 035305-1–035305-8, Jul. 2011.

[9] G. A. Garrett, P. Rotella, H. Shen, M. Wraback, T. Wunderer, C. L. Chua, Z. Yang, J. E. Northrup, and N. M. Johnson, "Sub-Threshold Time-Resolved Spectroscopy of Mid-UV AlGaN Laser Diode Structures Pseudomorphically Grown on Bulk AlN," in CLEO: Applications and Technology, OSA Technical Digest (online) (Optical Society of America, 2012), paper JTh1L.5.

[10] J. Zhang, H. Zhao, and N. Tansu, “Large optical gain AlGaN-delta-GaN quantum wells laser active regions in mid- and deep-ultraviolet spectral regimes,” Appl. Phys. Lett., vol. **98**, no. 17, pp. 171111-1–171111-3, Apr. 2011.

[11] Y. Taniyasu, and M. Kasu, “Polarization property of deep-ultraviolet light emission from C-plane AlN/GaN short-period superlattices,” Appl. Phys. Lett., vol. **99**, no. 25, pp. 251112-1–251112-4, Dec. 2011.

[12] H. Zhao, G. Liu, and N. Tansu, “Analysis of InGaN-Delta-InN Quantum Wells for Light-Emitting Diodes,” Appl. Phys. Lett., vol. 97. no. 13, pp. 131114-1–131114-3, Oct. 2010.

[13] H. Zhao, X. Jiao, and N. Tansu, “Analysis of Position and Thickness Dependences of Delta Layer in InGaN-Delta-InN Quantum Wells Light-Emitting Diodes”, Proceeding of Asia

Communications and Photonics Conference (ACP), LED Technologies and Applications (ATh1F), Nov. 2012.

[14] S. L. Chuang, “Optical Gain of Strained Wurtzite GaN Quantum-Well Lasers,” IEEE J. Quantum Electron., vol. **32**, no. 10, pp. 1791-1800, Oct. 1996.

[15] S. L. Chuang and C. S. Chang, “A band-structure model of strained quantum-well wurtzite semiconductors,” Semicond. Sci. Technol., vol. **12**, no. 3, pp. 252-263, Mar. 1997.

[16] S. L. Chuang, Physics of Photonic Devices 2nd ed. Wiley, New York, 2009, Chap. 4.

[17] H. Zhao, R. A. Arif, Y. K. Ee, and N. Tansu, “Self-Consistent Analysis of Strain-Compensated InGaN–AlGaN Quantum Wells for Lasers and Light-Emitting Diodes,” IEEE J. Quantum Electron., vol. **45**, no. 1, pp. 66-78, Jan. 2009.

[18] H. Zhao, and N. Tansu, “Optical gain characteristics of staggered InGaN quantum wells lasers,” J. Appl. Phys., vol. **107**, no. 11, pp. 113110-1–113110-12, Jun. 2010.

[19] I. Vurgaftman and J.R. Meyer, Chapter 2 in Nitride Semiconductor Devices, J. Piprek (Editor), Wiley, 2007.

[20] I. Vurgaftman and J.R. Meyer, “Band parameters for nitrogen-containing semiconductors,” J. Appl. Phys., vol. **94**, no. 6, pp. 3675-3696, Sep. 2003.

[21] E. F. Pecora, W. Zhang, A. Y. Nikiforov, L. Zhou, D. J. Smith, J. Yin, R. Paiella, L. D. Negro, and T. D. Moustakas, “Sub-250 nm room-temperature optical gain from AlGaN/AlN multiple quantum wells with strong band-structure potential fluctuations,” Appl. Phys. Lett., vol. **100**, no. 6, pp. 061111-1–061111-4, Feb. 2012.

[22] E. F. Pecora, W. Zhang, J. Yin, R. Paiella, L. D. Negro, and T. D. Moustakas, “Polarization Properties of Deep-Ultraviolet Optical Gain in Al-Rich AlGaN Structures,” Appl. Phys. Express, vol. **5**, pp. 032103-1–032103-3, Feb. 2012.

[23] H. Yoshida, M. Kuwabara, Y. Yamashita, Y. Takagi, K. Uchiyama, and H. Kan, “AlGaN-based laser diodes for the short-wavelength ultraviolet region,” New Journal of Physics, vol. **11**, no. 12, pp. 125013-125027 , Dec. 2009.

[24] S. H. Park, D. Ahn, and S. L. Chuang, "Electronic and Optical Properties of a- and m-plane Wurtzite InGaN/GaN Quantum Wells," IEEE. J. Quantum Electron., **43**, 1175-1182 (2007).

[25] M. C. Schmidt, K.-C. Kim, R. M. Farrell, D. F. Feezell, D. A. Cohen, M. Saito, K. Fujito, J. S. Speck, S. P. Denbaars, and S. Nakamura, “Demonstration of Nonpolar m-Plane InGaN/GaN Laser Diodes,” Jpn. J. Appl. Phys., **46**, L190-L191 (2007).

[26] R. M. Farrell, D. F. Feezell, M. C. Schmidt, D. A. Haeger, K.M. Kelchner, K. Iso, H. Yamada, M. Saito, K. Fujito, D. A. Cohen, J. S. Speck, S P. DenBaars, and S. Nakamura, “Continuous-wave Operation of AlGaN-cladding-free Nonpolar m-Plane InGaN/GaN Laser Diodes,” *Jpn. J. Appl. Phys.*, vol. 46, no. 32, pp. L761-L763, Aug. 2007.

[27] H. Zhao, G. Liu, X. H. Li, R. A. Arif, G. S. Huang, J. D. Poplawsky, S. Tafon Penn, V. Dierolf, and N. Tansu, “Design and Characteristics of Staggered InGaN Quantum Well Light-Emitting Diodes in the Green Spectral Regimes,” *IET Optoelectron.*, vol. 3, no. 6, pp. 283-295, Dec. 2009.

[28] S. H. Park, D. Ahn, B. H. Koo, and J. W. Kim, “Electronic and optical properties of staggered InGaN/InGaN quantum-well light-emitting diodes,” *Phys. Stat. Sol. A*, vol. 206, no. 11, pp. 2637-2640, Jun. 2009.

[29] S. H. Park, D. Ahn, B. H. Koo, and J. W. Kim, “Dip-shaped InGaN/GaN quantum-well light-emitting diodes with high efficiency,” *Appl. Phys. Lett.*, vol. 95, no. 6, p. 063507, Aug. 2009.

[30] S. H. Park, D. Ahn, and J. W. Kim, “High-efficiency staggered 530 nm InGaN/InGaN/GaN quantum-well light-emitting diodes,” *Appl. Phys. Lett.*, vol. 94, no. 4, p. 041109, Jan. 2009.

[31] C. T. Liao, M. C. Tsai, B. T. Liou, S. H. Yen, and Y. K. Kuo, “Improvement in Output Power of a 460 nm InGaN Light-emitting Diode using Staggered Quantum Well,” J. Appl. Phys., vol. 108, no. 6, pp. 063107-1 - 063107-6, Sep. 2010.

[32] J. H. Ryou, P. D. Yoder, J. Liu, Z. Lochner, H. Kim, S. Choi, H. J. Kim, R. D. Dupuis, “Control of Quantum-Confined Stark Effect in InGaN-Based Quantum Wells,” IEEE J. Sel. Top. Quantum Electron., vol. 15, no. 4, pp. 1080-1091, Jul./Aug. 2009.

[33] A. Venkatachalam, B. Klein, J.-H Ryou, S. C. Shen, R. D. Dupuis, P. D. Yoder, “Design Strategies for InGaN-Based Green Lasers,” IEEE J. Quantum Electron., **46**, 238-245 (2010).

[34] H. Zhao, G. Liu, and N. Tansu, “Analysis of InGaN-Delta-InN Quantum Wells for Light-Emitting Diodes,” Appl. Phys. Lett., vol. 97, Art. 131114, September 2010.

Chapter 11: Substrate Engineering for High-efficiency LEDs and Lasers

11.1 Introduction and Concept of Substrate Engineering

In Chapter 2, the current status of InGaN QWs LEDs and lasers has been reviewed, which includes the challenges of realizing high-efficiency conventional InGaN QWs LEDs and Lasers, as well as the motivations of substrate engineering.

In this chapter, we present a comprehensive study on the optical properties of InGaN QWs on ternary InGaN substrate. Specifically, the spontaneous emission rates of the InGaN QWs on $In_{0.15}Ga_{0.85}N$ substrate are compared with those of InGaN QWs on conventional GaN template for emission wavelength from green up to red spectral regimes. The spontaneous emission rate characteristics of the InGaN QW on different ternary substrates are also compared for green-emitting active region. The optical gain and threshold characteristics of InGaN QWs on ternary InGaN substrates for green- and yellow-emitting lasers are also compared with those of the conventional InGaN QWs / GaN substrate approach.

The band structures and wave functions are calculated by employing self-consistent 6-band ***k·p*** formalism for wurtzite semiconductor taking into account the valence band mixing, strain effect, spontaneous and piezoelectric polarization fields, and carrier screening effect [26-29]. The band parameters for the III-Nitride semiconductors in this work are obtained from references 28-31. The calculation details and band parameters can be found in Chapter 8.

11.1.1 Concept of InGaN QWs on Ternary InGaN Substrates

Figure 10-1 shows the energy band lineups of 3-nm $In_{0.325}Ga_{0.675}N$ QW surrounded by $In_{0.15}Ga_{0.85}N$ barriers on $In_{0.15}Ga_{0.85}N$ substrate with the corresponding ground state conduction subband (C1) wavefunction and the ground state valence subband (HH1) wavefunction at zone center.

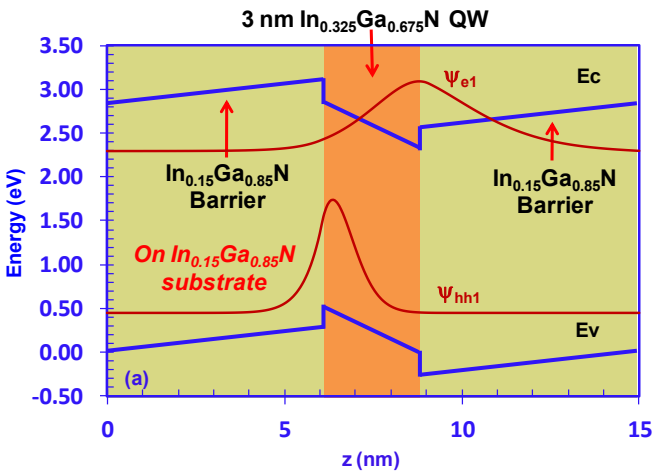

Figure 11-1: *The schematics of 3-nm $In_{0.325}Ga_{0.675}N$ QW with $In_{0.15}Ga_{0.85}N$ barriers on $In_{0.15}Ga_{0.85}N$ substrate with electron wavefunction EC1 and hole wave function HH1.*

The lattice constant of the $In_{0.325}Ga_{0.675}N$ QW is larger than that of $In_{0.15}Ga_{0.85}N$ barrier, which induces the compressive strain in the QW. However, by employing the ternary $In_{0.15}Ga_{0.85}N$ substrate, the lattice-mismatch between the QW and the ternary substrate is reduced in comparison with that of conventional approach, which leads to reduction in internal electrostatic field in the QW.

11.1.2 Strain and Polarization Field for InGaN QW with Ternary Substrates

Figures 11-2(a) and 11-2(b) show the in-plane (ε_{xx}) and cross-plane (ε_{zz}) strains in the active region layers as a function of In-contents (x) in the $In_xGa_{1-x}N$ QW. The comparisons of the strains in the $In_xGa_{1-x}N$ QWs QWs on $In_{0.15}Ga_{0.85}N$ substrate and conventional GaN substrate for x = 0.2 up to x = 0.4 were carried out. Attributing to the smaller lattice-mismatch, both the ε_{xx} and ε_{zz} are reduced by ~37.5% - 75 % in the QWs from the use of the ternary substrates, which in turn reduces the piezoelectric polarization fields [figure 11-2(c)] and electrostatic fields [figure 11-2(d)] in the QWs. In our studies, all the InGaN QW thicknesses were kept as 3-nm for comparison purpose.

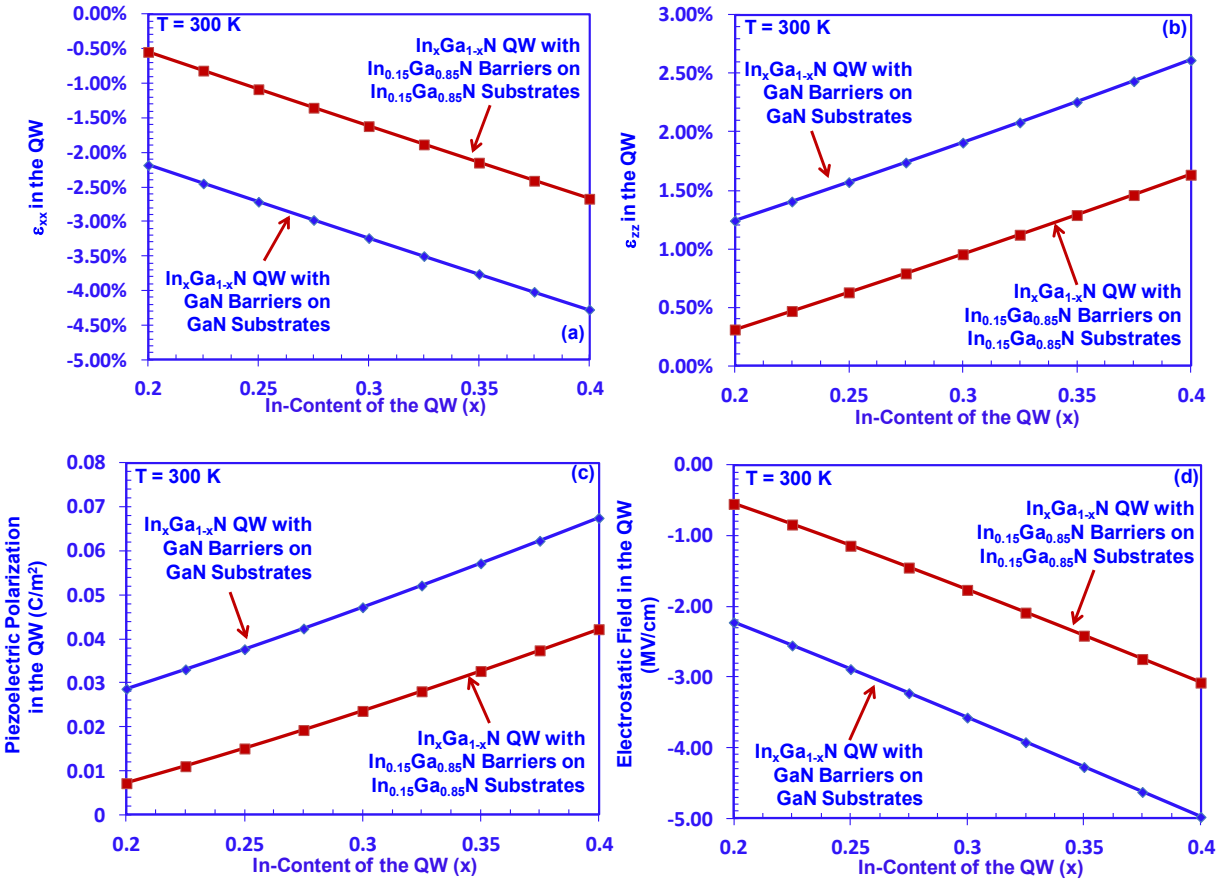

Figure 11-2: *(a) The strain parameter at x direction, (b) the strain parameter at z direction, (c) the piezoelectric polarization field, and (d) the electrostatic field in the $In_xGa_{1-x}N$ QWs as a function of In-content of the QW, for both $In_xGa_{1-x}N$ QWs with $In_{0.15}Ga_{0.85}N$ barriers on $In_{0.15}Ga_{0.85}N$ substrate and conventional $In_xGa_{1-x}N$ QWs with GaN barriers on GaN substrate.*

Figure 11-2(d) shows the comparison of the internal electrostatic fields in the QWs for both $In_xGa_{1-x}N$ QW on $In_{0.15}Ga_{0.85}N$ barrier / substrate and conventional $In_xGa_{1-x}N$ QW on GaN barrier / substrate, with the In-content (x) ranging from 20% up to 40%. The internal electrostatic field calculation was similar to the treatment in reference 28. The internal fields in the InGaN QWs grown on ternary substrate can be reduced by ~ 40% up to ~75% [figure 10-2(d)], in comparison to those obtained in identical QWs grown on conventional GaN substrate / barrier. Specifically, the internal fields in $In_{0.2}Ga_{0.8}N$ QW with GaN and $In_{0.15}Ga_{0.85}N$ substrates are -2.23 MV/cm and -0.55 MV/cm, respectively. In addition, the internal fields were calculated as -4.98 MV/cm and -3.08 MV/cm for $In_{0.4}Ga_{0.6}N$ QW/ GaN substrate and $In_{0.4}Ga_{0.6}N$ QW/ $In_{0.15}Ga_{0.85}N$ substrate, respectively.

11.2 Spontaneous Emission Characteristics of InGaN QWs on Ternary Substrates for LEDs

Figure 11-3 shows the spontaneous emission spectra for both 1) $In_xGa_{1-x}N$ QWs with $In_{0.15}Ga_{0.85}N$ barriers / substrate, and 2) conventional $In_yGa_{1-y}N$ QWs with GaN barriers / substrate for green and yellow emitting QWs at carrier density (n) of 1×10^{19} cm^{-3} at room temperature. In designing the respective QWs for comparison purpose, the In-contents (x and y) in the InGaN QWs were selected for similar emission wavelength at $n = 1 \times 10^{19}$ cm^{-3}. For green-emitting QWs at λ_{peak} ~ 525.4 nm (λ_{peak} ~ 548.7 nm), the spontaneous emission spectra peak of $In_{0.3}Ga_{0.7}N$ QW ($In_{0.325}Ga_{0.675}N$ QW) / $In_{0.15}Ga_{0.85}N$ substrate is ~3.1 times (~2.7 times) of that of $In_{0.28}Ga_{0.72}N$ QW ($In_{0.3}Ga_{0.7}N$ QW) on conventional GaN substrate. For yellow-emitting QWs (λ_{peak} ~ 576.7 nm), the peak of the spontaneous emission spectra for $In_{0.35}Ga_{0.65}N$ QW on $In_{0.15}Ga_{0.85}N$ substrate is ~2.5 times of that for $In_{0.322}Ga_{0.678}N$ QW on GaN substrate. Note that the ternary substrate requires slightly higher In-content in the InGaN QW due to the less red-shift from the reduced built-in quantum confined Stark effect, however larger of spontaneous emission spectra peaks are obtained for all the QWs on the ternary substrate.

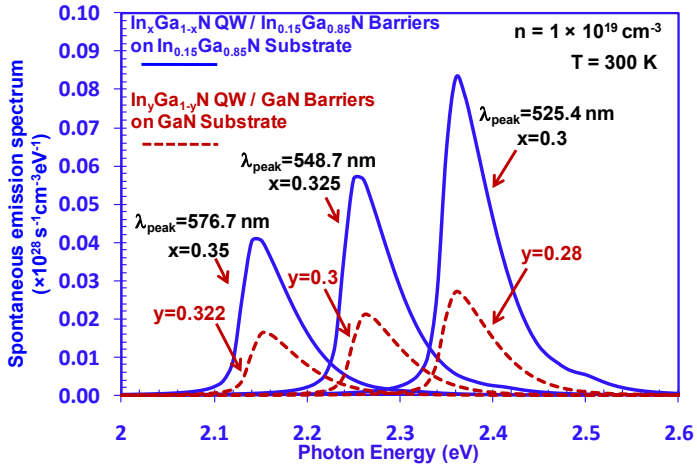

Figure 11-3: *Spontaneous emission spectrum for both $In_xGa_{1-x}N$ QWs with $In_{0.15}Ga_{0.85}N$ barriers on $In_{0.15}Ga_{0.85}N$ substrate and conventional $In_yGa_{1-y}N$ QWs with GaN barriers on GaN substrate for green and yellow spectra regimes at $n = 1 \times 10^{19}$ cm^{-3} at room temperature.*

Figures 11-4(a) and 11-4(b) show the spontaneous emission recombination rate per unit volume (R_{sp}) as a function of carrier density for both green- and yellow-emitting QWs at T = 300 K. For the green-emitting QWs (λ_{peak} ~ 548.7 nm) [figure 10-4(a)], the R_{sp} of $In_{0.325}Ga_{0.675}N$ QW /

$In_{0.15}Ga_{0.85}N$ substrate was calculated as ~3.2 times of that of conventional $In_{0.3}Ga_{0.7}N$ QW / GaN substrate at $n = 2 \times 10^{19}$ cm^{-3}. For the yellow emitting QWs (λ_{peak} ~ 576.7 nm) [figure 10-4(b)], the R_{sp} of $In_{0.35}Ga_{0.65}N$ QW / $In_{0.15}Ga_{0.85}N$ substrate is ~2.9 times of that of $In_{0.322}Ga_{0.678}N$ QW / GaN substrate at $n = 2 \times 10^{19}$ cm^{-3}. The improved R_{sp} of InGaN QWs on the ternary substrate can be attributed to the larger optical matrix elements arisen from the reduced strain and internal field in the QW.

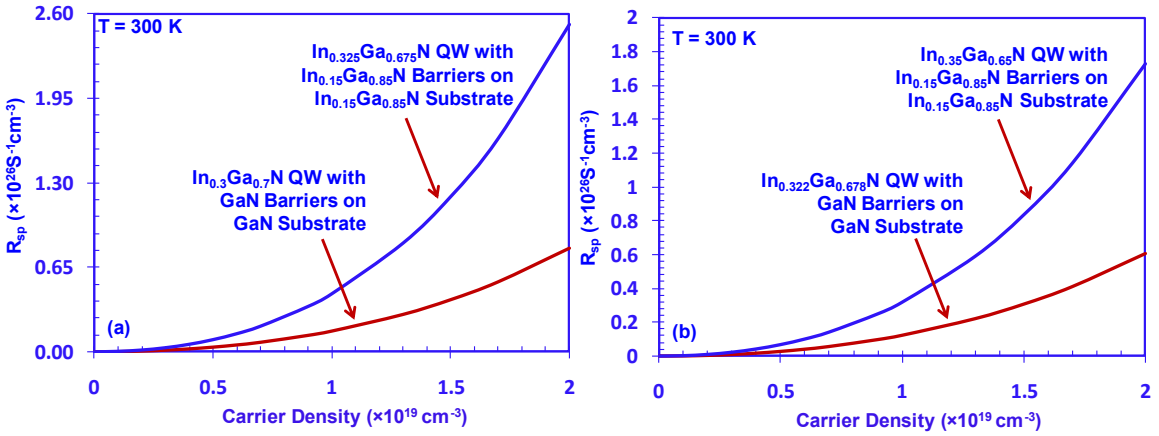

Figure 11-4: *Spontaneous emission spectrum for both $In_xGa_{1-x}N$ QWs with $In_{0.15}Ga_{0.85}N$ barriers on $In_{0.15}Ga_{0.85}N$ substrate and conventional $In_yGa_{1-y}N$ QWs with GaN barriers on GaN substrate for green and yellow spectra regimes at $n = 1 \times 10^{19}$ cm^{-3} at room temperature.*

Figure 11-5(a) shows spontaneous emission spectrum for $In_xGa_{1-x}N$ QWs with $In_{0.15}Ga_{0.85}N$ barriers on $In_{0.15}Ga_{0.85}N$ substrate with various In-contents (x) calculated for $n = 1 \times 10^{19}$ cm^{-3} at room temperature. By employing the $In_{0.15}Ga_{0.85}N$ substrate, large peaks of the spontaneous emission spectra can be obtained for InGaN QWs with peak emission wavelengths covering from blue (3.98×10^{27} $s^{-1}cm^{-3}eV^{-1}$, λ_{peak} = 452.6 nm) up to red (2.23×10^{26} $s^{-1}cm^{-3}eV^{-1}$, λ_{peak} = 645.8 nm) spectral regimes. The peaks of the spontaneous emission spectra decrease with longer emission wavelength, which is related to the increasing charge separation effect. In order to provide comparison for red-emitting QWs, figure 10-5(b) shows the comparison of the R_{sp} as a function of carrier density up to n = 2×10^{19} cm^{-3} for λ_{peak} ~ 645 nm. The R_{sp} of $In_{0.4}Ga_{0.6}N$ QW / $In_{0.15}Ga_{0.85}N$ substrate was obtained as ~2.5 times of that of $In_{0.368}Ga_{0.632}N$ QW / GaN substrate at $n = 2 \times 10^{19}$ cm^{-3}. The significantly-improved R_{sp} for InGaN QWs on ternary substrate for

emission wavelength across green and red spectral regimes confirm the strong potential for the use of ternary substrate to achieve high efficiency green- and red-emitting LEDs.

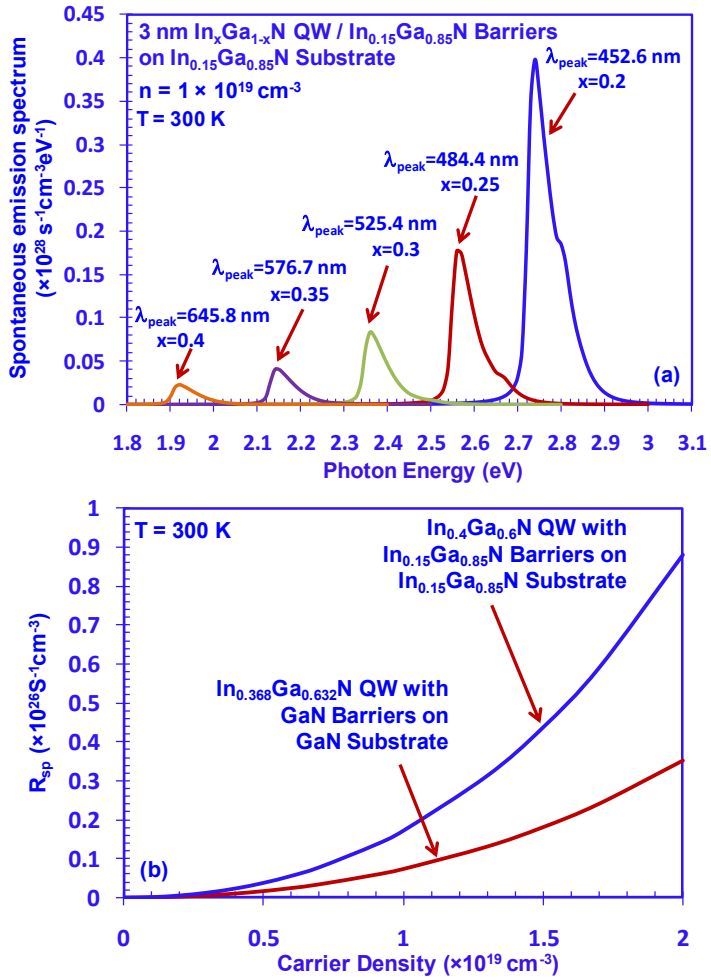

Figure 11-5: *(a) Spontaneous emission spectrum for both $In_xGa_{1-x}N$ QWs /$In_{0.15}Ga_{0.85}N$ substrate from blue up to red spectra regimes at $n = 1 \times 10^{19}$ cm^{-3} at room temperature and (b) comparison of R_{sp} as a function of carrier density for $In_{0.4}Ga_{0.6}N$ QWs /$In_{0.15}Ga_{0.85}N$ substrate and conventional $In_{0.368}Ga_{0.632}N$ QWs /GaN substrate.*

Figure 11-6 shows the comparison of the spontaneous emission spectrum for the $In_{0.3}Ga_{0.7}N$ QW on ternary InGaN substrates with In-contents from 5% to 20% calculated for $n = 1 \times 10^{19}$ cm^{-3} at room temperature, as the In-contents of the commercially-available InGaN substrates range from 5% up to 20% [19-21]. The emission wavelengths of the $In_{0.3}Ga_{0.7}N$ QW show redshift with lower In-content InGaN substrates. The peaks of the spontaneous emission spectra are larger for $In_{0.3}Ga_{0.7}N$ QW on higher In-content InGaN substrates (1.5×10^{27} $s^{-1}cm^{-3}eV^{-1}$ with λ_{peak} = 521 nm

for $In_{0.2}Ga_{0.8}N$ substrate), which can be attributed to the reduced lattice-mismatch strain and internal electrostatic fields in the QW.

The comparison of the wavelength shifts for $In_{0.3}Ga_{0.7}N$ QW on different ternary $In_yGa_{1-y}N$ substrates (y = 5% - 20%) are shown in Table 11-1. The peak spontaneous emission wavelengths show blueshift at higher carrier density ($n = 2 \times 10^{19}$ cm^{-3}) for the $In_{0.3}Ga_{0.7}N$ QW with ternary substrates. The blue-shift is suppressed by employing higher In-content InGaN substrate, as the lower lattice-mismatch strain leads to the reduction of the internal field. Specifically, the blue shift of 90 meV is obtained for $In_{0.3}Ga_{0.7}N$ QW/ $In_{0.2}Ga_{0.8}N$ substrate (Table 11-1), which is 40 meV less than that for $In_{0.3}Ga_{0.7}N$ QW/ $In_{0.05}Ga_{0.95}N$ substrate.

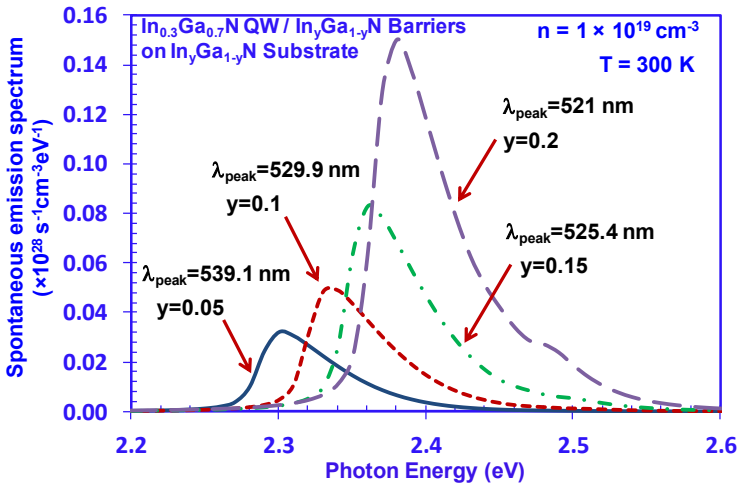

Figure 11-6: *Spontaneous emission spectrum for $In_{0.3}Ga_{0.7}N$ QW on $In_yGa_{1-y}N$ substrates (y = 5% - 20%) at $n = 1 \times 10^{19}$ cm^{-3} at room temperature.*

Substrate Composition	$In_{0.05}Ga_{0.95}N$	$In_{0.1}Ga_{0.9}N$	$In_{0.15}Ga_{0.85}N$	$In_{0.2}Ga_{0.8}N$
E21 at $n = 1x10^{18}$ cm^{-3}	2.24 eV	2.28 eV	2.30 eV	2.33 eV
E21 at $n = 2x10^{19}$ cm^{-3}	2.37 eV	2.39 eV	2.42 eV	2.42 eV
Blue Shift	130 meV	110 meV	120 meV	90 meV

Table 11-1: *The transition energy blue-shifts for $In_{0.3}Ga_{0.7}N$ QW on different ternary $In_yGa_{1-y}N$ substrates (y = 5% - 20%).*

Figure 11-7 shows the comparison of R_{sp} as a function of carrier density up to n = 2 × 10^{19} cm^{-3} for $In_{0.3}Ga_{0.7}N$ QW with $In_yGa_{1-y}N$ substrates (y = 5% - 20%) targeting at green spectral emission. The R_{sp} of $In_{0.3}Ga_{0.7}N$ QW / $In_{0.2}Ga_{0.8}N$ substrate was obtained as ~6 times of that of $In_{0.3}Ga_{0.7}N$ QW / $In_{0.05}Ga_{0.95}N$ substrate at n = 2 × 10^{19} cm^{-3}. Therefore, by employing the ternary substrate with less lattice-mismatch to the InGaN QW, this approach leads to increase in spontaneous emission rate attributed to the reduced charge separation issue in the QW.

The comparison of the peak emission wavelengths as a function of R_{sp} for $In_{0.3}Ga_{0.7}N$ QWs with various $In_yGa_{1-y}N$ substrates (y = 5% - 20%) at room temperature is shown in figure 10-8. As the carrier injection in the $In_{0.3}Ga_{0.7}N$ QWs with various ternary substrates increases, the spontaneous emission rate of the QWs increases. As the spontaneous emission rates for all QW structures increase, the peak emission wavelengths also reduce due to the carrier screening effect. The use of lower In-content $In_yGa_{1-y}N$ substrates (y = 5%, and 10%) leads to relatively low spontaneous emission rate, which is also accompanied by large emission wavelength blue-shift. In contrast, the use of higher In-content InGaN substrates (y = 15%, and 20%) leads to large spontaneous emission rate, as well as the significantly reduction in wavelength blue-shift. Specifically, the use of $In_{0.2}Ga_{0.8}N$ ternary substrate exhibits relatively low blue-shift (~ 10 nm) for achieving spontaneous emission rate (R_{sp}) of R_{sp} ~ 3.76 x 10^{26} $s^{-1}cm^{-3}$, while the use of $In_{0.15}Ga_{0.85}N$ ternary substrate will lead to blue-shift up to ~ 20 nm for achieving similar spontaneous emission rate.

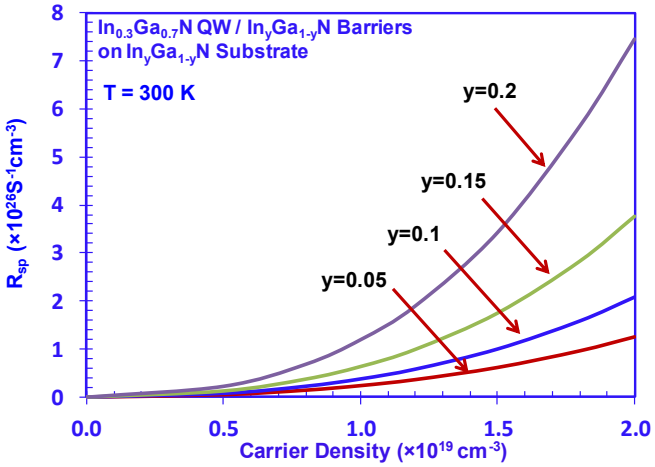

Figure 11-7: *Comparison of R_{sp} as a function of carrier density for $In_{0.3}Ga_{0.7}N$ QW with $In_yGa_{1-y}N$ substrates (y = 5% - 20%).*

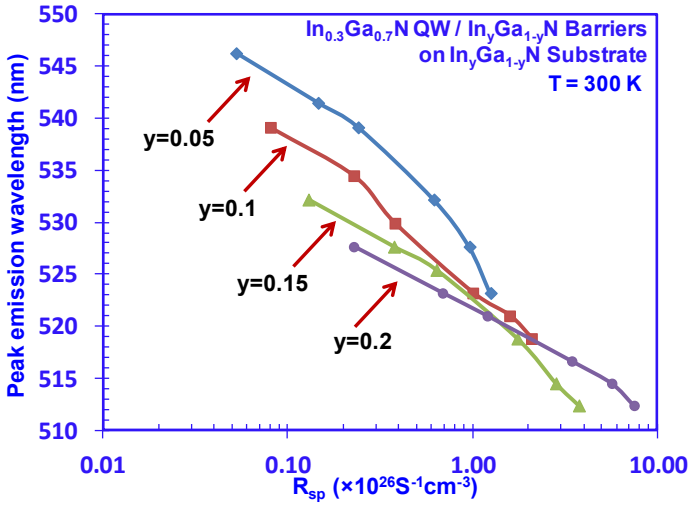

Figure 11-8: *Peak emission wavelength as a function of R_{sp} for $In_{0.3}Ga_{0.7}N$ QW with $In_yGa_{1-y}N$ substrates (y = 5% - 20%) at room temperature.*

Despite the potential advantages of ternary InGaN substrate for LED applications, it is important to note that the development of InGaN substrates is still relatively at early stage [19-21]. Further advances in the development of high quality InGaN substrate are of great importance for realizing high-efficiency LEDs based on this technology. Note that our current studies are primarily focused on the investigation of the spontaneous emission characteristics of the InGaN QWs on various ternary InGaN substrates as active regions for green- and red-emitting LEDs. However, future studies to investigate the optimized structures and compositions of the InGaN QW and barrier combinations on ternary substrates are of interest for achieving further improvement in the spontaneous emission rate of the LEDs active regions in particular for emission in the green up to red spectral regimes.

11.3 Optical Gain Characteristics of InGaN QWs on Ternary Substrates for Lasers

11.3.1 Optical Gain Analysis of InGaN QWs with Ternary Substrates

The gain properties of the InGaN QWs on ternary and GaN substrates are compared. In designing the respective QWs in this comparison, the In-contents in the InGaN QWs were chosen for similar emission wavelength at $n \sim 5 \times 10^{19}$ cm^{-3}. Figure 11-9(a) shows optical gain spectra for

$In_xGa_{1-x}N$ QWs (x = 0.325, 0.35) on $In_{0.15}Ga_{0.85}N$ substrate, and conventional $In_{0.32}Ga_{0.68}N$ QW on GaN substrate for green spectra regime at n = 5 × 10^{19} cm^{-3} at T=300 K. For $In_{0.32}Ga_{0.68}N$ QW on GaN substrate, relatively low material peak gain (g_{peak} ~ 474.1 cm^{-1}) is obtained with λ_{peak} ~ 516.7 nm. The material gain is defined as the peak value of the optical gain spectrum. The material gain of the $In_{0.325}Ga_{0.675}N$ QW / $In_{0.15}Ga_{0.85}N$ substrate (g_{peak} ~ 2039.7 cm^{-1}) is ~3.3 times higher than that of conventional method (g_{peak} ~ 474.1 cm^{-1}). The material gain of the $In_{0.35}Ga_{0.65}N$ QW / $In_{0.15}Ga_{0.85}N$ substrate (g_{peak} ~ 1527.7 cm^{-1}) with λ_{peak} ~ 532.2 nm is ~2.2 times higher than that of the conventional method. For yellow-emitting QWs comparison [figure (10-9 (b)], the use of the ternary substrate leads to 3.2 times increase in the material gain (g_{peak} ~ 861.4 cm^{-1}) over that of the conventional method.

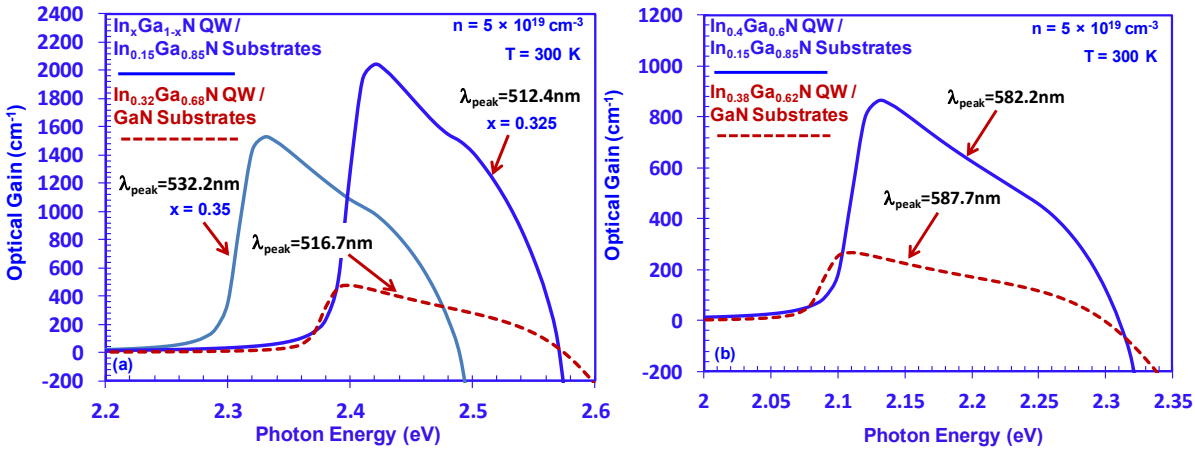

Figure 11-9: *Optical gain spectra for (a) $In_xGa_{1-x}N$ QWs (x = 0.325, 0.35) with $In_{0.15}Ga_{0.85}N$ barriers on $In_{0.15}Ga_{0.85}N$ substrate, and $In_{0.32}Ga_{0.68}N$ QW with GaN barriers on GaN substrate, and (b) $In_{0.4}Ga_{0.6}N$ QW with $In_{0.15}Ga_{0.85}N$ barriers on $In_{0.15}Ga_{0.85}N$ substrate, and $In_{0.38}Ga_{0.62}N$ QW with GaN barriers on GaN substrate with n = 5 × 10^{19} cm^{-3} at T = 300 K.*

The optical gain spectra for green-emitting InGaN QWs on $In_{0.15}Ga_{0.85}N$ substrate are shown for various carrier densities in figures 11-10(a) and 11-10(b). The peak wavelengths of the optical gain spectra show blue-shifts for both structures with higher carrier density due to the carrier screening effect. The higher In-content QW exhibits lower material gain and larger wavelength blue-shift, in comparison to those of lower In-content QW. By comparison the spectra at n = 3×10^{19} cm^{-3} and n = 5×10^{19} cm^{-3}, the wavelength blue-shifts for the lower [figure 11-10(a)] and higher In-content [figure (11-10(b)] InGaN QW are ~ 13 nm and ~ 19 nm, respectively. The

corresponding comparisons of the material gains for ternary and conventional methods were shown in figures 11-11(a) and 11-11(b) for green- and yellow-emitting QWs, respectively. At higher carrier densities, the material gains for green (yellow) -emitting InGaN QWs on $In_{0.15}Ga_{0.85}N$ substrate are ~3.2-5 times (3.2-3.5 times) higher than that of the conventional method, as shown in figure 11-11(a) [figure 11-11(b)]. The improved material gains in green and yellow spectral regimes obtained from the use of ternary substrates are attributed from the reduced lattice-mismatch strain resulting in reduced charge separation issue in the QWs, which leads to improved optical matrix element and larger material gains.

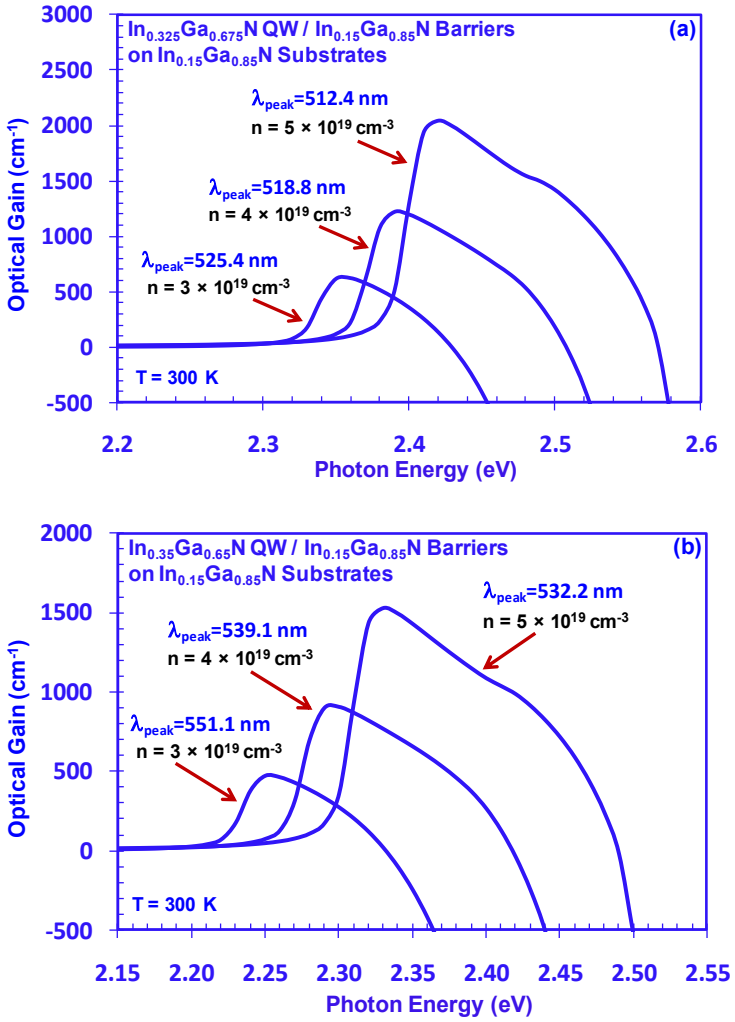

Figure 11-10: *Optical gain spectra for (a) $In_{0.325}Ga_{0.675}N$ QW, and (b) $In_{0.35}Ga_{0.65}N$ QW with $In_{0.15}Ga_{0.85}N$ barriers on $In_{0.15}Ga_{0.85}N$ substrate for green spectra regime at n = 3-5 × 10^{19} cm^{-3} at room temperature.*

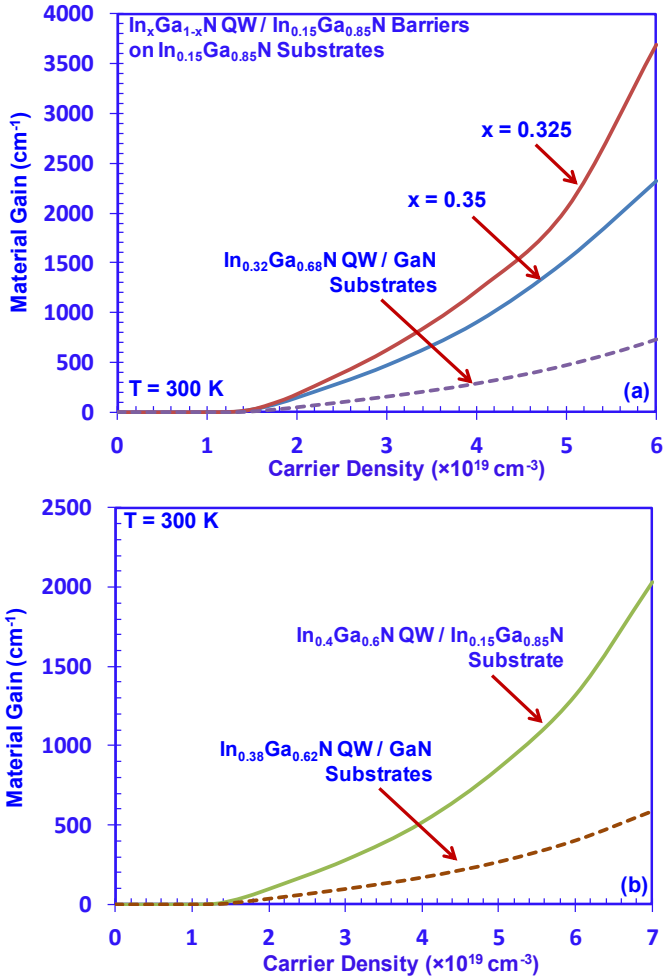

Figure 11-11: *Comparison of material peak gain as a function of carrier density for (a) $In_xGa_{1-x}N$ QWs (x = 0.325, 0.35) on $In_{0.15}Ga_{0.85}N$ substrate, and conventional $In_{0.32}Ga_{0.68}N$ QW on GaN substrate, and (b) $In_{0.4}Ga_{0.6}N$ QW on $In_{0.15}Ga_{0.85}N$ substrate, and conventional $In_{0.38}Ga_{0.62}N$ QW on GaN substrate at room temperature.*

The optical gain properties for InGaN QWs on ternary substrates with various In-contents were shown in figures 11-12(a) and 11-12(b). Note the second peak from the gain spectra of the $In_{0.3}Ga_{0.7}N$ QW/ $In_{0.15}Ga_{0.85}N$ substrate at 473.3 nm in figure 10-12(a) is attributed to the band filling effect leading to stronger excited state transitions. The use of GaN substrate, as well as lower In-content $In_yGa_{1-y}N$ substrates (y = 0.05, 0.1), lower optical gains are obtained due to the larger charge separation effect from the larger lattice-mismatch strain. In contrast, the use of higher In-content ternary substrate leads to reduction in charge separation effect in the QW, which results in improved material gain. The material gain for $In_{0.3}Ga_{0.7}N$ QW/ $In_{0.15}Ga_{0.85}N$ substrate is ~ 2135.9 cm^{-1} (n = 5 × 10^{19} cm^{-3}), which is higher than those employing lower In-

content ternary substrates. For comparison purpose, the material gain for the QWs using GaN substrate is relatively low with g_{peak} ~ 588.5 cm^{-1}.

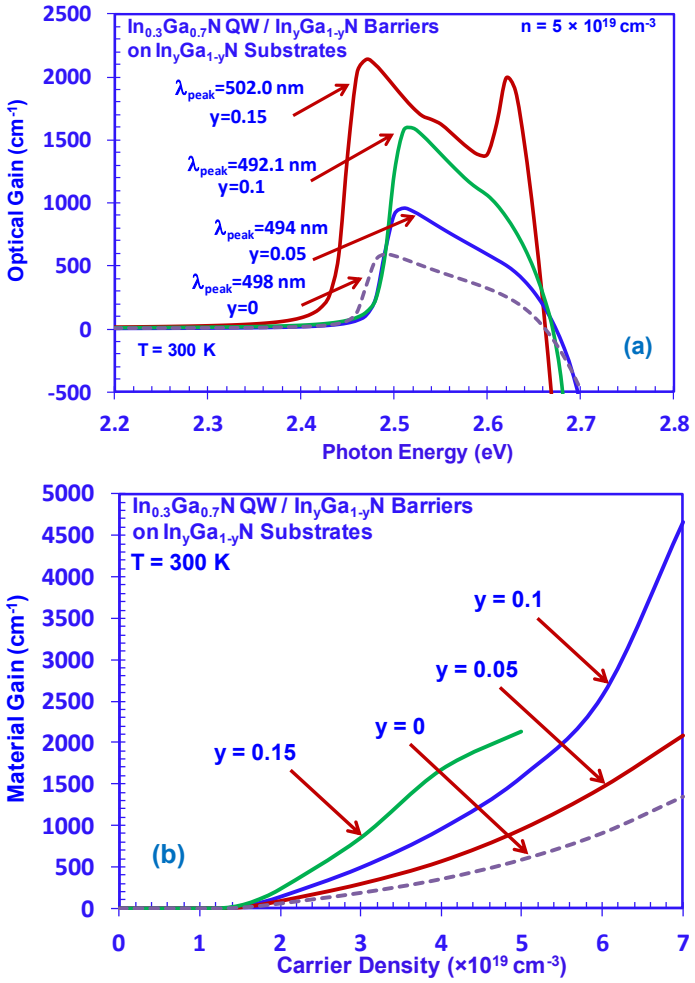

Figure 11-12: *(a) Optical gain spectra at n = 5 × 10^{19} cm^{-3} and (b) material gains as a function of carrier density for $In_{0.3}Ga_{0.7}N$ QW with $In_yGa_{1-y}N$ barriers on $In_yGa_{1-y}N$ substrate (y = 0, 0.05, 0.1 and 0.15).*

11.3.2 Differential Gains and Wavelength Shifts Characteristics

The differential gains (dg/dn) for InGaN QWs on ternary and GaN substrates were compared in figures 11-13(a)-(c). Figure 11-13(a) shows the dg/dn as a function of carrier density for $In_xGa_{1-x}N$ QWs (x = 0.325, 0.35) on $In_{0.15}Ga_{0.85}N$ substrate, and conventional $In_{0.32}Ga_{0.68}N$ QW on GaN substrate for green spectral regime at T=300K. The increasing trend of dg/dn for higher carrier density is primarily attributed to the carrier screening effect. The dg/dn for the $In_{0.35}Ga_{0.65}N$ QW and $In_{0.325}Ga_{0.675}N$ QW on $In_{0.15}Ga_{0.85}N$ substrate are ~3.6 and ~-4.9 times of that of the

conventional $In_{0.32}Ga_{0.68}N$ QW with n = 5×10^{19} cm^{-3}, respectively [figure 11-13(a)]. For yellow-emitting QWs, the dg/dn for $In_{0.4}Ga_{0.6}N$ QW/ $In_{0.15}Ga_{0.85}N$ substrate shows ~7.7 times improvement than that of the $In_{0.38}Ga_{0.62}N$ QW /GaN substrate with n = 5×10^{19} cm^{-3} [figure 11-13(b)]. The dg/dn are compared for $In_{0.3}Ga_{0.7}N$ QW on $In_yGa_{1-y}N$ substrate (y = 0 up to y = 0.15) at T = 300K [figure 11-13(c)]. For the use of $In_{0.15}Ga_{0.85}N$ substrate, higher differential gains are achieved for lower carrier densities (n< 3.5×10^{19} cm^{-3}) due to the enhanced matrix element. The decrease in the dg/dn for the ternary substrate with 15% In-content (n> 3.5×10^{19} cm^{-3}) can be attributed to the band filling effect. These findings indicate the potential advantage from the use of ternary substrate for high speed lasers applications.

The comparison of the wavelength shifts as a function of material gains for the green- and yellow-emitting QWs on ternary substrates are shown in figures 11-14(a) and 11-14(b). For green-emitting QWs [figure 11-14(a)], the peak emission wavelengths show blue-shift for increasing carrier densities for both QWs due to the carrier screening effect. Significantly higher material gains (g_{peak} > 2000 cm^{-1}) are obtained from the use of ternary substrates. In order to compare the wavelength shift quantitatively, the $\Delta\lambda$ ($\Delta\lambda = \lambda_0 - \lambda(n)$) as a function of material peak gains are extracted from figure 11-14(a), where λ_0 is the emission wavelength at n = 3×10^{18} cm^{-3} [figure 11-14(b)]. The use of ternary substrates leads to significantly improved material gain, accompanied with significantly reduced wavelength shift. To illustrate this improvement for $\Delta\lambda$ ~100 nm, the use of ternary substrate leads to increase in material gain ~ 2200 cm^{-1} in comparison to that of conventional method. This finding illustrates the feasibility of achieving high material gain with lower carrier density from the use of ternary substrate. Similar finding is also observed for yellow-emitting QWs [figures 11-14(c) and 11-14(d)], which indicates that the increase of ~1200 cm^{-1} in material gain from the use of ternary substrate method for $\Delta\lambda$ ~150 nm.

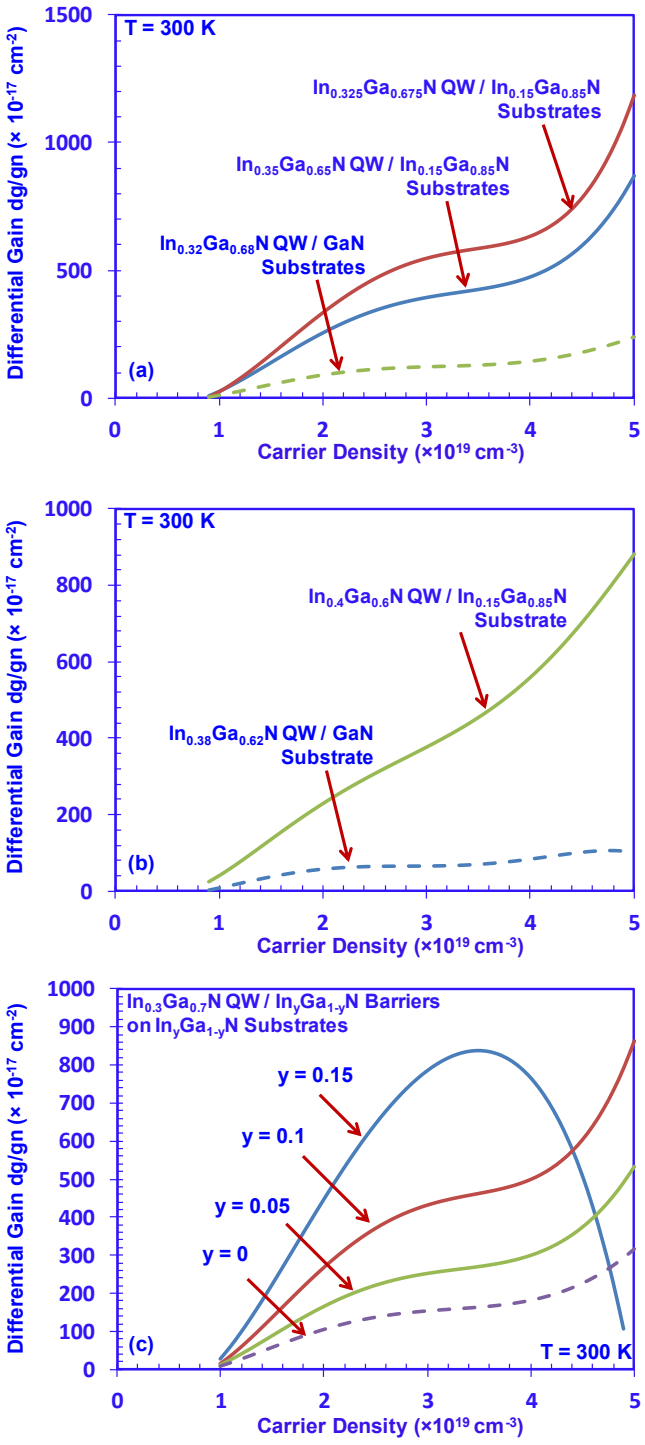

Figure 11-13: *Differential gain as a function of carrier density for (a) $In_xGa_{1-x}N$ QWs (x = 0.325, 0.35) on $In_{0.15}Ga_{0.85}N$ substrate, and $In_{0.32}Ga_{0.68}N$ QW on GaN substrate, (b) $In_{0.4}Ga_{0.6}N$ QW on $In_{0.15}Ga_{0.85}N$ substrate, and $In_{0.38}Ga_{0.62}N$ QW on GaN substrate, and (c) $In_{0.3}Ga_{0.7}N$ QW with $In_yGa_{1-y}N$ barriers on $In_yGa_{1-y}N$ substrate (y = 0, 0.05, 0.1 and 0.15) at T = 300 K.*

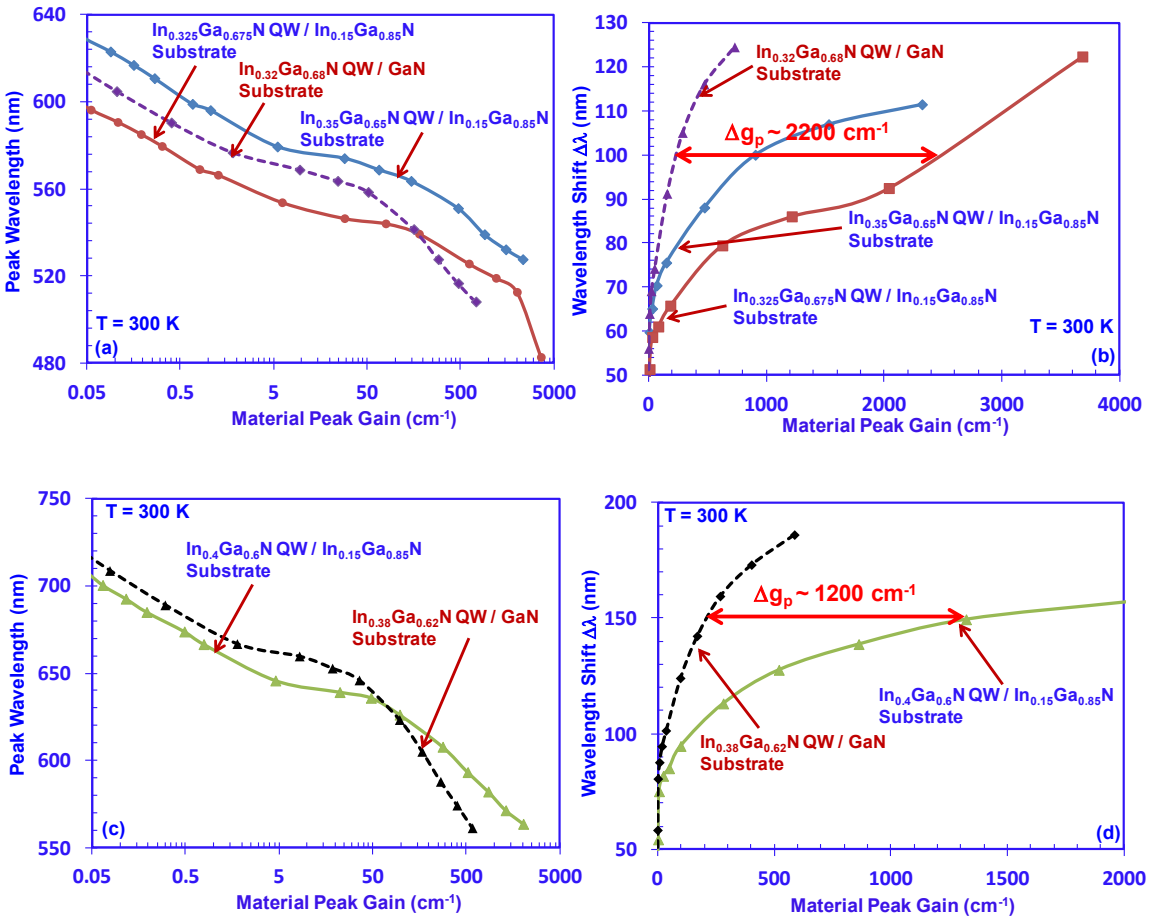

Figure 11-14: *(a) Peak emission wavelengths from gain spectra as a function of material peak gain, and (b) wavelength shift $\Delta\lambda$ ($\Delta\lambda = \lambda_0 - \lambda(n)$) for $In_xGa_{1-x}N$ QWs (x = 0.325, 0.35) on $In_{0.15}Ga_{0.85}N$ substrate, and conventional $In_{0.32}Ga_{0.68}N$ QW on GaN substrate. (c) Peak emission wavelengths as a function of material peak gain, and (d) wavelength shift $\Delta\lambda$ ($\Delta\lambda = \lambda_0 - \lambda(n)$) for $In_{0.4}Ga_{0.6}N$ QW on $In_{0.15}Ga_{0.85}N$ substrate, and conventional $In_{0.38}Ga_{0.62}N$ QW on GaN substrate at T=300 K.*

The effect of employing different substrates on the screening effect is presented in figures 11-15(a) and 11-15(b). Figure 11-15(a) compares the peak emission wavelengths as a function of material gain for the $In_{0.3}Ga_{0.7}N$ QW on various $In_yGa_{1-y}N$ substrates (y = 0, 0.05, 0.1 and 0.15). The use of ternary substrates leads to larger material gains than that of the conventional method. Note that the use of higher In-content substrate leads to larger material gain with reduced wavelength shift [figure 11-15(b)]. Specifically, for obtaining g_{peak} ~ 1000 cm^{-1}, the lowest wavelength shift $\Delta\lambda$ ~ 70 nm is obtained by using $In_{0.15}Ga_{0.85}N$ substrate. In addition, an increase

of ~1700 cm^{-1} in material gain is obtained by employing the $In_{0.1}Ga_{0.9}N$ substrate as compared to conventional method with $\Delta\lambda \sim 100$ nm.

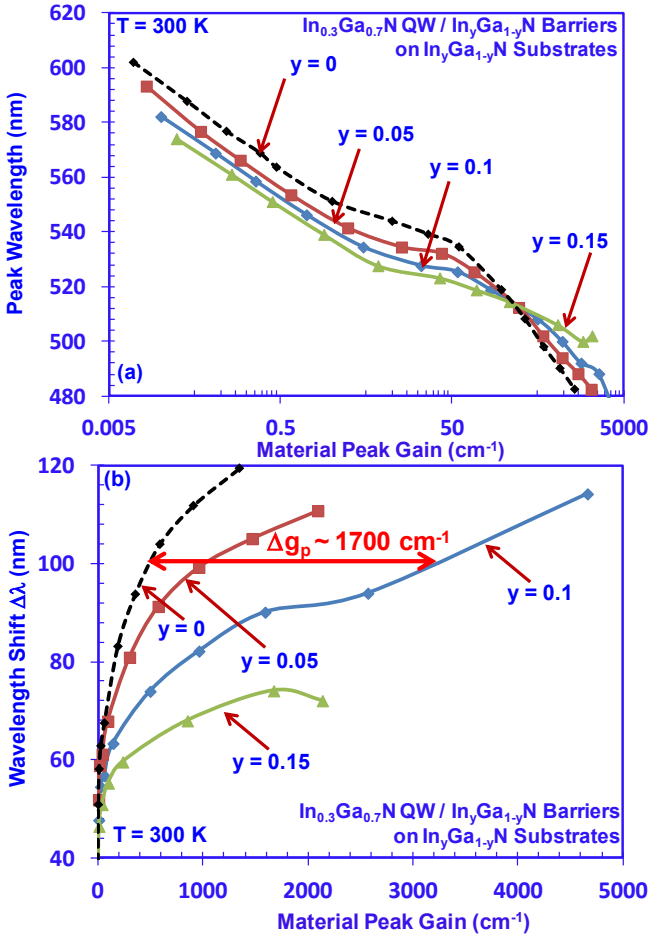

Figure 11-15: *(a) Peak emission wavelength from gain spectra as a function of material peak gain, and (b) wavelength shift $\Delta\lambda$ ($\Delta\lambda = \lambda_0 - \lambda(n)$) for $In_{0.3}Ga_{0.7}N$ QW with $In_yGa_{1-y}N$ barriers on $In_yGa_{1-y}N$ substrate (y = 0, 0.05, 0.1 and 0.15) at T = 300K.*

11.3.3 Threshold Characteristics of Green- and Yellow-Emitting Lasers

The threshold characteristics are analyzed for the green- and yellow-emitting lasers using ternary substrates. The threshold gain (g_{th}) is estimated as ~1500 cm^{-1} [29, 37]. The threshold carrier densities (n_{th}) can be obtained from the material peak gain and carrier density relation in figures 11-11(a) and 11-11(b). For green-emitting InGaN QWs on ternary substrates [figure 11-11(a)], the threshold carrier densities are $n_{th} \sim 4.4 \times 10^{19}$ cm^{-3} for $In_{0.325}Ga_{0.675}N$ QW/ $In_{0.15}Ga_{0.85}N$ substrate, and $n_{th} \sim 4.95 \times 10^{19}$ cm^{-3} for $In_{0.35}Ga_{0.65}N$ QW/ $In_{0.15}Ga_{0.85}N$ substrate. In contrast, the material gains obtained from the conventional active regions emitting in green spectral regime at

similar carrier density (n ~ 4.4-6.27×10^{19} cm^{-3}) range from ~ 200-400 cm^{-1}, which are significantly lower than those obtained from the ternary substrate approach. For yellow-emitting InGaN QWs on ternary substrates [figure 11-11(b)], the threshold carrier density is n_{th} ~ 6.27 ×10^{19} cm^{-3}. Similarly, the material gain obtained from the conventional QW at similar carrier density is as low as ~ 400 cm^{-1}, which indicates that significantly higher carrier density is required for the conventional approach in order to achieve g_{th} ~ 1500 cm^{-1}.

The threshold carrier densities of the green-emitting QWs on ternary substrates with various In-contents can be extracted from figure 11-12(b). For $In_{0.3}Ga_{0.7}N$ QW, the n_{th} are ~ 6.05 ×10^{19} cm^{-3}, 4.9 ×10^{19} cm^{-3}, and 3.75 ×10^{19} cm^{-3}, respectively, for $In_{0.05}Ga_{0.95}N$, $In_{0.1}Ga_{0.9}N$, and $In_{0.15}Ga_{0.85}N$ substrates. The corresponding n_{th} for the conventional method is larger than 7 ×10^{19} cm^{-3}. Thus, the finding indicates the use of ternary substrates leads to a significant reduction in n_{th}, which is important for suppressing the non-radiative recombination current density and threshold current density. To analyze the threshold current densities (J_{th}) for the green and yellow-emitting lasers, the relation of the material gain as a function of total current density (J_{tot} = J_{Rad} + J_{non_Rad}) for $In_xGa_{1-x}N$ QWs (x = 0.325, 0.35 and 0.4) on $In_{0.15}Ga_{0.85}N$ substrate is shown in figure 11-16. The monomolecular recombination rates of A = 6×10^8 s^{-1}, 1×10^9 s^{-1}, and 1.5×10^9 s^{-1} are used similar to reference 38. For achieving g_{th} ~ 1500 cm^{-1}, yellow-emitting QWs typically have ~30% higher J_{th} over that of green-emitting QWs.

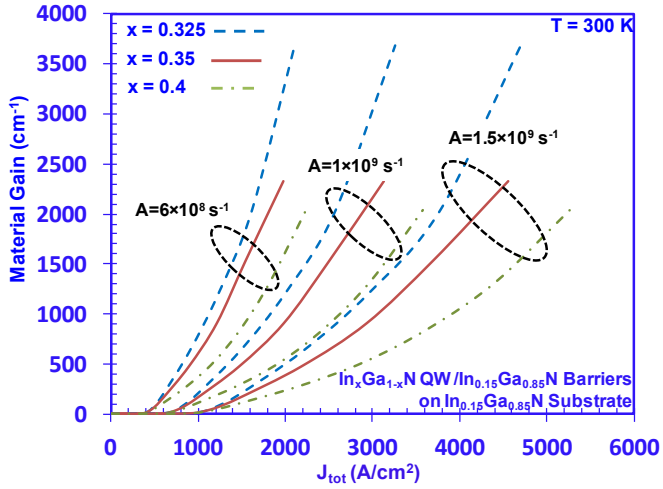

Figure 11-16: *Material gain as a function of total current density for $In_xGa_{1-x}N$ QWs (x = 0.325, 0.35, 0.4) with $In_{0.15}Ga_{0.85}N$ barriers on $In_{0.15}Ga_{0.85}N$ substrate at T=300 K. The monomolecular recombination rates are A = 6×10^8 s^{-1}, 1×10^9 s^{-1}, and 1.5×10^9 s^{-1}.*

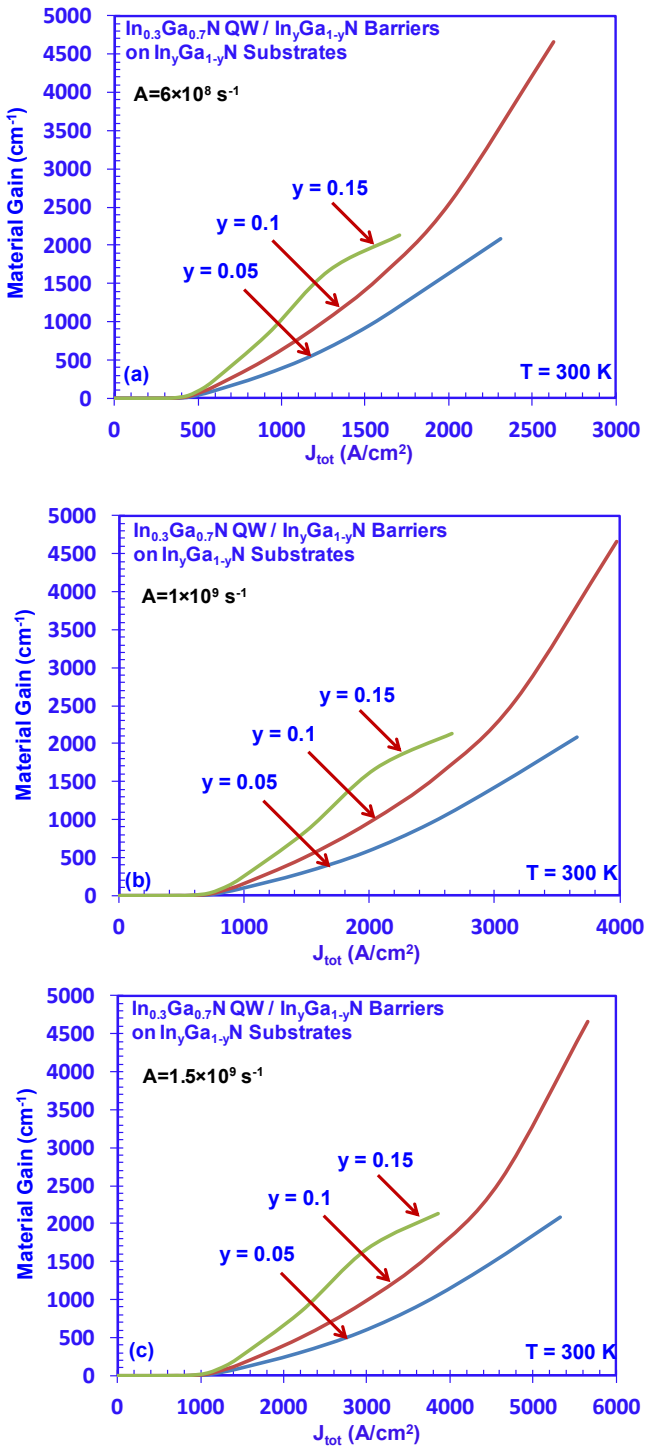

Figure 11-17: *Material gain as a function of total current density for $In_{0.3}Ga_{0.7}N$ QW with $In_yGa_{1-y}N$ barriers on $In_yGa_{1-y}N$ substrate (y = 0.05, 0.1 and 0.15) at T = 300 K. The monomolecular recombination rates are (a) A = 6×10^8 s^{-1}, (b) A = 1×10^9 s^{-1}, and (c) A = 1.5×10^9 s^{-1}.*

The threshold comparison from the use of ternary $In_yGa_{1-y}N$ substrates (with y = 0.05, 0.1 and 0.15) are presented for various monomolecular recombination rates [figures 10-17(a)-10-17(c)]. In this comparison, the active region was chosen as $In_{0.3}Ga_{0.7}N$ QW. The reduction in the n_{th} from the ternary substrate is important for suppressing the non-radiative current density, which in turn reduces the threshold current density. The threshold analysis here does not take into account the Auger recombination due to the low value of the Auger recombination rate (C_{Auger}~10^{-32} cm^6/sec) in InGaN [35, 40]. It is important to point out the large discrepancy on the C_{Auger} for InGaN QWs reported in the literatures [39-42]. The C_{Auger} of $3.5x10^{-34}$ cm^6/sec up to $1x10^{-32}$ cm^6/sec had been reported for InGaN QWs [39, 40], while values of $1.4\text{-}2x10^{-30}$ cm^6/sec had been reported in the bulk system [41, 42]. Further conclusive studies are still required for determining the C_{Auger} in InGaN QWs [39-42]. However, the reduction in the n_{th} from the use of ternary substrates will be important in reducing the Auger current density at threshold (J_{th_Auger} ~ n_{th}^3) by ~40% up to 85%.

11.4 Summary

In summary, the spontaneous emission characteristics of InGaN QWs on ternary $In_{0.15}Ga_{0.85}N$ substrate emitting in green and red spectral regimes are analyzed. The R_{sp} of the green- and yellow-emitting InGaN QWs grown on $In_{0.15}Ga_{0.85}N$ substrate were found as ~2.9-3.2 times of those of QWs grown on conventional GaN substrate. For red-emitting $In_{0.4}Ga_{0.6}N$ QW / $In_{0.15}Ga_{0.85}N$ substrate, the R_{sp} was ~2.5 times of that of the conventional approach. By using higher In-content InGaN substrates, significant increase in spontaneous emission rate and reduction in blue shift from carrier-screening effect are observed. The use of the ternary InGaN substrate leads to reduction in QW strain and increase in optical matrix element, which in turn results in large spontaneous emission rates for InGaN QWs applicable for green- and red-emitting LEDs.

The optical gain and threshold characteristics of InGaN QWs on ternary InGaN substrates or templates are analyzed for green- and yellow-emitting lasers, which are also compared with the InGaN QWs on conventional GaN substrates or templates. The effect of various ternary substrates are also studied and compared with conventional GaN substrate at green spectral

regime. The use of the ternary InGaN substrate leads to reduced compressive strain and the polarization field, which contributes to enhanced optical matrix element from the reduced charge separation effect. Thus, the use of ternary InGaN substrate is expected to result in large increase in material gain and significant reduction in threshold carrier density in the active region, accompanied with less wavelength shift, which may potentially lead to high performance diode lasers emitting in the green and yellow spectral regimes. Note that experimentally, the successful growths of bulk InGaN substrates have already been realized [19-21]. For the InGaN QWs grown on bulk ternary InGaN substrates, the In-contents of the InGaN QWs are lower than that of the substrates. Thus, the growth temperatures of the InGaN QWs should be lower than that of the ternary substrates, which are expected to be kept in good condition during the growths. However, it is important to note that the experimental challenge still needs to be addressed for optimized growths, as the ternary InGaN substrates have only been experimentally realized with In-contents ranging from 0.9% up to 20% [19-21].The development of the ternary substrate still requires further optimization, and the availability of this substrate is key for enabling the advantages deliberated in this study. In addition, the growths of high In-content InGaN alloy for QW active regions is still challenging attributed to the increased phase separation issue during the epitaxy.

References for Chapter 11

[1] J.H. Ryou, P.D. Yoder, J.P. Liu, Z. Lochner, H. Kim, S. Choi, H.J. Kim, R.D. Dupuis, “Control of Quantum-Confined Stark Effect in InGaN-Based Quantum Wells,” IEEE J. Sel. Top. Quantum Electron., vol. 15, no. 4, pp. 1080-1091, Aug. 2009.

[2] I. H. Brown, P. Blood, P. M. Smowton, J. D. Thomson, S. M. Olaizola, A. M. Fox, P. J. Parbrook, and W. W. Chow, “Time evolution of the screening of piezoelectric fields in InGaN quantum wells,” IEEE J. Quantum Electron., vol. 42, no. 12, pp. 1202–1208, Nov-Dec. 2006.

[3] S. H. Park, and S. L. Chuang, “Comparison of zinc-blende and wurtzite GaN semiconductors with spontaneous polarization and piezoelectric field effects,” J. Appl. Phys., vol. 87, no. 1, pp. 353-364, Sep. 2000.

[4] A. Venkatachalam, B. Klein, J.-H Ryou, S. C. Shen, R. D. Dupuis, P. D. Yoder, “Design Strategies for InGaN-Based Green Lasers,” IEEE J. Quantum Electron., vol. 46, no. 2, pp. 238-245, Feb. 2010.

[5] S. H. Park, D. Ahn, and S. L. Chuang, "Electronic and Optical Properties of a- and m-plane Wurtzite InGaN/GaN Quantum Wells," IEEE. J. Quantum Electron., vol. 43, no. 12, pp. 1175-1182, Dec. 2007.

[6] R.M. Farrell, E. C. Young, F. Wu, S.P. DenBaars, and J.S. Speck, “Materials and growth issues for high-performance nonpolar and semipolar light-emitting devices,” Semiconductor Science and Technology, vol. 27, no. 2, pp. 024001-024015, Jan. 2012.

[7] M. C. Schmidt, K.-C. Kim, R. M. Farrell, D. F. Feezell, D. A. Cohen, M. Saito, K. Fujito, J. S. Speck, S. P. Denbaars, and S. Nakamura, “Demonstration of Nonpolar m-Plane InGaN/GaN Laser Diodes,” Jpn. J. Appl. Phys., vol. 46, pp. L190-L191, Feb. 2007.

[8] R. M. Farrell, D. F. Feezell, M. C. Schmidt, D. A. Haeger, K.M. Kelchner, K. Iso, H. Yamada, M. Saito, K. Fujito, D. A. Cohen, J. S. Speck, S P. DenBaars, and S. Nakamura, “Continuous-wave Operation of AlGaN-cladding-free Nonpolar m-Plane InGaN/GaN Laser Diodes,” Jpn. J. Appl. Phys., vol. 46, no. 32, pp. L761-L763, Aug. 2007.

[9] D. Queren, A. Avramescu, G. Bruderl, A. Breidenassel, M. Schillgalies, S. Lutgen, and U. Strau, “500 nm electrically driven InGaN based laser diodes,” Appl. Phys. Lett., vol. 94, no. 8, pp. 081119-1 - 081119-3, Feb. 2009.

[10] R. A. Arif, Y. K. Ee, and N. Tansu, “Polarization Engineering via Staggered InGaN Quantum Wells for Radiative Efficiency Enhancement of Light Emitting Diodes,” Appl. Phys. Lett., vol. 91 (9), Art. 091110, August 2007.

[11] H.P. Zhao, G.Y. Liu, J.Zhang, J.D. Poplawsky, V. Dierolf, and N. Tansu, “Approaches for high internal quantum efficiency green InGaN light-emitting diodes with large overlap quantum wells,” Optics Express, vol. 19, no. 14, pp. A991-A1007, Jul. 2011.

[12] H. P. Zhao, G. Y. Liu, X. H. Li, R. A. Arif, G. S. Huang, J. D. Poplawsky, S. Tafon Penn, V. Dierolf, and N. Tansu, “Design and Characteristics of Staggered InGaN Quantum Well Light-

Emitting Diodes in the Green Spectral Regimes," IET Optoelectron., vol. 3, no. 6, pp. 283-295, Dec. 2009.

[13] H. P. Zhao, and N. Tansu, "Optical Gain Characteristics of Staggered InGaN Quantum Well Lasers," J. Appl. Phys., vol. 107, Art. 113110, June 2010.

[14] S. H. Park, D. Ahn, B. H. Koo, and J. W. Kim, "Electronic and optical properties of staggered InGaN/InGaN quantum-well light-emitting diodes," Phys. Stat. Sol. A, vol. 206, no. 11, pp. 2637-2640, Jun. 2009.

[15] S. H. Park, D. Ahn, B. H. Koo, and J. W. Kim, "Dip-shaped InGaN/GaN quantum-well light-emitting diodes with high efficiency," Appl. Phys. Lett., vol. 95, no. 6, p. 063507, Aug. 2009.

[16] S. H. Park, D. Ahn, and J. W. Kim, "High-efficiency staggered 530 nm InGaN/InGaN/GaN quantum-well light-emitting diodes," Appl. Phys. Lett., vol. 94, no. 4, pp. 041109-1-041109-3, Jan. 2009.

[17] C. T. Liao, M. C. Tsai, B. T. Liou, S. H. Yen, and Y. K. Kuo, "Improvement in Output Power of a 460 nm InGaN Light-emitting Diode using Staggered Quantum Well," J. Appl. Phys., vol. 108, no. 6, pp. 063107-1 - 063107-6, Sep. 2010.

[18] T. Shioda, H. Yoshida, K. Tachibana, N. Sugiyama, and S. Nunoue, "Enhanced Internal Quantum Efficiency of Green LEDs Employing AlGaN Interlayer in InGaN/GaN MQW Structure on Sapphire (0001) Substrate," 9th International Conference on Nitride Semiconductors, Glasgow, Scotland, July 2011.

[19] M. Shimizu, T. Kawaguchi, K. Hiramatsu, N. Sawaki, Solid-State Electron., vol. 41, no. 2, pp. 145-147, Feb. 1997.

[20] K. Pantzasa, Y. El Gmili, J. Dickerson,S. Gautier, L. Largeau, O. Mauguin, G. Patriarche, S. Suresh, T. Moudakir, C. Bishop, A. Ahaitouf, T. Rivera, C. Tanguy, P.L. Voss, and A. Ougazzaden, "Semibulk InGaN: A novel approach for thick, single phase, epitaxial InGaN layers grown by MOVPE," J. Crys. Growth (2012), DOI: 10.1016/j.jcrysgro.2012.08.041.

[21] www.eetimes.com/electronics-news/4189123/TDI-claims-first-InGaN-substrate

[22] T. K. Sharma, and E. Towe, "On ternary nitride substrates for visible semiconductor light-emitters," Appl. Phys. Lett., vol. 96, no. 19, pp. 191105-1-191105-3, May 2010.

[23] S.H. Park, Y.T. Moon, J.S. Lee, H.K. Kwon, J.S. Park, and D. Ahn, “Spontaneous emission rate of green strain-compensated InGaN/InGaN LEDs using InGaN substrate,” Phys. Stat. Sol. (A), vol. 208, no. 1, pp. 195-198, Jan. 2011.

[24] J. Zhang, and N. Tansu, “Improvement in spontaneous emission rates for InGaN quantum wells on ternary InGaN substrate for light-emitting diodes,”J. Appl. Phys., vol. 110, no. 11, pp. 113110-1-113110-5, Dec. 2011.

[25] P. S. Hsu, M. T. Hardy, F. Wu, I. Koslow, E. C. Young, A. E. Romanov, K. Fujito, D. F. Feezell, S. P. DenBaars, J. S. Speck, and S. Nakamura, “444.9 nm semipolar (1122) laser diode grown on an intentionally stress relaxed InGaN waveguiding layer,”Appl. Phys. Lett. vol. 100, no. 2, pp. 021104-1-021104-4, Jan. 2012.

[26] S. L. Chuang, “Optical Gain of Strained Wurtzite GaN Quantum-Well Lasers,” IEEE J. Quantum Electron., vol. 32, no. 10, pp. 1791-1800, Oct. 1996.

[27] S. L. Chuang and C. S. Chang, “A band-structure model of strained quantum-well wurtzite semiconductors,” Semicond. Sci. Technol., vol. 12, no. 3, pp. 252-263, Mar. 1997.

[28] S. L. Chuang, Physics of Photonic Devices 2nd ed. Wiley, New York, 2009, Chap. 4 and 11.

[29] H. Zhao, R. A. Arif, Y. K. Ee, and N. Tansu, “Self-Consistent Analysis of Strain-Compensated InGaN–AlGaN Quantum Wells for Lasers and Light-Emitting Diodes,” IEEE J. Quantum Electron., vol. 45, no. 1, pp. 66-78, Jan. 2009.

[30] I. Vurgaftman and J.R. Meyer, Chapter 2 in Nitride Semiconductor Devices, J. Piprek (Editor), Wiley, 2007.

[31] I. Vurgaftman and J.R. Meyer, “Band parameters for nitrogen-containing semiconductors,” J. Appl. Phys., vol. 94, no. 6, pp. 3675-3696, Sep. 2003.

[32] F. Bernardini and V. Fiorentini, “Spontaneous versus piezoelectric polarization in III–V Nitrides: Conceptual aspects and practical consequences,” Phys. Stat. Sol. (b), vol. 216, pp. 391–398, Nov. 1999.

[33] O. Ambacher, J.Majewski, C. Miskys, A. Link, M. Hermann, M. Eickhoff, M. Stutzmann, F. Bernardini, V. Fiorentini, V. Tilak, W. J. Schaff, and L. F. Eastman, “Pyroelectric properties of

Al(In)GaN/GaN heteroand quantum well structures," J. Phys.: Condens. Matter, vol. 14, pp. 3399–3434, Mar. 2002.

[34] G. Bester, X. Wu, D. Vanderbilt, and A. Zunger, "Importance of Second-Order Piezoelectric Effects in Zinc-Blende Semiconductors," Phys. Rev. Lett., vol. 96, pp. 187602-1– 187602-4, May 2006.

[35] G. Bester, A. Zunger, X. Wu and D. Vanderbilt, "Effects of linear and nonlinear piezoelectricity on the electronic properties of InAs/GaAs quantum dots," Phys. Rev. B, vol. 74, pp. 081305-1-081305-4, Aug. 2006.

[36] J. Pal, G. Tse, V. Haxha, M. A. Migliorato, and S. Tomic, "Importance of non linear piezoelectric effect in Wurtzite III-N semiconductors," Opt. Quant. Electron., vol. 44, no. 3-5, pp. 195-203, June 2012.

[37] H. Y. Ryu, K. H. Ha, S. N. Lee, T. Jang, J. K. Son, H. S. Paek, Y. J. Sung, H. K. Kim, K. S. Kim, O. H. Nam, Y. J. Park, and J. I. Shim, "High-performance blue InGaN lase diodes with single-quantum-well active layers." IEEE Photon. Technol. Lett., vol. 19, no. 21, pp. 1717-1719, Nov. 2007.

[38] W. W. Chow, M. Kneissl, "Laser gain properties of AlGaN quantum wells," J. Appl. Phys., vol. 98, no. 11, pp. 114502-1–114502-6, Dec. 2005.

[39] J. Hader, J. V. Moloney, A. Thranhardt, and S. W. Koch, in Nitride Semiconductor Devices, edited by J. Piprek (Wiley-CCH, Weinheim, 2007), Chap. 7.

[40] J. Hader, J. V. Moloney, B. Pasenow, S. W. Koch, M. Sabathil, N. Linder, and S. Lutgen, "On the importance of radiative and Auger losses in GaN-based quantum wells," Appl. Phys. Lett., vol. 92, Art. 261103, July 2008.

[41] Y. C. Shen, G. O. Mueller, S. Watanabe, N. F. Gardner, A. Munkholm, and M. R. Krames, "Auger recombination in InGaN measured by photoluminescence," Appl. Phys. Lett., vol. 91, Art. 141101, Oct. 2007.

[42] K. T. Delaney, P. Rinke, and C. G. Van de Walle, "Auger recombination rates in nitrides from first principles," Appl. Phys. Lett., vol. 94, Art. 191109, May 2009.

Chapter 12: Summary and Future Outlook

In this thesis, the research works have been accomplished involve in the area of semiconductor optoelectronic and thermoelectric materials and devices, and my specific research topics focus on 1) III-Nitride semiconductor nanostructures for thermoelectric applications, 2) III-Nitride based Ultraviolet (UV) lasers, and 3) novel approaches for high-efficiency III-Nitride light-emitting diodes (LEDs) and lasers. My research contributions in III-Nitride semiconductors are related to 1) studying and realizing Nitride based thermoelectric materials with high thermoelectric figure of merit, 2) addressing the challenges of feasibility for Nitride based deep- and mid-UV lasers, and 3) proposing novel approaches for enabling high-efficiency visible LEDs and lasers.

12.1 Summary

12.1.1 III-Nitride Semiconductors for Thermoelectricity

In our works, the high Z*T value for lattice-matched AlInN alloy grown by MOCVD has been reported. Further investigations of the thermoelectric characteristics for MOCVD-grown AlInN alloys with various In-contents are of great interest for improved understanding of the important parameters necessary to further optimize the *Z*T* value in this material system. The record *Z*T* values of the $Al_{1-x}In_xN$ alloys were measured as high as 0.391 up to 0.532 at T=300 K, which show significant improvement from the RF-sputtered AlInN (*Z*T*=0.005, T=300 K) and MOCVD-grown InGaN (*Z*T*=0.08, T=300 K). The improvement observed from the MOCVD-grown AlInN alloys can be attributed to the increase in Seebeck coefficient and electrical conductivity resulting in higher power factor, in comparison to those measured from MOCVD-grown InGaN and RF-sputtered AlInN. To optimize the high Z*T value in AlInN material system, it is important to employ crack-free AlInN thin film with large carrier concentration in order to obtain high power factor, while minimizing the thermal conductivity by employing AlInN alloy with In-content in the range of x = 17% - 22%. Our works represent the record Z*T values reported for any III-nitride semiconductors.

Furthermore, the Seebeck coeficients of AlInN alloys were characterized and analyzed from room temperature up to high temperature. The Seebeck coefficients of the n-type AlInN alloys show ~1.5–4 times improvement of the thermopower at higher temperatures. This finding indicates that MOCVD-grown AlInN alloys as excellent thermoelectric materials for III-Nitride device integration for high temperature applications.

From the simulation results, the figure of merit Z*T value for AlInN alloy is higher than those of AlGaN and InGaN alloys, attributing to the lower thermal conductivity and higher Seebeck coefficients, which agree with the experiment data. The theoretical finding confirms that ternary AlInN alloys as promising candidates for thermoelectric cooling application in nitride-based high power LEDs, lasers, and electronics.

The use of nanostructure engineering of thermoelectric materials such as supperlattice design will lead to further enhancement in the thermoelectric figure of merit Z*T, mainly attributed from the reduced thermal conductivity and enhanced electrical conductivity. Instead of using conventional two-layer superlattice design, we have proposed the novel structure of three-layer superlattice for enhanced thermoelectric properties. This finding indicates that the thermoelectric figure of merit for superlattice can further be enhanced by ~2-times from the use of the three-layer superlattice design.

12.1.2 Physics of AlGaN QW Based UV Lasers

The mid-UV (λ ~250-320 nm) and deep-UV (λ ~220-250 nm) lasers have important applications covering biochemical agent identification, flame detection, and space-to-space communications. However, the development of electrically-injected UV AlGaN QWs lasers have been limited to emission wavelength ~320-360 nm, while only optically-pumped deep-UV lasers had been realized for shorter emission wavelength. The pursuit of high-performance UV lasers has been limited to 1) the growth challenges to achieve high quality p-type AlN and high Al-content AlGaN gain media, and 2) the lack of understanding in the optical gain characteristics of the QW employed in this UV spectral regime.

My research work has pointed out the first time about the physical challenge of the AlGaN QWs, which is related to the valence subbands crossover in high Al-content AlGaN QWs gain media. In high Al-content AlGaN QWs, the valence subbands crossover leads to strong conduction (C) -crystal-field split-off hole (CH) transition, resulting in large transverse-magnetic (TM)-polarized optical gain for λ ~220-230 nm, which indicates the feasibility of TM-lasing for lasers emitting at deep-UV spectral regime. The finding represent the first identification of the possibility of achieving very large TM-polarized optical gain from deep UV AlGaN QW lasers. Subsequent experimental and theoretical works from other groups have confirmed our works and showed agreement with our finding.

In order to address the issue of low optical gain at λ ~ 250-300 nm, my research work has proposed the novel AlGaN-delta-GaN QW structure by inserting an ultra-thin GaN layer into high Al-content AlGaN-delta-GaN QW active region. The use of AlGaN-delta-GaN QWs resulted in strong valence subbands mixing, which led to large transverse-electric (TE) -polarized gain at λ ~ 240-300 nm, attributing to the dominant C-HH transition. Recent experimental work by NTT Basic Research Laboratories (Japan) has reported the polarization properties of the deep-UV emission from AlN/GaN short-period superlattices. The study revealed that stronger TE-polarized deep-UV emission can be obtained by inserting a very thin GaN layer into AlN active region, which is in agreement with our prediction based on high Al-content AlGaN-delta-GaN QW structure. Furthermore, we have also completed a comprehensive optimization study on the optical gain and threshold characteristics of AlGaN-delta-GaN QWs with varying delta-GaN positions and AlGaN QWs compositions for the mid- and deep-UV spectral regimes.

12.1.3 Substrate Engineering for High-efficiency LEDs and Lasers

Solid State Lighting (SSL) technology has the potential to reduce U.S. lighting energy usage by nearly one half and contribute significantly to the nation's climate change solutions, as stated by the U.S. Department of Energy, which encourages research and development breakthroughs in efficiency and performance related to SSL.

III-Nitride semiconductors have significant applications for lasers and energy-efficient technologies including SSL. Specifically, the use of InGaN alloy is of great interest as visible LEDs active region. In conventional approach, the growths of visible LEDs employ InGaN QWs grown on GaN templates, which lead to the existence of large QW strain arisen from the large lattice mismatch ($\Delta a/a$) between InGaN QW and GaN substrate / barrier materials. The compressive strain in InGaN QW, with respect to GaN substrate or template, leads to large piezoelectric polarization in the QW. The large piezoelectric polarization, in addition to spontaneous polarization, leads to charge separation effect in QW, which reduces the optical matrix element in InGaN QW. The large QW strain and charge separation issues lead to additional challenges in achieving high-efficiency green- and red-emitting InGaN QWs.

My research work has extended the approach by using ternary InGaN substrate for realizing QWs with reduced strain, which in turn results in reduced piezoelectric polarization fields in the QWs. For green- and red-emitting InGaN QWs on ternary substrate, the spontaneous emission rates were found as ~2.5-3.2 times of the conventional approach. The enhancement in spontaneous emission rate can be achieved by using higher In-content InGaN ternary substrate, which is also accompanied by a reduction in emission wavelength blue-shift from carrier screening effect. The use of InGaN substrate is expected to result in the ability for growing InGaN QWs with enhanced spontaneous emission rates, as well as reduced strain, applicable for green- and red-emitting LEDs. For laser applications, by employing the ternary substrates, the material gains were found as ~3-5 times higher than that of conventional method with reduced wavelength shift. The threshold carrier density is reduced by ~15%-50% from the use of ternary substrate method for green- and yellow-emitting lasers.

12.2 Future Outlook

III-Nitride semiconductors have tremendous applications towards different applications, especially for the main three topics I have covered in the thesis. For the research topics on UV LEDs and Lasers, further explorations at device level of novel AlGaN QW design will be of great interest for high-efficiency mid- and deep-UV LEDs and lasers, since the UV LEDs and lasers

have important applications for specific wavelengths, such as sterilization of surface areas and water with λ ~ 240-280nm, forensic and bodily fluid detection and analysis with λ ~ 250-405 nm, as well as protein analysis and drug discovery with λ ~ 270-300 nm.

Although solid state lighting technology has been pursued aggressively in the past decade, there are still two main challenges limiting the performance of Nitride base LEDs: 1) efficiency droop with increased operating current density, and 2) challenge in realizing high-efficiency green Nitride based LED, which require engineering approaches to enhance the device performance. Further development on the approach of substrate engineering will be of great importance in order to achieve higher efficiency for green LEDs or even longer emission wavelengths. Besides, novel engineering approaches for surface plasmon (SP) LEDs will result in enhanced efficiency for visible LEDs. For the research topics on III-Nitride based thermoelectricity, the enhanced thermoelectric figure of merit can be obtained by the approach of nanostructure engineering. Novel III-Nitride based superlattice structures will have great potential to lead to higher Z*T values. Besides, MOCVD growths and thermoelectric characterizations of III-Nitride nanostructure thermoelectric materials such as quantum dot, quantum wire, and quantum well structures are of great interest for enhanced Z*T values.

Curriculum Vitae

(Ms.) Jing Zhang, Ph.D.

Education

August 2009 – May 2013, ***Lehigh University (Bethlehem, Pennsylvania, USA)***

Doctor of Philosophy (Ph.D.) in Electrical Engineering, Department of Electrical and Computer Engineering

- PhD Advisor: Prof. Nelson Tansu (ECE, Lehigh)
- Dissertation Title: "Ternary III-Nitride Semiconductors for Thermoelectricity and Light Emitters"
- Research Areas: III-Nitride semiconductor nanostructures for thermoelectric and solid state lighting technologies.

Sep. 2005 – Jul. 2009, ***Huazhong University of Science and Technology (Wuhan, China)***

Bachelor of Science (B.S.) in Electronic Science and Technology

Bachelor of Art (B.A.) in English

- Excellent graduate award of Huazhong University of Science and Technology
- Thesis: The Design of cross-coupling planar microwave filters with transmission zeros
- Awarded "Best Graduation Thesis"

Professional Experiences

May 2013 – Present, ***Lehigh University (Bethlehem, PA, USA)***

Postdoctoral Research Fellow

Department of Electrical and Computer Engineering (ECE)

P. C. Rossin College of Engineering and Applied Science & Center for Photonics and Nanoelectronics

Postdoctoral Research Advisor: Prof. Nelson Tansu

August 2009 – May 2013, ***Lehigh University (Bethlehem, PA, USA)***

Ph.D. Candidate and Research Assistant

Department of Electrical and Computer Engineering (ECE)

P. C. Rossin College of Engineering and Applied Science & Center for Photonics and Nanoelectronics

Ph.D. Advisor: Prof. Nelson Tansu

Spring 2012 ***Lehigh University (Bethlehem, PA, USA)***

Substitute Lecturer

ECE 203: Engineering Electromagnetics (Junior UG level) – Spring 2012

Department of Electrical and Computer Engineering

P. C. Rossin College of Engineering and Applied Science

Research Interests and Areas

My research works cover various aspects of computational / advanced simulations, MOCVD growths (epitaxy), and device fabrication of III-Nitride semiconductor for photonics, thermoelectric, and solid state lighting applications. My research topics include the pursuit of novel materials for high thermoelectric figure of merit by using lattice-matched III-Nitride alloys, and the development of novel active regions and substrate engineering for enabling high performance UV and visible light-emitting diodes (LEDs) / lasers, and the engineering of advanced device concept (surface plasmon and nanostructure engineering) for achieving high internal quantum efficiency in III-Nitride LEDs for solid state lighting applications.

Awards & Honors Received

- ***2012 SPIE Scholarship in Optics and Photonics***, SPIE
- ***Sherman-Fairchild Fellowship for Solid State Studies*** (2012-2013), Lehigh University
- ***Sherman-Fairchild Fellowship for Solid State Studies*** (2011-2012), Lehigh University
- ***Lehigh University Research Assistantship*** (Aug. 2009- present), Lehigh University
- ***Lehigh University Dean's Scholarship*** (Aug. 2009- present), Lehigh University
- ***Best Graduation Thesis*** (June, 2009), Huazhong University of Science and Technology
- ***Excellent Graduate Award*** (June, 2009), Huazhong University of Science and Technology
- ***Public Scholarship*** (2005-2007), Huazhong University of Science and Technology
- ***Excellent Youth League Member*** (2005-2006), Huazhong University of Science and Technology
- ***Certificates for TEM-8 (Test for English Majors) and TEM-4***

Professional Affiliations

2010 – present, Student Member, Institute of Electrical and Electronics Engineers (IEEE)
2010 – present, Student Member, International Society for Optical Engineering (SPIE)
2010 – present, Student Member, American Physical Society (APS)

Refereed Journal and Conference Publications

Total First Authorship Refereed Publications: 21; Total Refereed Journal Publications: 22

1. (**Invited Conference Paper**) H. Zhao, G. Liu, R. A. Arif, Y. K. Ee, X. H. Li, **J. Zhang**, H. Tong, G. S. Huang, and N. Tansu, "Novel Approaches for Efficiency Enhancement in InGaN-Based Light-Emitting Diodes", in *Proc. of the 2nd International Conference on White LEDs and Solid State Lighting 2009*, Taipei, Taiwan, December 2009.
2. (**Invited Conference Paper**) H. Zhao, G. Liu, X. H. Li, Y. K. Ee, H. Tong, **J. Zhang**, G. S. Huang, and N. Tansu, "Novel Growth and Device Concepts for High-Efficiency InGaN Quantum Wells Light-Emitting Diodes," in *Proc. of the IEEE/OSA Conference on Lasers and Electro-Optics (CLEO) 2010*, San Jose, CA, May 2010.
3. G. Y. Liu, H. P. Zhao, **J. Zhang**, G. S. Huang, and N. Tansu, "Growths of Lattice-Matched AlInN Alloys on GaN," in *Proc. of the American Physical Society (APS) Annual March Meeting 2010*, Portland, Oregon, March 2010.
4. **J. Zhang**, H. Tong, G. Y. Liu, J. A. Herbsommer, G. S. Huang, and N. Tansu, "Thermoelectric Properties of MOVPE Grown AlInN Lattice-Matched to GaN," in *Proc. of the American Physical Society (APS) Annual March Meeting 2010*, Portland, Oregon, March 2010.
5. (**Invited Review Article**) N. Tansu, H. P. Zhao, G. Y. Liu, X. H. Li, **J. Zhang**, H. Tong, and Y. K. Ee, "Breakthrough in Photonics 2009: III-Nitride Photonics", *IEEE Photonics Journal*, vol. 2 (2), pp. 241-248, April 2010.
6. (**Invited Conference Paper**) H. P. Zhao, **J. Zhang**, G. Y. Liu, X. H. Li, Y. K. Ee, H. Tong, T. Toma, G. S. Huang, and N. Tansu, "Approaches for High-Efficiency InGaN Quantum Wells Light-Emitting Diodes – Device Physics and Epitaxy Engineering," in *Proc. of the American Vacuum Society (AVS) Meeting 2010*, Ann-Arbor, MI, May 2010.
7. (**Invited Conference Paper**) N. Tansu, H. P. Zhao, **J. Zhang**, G. Y. Liu, X. H. Li, H. Tong, T. Toma, G. S. Huang, and Y. K. Ee, "Device Physics and Epitaxy Engineering for High-Efficiency III-Nitride Light-Emitting Diodes," in *Proc. of the International Union of Materials Research Societies - International Conference on Electronic Materials (IUMRS-ICEM) 2010*, Seoul, Korea, August 2010.
8. **J. Zhang**, H. P. Zhao, and N. Tansu, "Effect of Crystal-Field Split-Off Hole and Heavy-Hole Bands Crossover on Gain Characteristics of High Al-Content AlGaN Quantum Well Lasers," *Appl. Phys. Lett.* vol. 97, Art. 111105, September 2010.
9. H. Tong [*], **J. Zhang** [*], G. Y. Liu, J. Herbsommer, G. S. Huang, and N. Tansu, "Thermoelectric Properties of Lattice-Matched AlInN Alloy Grown by Metalorganic Chemical Vapor

Deposition," *Appl. Phys. Lett.*, vol. 97, Art. 112105, September 2010. (* refers to co-first-authors)

10. (**Late Breaking News Paper**) H. Tong, J. Zhang, J. A. Herbsommer, G. S. Huang, and N. Tansu, "Record Thermoelectric Figure of Merit for MOVPE-Grown AlInN Alloys with Various In-Contents," *Proc. of the International Workshop on Nitride semiconductors (IWN) 2010*, Tampa Bay, FL, September 2010.
11. H. P. Zhao, J. Zhang, T. Toma, G. Y. Liu, J. D. Poplawsky, V. Dierolf, and N. Tansu, "Cathodoluminescence Characteristics of Linearly-Shaped Staggered InGaN Quantum Wells Light-Emitting Diodes," in *Proc. of the 23rd Annual Meeting of the IEEE Photonics Society*, Paper WY4, Denver, CO, November 2010.
12. J. Zhang, H. P. Zhao, and N. Tansu, "Gain and Spontaneous Emission Characteristics of High Al-Content AlGaN Quantum Well Lasers," in *Proc. of the 23rd Annual Meeting of the IEEE Photonics Society*, Paper MI4, Denver, CO, November 2010.
13. G. Y. Liu, H. P. Zhao, J. Zhang, H. Tong, G. S. Huang, and N. Tansu, "Growths of Lattice-Matched AlInN / GaN for Optoelectronics Applications," in *Proc. of the 23rd Annual Meeting of the IEEE Photonics Society*, Paper WY5, Denver, CO, November 2010.
14. G. Y. Liu, H. P. Zhao, J. Zhang, J. H. Park, L. J. Mawst, and N. Tansu, "Selective Area Epitaxy of Ultra-High Density InGaN Based Quantum Dots," in *Proc. of the 2011 IEEE Photonics Society Winter Topical Meeting on Low Dimensional Nanostructures and Sub-Wavelength Photonics*, Paper WA1.3, Keystone, CO, January 2011.
15. (**Invited Conference Paper**) N. Tansu, H. P. Zhao, J. Zhang, G. Y. Liu, X. H. Li, Y. K. Ee, R. B. Song, T. Toma, L. Zhao, and G. S. Huang, "Novel Approaches for High-Efficiency InGaN Quantum Wells Light-Emitting Diodes – Device Physics and Epitaxy Engineering," in *Proc. of the SPIE Photonics West 2011*, *LEDs: Materials, Devices, and Applications for Solid State Lighting XV*, Paper 7954-42, San Francisco, CA, Jan 2011.
16. H. P. Zhao, J. Zhang, T. Toma, G. Y. Liu, J. D. Poplawsky, V. Dierolf, and N. Tansu, "MOCVD Growths of Linearly-Shaped Staggered InGaN Quantum Wells Light-Emitting Diodes at Green Spectral Regime," in *Proc. of the SPIE Photonics West 2011*, *Gallium Nitride Materials and Devices VI*, Paper 7939-4, San Francisco, CA, Jan 2011.
17. J. Zhang, H. P. Zhao, and N. Tansu, "Gain Characteristics of Deep UV AlGaN Quantum Wells Lasers," in *Proc. of the SPIE Photonics West 2011*, *Novel In-Plane Semiconductor Lasers X*, Paper 7953-16, San Francisco, CA, Jan 2011.
18. J. Zhang, H. Tong, G. Y. Liu, J. A. Herbsommer, G. S. Huang, and N. Tansu, "Thermoelectric Properties of MOCVD-Grown AlInN Alloys with Various Compositions," in *Proc. of the SPIE Photonics West 2011*, *Gallium Nitride Materials and Devices VI*, Paper 7939-37, San Francisco, CA, Jan 2011.
19. J. Zhang, H. *Tong*, J. A. Herbsommer, and N. Tansu, "Analysis of Thermoelectric Properties of AlInN Semiconductor Alloys," in *Proc. of the SPIE Photonics West 2011*, *Physics and Simulation of Optoelectronics Devices XIX*, Paper 7933-32, San Francisco, CA, Jan 2011.
20. G. Sun, G. Xu, Y. J. Ding, H. P. Zhao, G. Y. Liu, J. Zhang, and N. Tansu, "Efficient Terahertz Generation from Multiple InGaN / GaN Quantum Wells," *IEEE J. Sel. Top. Quantum Electron.*, vol. 17(1), pp. 48-53, January-February 2011.
21. J. Zhang, H. Tong, G. Y. Liu, J. A. Herbsommer, G. S. Huang, and N. Tansu, "Characterizations of Seebeck Coefficients and Thermoelectric Figures of Merit for AlInN Alloys with Various In-Contents," *J. Appl. Phys.*, vol. 109(5), Art. 053706, March 2011.
22. J. Zhang, H. Tong, and N. Tansu, "Thermal Conductivity Characteristics of Three-Layer Superlattices," in *Proc. of the American Physical Society (APS) Annual March Meeting 2011*, Dallas, Texas, March 2011.
23. H. P. Zhao, J. Zhang, T. Toma, G. Y. Liu, J. D. Poplawsky, V. Dierolf, and N. Tansu, "MOCVD Growths of Linearly-Shaped Staggered InGaN Quantum Wells Light-Emitting Diodes," in *Proc. of the American Physical Society (APS) Annual March Meeting 2011*, Dallas, Texas, March 2011.

24. R. B. Song, L. Zhao, G. Y. Liu, J. Zhang, and N. Tansu, "Growths of InGaN Quantum Wells on GaN Micropyramids," in *Proc. of the American Physical Society (APS) Annual March Meeting 2011*, Dallas, Texas, March 2011.
25. G. Y. Liu, H. P. Zhao, J. Zhang, J. H. Park, L. J. Mawst, and N. Tansu, "Selective Area Epitaxy of Ultra-High Density InGaN Quantum Dots by Diblock Copolymer," *Nanoscale Res. Lett.*, vol. 6, Art. 342, April 2011.
26. H. P. Zhao, J. Zhang, G. Y. Liu, and N. Tansu, "Surface Plasmon Dispersion Engineering via Double-Metallic Au / Ag Layers for III-Nitride Based Light-Emitting Diodes," *Appl. Phys. Lett.*, vol. 98, Art. 151115, April 2011.
27. J. Zhang, H. P. Zhao, and N. Tansu, "Large Optical Gain AlGaN-Delta-GaN Quantum Wells Laser Active Regions in Mid- and Deep-Ultraviolet Spectral Regimes," *Appl. Phys. Lett.*, vol. 98, Art. 171111, April 2011.
28. H. P. Zhao, J. Zhang, G. Y. Liu, and N. Tansu, "Surface Plasmon Dispersion Engineering via Double-Metallic Au / Ag Layers for Nitride Light-Emitting Diodes," in *Proc. of the IEEE/OSA Conference on Lasers and Electro-Optics (CLEO) 2011*, Paper CWF5, Baltimore, MD, May 2011.
29. J. Zhang, H. P. Zhao, and N. Tansu, "High TE-Polarized Optical Gain from AlGaN-Delta-GaN Quantum Well for Deep UV Lasers," in *Proc. of the IEEE/OSA Conference on Lasers and Electro-Optics (CLEO) 2011*, Paper JTuD4, Baltimore, MD, May 2011.
30. G Y. Liu, H. P. Zhao, J. Zhang, and N. Tansu, "Growths of InGaN-Based Light-Emitting Diodes with AlInN Thin Barrier for Efficiency Droop Suppression," in *Proc. of the IEEE/OSA Conference on Lasers and Electro-Optics (CLEO) 2011*, Paper CMDD6, Baltimore, MD, May 2011.
31. G. Sun, G. B. Xu, Y. J. Ding, H. P. Zhao, G Y. Liu, J. Zhang, and N. Tansu, "High-Power Terahertz Generation due to Dipole Radiation within InGaN/GaN Multiple Quantum Wells," in *Proc. of the IEEE/OSA Conference on Lasers and Electro-Optics (CLEO) 2011*, Paper CMM4, Baltimore, MD, May 2011.
32. G. B. Xu, G. Sun, Y. J. Ding, H. P. Zhao, G. Y. Liu, J. Zhang, and N. Tansu, "Investigation of Blueshift of Photoluminescence Emission Peak in InGaN/GaN Multiple Quantum Wells," in *Proc. of the IEEE/OSA Conference on Lasers and Electro-Optics (CLEO) 2011*, Paper JWA70, Baltimore, MD, May 2011.
33. (**Invited Journal Paper**) H. P. Zhao, G. Y. Liu, J. Zhang, J. D. Poplawsky, V. Dierolf, and N. Tansu, "Approaches for high internal quantum efficiency green InGaN light-emitting diodes with large overlap quantum wells," *Optics Express*, vol. 19(S4), Pp. A991-A1007, July 2011.
34. G. Sun, G. B. Xu, Y. J. Ding, H. P. Zhao, G Y. Liu, J. Zhang, and N. Tansu, "Investigation of fast and slow decays in InGaN/GaN quantum wells," *Appl. Phys. Lett.*, vol. 99, Art. 081104, August 2011.
35. J. Zhang, S. Kutlu, G. Y. Liu, and N. Tansu, "High-Temperature Characteristics of Seebeck Coefficients for AlInN Alloys Grown by Metalorganic Vapor Phase Epitaxy," *J. Appl. Phys.*, vol. 110, Art. 043710, August 2011.
36. (**Invited Conference Paper**) H. P. Zhao, J. Zhang, and N. Tansu, "Physics of Novel III-Nitride Gain Media for Visible and Ultraviolet Lasers," *Proc. of the 24th Annual Meeting of the IEEE Photonics Society*, Arlington, VA, October 2011.
37. J. Zhang, and N. Tansu, "Improvement in spontaneous emission rates for InGaN quantum wells on ternary InGaN substrate for light-emitting diodes," *J. Appl. Phys.*, vol. 110, Art. 113110, December 2011.
38. J. Zhang, H. P. Zhao, and N. Tansu, "Engineering of AlGaN-Delta-GaN Quantum Wells Gain Media for Mid- and Deep-Ultraviolet Lasers," in *Proc. of the SPIE Photonics West 2012*, *Novel In-Plane Semiconductor Lasers XI*, San Francisco, CA, Jan 2012.
39. J. Zhang, and N. Tansu, "Spontaneous Emission Characteristics of InGaN Quantum Wells Light-Emitting Diodes on Ternary InGaN Substrates," in *Proc. of the SPIE Photonics West 2012*, *LEDs: Materials, Devices, and Applications for Solid State Lighting XVI*, San Francisco, CA, Jan 2012.

40. G. Y. Liu, **J. Zhang**, H. P. Zhao, and N. Tansu, "Device Characteristics of InGaN Quantum Well Light-Emitting Diodes with AlInN Thin Barrier Insertion," in *Proc. of the SPIE Photonics West 2012*, *Gallium Nitride Materials and Devices VII*, San Francisco, CA, Jan 2012.
41. G. Y. Liu, J. D. Poplawsky, **J. Zhang**, V. Dierolf, H. P. Zhao, and N. Tansu, "Quantum Efficiency Characterizations of Staggered InGaN Quantum Wells Light-Emitting Diodes by Temperature-Dependent Electroluminescence Measurement," in *Proc. of the SPIE Photonics West 2012*, *LEDs: Materials, Devices, and Applications for Solid State Lighting XVI*, San Francisco, CA, Jan 2012.
42. G. Y. Liu, **J. Zhang**, X. H. Li, G. S. Huang, T. Paskova, K. R. Evans, H. P. Zhao, and N. Tansu, "Metalorganic Vapor Phase Epitaxy and Characterizations of Nearly-Lattice-Matched AlInN Alloys on GaN / Sapphire Templates and Free-Standing GaN Substrates," *J. Crys. Growth*, vol. 340 (1), pp. 66-73, February 2012.
43. **(Invited Conference Talk)** N. Tansu, **J. Zhang**, G. Y. Liu, C. K. Tan, P. F. Zhu, and H. P. Zhao, "Advances in III-Nitride Semiconductors for Energy Efficiency Applications," in *Proc. of the KAUST-UCSB-NSF Solid State Lighting Workshop 2012*, Thuwal, Saudi Arabia, February 2012.
44. G. Sun, R. Chen, Y. J. Ding, H. P. Zhao, G. Y. Liu, **J. Zhang**, and N. Tansu, "Strikingly Different Behaviors of Photoluminescence Intensity and Terahertz Output Power versus Period of InGaN/GaN Quantum Wells," in *Proc. of the IEEE/OSA Conference on Lasers and Electro-Optics (CLEO) 2012*, San Francisco, CA, May 2012.
45. **(Invited Keynote Plenary Conference Talk)** N. Tansu, **J. Zhang**, G. Y. Liu, C. K. Tan, P. F. Zhu, and H. P. Zhao, "Physics and Technology of III-Nitride Semiconductors for Energy Efficiency Applications," in *Proc. of the IUMRS-ICYRAM Conference 2012*, Material Research Society (MRS), Singapore, July 2012.
46. **(Invited Conference Paper)** **J. Zhang**, G. Y. Liu, C. K. Tan, P. F. Zhu, H. P. Zhao, and N. Tansu, "Engineering Nanostructures in Active Regions and Devices for High-Efficiency III-Nitride Light-Emitting Diodes – Epitaxy and Physics," in *Proc. of the SPIE Optics + Photonics 2012*, NanoEpitaxy : Materials and Devices IV, San Diego, CA, August 2012.
47. G. Y. Liu, **J. Zhang**, C. K. Tan, and N. Tansu, "Characteristics of InGaN Quantum Wells Light-Emitting Diodes with Thin AlGaInN Barrier Layers," in *Proc. of the IEEE Photonics Conference 2012*, Burlingame, CA, Sep 2012.
48. **J. Zhang**, and N. Tansu, "Gain and Laser Characteristics of InGaN Quantum Wells on Ternary InGaN Substrates," in *Proc. of the IEEE Photonics Conference 2012*, Burlingame, CA, September 2012.
49. C. K. Tan, **J. Zhang**, X. H. Li, G. Y. Liu, and N. Tansu, "Dilute-As GaNAs Semiconductor for Visible Emitters," in *Proc. of the IEEE Photonics Conference 2012*, Burlingame, CA, September 2012.
50. P. F. Zhu, **J. Zhang**, G. Y. Liu, and N. Tansu, "FDTD Modeling of InGaN-Based Light-Emitting Diodes with Microsphere Arrays," in *Proc. of the IEEE Photonics Conference 2012*, Burlingame, CA, September 2012.
51. **(Invited Conference Paper)** N. Tansu, **J. Zhang**, G. Y. Liu, H. P. Zhao, C. K. Tan, and P. F. Zhu, "Physics of High-Efficiency III-Nitride Quantum Wells Light-Emitting Diodes," in *Proc. of the Asian Communications and Photonics (ACP) Conference 2012*, Guangzhou, China, November 2012.
52. **(Invited Conference Paper)** **J. Zhang**, H. Tong, G. Y. Liu, and N. Tansu, "III-Nitride Based Thermoelectric – Current Status and Future Potential," in *Proc. of the Asian Communications and Photonics (ACP) Conference 2012*, Guangzhou, China, November 2012.
53. G. Y. Liu, **J. Zhang**, C. K. Tan, and N. Tansu, "InGaN-Delta-InN Quantum Well Light-Emitting Diodes with Carrier Transport Effect," *Proc. of the SPIE Photonics West 2013*, San Francisco, CA, January 2013.
54. **J. Zhang**, and N. Tansu, "Optical and Polarization Properties with Staggered AlGaN Quantum Wells for Mid- and Deep-Ultraviolet Lasers and Light Emitting Diodes," *Proc. of the SPIE Photonics West 2013*, San Francisco, CA, January 2013.

55. P. F. Zhu, P. O. Weigel, G. Y. Liu, **J. Zhang**, A. L. Weldon, T. Muangnaphor, J. F. Gilchrist, and N. Tansu, "Optimization of Deposition Conditions for Silica / Polystyrene Microlens and Nanolens Arrays for Light Extraction Enhancement in GaN Light-Emitting Diodes," *Proc. of the SPIE Photonics West 2013*, San Francisco, CA, January 2013.
56. C. K. Tan, **J. Zhang**, G. Y. Liu, and N. Tansu, "Effect of Interband Energy Separation on the Interband Auger Processes in III-Nitride Semiconductors," *Proc. of the SPIE Photonics West 2013*, San Francisco, CA, Jan 2013.
57. G. Sun, R. Chen, Y. Ding, H. Zhao, G. Liu, **J. Zhang**, and N. Tansu, "Strikingly Different Behaviors of Photoluminescence and Terahertz Generation in InGaN/GaN Quantum Wells," IEEE J. Sel. Top. Quantum Electron., vol. 19, no. 1, Art. 8400106, January / February 2013. DOI: 10.1109/JSTQE.2012.2218093.
58. G. Xu, G. Sun, Y. J. Ding, H. P. Zhao, G. Y. Liu, **J. Zhang**, and N. Tansu, "Investigation of Large Stark Shifts in InGaN / GaN Multiple Quantum Wells", *J. Appl. Phys.*, vol. 113, Art. 033104, January 2013.
59. **J. Zhang**, and N. Tansu, "Optical Gain and Laser Characteristics of InGaN Quantum Wells on Ternary InGaN Substrates", *IEEE Photonics Journal*, vol. 5, no. 2, Art. 2600111, April 2013. DOI: 10.1109/JPHOT.2013.2247587
60. **J. Zhang**, and N. Tansu, "Engineering of AlGaN-Delta-GaN Quantum Wells Gain Media for Mid- and Deep-Ultraviolet Lasers", *IEEE Photonics Journal,* vol. 5, no. 2, Art. 2600209, April 2013. DOI: 10.1109/JPHOT.2013.2248705
61. H. P. Zhao, G. Y. Liu, **J. Zhang**, and N. Tansu, "Analysis of Internal Quantum Efficiency and Current Injection Efficiency in Nitride Light-Emitting Diodes", *Journal of Display Technology*, vol. 9, no. 4, pp. 212-225, April 2013. DOI: 10.1109/JDT.2013.2250252
62. C. K. Tan, **J. Zhang**, X. H. Li, G. Y. Liu, B. O. Tayo, and N. Tansu, "First-Principle Electronic Properties of Dilute-As GaNAs Alloy for Visible Light Emitters", *Journal of Display Technology*, vol. 9, no. 4, pp. 272-279, April 2013. DOI: 10.1109/JDT.2013.2248342
63. G. Y. Liu, **J. Zhang**, C. K. Tan, and N. Tansu, "Efficiency-Droop Suppression by Using Large-Bandgap AlGaInN Thin Barrier Layers in InGaN Quantum Wells Light-Emitting Diodes", *IEEE Photonics Journal*, vol. 5, no. 2, Art. 2201011, April 2013. DOI: 10.1109/JPHOT.2013.2255028
64. P. F. Zhu, G. Y. Liu, **J. Zhang**, and N. Tansu, "FDTD Analysis on Extraction Efficiency of GaN Light-Emitting Diodes with Microsphere Arrays", *Journal of Display Technology*, vol. 9, no. 5, pp. 313-319, May 2013. DOI: 10.1109/JDT.2013.2250253
65. X. H. Li, P. F. Zhu, G. Y. Liu, **J. Zhang**, R. B. Song, Y. K. Ee, P. Kumnorkaew, and J. F. Gilchrist, and N. Tansu, "Light Extraction Efficiency Enhancement of III-Nitride Light-Emitting Diodes by using 2-D Close-Packed TiO_2 Microsphere Arrays", *Journal of Display Technology,* vol. 9, no. 5, pp. 320-328, May 2013. DOI: 10.1109/JDT.2013.2246541

Submitted Refereed Journal and Conference Publications

66. **J. Zhang**, Hua Tong, Nelson Tansu, "Minimum Thermal Conductivity of Three-Layer Superlattices", *New Journal of Physics* (submitted).
67. Y. K. Ee, X. H. Li, **J. Zhang**, G. Y. Liu, H. P. Zhao, J. M. Biser, W. Cao, H. M. Chan, R.. P. Vinci, and N. Tansu, "Nano-pattern Pitch Dimension Dependence and Time-resolved Photoluminescence Study of InGaN Quantum Well Light-Emitting Diodes Grown by Abbreviated Growth Mode on Nano-patterned AGOG Substrate", *IEEE / OSA Journal of Display Technology* (submitted).
68. G. Y. Liu, **J. Zhang**, C. K. Tan, and N. Tansu, "Charateristics of InGaN-Delta-InN Quantum Wells Light-Emitting Diodes for Green, Yellow and Red Emission", *IEEE Photonics Journal* (submitted).

69. C. K. Tan, B. Tayo, J. Zhang, G. Y. Liu, N. Tansu, "First-Principle Natural Band Alignment of Dilute-As GaNAs Alloy", *IEEE / OSA Journal of Display Technology* (submitted).

Other Technical Publications

1. J. Zhang, W. Z. Lu, G. F. Fan, and F. Liang, "Microstructures and Electrical Properties of $Bi_{0.5}(Na_{1-x-y}K_xLi_y)_{0.5}TiO_3$ Lead-free Piezoelectric Ceramics", *Journal of Wuhan University of Technology-Materials Science Edition*, 25(3), 361-364, June 2010.

Selected Research Works Featured in Magazine / Newspapers

1. **"You build yourself into what you do"** in ***Lehigh News Center Highlight***, August 15th, 2012.
   http://www4.lehigh.edu/news/newsarticle.aspx?Channel=%2fChannels%2fNews%3a+2012&WorkflowItemID=aab27191-029a-43fa-9abe-198d4e34aea2
2. **"A Revolution in Lighting"** in Feature Section of **Resolve magazine**, vol. 2, Fall 2012.
   http://www.nxtbook.com/nxtbooks/lehigh/resolve_2012vol2/#/20
3. **"Nanoscale Work Yields Greener Lighting"** in Research Section of ***Lehigh Alumni Bulletin***, Winter 2012-2013.
   http://www.nxtbook.com/nxtbooks/lehigh/alumni_2013winter/#/14

Patents or Invention Disclosures

1. Nelson Tansu, Hua Tong, J. Zhang, Guangyu Liu, and Gensheng Huang, Novel techniques to achieve high thermoelectric figure of merit based on nitride semiconductor. (US Patent Pending).

Invited Seminars

1. J. Zhang, "III-Nitride Semiconductors for Photonics and Energy-Efficiency Technologies," School of Electrical, Computer and Energy Engineering, Ira A. Fulton Schools of Engineering, ***Arizona State University***, Tempe, Arizona, April 2013.
2. J. Zhang, "III-Nitride Semiconductors for Photonics and Energy-Efficiency Technologies," Department of Physics, ***St. John's University***, Queens, New York, April 2013.

Refereed Conference Program Committee / Presider

1. ***Conference Presider (Session Chair)*** – IEEE / SPIE / OSA Asia Communications and Photonics Conference (ACP) 2012, LED Technologies and Applications, Guangzhou, China, November 2012.

Journal Reviewing

1. ***IEEE Photonics Journal (IEEE)***
2. ***Optical Materials Express (Optical Society of America)***
3. ***Nanoscale Research Letters (Springer)***
4. ***IEEE/OSA Journal of Display Technology (IEEE / OSA)***
5. ***Nanoscale (RSC Publishing)***
6. ***Journal of Applied Physics (American Institute of Physics)***
7. ***Journal of Photonics for Energy (SPIE)***
8. ***Optics Letters (OSA)***

Internal Scientific Lectures & Seminars (Non-Refereed)

1. H. P. Zhao, G. Y. Liu, X. H. Li, J. Zhang, G. S. Huang, J. D. Poplawsky, V. Dierolf, and N. Tansu, "Enhancement of Radiative Efficiency via Staggered InGaN Quantum Well Light Emitting Diodes," Invited Poster Presentation in *Transformation in Lighting 2010,* DOE R&D Workshop on Solid State Lighting 2010, Raleigh, NC, USA, February 2010.
2. H. P. Zhao, G. Y. Liu, J. Zhang, T. Toma, G. S. Huang, J. Poplawsky, V. Dierolf, and N. Tansu, "Enhancement of Internal Quantum Efficiency with Staggered InGaN Quantum Wells Light

Emitting Diodes," Poster Presentation in *Lehigh Nano-Energy Workshop 2010,* ***Lehigh University***, Bethlehem, Pennsylvania, USA, September 2010.

3. H. Tong, **J. Zhang**, J. A. Herbsommer, G. Y. Liu, G.S. Huang, and N. Tansu, "Thermoelectric Characteristics and Measurements of AlInN," Poster Presentation in *Lehigh Nano-Energy Workshop 2010,* ***Lehigh University***, Bethlehem, Pennsylvania, USA, September 2010.
4. H. P. Zhao, G. Y. Liu, **J. Zhang**, T. Toma, G. S. Huang, J. Poplawsky, V. Dierolf, and N. Tansu, "Enhancement of Internal Quantum Efficiency with Staggered InGaN Quantum Wells Light Emitting Diodes," Poster Presentation in *Lehigh Center for Optical Technologies (COT) Open House 2010,* ***Lehigh University***, Bethlehem, Pennsylvania, USA, October 2010.
5. H. Tong, **J. Zhang**, J. A. Herbsommer, G. Y. Liu, G.S. Huang, and N. Tansu, "Thermoelectric Characteristics and Measurements of AlInN," Poster Presentation in *Lehigh Center for Optical Technologies (COT) Open House 2010,* ***Lehigh University***, Bethlehem, Pennsylvania, USA, October 2010.
6. **J. Zhang**, H. P. Zhao, and N. Tansu, "Physics of AlGaN Quantum Well Gain Media," Poster Presentation in *Lehigh Center for Optical Technologies (COT) Open House 2010,* ***Lehigh University***, Bethlehem, Pennsylvania, USA, November 2011.
7. H. P. Zhao, G. Y. Liu, **J. Zhang**, J. Poplawsky, V. Dierolf, and N. Tansu, "Enhancement of Internal Quantum Efficiency with InGaN Quantum Wells Light-Emitting Diodes with Large Overlap Design," Poster Presentation in *Lehigh Center for Optical Technologies (COT) Open House 2011,* ***Lehigh University***, Bethlehem, Pennsylvania, USA, November 2011.
8. **J. Zhang**, H. Tong, J. A. Herbsommer, G. Y. Liu, G.S. Huang, and N. Tansu, "Thermoelectric Characteristics and Measurements of III-Nitride Allloys," Poster Presentation in *Lehigh Center for Optical Technologies (COT) Open House 2011,* ***Lehigh University***, Bethlehem, Pennsylvania, USA, November 2011.

References

1. **Prof. Nelson Tansu** (PhD Advisor)
   New Century Endowed Chair Associate Professor in Engineering and Applied Science
   Department of Electrical and Computer Engineering
   Center for Photonics and Nanoelectronics
   Lehigh University, Bethlehem, PA 18015, USA
   Email: Tansu@Lehigh.Edu
   Cell Phone (484) 547-4818, Phone: (610) 758-2678, Fax: (610) 758-2605
   Research Group: http://www.ece.lehigh.edu/~tansu

2. **Prof. Filbert J. Bartoli**
   Chandler Weaver Chair Professor, and ECE Department Chair
   Department of Electrical and Computer Engineering
   Lehigh University
   Bethlehem, PA 18015, USA
   Email: fjb205@Lehigh.Edu Phone: (610) 758-4069
   http://www.ece.lehigh.edu/index.php?page=filbert-j-bartoli

3. **Prof. Luke J. Mawst**
   Professor
   Department of Electrical and Computer Engineering
   Reed Center for Photonics
   University of Wisconsin-Madison
   1415 Engineering Dr., Madison, WI 53706, USA
   Email: mawst@engr.wisc.edu Phone: (608) 263-1705
   http://www.engr.wisc.edu/ece/faculty/mawst_luke.html

4. **Prof. Xiuling Li**
   Associate Professor
   Department of Electrical and Computer Engineering
   University of Illinois at Urbana-Champaign
   2262 Micro and Nanotechnology Lab, 208 N. Wright Street, Urbana, Illinois 61801, USA
   Email: xiuling@Illinois.Edu Phone: (217) 265-6354
   http://wwwdev.ece.illinois.edu/directory/profile.asp?xiuling

5. **Prof. Michael J. Stavola**
   Sherman Fairchild Chair Professor of Physics
   Associate Dean for Research and Graduate Studies, College of Arts and Sciences
   Department of Physics
   Lehigh University, Bethlehem, PA 18015, USA
   Email: mjsa@Lehigh.Edu
   Phone: (610) 758-4282
   http://www.lehigh.edu/~mjsa/mjsa.html

6. **Prof. Hongping Zhao**
   Assistant Professor
   Department of Electrical Engineering and Computer Science
   Case Western Reserve University
   712 Glennan Building, 10900 Euclid Avenue, Cleveland, OH 44106, USA
   Email: hongping.zhao@case.edu Phone: (216) 368-4120
   http://engineering.case.edu/profiles/hxz168